Structural control for the applications of gelators

Thesis submitted in accordance with the requirements of the University of Liverpool for the degree of Doctor in Philosophy by Michael Nolan

June 2019

Abstract

The self-assembly of a phenylalanine-substituted perylene bisimide (PBI) gelator in aqueous solution triggered using a pH switch is studied in detail. Spectroscopy, rheology and neutron scattering are used as complementary techniques to characterize the anisotropic structures forming in solution as the pH is decreased. We show that the pH-drop results in worm-like micelles and longer fibres being formed. Photocatalytic solutions are prepared by mixing the PBI solutions with a hydrogen evolution catalyst, Pt, and an electron hole scavenger, methanol, to study the photocatalytic potential of the PBI aggregates. We show, through electrochemical and spectroscopic studies, that illumination of PBI solutions results in the formation of the radical anion and dianion reduced species. We provide evidence that the reduced anisotropic PBI aggregates are active photocatalysts for driving the hydrogen evolution reaction.

We expand the photocatalysis study to provide further intrinsic comparisons between self-assembled aggregates. A library of amino acid-substituted PBIs has been studied along with a range of solution compositions. We observe a wide range of photocatalytic activity between the different PBIs which can be related to the different packing arrangements. The addition of an anti-solvent also results in aggregation; at the pH values which show low photocatalytic activity, where there is a low concentration of aggregates, the addition of a solvent results in solvent-induced aggregation and a turn on in photocatalytic activity. This provides further evidence that self-assembly should be carefully considered when designing photocatalytic systems. We also show that when the PBI concentration is increased too high the amount of reduced PBI formed in solution reaches a plateau. Above 5 mg/mL PBI, the amount of radical anion formed during illumination remains the same. However, when lowering the PBI concentration, the rate of hydrogen evolution can dramatically increase. We find an optimum of ~150 $\mu molg^{-1}h^{-1}$ H_2 for PBI-V at 0.1 mg/mL under white light illumination.

Finally, we prepared a selection of gels using pH-switch and solvent-switch gelation methods and investigate their ability to recover their original morphology after shear. The networks of the gels before and after extrusion have been characterised in detail using confocal microscopy and neutron scattering. The solvent-switch gels are comprised of spherical domains which show good recovery after extrusion. On the other hand, the pH-switch gels which are comprised of a homogeneous dense fibrous network become fragmented after extrusion. This work

highlights the need to consider the morphology of low molecular weight gels when used for extrusion-based applications such as 3D printing and drug delivery and proposes design considerations when developing new materials.

Acknowledgements

I would like to express my gratitude to the University of Liverpool and the EPSRC for funding my studentship to carry out the work for this thesis. Thank you to all the technical and support staff at both the University of Liverpool and the University of Glasgow who have supported me and provided training throughout my PhD.

I would like to thank Professor Dave Adams and Dr Alex Cowan for their supervision over the last 4 years. Thank you for providing the invaluable opportunities for me to travel for conferences and for experiments. These experiences have opened my eyes to the wider scientific community and I am very grateful to have had the opportunities.

My thanks go to Dr James Walsh in the SIRE for his close support and training for photocatalytic, electrochemical and spectroscopy experiments. Thank you to Laura for her support and training for the neutron scattering experiments and to Emily, Charlotte, Bart, Steve, Sarah and Markus for their company and sanity (or lack of) during the various beam line experiments, these were my favourite experiments.

A big thank you to all those in the Adams group for their help and support. Thank you to Bart for the 3D printed menagerie, to Emily for the hashtags, to Ana-Mari for the omelettes, to Reza for the coffees, and to Sam and Kate for their bringing of all things Scottish. Glasgow will be dearly missed.

I am grateful to have had such strong support at home. The effortless support from my best friends Oli and Jamie has been invaluable. The biggest support, however, cannot easily be put into words. To Meghan, thank you for always being there, for all the train rides, the cups of tea, and for not surrendering me to the North.

Finally, thank you to all those who have shown me respect and have been patient with me during this time, qualities like these are by far the greatest motivators and it will always be appreciated.

List of Abbreviations

3D	3-dimensional
CB	Conductive band
CV	Cyclic voltammetry (or cyclic voltammogram)
DLS	Dynamic light scattering
DMF	Dimethylformamide
DMSO	Dimethyl sulfoxide
Eg	Optical band gap
FC	Flexible cylinder model
FTIR	Fourier transform infrared
G′	Storage modulus
G″	Loss modulus
GC	Gas chromatography
GdL	Glucono-δ-lactone
HER	Hydrogen evolution reaction
HOMO	Highest occupied molecular orbital
LED	Light emitting diode
LMWG	Low molecular weight gelator
LUMO	Lowest unoccupied molecular orbital
MeOH	Methanol
NMR	Nuclear magnetic resonance
NOE	Nuclear Overhauser effect
OD	Optical density
PBI	Perylene bisimide
PD	Polydispersity
PDI	Perylene diimide
PFG-NMR	Pulsed-field gradient nuclear magnetic resonance
PL	Power law model
PTCDA	Perylenetetracarboxylicacid dianhydride
PTCDI	Perylenetetracarboxylicacid diimide
PVP	Polyvinylpyrrolidone
RHE	Reversible hydrogen electrode
SANS	Small angle neutron scattering

SCE	Standard calomel electrode
SEC	Spectroelectrochemistry
SEM	Scanning electron microscopy
SHE	Standard hydrogen electrode
SLD	Scattering length density
Sp	Sphere model
SWV	Square wave voltammetry
TBAHFB	Tetrabutylammonium hexafluoroborate
TEM	Transmission electron microscopy
TGA	Thermogravimetric analysis
THF	Tetrahydrofuran
USANS	Ultra small angle neutron scattering
UV	Ultra violet
UV-Vis	Ultra-Violet Visible
VB	Valence Band
WSR	Water splitting reaction

Table of Contents

CHAPTER 1

Introduction

1.1. Low molecular weight gelators (LMWGs)

1.1.1. Introduction to LMWGs

It is common for molecules to be able to interact with each other spontaneously in solution. The process of spontaneous interactions directing the formation of larger structures containing many molecules is called self-assembly which is a thermodynamic process driven by non-covalent interactions such as π–π stacking, hydrophobic interactions and hydrogen bonding.[1] Low molecular weight gelators (LMWGs) are a class of materials with a low molecular weight, typically containing hydrophobic and hydrophilic groups which allow them to self-assemble into anisotropic one-dimensional structures in solution via intermolecular interactions. The one-dimensional structures can then cross-link and entangle into a 3D matrix which can immobilise a solvent via surface tension and capillary forces, forming a gel (Figure 1).[2–4] In some cases, LMWGs form self-assembled aggregates which are suspended in solutions.[5,6] The non-covalent nature of the interactions within low molecular weight gels means that their formation is reversible. For this class of material, the majority of the system is generally the solvent. In cases where the solvent is water (or predominantly water), the gels are called hydrogels. Hydrogels are useful in many applications such medicine,[7–9] electronics and sensing,[7,10,11] and 3D printing.[12,13] The hierarchical assembly of the LMWG is an important feature of their networks.

To prepare gel networks, the gelator is dissolved or dispersed in a solution and then a trigger is applied to promote self-assembly or entangling of networks by reducing the solubility of the gelator. Gelation triggers could be based on pH,[14–16] a heat-cool cycle, solvation,[17,33] addition of salts,[15,18] and mechanical agitation.[19]

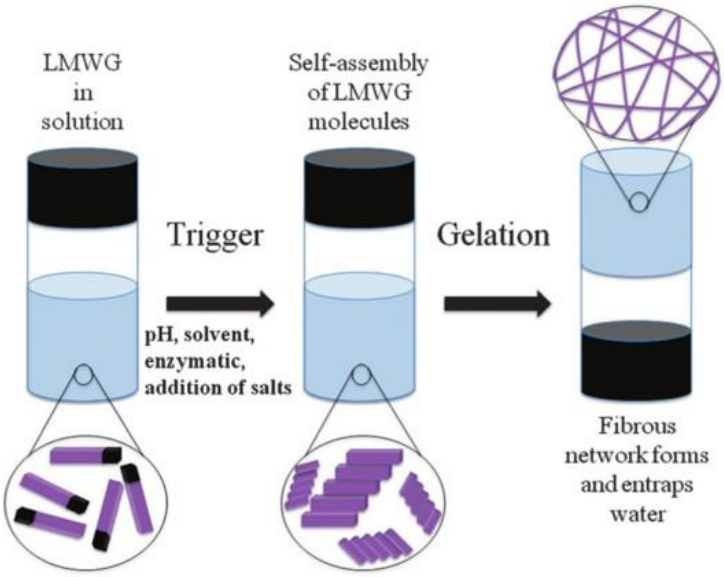

Figure 1. Schematic representation of the gelation process.[20]

The self-assembly of LMWGs in solution depends on the molecular structure of the gelator and the environment.[1] Environmental aspects such as temperature, solvent and pH all affect the extent and type of self-assembly.[20] For self-assembly to become prevalent, the intermolecular interactions should direct self-assembly into one-dimensional fibres and should overcome the solvation forces.[17,33] Figure 2 shows the intricacy of the hierarchical self-assembly. Interactions such as hydrophobic interactions, π–π stacking, hydrogen bonding and Van der Waals are factors in the self-assembly process. The molecular structure helps to direct self-assembly into one dimensional fibres which can be altered by the use of functional groups and sterics. The one-dimensional fibres of π-π stacked molecules can bundle and entangle together and, depending on their hydrophobicity and interactions with each other, can form networks of different morphologies. The type of gelation trigger can result in networks of different long-range order and can result in homogeneous or heterogeneous networks.

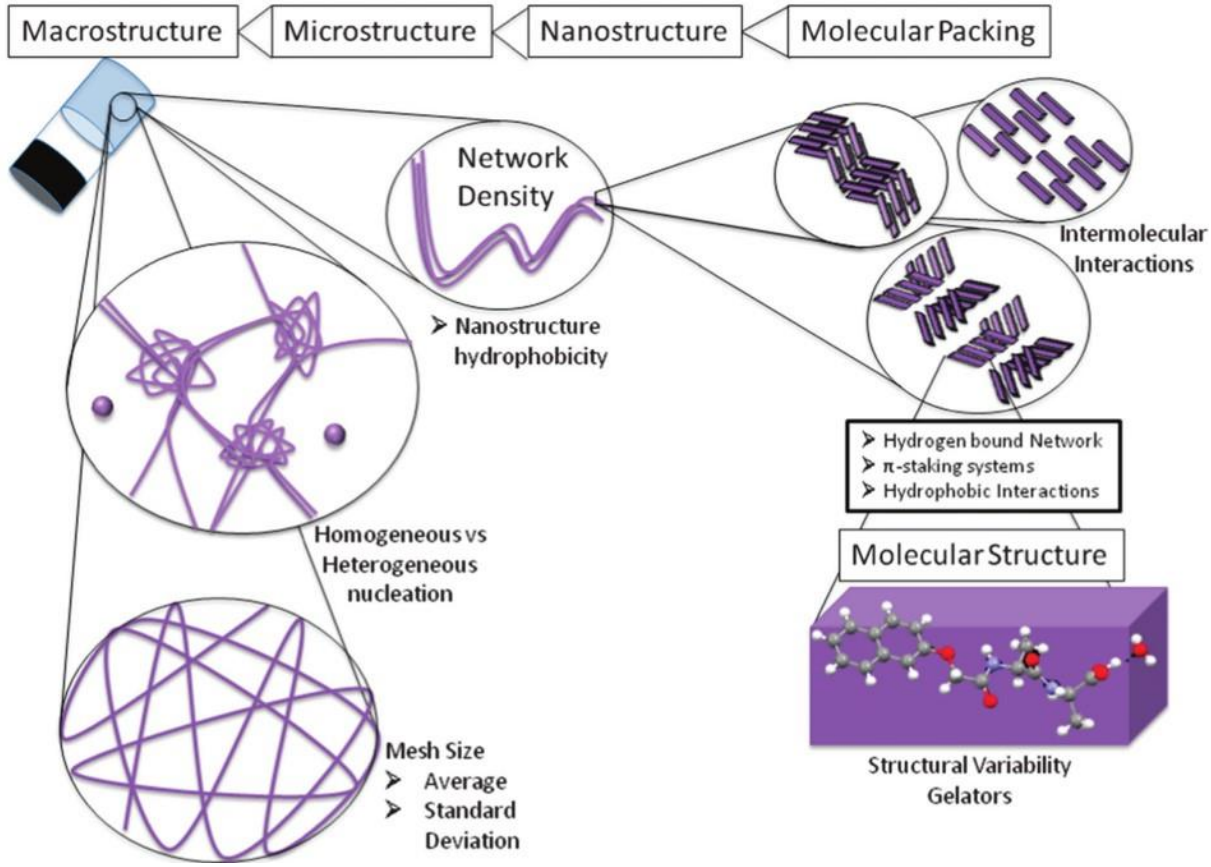

Figure 2. Schematic representation depicting the typical hierarchical assembly which makes up a LMWG gel.[20]

1.1.2. Formation of gel networks

Gels and LMWG suspensions can be prepared in many different ways and the different approaches can affect the final properties of the material.[20] The design of supramolecular gels and LMWG suspensions and the effect of this on the final properties is of key interest in this thesis. Although the preparation process can be easy, such as mixing two solutions together, there are many intricacies on the molecular scale which are not fully understood.[21] Furthermore, there are areas of discovery for gel applications which may have unlocked potential, such as their use in optoelectronics and photocatalysis. Understanding and controlling the self-assembly process helps to achieve the final network morphology, where certain network morphologies can give rise to tailored properties. For example, a highly crosslinked fibrous network can be mechanically stronger compared to a network containing many smaller, un-crosslinked fibres.[22] In many cases, the aggregation on a molecular scale may appear to be similar but the differences in the hierarchical assembly of gel networks can result in variable material properties.[23] The typical concentration needed for a LMWG to form a gel

is <1 wt% but the minimum gelation concentration will vary depending on the environment and type of gelator used.[23]

1.2. Structure of LMWGs

Altering the molecular structure of the molecules changes how adjacent molecules interact and stack together. Small changes on the molecular level can have a large effect on the 1-dimensional structures formed which can affect the overall gel morphology.[23] LMWGs often contain both hydrophobic and hydrophilic domains which can be tailored for gelation in organic or aqueous solvents. An understanding as to how molecules may interact together can drive the design process. However, suitable gelators are often found through serendipity[3,23] as only small changes in the molecular structure can change if it is able to form a gel or not,[23] making the design of suitable gelators difficult to predict. Computational methods are able to suggest particular molecular structures which are likely to form gels and descriptive-based methods have also been published to help direct the design of LMWGs.[24] Commonly however, iterations of molecules that are already known to gel are developed by altering the side chains to improve on properties of the aggregated material.[23] Functional groups can introduce extra interactions such as hydrophobicity, steric hindrance and directional hydrogen bonding. Functional groups can direct the way the LMWG can be gelled; for example, if carboxylic acid groups are present on the molecule then self-assembly in water can be controlled by decreasing the pH to lower the solubility in water which would promote intermolecular interactions. The main advantage of LMWG over polymer gels is the intermolecular interactions which allow physical responsivity to external stimuli, giving rise to functional materials. Also, many π-gelators are reported to exhibit a wide range of responsiveness to external stimuli, such as the photoresponsive properties of azobenzenes and stilbenes and optical properties of dye-based gelators like napthalimides and azo dyes.[25] π-gelators have applications in organic electronics, imaging and sensing.[25]

1.2.1. Ureas

Urea-based compounds can have the ability to form self-assembled structures and hydrogels due to the hydrogen bonding nature of the urea linkage (Figure 3).[26] Typically, ureas are organogelators. However, Feringa and co-workers established water soluble bis-ureas which included hydropohobic spacers and hydrophilic functionalitities for solubility in water (Figure 4).[27]

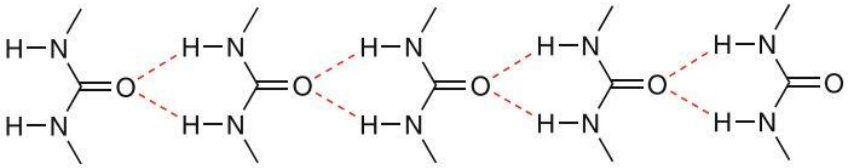

Figure 3. Hydrogen bonding (dotted lines) between urea linkages. Figure taken from Yamananka.[26]

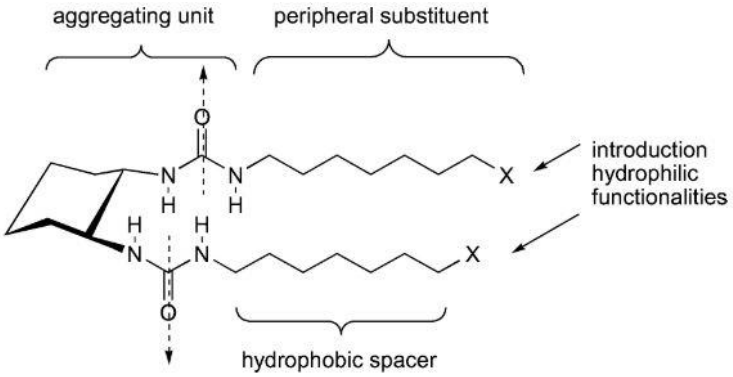

Figure 4. Modification of a cyclohexane bis-urea with hydrophilic functionality for water-based gelation. Figure from De Loos et al.[27]

Through a similar rational design another family of bis-ureas were developed where Hamilton and co-workers substituted free carboxylic acids and hydrophilic groups onto the bis-urea functionality (Figure 5).[28] The presence of carboxylic acids promoted water solubility and pH responsiveness. This is a similar rational design to the pH responsive amino-acid substituted compounds more recently prepared and studied by Adams et al.[15]

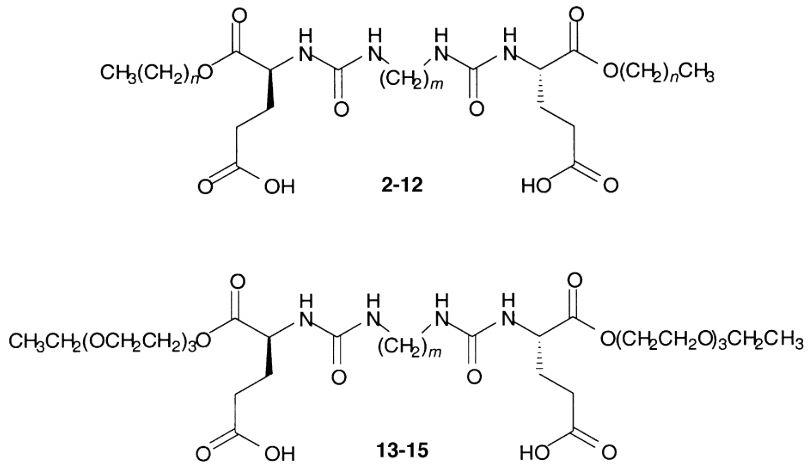

Figure 5. Substituted bis-urea compounds prepared by Hamilton and co-workers to gel water.[28]

1.2.2. Bile Acids

Bile acid derivates are rigid aliphatics which can form gels.[9,29] Bile acids are steroid compounds (Figure 6) found naturally within the body so their gels are commonly studied for biomedical applications.[29,30] The nature of the intermolecular interactions of molecular hydrogels means they can exhibit thixotropic and healing properties which is a keen area of interest for biocompatible gelators.[29] Self-assembly can be directed by utilising the hydrophilic and hydrophobic faces of the aliphatic group and the hydroxy groups present on the steroid unit can have a pronounced effect on the gelation ability.

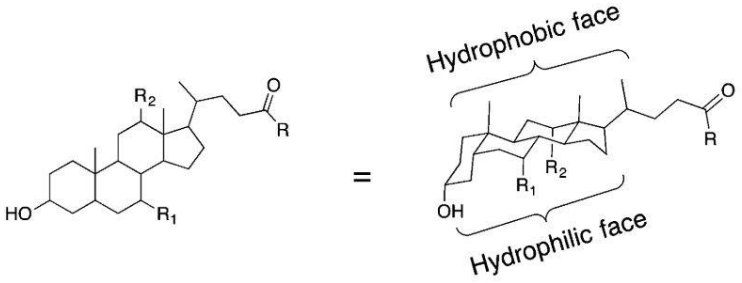

Figure 6. Bile acid structure.[31]

In 2004, Terech et al. prepared cationic bile salts (**Figure 7**) and studied their supramolecular structures in detail using scattering techniques and found that the gels contained distinct fibres which, depending on the molecular structure, bundled or entwined together.[32]

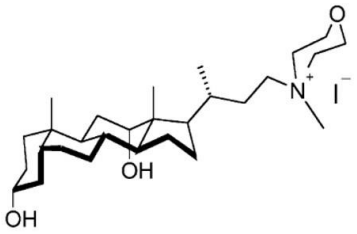

Figure 7. Cationic bile acid derivative.

Maitra and co-workers have provided useful reviews in the area of bile acid gelators and have also developed neutral bile acids which can assemble in solution such as in Figure 8.[30,33]

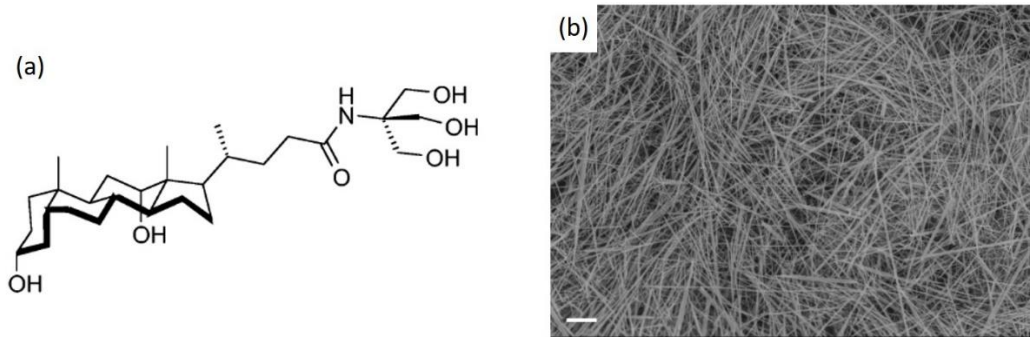

Figure 8. (a) Neutral bile acid derivative and (b) SEM image of a xerogel indicating the assembled fibres present from a 20% methanol/water gel. Scale bar indicates 10 μm[34]

1.2.3. Saccharides

Saccharides are hydrophilic and water-processable and contain several hydroxyl groups which provide areas for hydrogen bonding which can direct self-assembly and promote gelation (Figure 9).[35]

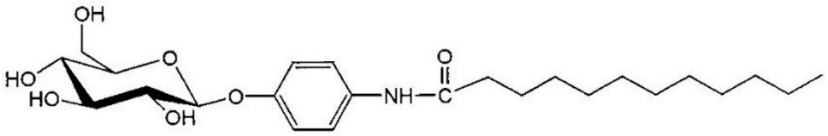

Figure 9. Saccharide-based gelator.[35]

Depending on the molecular structure, saccharides can also gel organic solvents.[36] Xu and co-workers summarise some of the many examples of monosaccharides and oligosaccharides which can aggregate in aqueous solutions to form gels[9] while Hamachi and co-workers describe a screening approach for finding saccharide gelators.[37] Hamachi et al. used one of their saccharide gelators to immobilise myoglobin within the gel matrix and they report that the myoglobin stays active for long periods. Protein activity upon immobilisation is usually reduced in polymer gels, so this work shows the advantage of low molecular weight gels. Furthermore, Shimizu and co-workers demonstrate the use of several sugar-based gelators and predict the molecular orientation for supramolecular packing for self-assembled fibres which are depicted in 3D as nanotubes.[38]

1.2.4. Dendrimers

Dendrimers are tree-like structures composed of repeated branched building blocks called dendrons. Dendrimers can be synthesised in a step-wise fashion by building up individual

layers of dendrons, this approach allows for careful design of the 3D environment of the dendrimer and provides opportunities for localised environments which can be tailored for applications and desired interactions. In 2005, Smith et al. provided an extensive review on the developments of the field of dendrimers, expressing the difficulty of dendrimer synthesis and the importance of using smaller dendrimers to build more complex supramolecular architectures.[39] Drugs can be encapsulated within dendrimers by utilising the localised environments and intermolecular interactions. Alternatively, drugs can be covalently attached allowing for slow release of the drug in vivo.[40]

Majoral and co-workers developed phosphorus containing dendrimers which are water soluble and have the ability to form supramolecular hydrogels, an example of one of these dendrimers can be found in Figure 10, where the tree-like architecture of the dendrimer is apparent.[41,42]

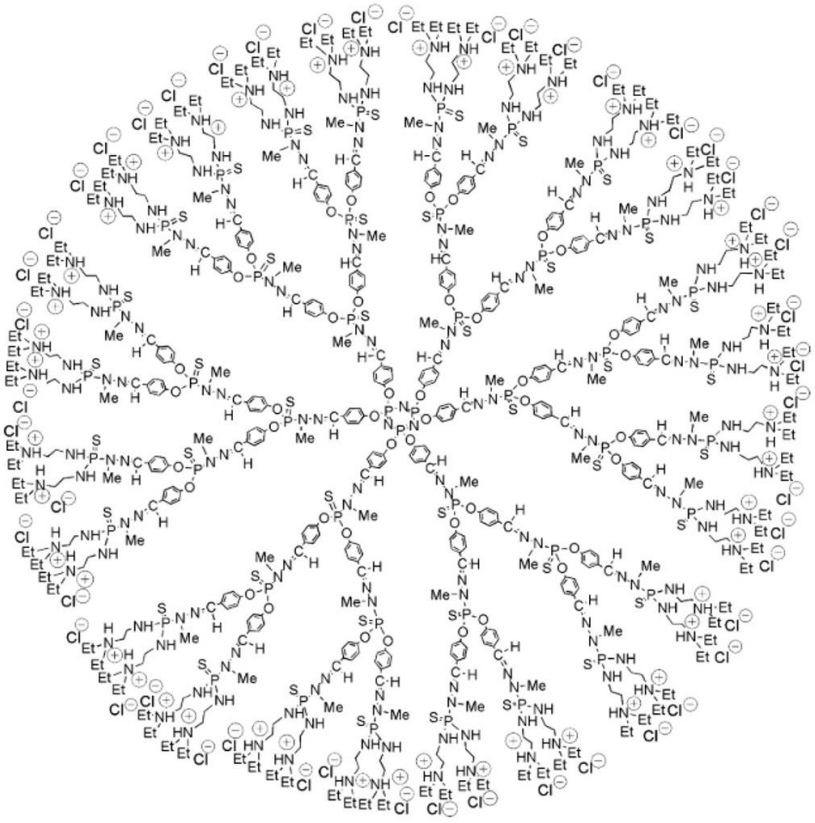

Figure 10. Phosphorus-containing water soluble dendrimer. Figure adapted from Caminade et al.[41]

Smith and co-workers have prepared two-component dendrimer gelators utilising an aliphatic diamine spacer linking two dendritic peptide groups.[43,44] Two-component dendrimers such as the one found in Figure 11 allows the opportunity for a higher degree of structural control. The

dendrimer can be prepared with a modified spacer or modified dendritic groups which allows for a finer structural control over the resulting supramolecular self-assembly.[43]

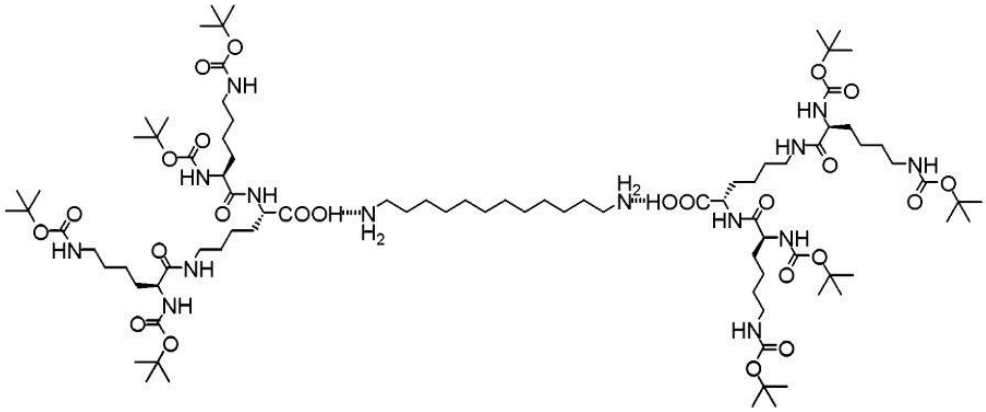

Figure 11. Two-component gelator. Figure adapted from Smith et al.[43]

1.2.5. Dye-derived Gelators

An extensive review published by Ajayaghosh and co-workers covers many dye-derived gelators which can self-assemble through π–π interactions and generally have a unique conjugation which is responsible for the optical properties.[25] Examples of such molecules are naphthalimides, perylene bisimides, azo dyes, stilbenes and coumarins. The photosensitivity of some of these compounds allows for functional gelators to be developed. For example, Draper et al. reported a coumarin-dipeptide based gelator which was modified post-gelation by UV photodimerization. Here, the UV irradiation promotes crosslinking chemistry and strengthens individual fibres.[22] Draper et al. then continued to report the subtle approach of spatially resolving multicomponent dyes (Figure 12) by exploiting the photosensitivity of a single stilbene-based dye component which, upon irradiation, undergoes a conformation change from *trans* (which gels) to *cis* (which cannot gel) and so selectively removes that single gel component.[45]

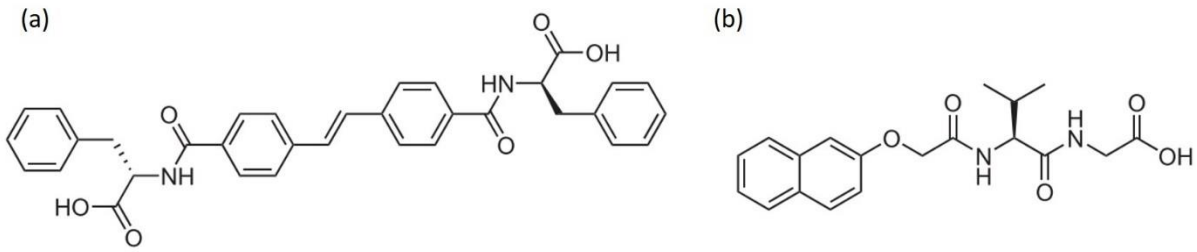

Figure 12. Two-component dye based gelator system composed of (a) *trans*-stilbene diphenylalanine and (b) a napthalene dipeptide.[45]

Perylene bisimides (PBIs) are widely studied as functional dye materials and Würthner et al. have published an extensive review on the use of these compounds as functional supramolecular materials.[46] The hydrophobic core promotes π–π interactions between molecules which helps to promote supramolecular organisation. Due to the highly absorbing and fluorescent core, PBIs are commonly studied for electronic applications. The structure of the perylene bisimide allows for substitution in various regions to give subtle control over the optical and physical properties. Figure 13 summarises how simple changes to the core structure of a PBI can have a profound effect on the highest occupied molecular orbital (HOMO) and lowest unoccupied molecular orbital (LUMO) values. The properties and uses of perylene bisimides will be discussed in more detail later in this chapter and will be a large focus within the experimental chapters of this thesis.

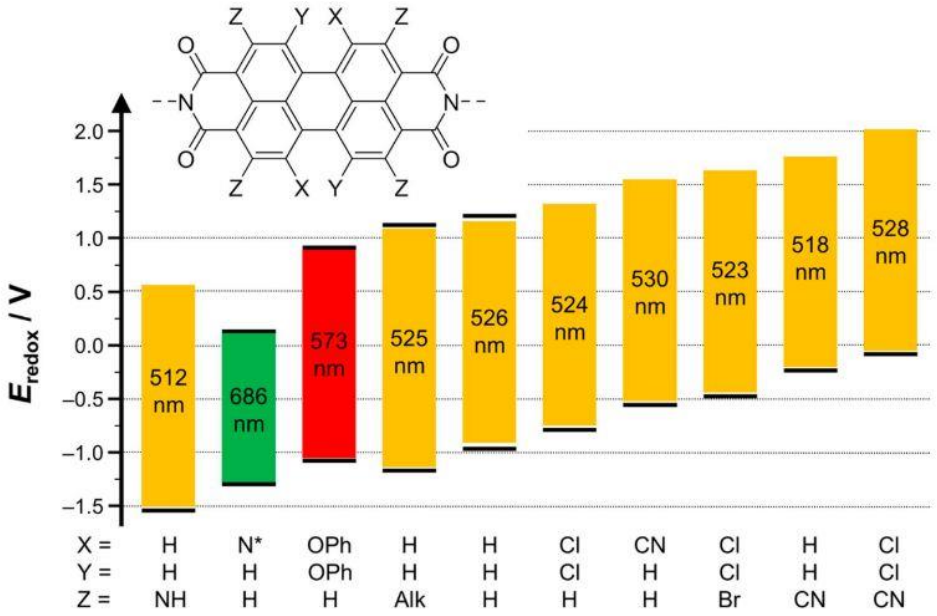

Figure 13. Comparison between side groups on a PBI and the resulting HOMO and LUMO values. Figure adapted from Würthner et al.[46]

1.2.6. Peptides

Short chains formed from various sequences of amino acids can result in supramolecular architectures with a wealth of self-assembled structures and architectures. Factors such as the pH, the type and concentration of electrolyte and gelator, the peptide type and sequence are key factors in the design of these materials.[47,48] Since these gelators are based around amino acids, they are often non-toxic and have use in biological applications. Koutsopoulos provides a useful review of the use of peptide structures for tissue engineering.[47] Tomasini et al. also

review the use of peptides and peptidomimetics, 'peptide-mimics', as low molecular weight gelators and summarise the use of various structures to append peptides such as Fmoc, pyrene, naphthyl, naphthalene and pyridines, all of which provide various sterics and physical interactions which can direct self-assembly alongside the unique hydrophobicity, sterics and directional H-bonding provided by the individual peptide chains (Figure 14).[48] Ulijn and co-workers also provide an informative review in the area of aromatic-based peptides and with a closer insight into those exhibiting amphiphilic structures, with a consideration of the effect of the peptide sequences on self-assembly.[49]

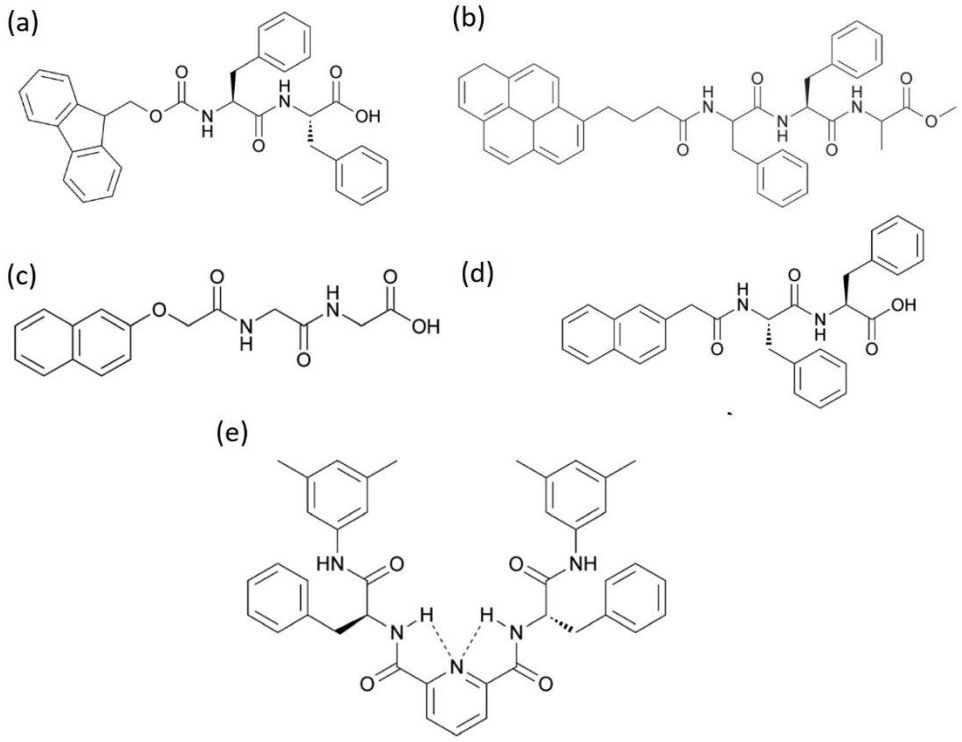

Figure 14. Structures of peptide-based low molecular weight gelators with various groups: (a) Fmoc, (b) pyrene, (c) naphthyl, (d) naphthalene and (e) pyridine-based peptide gelators. Figure adapted from Tomasini et al.[48]

Peptide amphiphiles have been studied extensively by Stupp and co-workers.[50] These molecules are short peptide chains with a hydrophobic segments attached which can give rise to many supramolecular structures (Figure 15). The centre of the peptide amphiphile contains peptides which supply hydrogen bonding interactions while the opposite ends are hydrophobic and hydrophilic directing the orientation of the molecule in assemblies to micellar, tubular and ribbon-type structures, typically where the primary structure is β-sheets.[51,52] The diversity of the interactions which can be used on the chain allows for optimisation for biological functions,

Stupp and co-workers have studied the use of these for regenerative medicine and cancer therapy.[52]

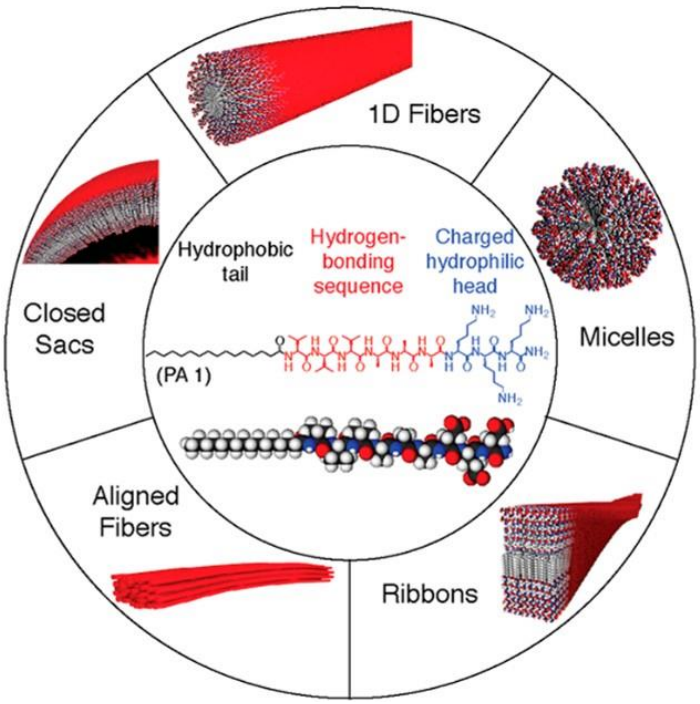

Figure 15. General structure of a peptide amphiphile (centre) surrounded by the possible supramolecular structures they can form. Figure adapted from Stupp and co-workers.[50]

Charge-complimentary peptides are another example of peptide-based low molecular weight gelators, Saiani and Miller and co-workers report on many of these compounds for structural analysis as well as for applications in drug release.[51,53,54] By controlling the charged state on the peptide and the fibrillar network, it is possible to control the rate of release of drug molecules from within the network. Figure 16 shows examples of differently charged peptides at neutral pH.[51]

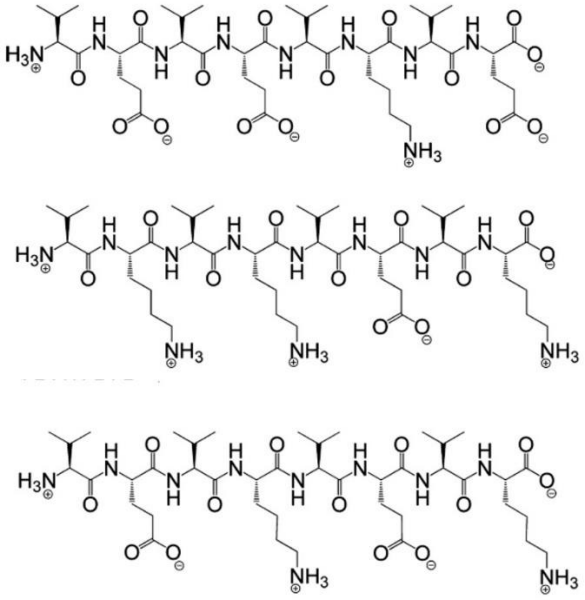

Figure 16. Three examples of the charges on peptides at pH 7. Figure adapted from Miller and co-workers.[51]

1.2.7. Aggregation

In many cases, LMWG are built around aromatic molecules that have the propensity to π stack. The close relationship between LMWG aggregation through π–π stacking and optical properties is an important attribute of the self-assembly processes and can be used to monitor the self-assembly process as well as help determine the type of molecular packing involved.[4,18,55–57] Generally, self-assembled aggregates of low molecular weight gelators which contain large aromatic domains are categorised into two arrangements: H and J-aggregates. H-aggregation describes a face-to-face stacked structure and a J-aggregate is a slip-stacked structure (Figure 17).[46] H aggregation gets its name from "hypochromic" as this type of aggregation results in a hypochromic (blue) shift of the absorption spectrum compared to the monomeric solution, due to a strong excitonic coupling between the closely packed molecules (Figure 17).[58] J-aggregation is named 'J' after E. Jelley who discovered the phenomenon.[59] In comparison, J-aggregation results in a bathochromic (red) shift of the absorbance bands. Concentration and temperature-dependent FTIR and ^{1}H NMR spectroscopy can be used to characterise the nature of the hydrogen bonds to understand the packing in more detail, as well as theoretical calculations.[60] Aggregation can be monitored by the emission intensity.[61,58,62] Fluorescent gelators may self-quench when more aggregated and so self-assembly can be followed by monitoring the emission intensity.

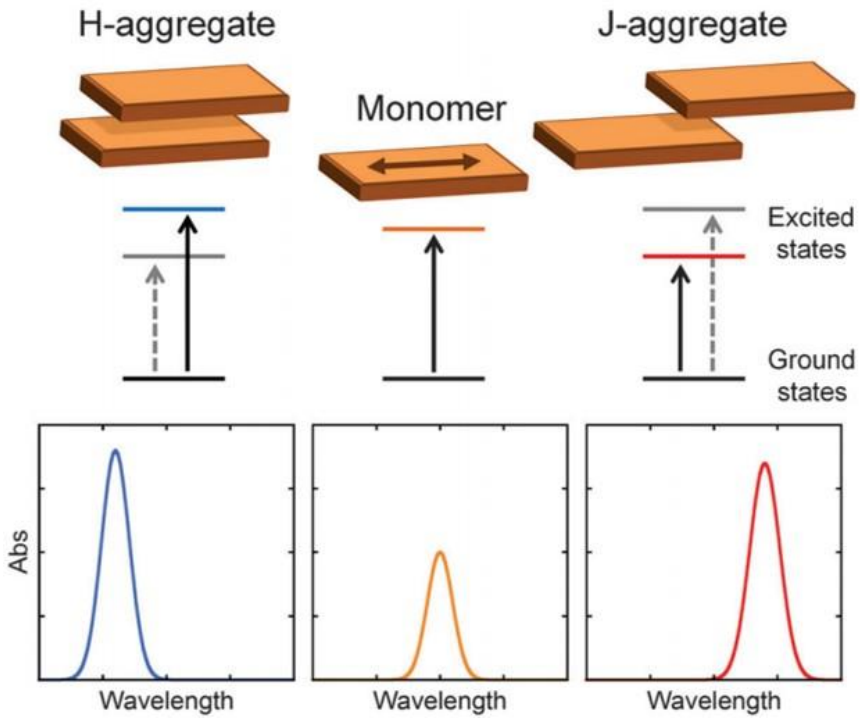

Figure 17. Schematic illustrating the stacking of PBI monomers (centre) to produce H-aggregates (left) and J-aggregates (right), and below the corresponding UV-Vis absorption spectra showing the blue and red shifts in spectra with respect to the monomer.[56]

1.3. Applications of LMWGs

The diverse range of LMWGs and the many triggers which can be used to promote aggregation can lead to many fascinating applications. The hierarchical assembly displayed by this class of material, along with their ease of preparation, makes them excellent candidates for industrial applications, of which a few will be described below.[2,3] Many LMWGs are peptide-based molecules which have good biocompatibility.[4] In biological applications, gelation can be used for the encapsulation of drugs where the solubility and pore size can determine the kinetics of dosage.[3] In some cases, the LMWG itself can be a modified drug molecule which can be dosed to a specific area to help provide a stable and localised high concentration of drug.[3] The drag effect, where diffusion is controlled by the morphology and interactions within the amorphous gel network, lends its use to membrane and separations technology using both wet and dried gel materials.[4] Additionally, hydrogels can be used as scaffolds for regenerative medicine.[7] The 3D matrix of a gel can act as a bridging matrix to help direct cell proliferation for tissue regeneration.[7] The design process is tailored so gels can form at physiological pH and promote the diffusion of biological components in and out of the gel, features of the biological components can be incorporated at the molecular design phase to help promote interactions.[7]

For this, the gelators should be able to gel under physiological conditions and be able to promote the diffusion of cells and biological components in and out of the matrix. Gelators are designed to form gels under physiological conditions. Also, when suitable gelators are used, the anisotropic features can provide use in optoelectronic applications where long-range electron transport materials have been developed and utilised in photovoltaics. Finally, as the gelation process can be highly responsive to external stimuli, LMWG can be designed for sensing applications. For example, a compound may change the solubility of a gel matrix which results in a change in fluorescence as the self-quenching fluorescence is altered and so certain molecules can be detected.[2,3]

1.3.1. Breaking and recovery of hydrogel networks

Low molecular weight gelator-based solutions and gels are non-Newtonian materials, i.e. they have a viscosity which is dependent on shear-rate.[63] The physical nature of these applications means the rheological properties of the gels are key. For many applications, polymeric gels are already used; common uses are for medicinal purposes such as in drug delivery and wound healing,[64–68] and they are also used in 3D printing.[69–72] However, such gels are often covalently cross-linked, meaning they are non-reversible. Whilst this can be a benefit, there are also potential drawbacks. In comparison, the non-covalent nature and reversible formation of low molecular weight gels means there is an interest in using these materials for their flow properties, such as for drug delivery and 3D printing.[3] LMWG gels have reversible physical properties and can be easily prepared and can be considered as alternatives to polymer gels for these applications.

Cells, drugs and catalysts can be encapsulated in regions of the gels which are trapped within the 3D network.[3,73] The network properties, such as pore size and hydrophobicity, determine the diffusion kinetics through the gel.[74–76] Many applications require the gel to flow and for the network to recover once the flow has ceased. Depending on the network and types of interactions within a gel, they may exhibit different physical properties during flow[77,78] such as shear thickening or thinning, thixotropic, as well as recovery properties. A gel is shear thickening or thinning when it becomes stronger or weaker when a high shear is applied respectively, and it can be thixotropic if it is able to flow through a capillary and recover its properties.[77] If gels are need to flow, then ideally only parts of the network will break during extrusion which can easily reform after shear,[79] during this time the primary fibres remain

stable and unchanged. Pochan and co-workers investigated the flow properties of β-hairpin peptide sheets using flow small angle neutron scattering (SANS); after the cessation of shear, the gels recovered immediately.[79] A model was proposed from the scattering measurements suggesting how, upon the application of shear, the network breaks into domains which can then flow past each other and recover quickly once shear has stopped (Figure 18).

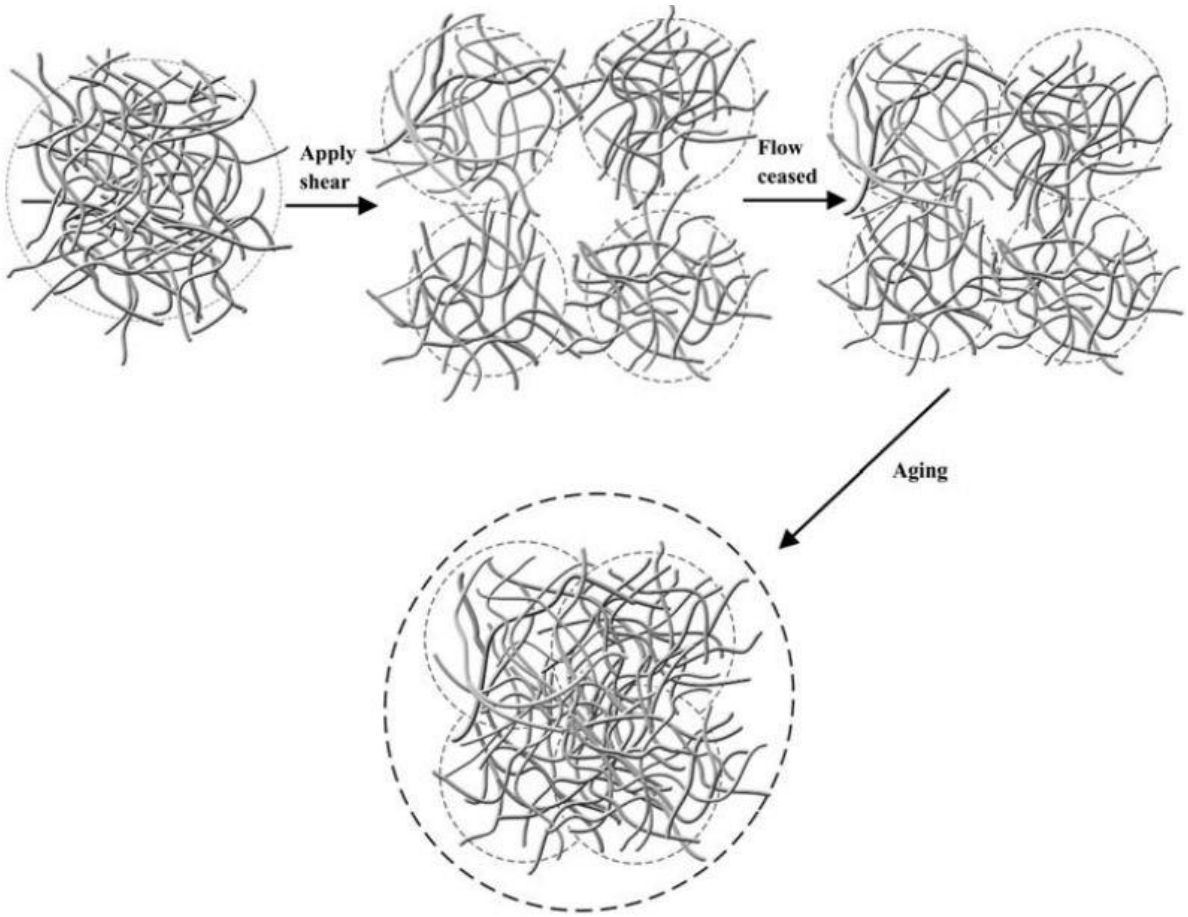

Figure 18. Suggested model of gel flow of a β-hairpin hydrogel. The gel structure fractures into domains under shear which allow the gel to flow. The gel recovers once shear is ceased.[79]

1.3.2. Organic Electronics

The advantage of LMWGs for organic electronics is that the shape, size, network morphology and optoelectronic properties can be finely tuned.[25,46,80–82] The stacking of low molecular weight gelators means they can create extended, intermolecularly π-conjugated systems suitable for optoelectronic applications.[25,46,80–82]

Semiconductors become conductive when a trigger is applied such as applying an electrical current or activating with a light source.[83,84] Photoconductive gelators have the ability to absorb light to create free electron charge carriers and holes, which can then be used for oxidation and reduction processes. This family of compounds is becoming an increasingly interesting focus of research due to their tuneable mechanical, electrical and optical properties.[85] Self-assembled photoconductive gelators are frequently researched for optoelectronic applications due to the many core compounds and derivatives which can be used, along with the wide range of processing methods which together provide a wealth of data and many areas for optimisation.[25,81,83,84,86–88]

Draper et al. studied the photoconductive ability of self-assembled perylene bisimides gelators.[89] An excited state, characterised as the reduced radical anion species by UV-Vis spectroscopy, was observed during and after UV irradiation. However, more importantly it was showcased that the gelators form 1-dimesional structures in solutions and that the excited state was remarkably long-lived in excess of 18 hours both in air and in the presence of water (Figure 19). Structural control over the activity of the gelators was also showcased where just small changes in the molecular structure by changing the amino acid side group resulted in largely different self-assembling and conductive properties, where the more ordered structures show higher conductivity.

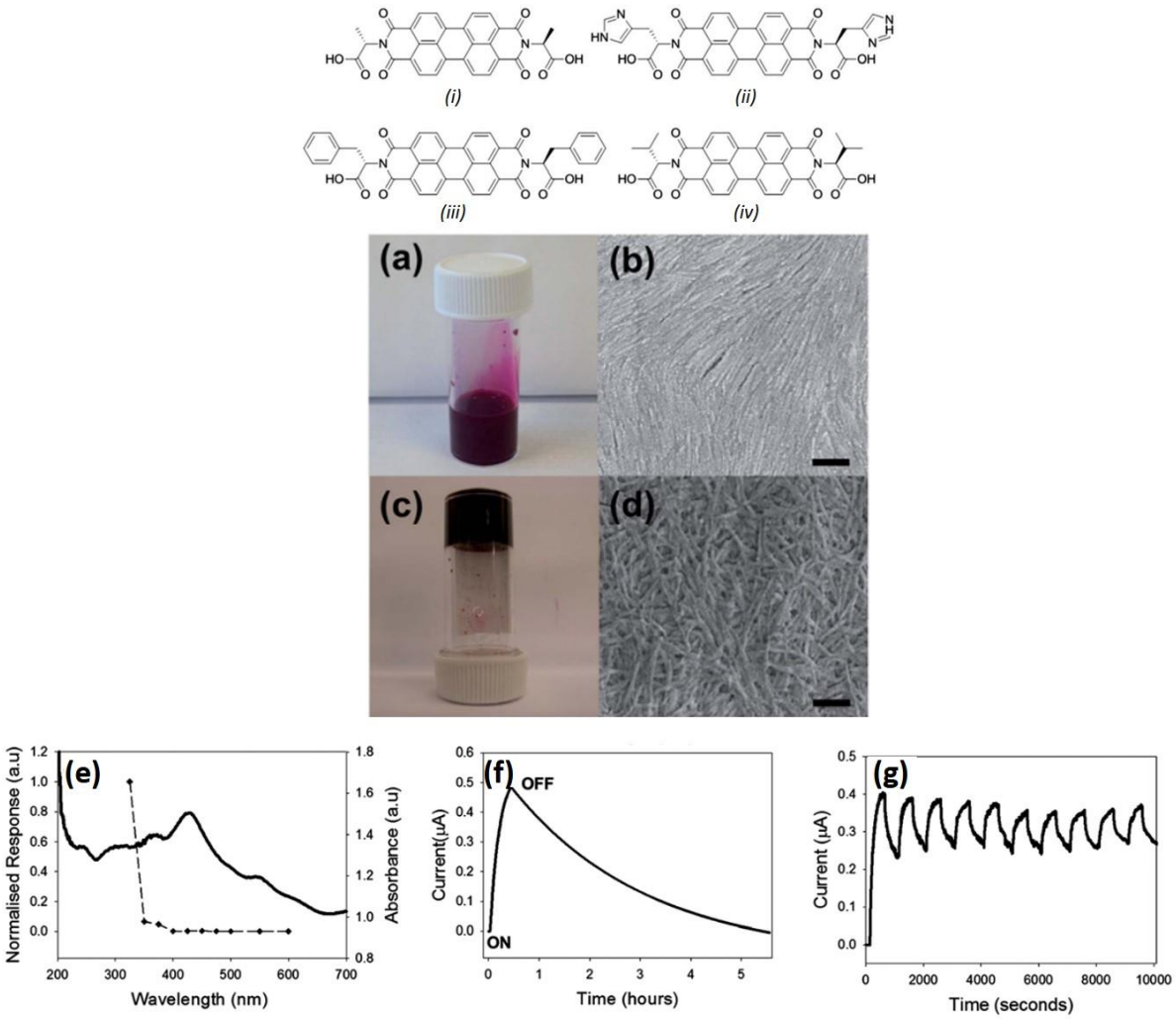

Figure 19. *(i-iv)* Perylene bisimide gelator compounds studied by Draper et al.; (a) Gelator *(i)* as a high pH solution; (b) SEM image of dried solution; (c) acidified solution of *(i)* forming a gel; (d) SEM image of dried gel; (e) photocurrent and irradiation wavelength of dried solution of *(i)* with UV-Vis spectrum; (f) photocurrent response of xerogel (i) with light on and off measurements; (g) ON-OFF photo-response of dried solution *(i)* showing cyclability. Figure Adapted from Draper et al.[89]

As mentioned above, the 3D network can also allow for additives such as electron acceptors or catalysts to be incorporated into the gel matrix. An efficient donor-acceptor system is required in photovoltaics, where the excited electrons can be donated to the acceptor to generate long lived free electrons and holes. Multi-component gels have been designed using p and n-type LMWGs which provide control over the p-n heterojunctions for applications in bulk heterojunction photovoltaics.[82,90–92] In 2015, Ajayaghosh and co-workers reported a two-component system where a p-type gelator and n-type gelator assembled separately, also known as self-sorting, which then formed heterojunctions between the fibres which increased

photoconductivity.[93] The choice of gelators were a trithienylenevinylene derivative (TTV) as a p-type gelator and a perylene bisimide derivative (PBI) as the accepting n-type gelator, the overlapping nature of the UV-Vis and the absorbance at longer wavelengths for the electron-accepting PBI fibres shows the suitability of the system (**Figure 20**).

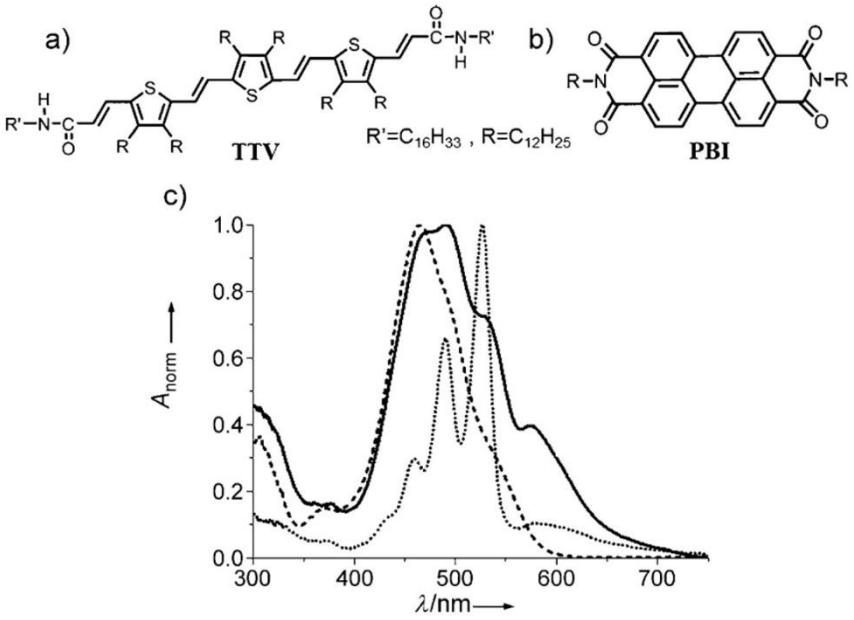

Figure 20. Structure of gelators (a) TTV and (b) PBI used in the two-component system, (c) UV-Vis absorption spectra of TTV (dashed line), PBI (dotted line) and 1:1 mixture (solid line) in *n*-decane. Figure adapted from Prasanthkumar et al.[93]

1.3.3. Organic Photocatalysis

Solar energy is a readily available and direct source of energy. As sunlight is intermittent and diffuse it needs to be harvested and stored so it can be used as a fuel source.[94] Photovoltaic cells convert solar energy into electrical energy, however as much of the energy used is from fuel the conversion of solar energy into a fuel source is important.[95] Because of this, there has been a growing interest in the area of photocatalysis. Photocatalysts harvest light energy and can transfer this to chemical energy, this can then be used to help process toxic chemicals in the environment which are released from industrial processes, catalyse the conversion of CO_2 to useful hydrocarbons, and aid the production of renewable fuels such as the production of hydrogen from the water splitting process.[96–98] Usually, these processes require a specific experimental setup and combination of materials which increases their complexity.[85,99–110] A wide range of materials can be used as photocatalysts including metal oxides, complex molecular catalysts and polymers.[111] As mentioned above, the highly tuneable characteristics

and use of abundant elements in organic molecules means there is a lot of interest in the use of organic photocatalysts.[95,112] Many organic photocatalysts are active under UV light illumination.[95,112,113] The activity of these systems are sensitive to the specific photocatalytic setup[114] and although this provides many opportunities to optimise a system it also means that comparisons between materials should be made using the same setup, which is difficult to reproduce across laboratories. Sprick et al. report different polymers which have strong sensitivity to the irradiation wavelength which can result in largely different activities.[114] It has also been reported by Schwarze et al. that the mixing of the system is important to produce reproducibility and that stirring of solutions, rather than circulation, is optimal for reproducibility within the same batch due to the lower shear stress.[115]

Water Splitting and the Hydrogen Evolution Reaction

Photochemical water splitting provides the ability to store solar energy in the stable chemical bonds found in H_2 and O_2 (Equation 1-Equation 3).[116,117]

Equation 1: $H_2O \rightarrow H_2 + ½O_2$

Equation 2: $H_2O \rightarrow ½O_2 + 2H^+ + 2e^-$

Equation 3: $2H^+ + 2e^- \rightarrow H_2$

The water splitting reaction (WSR) is a redox reaction which consists of two half-reactions, water oxidation (or oxygen evolution) and proton reduction (or hydrogen evolution). When completed all at once, the WSR can be housed in a cell which separates the explosive mixture of H_2 and O_2.[117] Z-scheme water splitting can help allow for the splitting of H_2 and O_2, here a 2-step excitation mechanism involving proton reduction and water oxidation are linked via a 'shuttle' redox couple such as I^-/IO_3^-.[117,118] This process requires the cumulative absorption of 4 photons to drive the two half reactions. A minimum potential required for proton reduction is 1.23 V *vs* the Normal Hydrogen Electrode (NHE) and for water oxidation is 0V vs NHE.[119] Running Equation 2 is challenging as it requires the oxidation of two water molecules in a four hole mechanism, making it necessary to use a suitable catalyst that can carry out a concerted mechanism.[120,121]

When proton reduction (Equation 3), also known as the hydrogen evolution reaction (HER), is run in isolation of the other water splitting half reaction then a source of electrons is needed to

provide the electrons for the proton reduction. A hole scavenger such as an alcohol or an amine will fill, or scavenge, the holes formed in the conduction band of the photocatalyst formed from excitation. Efficient scavenging of the holes of the photocatalyst is important in order to improve electron-hole separation and reduce the rate of recombination. Electron hole scavengers such as triethylamine and methanol can increase the efficiency of the hydrogen evolution reaction due to their oxidation potential being more negative than water.[122,123,124] The use of a sacrificial electron donor is not sustainable for a water splitting system but allows for one half reaction to be optimised in isolation. An energy diagram describing the photocatalytic hydrogen generation is shown in Figure 21.[95,125]

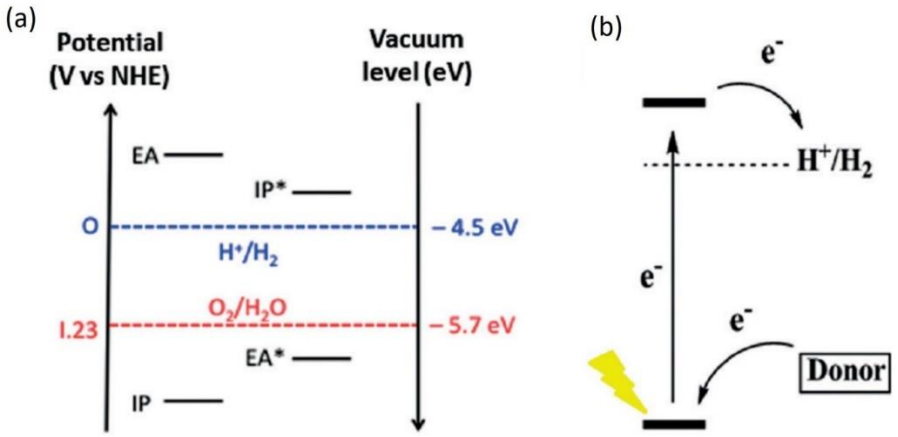

Figure 21. (a) Energy diagram for the water splitting reaction and (b) Photocatalytic hydrogen evolution with a photocatalyst and a sacrificial electron donor. Figure adapted from Pati et al.[95]

1.3.3.1. Conjugated Organic Photocatalysts

Organic semiconductors are carbon-based materials, often with functional groups attached. As carbon has tightly bound valence electrons compared to the third-row elements such as silicon,[126] the materials have a lower dielectric constant and are less polarisable compared to inorganic semi-conductors which results in the formation of excitons, rather than free charge carriers. However, the formation of the excited electrons can be easier as the absorption of these materials can span across the visible range of the spectrum and are not just confined to the UV wavelengths. Nano-structuring the material can help increase the diffusion of electrons from the tightly bound excitons to form free charge carriers, therefore supramolecular aggregation of organic dyes would help improve the mobility for free charge carrier.[121] It is common for complex molecular photocatalysts and nanostructured inorganic semiconductors to be studied for water splitting.[127] Typical inorganic semiconductors and many newly

developed photocatalysts for this process are produced from high energy-consuming processes which, upon industrial scale-up, may become difficult to justify.[108] Of course, the key to any emerging technology is its simplicity and economic viability. Many organic dyes are industrially available and comprised of abundant elements which help to satisfy the viability of using these as photocatalysts. Additionally, if their self-assembling properties can be utilised with simple preparation methods then the simplicity of LMWG use will help promote their future use in the field.

Carbon Nitride

Carbon-based nanomaterials such as carbon nanotubes, graphene and polymeric carbon nitride, C_3N_4, have been studied as organic photocatalysts. Polymeric C_3N_4 in particular has shown promising behaviour as a photocatalyst for both proton reduction and water oxidation in the presence of co-catalysts.[128–130] The averaged formula, C_3N_4, is spanned across sheets of carbon nitride which pack together to form a 3D framework. Polymeric C_3N_4 has high thermal and chemical stability, as shown by the repeated photocatalytic studies shown in Figure 22.[128] Steps have been taken to increase the absorption characteristics of C_3N_4 by complexing with dyes. Chen et al. show that complexing C_3N_4 with aggregates of perylene bisimide dyes leads to a significant increase in hydrogen production under visible light illumination.[107] Although the tightly bound structure does not allow for easy alteration of the structure for optimisation, many recent developments show much promise in the area of carbon nitride photocatalysis.[129]

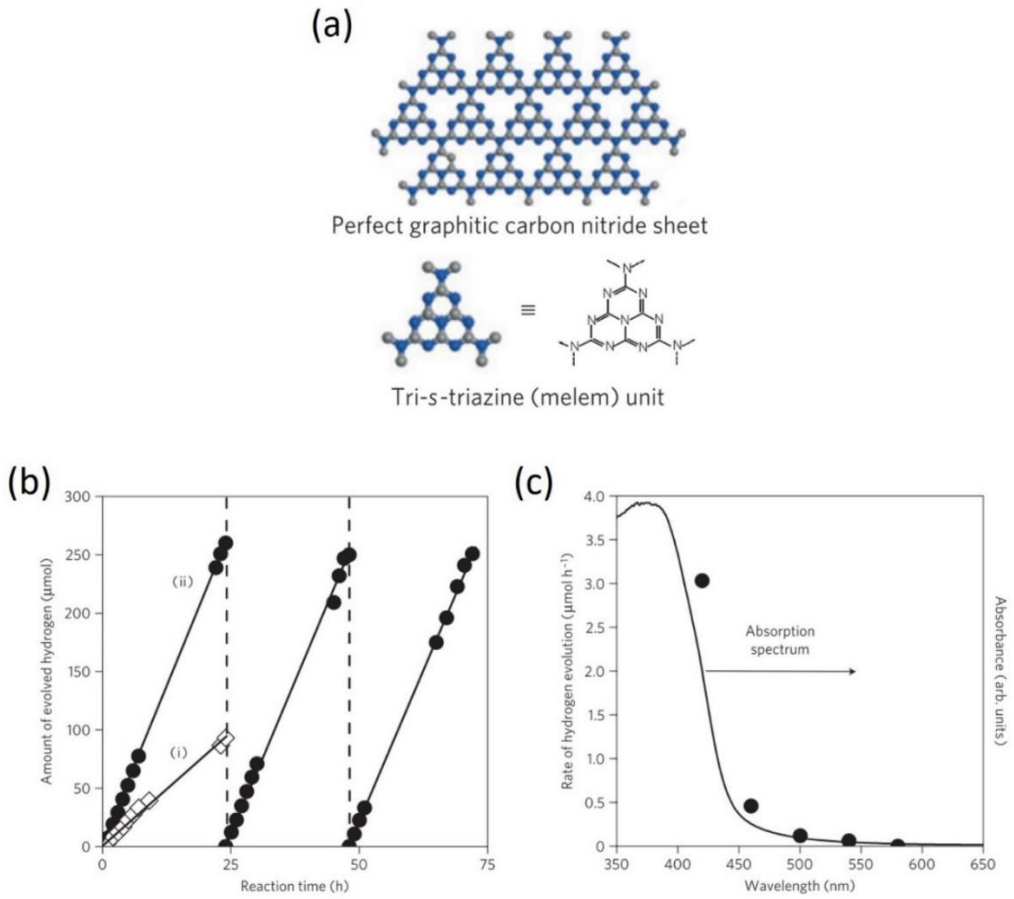

Figure 22. (a) Structure of perfect graphitic carbon nitride; (b) hydrogen evolution from water while irradiating C_3N_4/10 % triethanolamine solutions with light of wavelength >420 nm. (i) represents unmodified C_3N_4 and (ii) represents 3 wt% Pt-deposited C_3N_4; (c) Wavelength dependant hydrogen production from 0.5 wt% Pt-deposited C_3N_4 with 10% methanol, overlaid with the UV-Vis spectrum of C_3N_4. Figure adapted from Wang et al.[128]

Covalent Organic Frameworks

Covalent Organic Frameworks (COFs) are (often) crystalline polymers with a high degree of order. They are porous with a high surface area which can be highly tuned.[131] COFs have shown promise as photocatalytic materials.[95] Conjugated frameworks have the advantage that they can be easily modified in many ways to achieve the desired results for their physical, chemical and optical properties. Although many COFs show low solubility and poor dispersion in aqueous solutions, these can be tuned further to improve their processing properties. Stegbauer et al. prepared a crystalline hydrazine-based COF which showed activity for hydrogen evolution in the presence of platinum and a sacrificial electron donor (Figure 23).[132] Here, the energy difference between the highest occupied molecular orbital and the lowest unoccupied

molecular orbitals, known as the band gap, is 2.8 eV which means the material has visible light absorption properties. COFs have highly tuneable scaffolds, a high surface area and many areas on their framework to provide functionality and show much promise for the future. Triazine-based frameworks have also been developed where the substitution of the more electronegative nitrogen atoms can lower the band gap which may increase hydrogen evolution activity.[133,134]

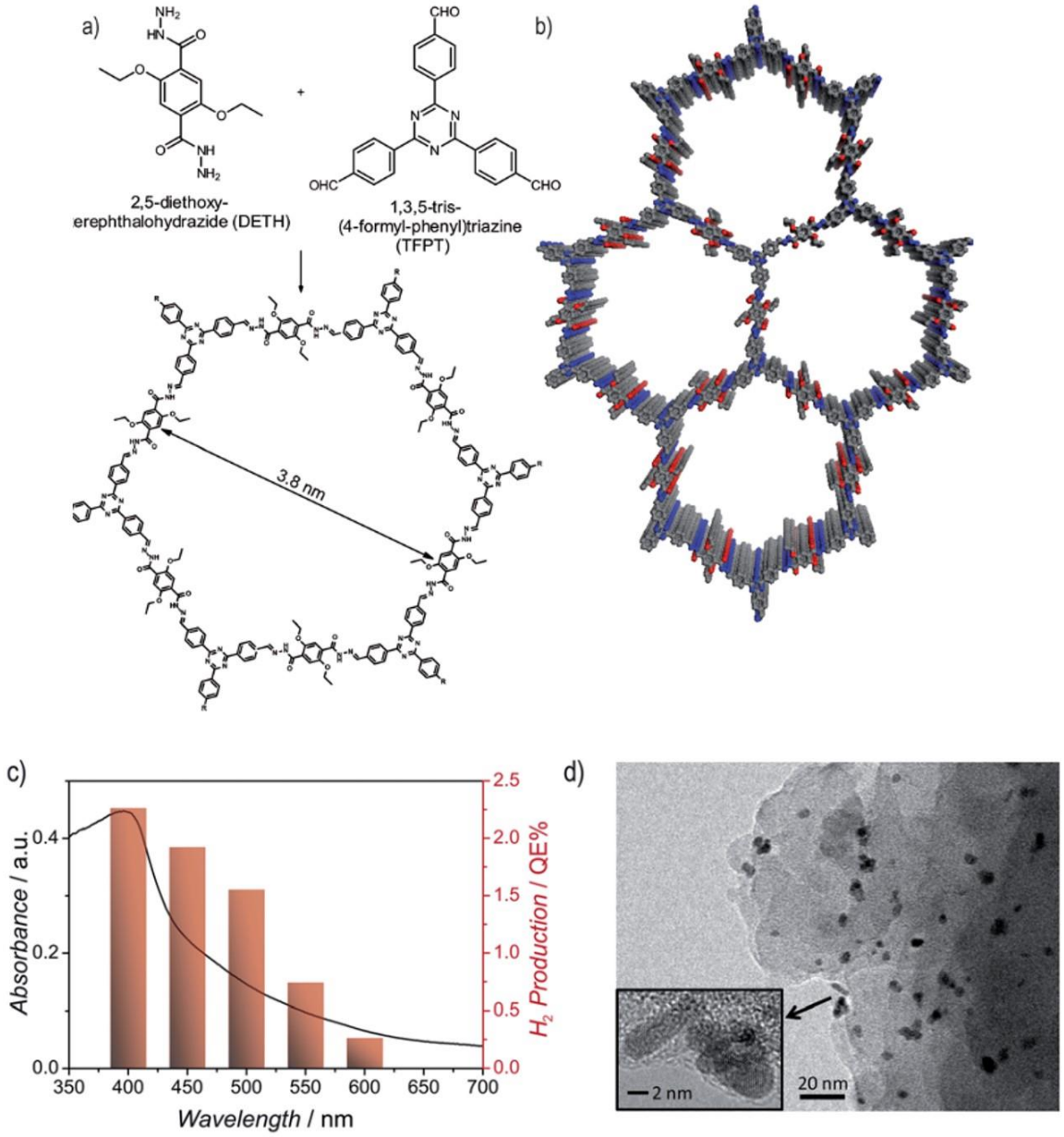

Figure 23. (a) Condensation reaction showing the formation of a planar honeycomb-type COF (b) Cofacial stacking of the 2D COF segments, resulting in a 3D porous hexagonal lattice (grey: carbon, blue: nitrogen, red: oxygen), (c) UV-Vis absorption of COF with wavelength-dependant hydrogen production of Pt-modified COF in 10 vol% triethanolamine using 40 nm Full-width-half-maximum band-pass filters, (d) TEM image of COF after 84 hours illumination showing Pt nanoparticles (5 nm) alongside the COF. Figure adapted from Deblase et al.[132]

Conjugated Polymers

Polymers can be highly conjugated materials and as they can be prepared from monomers they can be easily synthesised up by a step-wise preparation, creating a wealth of polymeric materials. Typical considerations when preparing conjugated polymers are conjugation length and the use of heterojunctions. For example, Sprick et al. showed that hydrogen evolution activity increased when the conjugation length of the polymer photocatalyst increases.[113] Surface area and optical band gap were also tuned by control over the monomer composition of the polymers. A consideration of the efficiency of charge separation can also be implemented, such as creating a co-polymer comprised of electron-rich and electron-defficient monomers, creating an intra-molecular donor-acceptor system.[135–137] The donor-acceptor system results in increased charge separation due to efficient charge transfer along the polymer.

Low Molecular Weight Photocatalysts

Self-assembled small organic molecules for photocatalysis have recently gained interest.[85,99,103] Using low molecular weight gelators as photocatalysts to drive reactions is an interesting concept and examples of their uses vary, many involve combining the organic gelator with metal co-catalysts.[100–102,104–106,108–110] For example, Stupp and co-workers utilised a perylene monoimide with a salt-switch gelation method in conjunction with a nickel photocatalyst for hydrogen evolution. This work will be described in more detail later in this chapter.[138] Using organic dyes which can self-assemble has many advantages. Dyes have strong absorption bands in the visible light region of the spectrum meaning they have access to a lot of the Sun's energy. They can also be adsorbed onto the surface of semi-conductors such as metal oxides to help improve efficiency by donating more electrons into the conduction band. For example, Finke and co-workers utilised an indium tin oxide semiconducting layer as a charge transport layer while a perylene bisimide photocatalyst and cobalt oxide metal co-catalyst were deposited onto the surface.[139] As many metal oxide catalysts only show absorption bands in the UV region of the spectrum then using dyes can help utilise a wider range of light.

1.4. Perylene bisimides

Perylene diimides, or perylene bisimides (PBIs) are interesting candidates as photocatalysts as they exhibit large absorption coefficients in the visible absorption spectrum, can be modified to express self-assembling properties as LMWGs and are organic n-type semiconductors.[85] PBIs are comprised of earth-abundant elements and the parent compound perylene-3,4,9,10-

tetracarboxylic dianhydride is widely available and used as an industrial dye, Pigment Red 224. The imidization of the anhydride groups is an easy one-pot synthesis and uses cheap and readily available materials.[140] As mentioned previously, the key to any emerging technology is its simplicity and economic viability and PBIs are able to satisfy these parameters. As a result, PBIs have been regularly used in dye sensitised solar cells and in bulk heterojunction photovoltaics and are being studied for applications in photocatalysis.[85,88,89,105,108,141,142]

Perylene derivatives have been studied for many years with their structures advancing over time with substituents on the *bay*, *ortho* and *peri* positions (Figure 24).[85] PBIs have a tendency to assemble in low concentrations via intermolecular forces such as π -stacking, hydrogen bonding and Van der Waals forces to form viscous solutions and hydrogels.[105,143–146] Characteristically, the perylene core has a strong absorbance in the visible region of the electromagnetic spectrum. When self-assembled into 1-dimensional structures, the overlapping of the molecular orbitals allow the transfer of π-electrons through the network.[85] The type and extent of the interactions between adjacent molecules alters the optical properties of the bulk material. Adding substituents on both the aromatic core and peripheral imides is commonly used to tune both their optical and physical properties.[46,85,108,140,147]

A closely packed system like the π–π stacked PBIs is ideal for the transport of electrons. Providing the exciton can separate, then the free electron can be transferred to a hydrogen evolution catalyst and depending on the exciton diffusion length then the electron donation could occur some distance away from where the photons were absorbed. Würthner and co-workers report many examples of exciton diffusion in perylene bisimide materials[148–151] and in some cases showing unprecedented distances of up to 100 nm.[149]

The type of aggregation is key to the electron transport properties. Many examples in the literature state the differences between H- and J-aggregation,[59] however the extent of hierarchical self-assembly is much more complex than just H- and J-aggregation.[142] As mentioned above, the same molecule can be exposed to different conditions which can result in largely different self-assembled networks. The subtlety of this approach means that comparisons between different self-assembled aggregates can be made while using the same molecule. This concept is explored within this thesis.

1.4.1. Structure and self-assembly of perylene bisimides

Substitution onto the perylene core can be optimised to fine tune the desired properties of the material. Functionalising the perylene core in both the *bay* and *ortho* positions can fine tune the solubility, orbital energies and optical properties (Figure 24).[140] *Ortho*-substitution in particular provides a way to modify the electronic properties of the perylene core without introducing unwanted torsion,[85] however adding bulky substituents into the bay position can induce torsion onto the planar core.[152] For instance, bulky *ortho*-substituted PBIs show less self-assembly than *bay*- and *non*-substituted PBIs. Distortions of the perylene core can inhibit the close packing between molecules and inhibit intermolecular forces such as π–π stacking, van der Waals and hydrogen bonding between adjacent PBIs which will alter the absorption, emission, conductivity and supramolecular structure of the material.[140] Those PBIs which have unsubstituted perylene cores also usually have lower solubility in aqueous solvents due to the large planar hydrophobic aromatic core.[140]

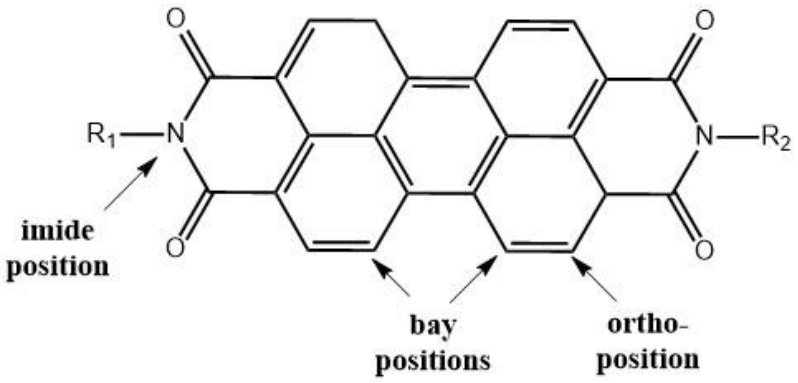

Figure 24. Molecular structure of the perylene bisimide core, where R^1 and R^2 represent substituents at the imide position.

Substitutions on the imide position of PBIs have a minimal effect on the absorbance properties as an orbital node is present at the imide position[46] Therefore, the addition of imide substituents can be used to tune the solubility and self-assembly of the molecules without affecting the core optical properties.[46,140,147,153] The role of the imide substituents can have additional effects such as the addition of the electron donating aniline can undergo intramolecular electron donation to effectively scavenge the electron deficient hole and aid charge separation.[108]

As mentioned above, analysing the optical properties of a gelator can help determine the extent of aggregation in solution. For example, some PBIs can form aggregates in chloroform which

become more monomeric in more protic solvents such as methanol.[61,154] A PBI derivative has been aggregated into 1-D nanofibers with the use of aprotic chloroform, whereas polar THF promotes dissolution of this PBI which results in the formation of more particle-like aggregates on glass substrates after spin-coating (Figure 25).[155]

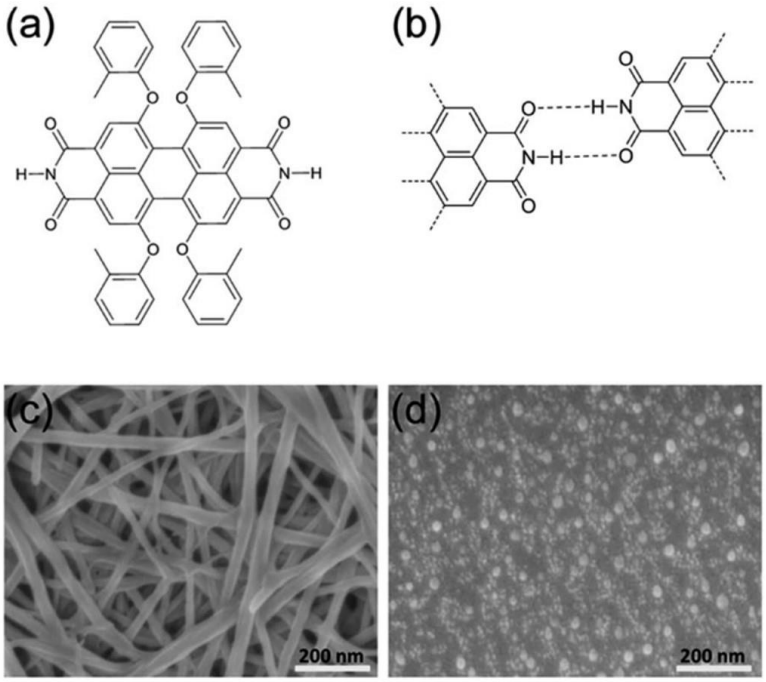

Figure 25. (a) Structure of PBI derivative and (b) suggested hydrogen bonding between molecules. (c) and (d) are SEM images of the PBI spin-coated onto a glass substrates from solutions of PBI in (c) $CHCl_3$ and (d) THF. Concentrations of solution were 1 mg/mL. Figure adapted from Zhang et al.[155]

1.4.2. Electronic and Photocatalytic Properties of Perylene Bisimides

The perylene core exhibits a S_0-S_1 transition which corresponds to a strong absorbance in the visible light region of the spectrum. Upon irradiation, the PBI can become reduced, forming radical anion and dianion species. The radical anion has many uses, it can readily react with O_2 and can be used as an O_2 sensor,[156] in some cases the radical anion has been found to be stable under ambient conditions.[89,157,158] The presence of the radical anion has been linked to a turn on in the conductivity and there have been many studies investigating the use of this in photovoltaics and photocatalysis. Cyclic voltammetry studies on PBI solutions show the presence of two reduced PBI species, the radical anion and dianion.[157] The formation of the reduced species coincides with the increase in absorption bands at ~610 nm for the dianion and at ~750, 930 and 1050 nm for the radical anion.[159]

When studying the effect of packing arrangements on optical and electrical properties, it is common to use dimer complexes, the predetermined orientation of the dimer can be correlated with its properties and compared with other arrangements giving insight into the effects of molecular packing.[160] The change in absorption between a PBI monomer and a rotationally displaced cyclic dimer showed an increase in absorption at 540 nm compared to the 580 nm band. Compared to the monomer, the dimer also shows a large stokes shift in the fluorescence spectra, a loss of the vibronic structure and a decrease in fluorescence quantum yield by 94%; these effects are a result of the increased electronic coupling between the dimer molecules showing that multiple molecules can undergo charge transfer. The reduction of a PBI dimer has been related to changes in orientation of stacked molecules showing that in-situ rearrangements could be common during reduction processes, the understanding of the localised packing during reduction events may be important for the future optimisation of self-assembled PBIs.[160]

At low concentrations, PBIs exhibit high fluorescence quantum yields above 95% in all common solvents and >90% in H_2O, which indicates that proton transfer is not a major quenching factor.[46] Intersystem crossing in PBIs is unlikely due to the inefficient energy overlap of the low-lying triplet level, T_1, compared to the excited S_1 state, this means that fluorescence is the main pathway for radiative decay and that the rate phosphorescence is considered negligible.[46,153,161] The increase in self-assembly of PBIs, however, results in self-quenching and the reduction of fluorescence. Increased aggregation and strong intermolecular charge transfer can be favourable for high efficiency devices but the rate of electron-hole recombination within a material greatly affects the efficiency of the device; this must be carefully considered in aggregated systems. As well as providing a closer network for fast charge transfer, aggregation also opens up more pathways for both radiative and non-radiative decay.[154,122]

Long exciton diffusion lengths have been reported for J-aggregates which are generally much higher than those observed in H-aggregates.[149,150,162] Theoretical calculations of the excited states of H-aggregates shows that exciton trapping could occur, leading to a dead end route of exciton energy transfer.[147] The head-to-tail stacking of J-aggregates may, however, result in a

smaller π-electron conjugation due to less overlap of the perylene core which results in a reduced long-range conductivity.[144]

As mentioned previously, Draper et al. observed that amino-acid substituted PBIs can self-assemble into 1-dimensional structures using a pH switch (Figure 19).[89] Gels and solutions of PBIs were dried down to films so that the 1-dimensional anisotropic structures could be analysed for their photoconductivity. It was observed that the PBIs become reduced and form radical anion and dianion species when illuminated. Remarkably, the reduced species were stable under ambient conditions for up to 18 hours.[89] The one dimensional fibres became conductive upon illumination showing that these self-assembled structures have the ability to transport electrons over long distances when the radical anion and dianion are present. Changing the molecular structure has an impact on the self-assembly and photoconductivity of the structures where the more ordered structures show superior photoconductivity.[89,163,164] Electrochemical characterisation of the radical anion and dianion shows that the potential should be sufficient to reduce protons.[163,165] This rationale is used for the work in this thesis where self-assembled PBI structures have been studied for their ability to drive the hydrogen evolution reaction.

1.4.3. Applications of PBIs as photocatalysts

There are many examples of systems where perylene-based compounds are used as n-type semiconductors to transfer the excited electrons to a co-catalyst which is specifically designed to drive a reaction.[101,104,108,138,154,154,166–176] A two-step excitation process can provide enough potential to drive the reduction of aryl halides.[106,177–179] The key to high efficiency in these devices is to increase rate of electron transfer from the perylene to the co-catalyst.[180,181] Perylene-based compounds are good charge transfer materials[11] and promoting electron transfer to the co-catalyst is an important area of study. Interestingly, reduced perylene species have been found to be stable in air for several hours, as measured by UV-Vis spectroscopy.[89] Both the radical anion and the dianion species can be used in reduction processes, where the dianion has a larger potential driving force compared to the radical anion.[106]

Many examples using perylenes as photocatalysts employ them as crystalline materials[176] or complexed with a metal oxide surface,[182,183] including graphene oxide.[183] The downside of semiconductors such as graphene oxide and titanium dioxide is their low conversion

efficiencies. Metal oxide films show fast electron transport properties and are commonly combined with co-catalysts and dyes to improve their properties.[184,185] Doped semiconductors can proceed to drive organic reactions such as degrading toxic chemicals in both reduction and oxidation processes.[186–188] Co-catalysts, such as metal-based co-catalysts like platinum for proton reduction, can be adsorbed onto the surface to accept the electron from the TiO_2 and reduce electron recombination.[108] Perylene bisimide compounds have been used as dye-sensitisers to increase the activity of these materials.[182,183,189] Although many of these designs show promising data they do not address the science of self-assembly nor of short and long range order of aggregates and networks. More interesting in terms of this thesis, however, are those which focus on aggregation of the photoconductive gelators such as with the solution processing of PBIs with graphitic carbon nitride, which resulted in an increase in hydrogen evolution activity of the carbon nitride under visible light (≥420 nm) (Figure 26).[107] Here, the irradiation of platinum-coated carbon nitride in a closed cell resulted in a small amount of hydrogen being evolved from water which was repurged with inert gas and repeated successfully three times. However, the presence of the perylene bisimide resulted in a large increase in hydrogen evolution activity as the PBI utilised more of the light energy which can be directed for use in the process.

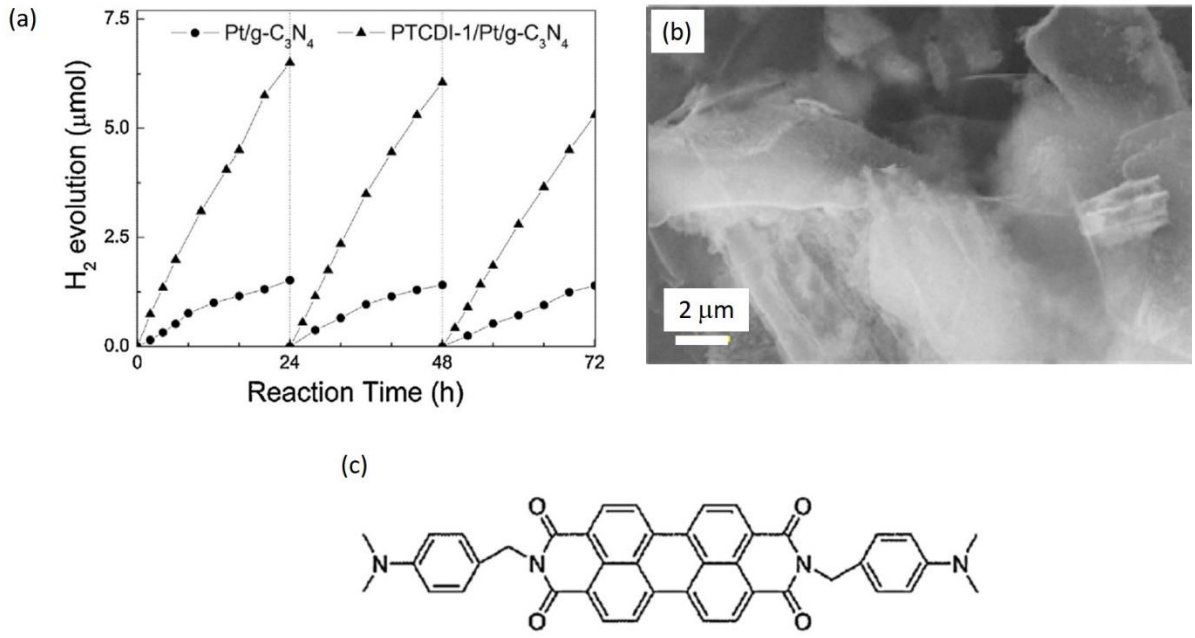

Figure 26. (a) Stability experiment showing H_2 evolution from water using PTCDI/Pt/g-C_3N_4 composite, (b) SEM image of the the aggregates and (c) molecular structure of the PTCDI. Figure adapted from Chen et al.[107]

Chen et al. reported the use of PBIs in solution with excess electron donor triethanolamine and Pt/TiO_2 composites.[141] The solution evolved hydrogen in water upon irradiation under UV and visible wavelengths (Figure 27). The substitution of carboxylic acid groups on the imide positions of ther PBI allowed for the anchoring of the fibres onto the TiO_2 surface[7] and as TiO_2 is strongly absorbing in the UV region, the PBI dye is used as a dye-sensitizer to exploit more of the visible spectrum. The use of excess electron donor ensured the electron hole in the HOMO was quickly scavenged, reducing the effect of electron recombination. An optimal ratio of PBI to Pt/TiO_2 was observed at 1% PBI.[141] Here, PBI was aggregated by the addition of a less solubilising solvent allowing for π–π stacking to occur, which increased hydrogen evolution rates.[141] Chen et al. also state that fibre-like morphologies, which help increase long-range charge separation, result in increased hydrogen evolution compared to nanoparticles.[108] Furthermore, hydrogen evolution activity was also increased by utilising an electron-donating aniline imide substituent which quickly scavenges the electron hole on the perylene core via intramolecular charge transfer.[108] This approach helps to show the importance of reducing electron recombination pathways.

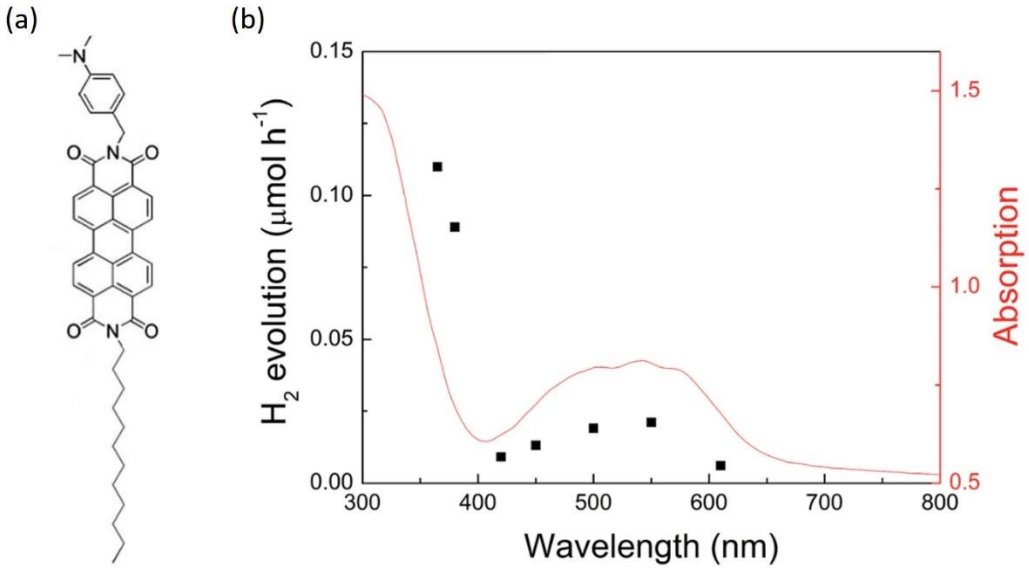

Figure 27. (a) Structure of PBI, (b) UV-Vis Absorption spectrum (line, right axis) and hydrogen evolution photocatalytic activity (scatter, left axis) of $PBI/Pt/TiO_2$ under monochromatic irradiation. Figure adapted from Chen et al.[141]

Nanofibre-type PBI aggregates have also shown an increase in power conversion efficiency compared to nanoparticles of the same compound, when used as a conductive layer in a photovoltaic cell.[155] The formation of fibres allows for a direct 1-dimensional pathway for electron transport across the layer. Electron-hole separation and controlling the pathway for

electron transfer are crucial for PBI-based devices to reach their maximum efficiency.[155] Many groups are reporting the combined use of dye photocatalysts such as perylene diimides, PBIs, with fast electron transport materials such as WO_3 and TiO_2 to increase charge separation.[108,141,154] Electron injection into a nearby WO_3 co-catalyst showed that the transfer of the electron into WO_3 is much faster than the electron recapture of the oxidised perylene, therefore reducing electron recombination and increasing efficiency.[154,169]

Covalently binding a perylene to a metal catalyst can help promote electron transfer directly to the active metal core;[169] recently, perylene imide ligands have been added into the axial positions of a ruthenium(II) water oxidation catalyst for water oxidation. The complex allowed for good intramolecular electron transfer to the co-catalyst while crucially still allowing the co-catalyst to become directly involved in the self-assembly process.[169] The embedding of the catalyst deep within the fibres, however, seems to induce a diffusion limited lag phase in activity.[169] As is evident here, there are many parameters to balance when designing a supramolecular photocatalytic system.

A self-assembled gel prepared using a salt trigger from a mono-substituted perylene imide has been used for photocatalytic hydrogen evolution.[138] The monoimide was imaged and was found to have a ribbon-type structure (Figure 28).

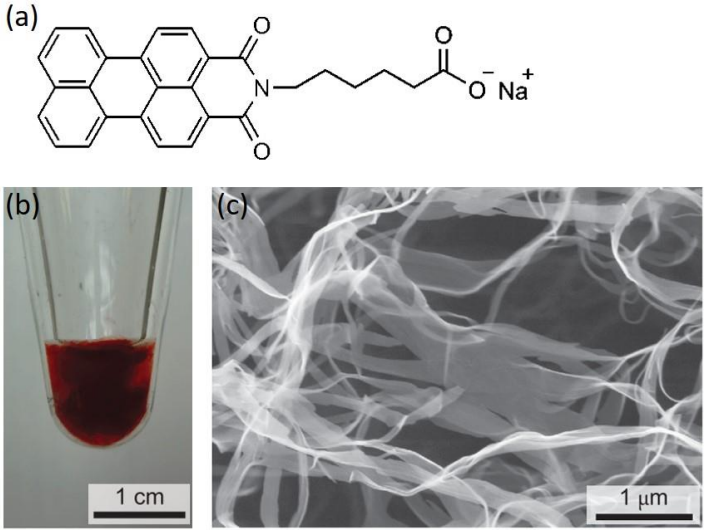

Figure 28. (a) Structure of the perylene gelator, (b) Photograph and (c) SEM of the gel containing 11.5 mM of the gelator gelled with the addition of a poly(diallyldimethylammonium) chloride salt. Figure adapted from Stupp and co-workers.[138]

The hydrogel was immersed in aqueous solution containing a nickel hydrogen evolution co-catalyst and irradiated with white light; the self-assembled gel showed superior activity for hydrogen evolution compared to the solid perylene precipitate proving that self-assembly can increase photocatalytic performance. An optimal pH of 4 was found for this system, where [e^-] = [H^+]; deviations above and below this by 1 pH unit reduced the H_2 output 3-fold.[138] As mentioned previously, the type and extent of interactions between the perylene fibres and the co-catalyst are of key importance. Localised crystallisation of fibres have been found within the matrix of salt-triggered gels and a direct correlation has been made between the presence of these and hydrogen evolution activity.[190] Although fibres can be crystallised locally, the whole network can still form an amorphous gel state. The close packing of the crystallised molecules enables efficient charge transfer.[190]

This work was expanded, and it was observed that the stacking arrangements affected the photocatalytic activity; increasing the carbon chain lengths on the imide position resulted in larger spacing between molecules when assembled together which reduced charge transfer. This work by Weingarten and Stupp et al. is a key precedent to the work within this thesis. The link between the type and shape of self-assembled fibres, the 3-dimensional supramolecular structure, and the resulting activity of the material towards photocatalytic hydrogen evolution can be expanded and understood in more detail.

1.5. Introduction to work in this thesis

The overall aim of the work in this thesis is to investigate the effect of different supramolecular assemblies on their properties. Perylene bisimide materials have been aggregated in solutions via a pH switch and then investigated as part of a photocatalytic system. This work is an expansion of the works by Draper et al. where the presence of self-assembled fibres of amino-acid substituted perylene bisimides and the further alignment of fibres has had a direct link to increased photoconductive performance.[89,163,164,191] Much of this work involves drying down the wet solutions and 3D structures of gels into 2D films, however the work in this thesis will focus on wet solutions and gels which reduces a technical processing step and opens up avenues for 3D structure analysis and trends. The work in this thesis also pulls on the works by Stupp and co-workers where the 3D supramolecular structure has been investigated in detail and associated with photocatalytic performance.[138,167,176,190,192] We investigate the effect of pH on the self-assembly in solution, the effect of pH on the networks, and the resulting efficiency of

photocatalysis at different pH. This is the focus of Chapter 2. This detailed investigation was very time-consuming. Hence, in Chapter 3, we expand the study to use high throughput methods to allow us to understand a library of PBIs. In Chapter 4, we investigate the use of 3D printing to form patterned gels. We focus mainly on proof-of-principle gelators to allow us to understand the importance of microstructure and network type on the ability to 3D print the gels. We then briefly discuss the potential of 3D printing PBI-based gels.

1.6. References

1 A. R. Hirst, I. A. Coates, T. R. Boucheteau, J. F. Miravet, B. Escuder, V. Castelletto, I. W. Hamley and D. K. Smith, *J. Am. Chem. Soc.*, 2008, **28**, 1–8.

2 P. Terech and R. G. Weiss, *Chem. Rev.*, 1997, **97**, 3133–3160.

3 M. De Loos, B. L. Feringa and J. H. Van Esch, *Eur. J. Org. Chem.*, 2005, **17**, 3615–3631.

4 L. A. Estroff and A. D. Hamilton, *Chem. Rev.*, 2004, **104**, 1201–1217.

5 C. A. Dreiss, *Soft Matter*, 2007, **3**, 956–970.

6 J. Yang, *Curr. Opin. Colloid Interface Sci.*, 2002, **7**, 276–281.

7 A. R. Hirst, B. Escuder, J. F. Miravet and D. K. Smith, *Angew. Chem. Int. Ed.*, 2008, **47**, 8002–8018.

8 T. R. Hoare and D. S. Kohane, *Polymer*, 2008, **49**, 1993–2007.

9 X. Du, J. Zhou, J. Shi and B. Xu, *Chem. Rev.*, 2015, **115**, 13165–13307.

10 N. M. Sangeetha and U. Maitra, *Chem. Soc. Rev.*, 2005, **34**, 821–836.

11 F. Würthner, *Chem. Commun.*, 2004, **14**, 1564–1579.

12 D. Chimene, K. K. Lennox, R. R. Kaunas and A. K. Gaharwar, *Ann. Biomed. Eng.*, 2016, **44**, 2090–2102.

13 T. Jungst, W. Smolan, K. Schacht, T. Scheibel and J. Groll, *Chem. Rev.*, 2016, **116**, 1496–1539.

14 Z. Yang, G. Liang, M. Ma, Y. Gao and B. Xu, *J. Mater. Chem.*, 2007, **17**, 850–854.

15 D. J. Adams, M. F. Butler, W. J. Frith, M. Kirkland, L. Mullen and P. Sanderson, *Soft Matter*, 2009, **5**, 1856–1862.

16 J. Raeburn, A. Z. Cardoso and D. J. Adams, *Chem. Soc. Rev.*, 2013, **42**, 5143–56.

17 B. P. Jiang, D. S. Guo and Y. Liu, *J. Org. Chem.*, 2010, **75**, 7258–7264.

18 G. O. Lloyd and J. W. Steed, *Nat. Chem.*, 2009, **1**, 437–442.

19 X. Yu, L. Chen, M. Zhang and T. Yi, *Chem. Soc. Rev.*, 2014, **43**, 5346–5371.

20 J. Raeburn, A. Z. Cardoso and D. J. Adams, *Chem. Soc. Rev.*, 2013, **42**, 5143–56.

21 J. H. Van Esch, *Langmuir*, 2009, **25**, 8392–8394.

22 E. R. Draper, T. O. McDonald and D. J. Adams, *Chem. Commun.*, 2015, **51**, 12827–30.

23 L. Chen, S. Revel, K. Morris, L. C. Serpell and D. J. Adams, *Langmuir*, 2010, **26**, 13466–13471.

24 J. K. Gupta, D. J. Adams and N. G. Berry, *Chem. Sci.*, 2016, **7**, 4713–4719.

25 S. S. Babu, V. K. Praveen and A. Ajayaghosh, *Chem. Rev.*, 2014, **114**, 1973–2129.

26 M. Yamanaka, *J. Incl. Phenom. Macrocycl. Chem.*, 2013, **77**, 33–48.

27 M. De Loos, A. Friggeri, J. Van Esch, R. M. Kellogg and B. L. Feringa, *Org. Biomol. Chem.*, 2005, **3**, 1631–1639.

28 L. A. Estroff and A. D. Hamilton, *Angew. Chem. Int. Ed.*, 2000, 3447–3450.

29 E. Virtanen and E. Kolehmainen, *Eur. J. Org. Chem.*, 2004, 3385–3399.

30 S. Mukhopadhyay and U. Maitra, *Curr. Sci.*, 2004, **87**, 1666–1683.

31 M. Zhang, S. Strandman, K. C. Waldron and X. X. Zhu, *J. Mater. Chem. B*, 2016, **4**, 7506–7520.

32 N. M. Sangeetha, S. Bhat, A. R. Choudhury, U. Maitra and P. Terech, *J. Phys. Chem. B*, 2004, **108**, 16056–16063.

33 P. Babu, N. M. Sangeetha and U. Maitra, *Macromol. Symp.*, 2006, **241**, 60–67.

34 P. Terech, N. M. Sangeetha and U. Maitra, *J. Phys. Chem. B*, 2006, **110**, 15224–15233.

35 J. H. Jung, G. John, M. Masuda, K. Yoshida, S. Shinkai and T. Shimizu, *Langmuir*, 2001, **17**, 7229–7232.

36 O. Gronwald and S. Shinkai, *Chem. - A Eur. J.*, 2001, **7**, 4328–4334.

37 S. Kiyonaka, S. Shinkai and I. Hamachi, *Chem. Eur. J.*, 2003, **9**, 976–983.

38 G. John, M. Masuda, Y. Okada, K. Yase and T. Shimizu, *Adv. Mater.*, 2001, **13**, 715–718.

39 D. K. Smith, A. R. Hirst, C. S. Love, J. G. Hardy, S. V. Brignell and B. Huang, *Prog. Polym. Sci.*, 2005, **30**, 220–293.

40 M. A. Mintzer and M. W. Grinstaff, *Chem. Soc. Rev.*, 2011, **40**, 173–190.

41 A. M. Caminade and J. P. Majoral, *Prog. Polym. Sci.*, 2005, **30**, 491–505.

42 E. Rump, F. Gauffre, J.-P. Vors, J.-P. Majoral, T. Gulik-Krzywicki, A.-M. Caminade, C. Marmillon and C. Loup, *Angew. Chem. Int. Ed.*, 2002, **40**, 2626–2629.

43 A. R. Hirst, D. K. Smith, M. C. Feiters, H. P. M. Geurts and A. C. Wright, *J. Am. Chem. Soc.*, 2013, **45**, 73–82.

44 K. S. Partridge, D. K. Smith, G. M. Dykes and P. T. McGrail, *Chem. Commun.*, 2001,

319–320.

45 E. R. Draper, E. G. B. Eden, T. O. McDonald and D. J. Adams, *Nat. Chem.*, 2015, **7**, 848–852.

46 F. Würthner, C. R. Saha-Moller, B. Fimmel, S. Ogi, P. Leowanawat and D. Schmidt, *Chem. Rev.*, 2016, **116**, 962–1052.

47 S. Koutsopoulos, *J. Biomed. Mater. Res. - Part A*, 2016, **104**, 1002–1016.

48 C. Tomasini and N. Castellucci, *Chem. Soc. Rev.*, 2013, **42**, 156–172.

49 S. Fleming and R. V. Ulijn, *Chem. Soc. Rev.*, 2014, **43**, 8150–8177.

50 M. P. Hendricks, K. Sato, L. C. Palmer and S. I. Stupp, *Acc. Chem. Res.*, 2017, **50**, 2440–2448.

51 D. Roberts, C. Rochas, A. Saiani and A. F. Miller, *Langmuir*, 2012, **28**, 16196–16206.

52 H. Cui, M. J. Webber and S. I. Stupp, *Biopolymers*, 2010, **94**, 1–18.

53 A. Saiani, A. Mohammed, H. Frielinghaus, R. Collins, N. Hodson, C. M. Kielty, M. J. Sherratt and A. F. Miller, *Soft Matter*, 2009, **5**, 193–202.

54 A. Mohammed, A. F. Miller and A. Saiani, *Macromol. Symp.*, 2007, **251**, 88–95.

55 S. Yagai, T. Seki, T. Karatsu, A. Kitamura and F. Würthner, *Angew. Chem. Int. Ed.*, 2008, **47**, 3367–3371.

56 G. Pescitelli, L. Di Bari and N. Berova, *Chem. Soc. Rev.*, 2014, **43**, 5211–5233.

57 P.-A. Plötz, S. Polyutov, S. D. Ivanov, F. Fennel, S. Wolter, T. A. Niehaus, Z. Xie, S. Lochbrunner, F. Würthner and O. Kuehn, *Phys. Chem. Chem. Phys.*, 2016, **53**, 1689–1699.

58 G. Griffini, M. Levi and S. Turri, *Renew. Energy*, 2015, **78**, 288–294.

59 F. Würthner, T. E. Kaiser and C. R. Saha-Möller, *Angew. Chem. Int. Ed.*, 2011, **50**, 3376–3410.

60 T. E. Kaiser, H. Wang, V. Stepanenko and F. Würthner, *Angew. Chem. Int. Ed.*, 2007, **46**, 5541–5544.

61 F. D'Anna, S. Marullo, G. Lazzara, P. Vitale and R. Noto, *Chem. - A Eur. J.*, 2015, **21**, 14780–14790.

62 H. Yoo, J. Yang, A. Yousef, M. R. Wasielewski and D. Kim, *J. Am. Chem. Soc.*, 2010, **132**, 3939–3944.

63 A. V. Shenoy, *Rheology of filled polymer systems*, Springer-Science+Business Media, B.V., 1999.

64 Y. Qiu and K. Park, *Adv. Drug Deliv. Rev.*, 2012, **64**, 49–60.

65 P. Gupta, K. Vermani and S. Garg, *Drug Discov. Today*, 2002, **7**, 569–579.

66 D. Schmaljohann, *Adv. Drug Deliv. Rev.*, 2006, **58**, 1655–1670.

67 N. A. Peppas, Y. Huang, M. Torres-Lugo, J. H. Ward and J. Zhang, *Annu. Rev Biomed. Eng.*, 2000, 9–29.

68 C. De Las Heras Alarcón, S. Pennadam and C. Alexander, *Chem. Soc. Rev.*, 2005, **34**, 276–285.

69 J. W. Stansbury and M. J. Idacavage, *Dent. Mater.*, 2016, **32**, 54–64.

70 D. M. Kirchmajer, R. Gorkin and M. In Het Panhuis, *J. Mater. Chem. B*, 2015, **3**, 4105–4117.

71 X. Wang, M. Jiang, Z. Zhou, J. Gou and D. Hui, *Compos. Part B Eng.*, 2017, **110**, 442–458.

72 N. E. Fedorovich, J. Alblas, J. R. de Wijn, W. E. Hennink, A. J. Verbout and W. J. A. Dhert, *Tissue Eng.*, 2007, **13**, 1905–1925.

73 A. V. Kabanov and S. V. Vinogradov, *Angew. Chem. Int. Ed.*, 2009, **48**, 5418–5429.

74 Z. Yang, K. Xu, L. Wang, H. Gu, H. Wei, M. Zhang and B. Xu, *Chem. Commun.*, 2005, **35**, 4414–4416.

75 Z. Yang, G. Liang, M. Ma, Y. Gao and B. Xu, *Small*, 2007, **3**, 558–562.

76 S. Sutton, N. L. Campbell, A. I. Cooper, M. Kirkland, W. J. Frith and D. J. Adams, *Langmuir*, 2009, **25**, 10285–10291.

77 J. Gao, C. Tang, M. A. Elsawy, A. M. Smith, A. F. Miller and A. Saiani, *Biomacromolecules*, 2017, **18**, 826–834.

78 C. Yan and D. J. Pochan, *Chem. Soc. Rev.*, 2010, **39**, 3528–40.

79 C. Yan, A. Altunbas, T. Yucel, R. P. Nagarkar, J. P. Schneider and D. J. Pochan, *Soft Matter*, 2010, **6**, 5143–5156.

80 E. R. Draper and D. J. Adams, *Chem*, 2017, **3**, 390–410.

81 S. S. Babu, S. Prasanthkumar and A. Ajayaghosh, *Angew. Chem. Int. Ed.*, 2012, **51**, 1766–1776.

82 S. Ghosh, V. K. Praveen and A. Ajayaghosh, *Annu. Rev. Mater. Res.*, 2016, **46**, 235.

83 D. S. Weiss and M. Abkowitz, *Chem. Rev.*, 2010, **110**, 479–526.

84 K. Y. Law, *Chem. Rev.*, 1993, **93**, 449–486.

85 C. Li and H. Wonneberger, *Adv. Mater.*, 2012, **24**, 613–636.

86 K. Sakakibara, P. Chithra, B. Das, T. Mori, M. Akada, J. Labuta, T. Tsuruoka, S. Maji, S. Furumi, L. K. Shrestha, J. P. Hill, S. Acharya, K. Ariga and A. Ajayaghosh, *J. Am. Chem. Soc.*, 2014, **136**, 8548–8551.

87 A. Wicklein, S. Ghosh, M. Sommer, F. Würthner and M. Thelakkat, *ACS Nano*, 2009,

3, 1107–1114.

88 X. Zhan, A. Facchetti, S. Barlow, T. J. Marks, M. A. Ratner, M. R. Wasielewski and S. R. Marder, *Adv. Mater.*, 2011, **23**, 268–284.

89 E. R. Draper, J. J. Walsh, T. O. McDonald, M. A. Zwijnenburg, P. J. Cameron, A. J. Cowan and D. J. Adams, *J. Mater. Chem. C*, 2014, **2**, 5570–5575.

90 E. R. Draper, J. R. Lee, M. Wallace, F. Jackel, A. J. Cowan and D. J. Adams, *Chem. Sci.*, 2016, **7**, 6499–6505.

91 K. L. Morris, L. Chen, J. Raeburn, O. R. Sellick, P. Cotanda, A. Paul, P. C. Griffiths, S. M. King, R. K. O'Reilly, L. C. Serpell and D. J. Adams, *Nat. Commun.*, 2013, **4**, 1480.

92 J. Raeburn and D. J. Adams, *Chem. Commun.*, 2015, **51**, 5170–5180.

93 S. Prasanthkumar, A. Saeki, V. C. Nair, S. Seki, S. Ghosh and A. Ajayaghosh, *Angew. Chem. Int. Ed.*, 2014, **54**, 946–950.

94 N. S. Lewis and D. G. Nocera, *Proc Natl Acad Sci*, 2006, **103**, 15729–15735.

95 P. B. Pati, S.-I. In and H. Tian, *IntechOpen*, 2016, 137–154.

96 K. Pirkanniemi and M. Sillanpää, *Chemosphere*, 2002, **48**, 1047–1060.

97 S. Bee, A. Hamid, S. J. Teh and C. W. Lai, *Catalysts*, 2017, **7**, 93.

98 K. Maeda and K. Domen, *J. Phys. Chem. Lett.*, 2010, **1**, 2655–2661.

99 J. Roncali, P. Leriche and P. Blanchard, *Adv. Mater.*, 2014, **26**, 3821–3838.

100 L. Zhang, X.-H. Huang, J.-S. Hu, J. Song and I. Kim, *Langmuir*, 2017, **33**, 1867–1871.

101 Z. Zhang, J. Wang, D. Liu, W. Luo, M. Zhang, W. Jiang and Y. Zhu, *ACS Appl. Mater. Interfaces*, 2016, **8**, 30225–30231.

102 P. Liao, Y. Hu, Z. Liang, J. Zhang, H. Yang, L. Q. He, Y. X. Tong, J. M. Liu, L. Chen and C. Y. Su, *J. Mater. Chem. A*, 2018, **6**, 3195–3201.

103 F. Fernández-Lázaro, N. Zink-Lorre and Á. Sastre-Santos, *J. Mater. Chem. A*, 2016, **4**, 9336–9346.

104 D. Liu, J. Wang, X. Bai, R. Zong and Y. Zhu, *Adv. Mater.*, 2016, **28**, 7284–7290.

105 S. Chen, P. Slattum, C. Wang and L. Zang, *Chem. Rev.*, 2015, **115**, 11967–11998.

106 I. Ghosh, T. Ghosh, J. I. Bardagi and B. König, *Science*, 2014, **346**, 725–728.

107 S. Chen, C. Wang, B. R. Bunes, Y. Li, C. Wang and L. Zang, *Appl. Catal. A Gen.*, 2015, **498**, 63–68.

108 S. Chen, D. L. Jacobs, J. Xu, Y. Li, C. Wang and L. Zang, *RSC Adv.*, 2014, **4**, 48486–48491.

109 E. Busseron, Y. Ruff, E. Moulin and N. Giuseppone, *Nanoscale*, 2013, **5**, 7098–7140.

110 Y. Chen, A. Li, Z.-H. Huang, L.-N. Wang and F. Kang, *Nanomaterials*, 2016, **6**, 51.

111 G. Zhang, Z. Lan and X. Wang, *Angew. Chem. Int. Ed.*, 2016, **55**, 15712–15727.

112 A. Savateev and M. Antonietti, *ACS Catal.*, 2018, DOI: 10.1021/acscatal.8b02595.

113 R. S. Sprick, J. X. Jiang, B. Bonillo, S. Ren, T. Ratvijitvech, P. Guiglion, M. A. Zwijnenburg, D. J. Adams and A. I. Cooper, *J. Am. Chem. Soc.*, 2015, **137**, 3265–3270.

114 R. S. Sprick, B. Bonillo, R. Clowes, P. Guiglion, N. J. Brownbill, B. J. Slater, F. Blanc, M. A. Zwijnenburg, D. J. Adams and A. I. Cooper, *Angew. Chem. Int. Ed.*, 2016, **55**, 1792–1796.

115 M. Schwarze, D. Stellmach, M. Schröder, K. Kailasam, R. Reske, A. Thomas and R. Schomäcker, *Phys. Chem. Chem. Phys.*, 2013, **15**, 3466.

116 H. Ahmad, S. K. Kamarudin, L. J. Minggu and M. Kassim, *Renew. Sustain. Energy Rev.*, 2015, **43**, 599–610.

117 A. A. Ismail and D. W. Bahnemann, *Sol. Energy Mater. Sol. Cells*, 2014, **128**, 85–101.

118 S. Chen, Y. Qi, T. Hisatomi, Q. Ding, T. Asai, Z. Li, S. S. K. Ma, F. Zhang, K. Domen and C. Li, *Angew. Chem. Int. Ed.*, 2015, **54**, 8498–8501.

119 A. J. Bard and L. R. Faulkner, *Electrochemical methods : fundamentals and applications*, Wiley, 2001.

120 I. Roger, M. A. Shipman and M. D. Symes, *Nat. Rev. Chem.*, 2017, **1**, 0003.

121 J. T. Kirner and R. G. Finke, *J. Mater. Chem. A*, 2017, **5**, 19560–19592.

122 A. Galińska and J. Walendziewski, *Energy and Fuels*, 2005, **19**, 1143–1147.

123 V. N. H. Nguyen, R. Amal and D. Beydoun, *Chem. Eng. Sci.*, 2003, **58**, 4429–4439.

124 E. P. Melián, O. G. Díaz, A. O. Méndez, C. R. López, M. N. Suárez, J. M. D. Rodríguez, J. A. Navío, D. F. Hevia and J. P. Peña, *Int. J. Hydrogen Energy*, 2013, **38**, 2144–2155.

125 X. . Chen, S. . b Shen, L. . Guo and S. S. . Mao, *Chem. Rev.*, 2010, **110**, 6503–6570.

126 A. W. Hains, Z. Liang, M. A. Woodhouse and B. A. Gregg, *Chem. Rev.*, 2010, **110**, 6689–6735.

127 R. Abe, *J. Photochem. Photobiol. C Photochem. Rev.*, 2010, **11**, 179–209.

128 X. Wang, K. Maeda, A. Thomas, K. Takanabe, G. Xin, J. M. Carlsson, K. Domen and M. Antonietti, *Nat. Mater.*, 2009, **8**, 76–80.

129 S. Ye, R. Wang, M. Z. Wu and Y. P. Yuan, *Appl. Surf. Sci.*, 2015, **358**, 15–27.

130 X. Wang, K. Maeda, X. Chen, K. Takanabe, K. Domen, Y. Hou, X. Fu and M. Antonietti, *J. Am. Chem. Soc.*, 2009, **131**, 1680–1681.

131 K. Zhang, D. Kopetzki, P. H. Seeberger, M. Antonietti and F. Vilela, *Angew. Chem. Int. Ed.*, 2013, **52**, 1432–1436.

132 C. R. Deblase, K. Hernández-Burgos, J. M. Rotter, D. J. Fortman, D. Dos S. Abreu, R.

A. Timm, I. C. N. Diógenes, L. T. Kubota, H. D. Abruña and W. R. Dichtel, *Angew. Chem. Int. Ed.*, 2015, **54**, 13225–13229.

133 P. Kuhn, M. Antonietti and A. Thomas, *Angew. Chem. Int. Ed.*, 2008, **47**, 3450–3453.

134 K. Schwinghammer, S. Hug, M. B. Mesch, J. Senker and B. V. Lotsch, *Energy Environ. Sci.*, 2015, **8**, 3345–3353.

135 L. Li, Z. Cai, Q. Wu, W. Y. Lo, N. Zhang, L. X. Chen and L. Yu, *J. Am. Chem. Soc.*, 2016, **138**, 7681–7686.

136 C. Yang, B. C. Ma, L. Zhang, S. Lin, S. Ghasimi, K. Landfester, K. A. I. Zhang and X. Wang, *Angew. Chem. Int. Ed.*, 2016, **55**, 9202–9206.

137 N. J. L. K. Davis, R. W. Macqueen, D. A. Roberts, A. Danos, S. Dehn, S. Perrier and T. W. Schmidt, *J. Mater. Chem. C*, 2016, **4**, 8270–8275.

138 A. S. Weingarten, R. V Kazantsev, L. C. Palmer, M. McClendon, A. R. Koltonow, A. P. S. Samuel, D. J. Kiebala, M. R. Wasielewski and S. I. Stupp, *Nat. Chem.*, 2014, **6**, 964–970.

139 J. T. Kirner, J. J. Stracke, B. A. Gregg and R. G. Finke, *ACS Appl. Mater. Interfaces*, 2014, **6**, 13367–13377.

140 C. Huang, S. Barlow and S. R. Marder, *J. Org. Chem.*, 2011, **76**, 2386–2407.

141 S. Chen, Y. X. Li and C. Y. Wang, *RSC Adv.*, 2015, **5**, 15880–15885.

142 F. Würthner, *Chem. Commun.*, 2004, **14**, 1564–1579.

143 J. A. A. W. Elemans, R. Van Hameren, R. J. M. Nolte and A. E. Rowan, *Adv. Mater.*, 2006, **18**, 1251–1266.

144 J. Wang, D. Liu, Y. Zhu, S. Zhou and S. Guan, *Appl. Catal. B Environ.*, 2018, **231**, 251–261.

145 P. Alessio, M. L. Braunger, R. F. Aroca, C. de Almeida Olivati and C. J. L. Constantino, *J. Phys. Chem. C*, 2015, **119**, 12055–12064.

146 J. Seibt, P. Marquetand, V. Engel, Z. Chen, V. Dehm and F. Würthner, *Chem. Phys.*, 2006, **328**, 354–362.

147 R. F. Fink, J. Seibt, V. Engel, M. Renz, M. Kaupp, S. Lochbrunner, H. M. Zhao, J. Pfister, F. Würthner and B. Engels, *J. Am. Chem. Soc.*, 2008, **130**, 12858–12859.

148 A. T. Haedler, K. Kreger, A. Issac, B. Wittmann, M. Kivala, N. Hammer, J. Köhler, H.-W. Schmidt and R. Hildner, *Nature*, 2015, **523**, 196–199.

149 H. Marciniak, X. Q. Li, F. Würthner and S. Lochbrunner, *J. Phys. Chem. A*, 2011, **115**, 648–654.

150 H. Lin, R. Camacho, Y. Tian, T. E. Kaiser, F. Würthner and I. G. Scheblykin, *Nano*

Lett., 2010, **10**, 620–626.

151 J. Sung, P. Kim, B. Fimmel, F. Würthner and D. Kim, *Nat. Commun.*, 2015, **6**, 8646.

152 P. Osswald and F. Würthner, *J. Am. Chem. Soc.*, 2007, **129**, 14319–14326.

153 G. Seybold and G. Wagenblast, *Dye. Pigment.*, 1989, **11**, 303–317.

154 F. Ronconi, Z. Syrgiannis, A. Bonasera, M. Prato, R. Argazzi, S. Caramori, V. Cristino and C. A. Bignozzi, *J. Am. Chem. Soc.*, 2015, **137**, 4630–4633.

155 W. Zhang, S. Zhong, L. Nian, Y. Chen, Z. Xie, L. Liu, M. Hanif, W. Chen and Y. Ma, *RSC Adv.*, 2015, **5**, 39973–39977.

156 I. S. Shin, T. Hirsch, B. Ehrl, D. H. Jang, O. S. Wolfbeis and J. I. Hong, *Anal. Chem.*, 2012, **84**, 9163–9168.

157 D. Schmidt, D. Bialas and F. Würthner, *Angew. Chem. Int. Ed.*, 2015, **54**, 3682–3685.

158 T. H. Reilly, A. W. Hains, H. Y. Chen and B. A. Gregg, *Adv. Energy Mater.*, 2012, **2**, 455–460.

159 R. O. Marcon and S. Brochsztain, *J. Phys. Chem. A*, 2009, **113**, 1747–1752.

160 F. Schlosser, M. Moos, C. Lambert and F. Würthner, *Adv. Mater.*, 2013, **25**, 410–414.

161 W. E. Ford and P. V. Kamat, *J. Phys. Chem.*, 1987, **91**, 6373–6380.

162 D. Kurrle and J. Pflaum, *Appl. Phys. Lett.*, 2008, **92**, 1333061–1333063.

163 J. J. Walsh, J. R. Lee, E. R. Draper, S. M. King, F. Jäckel, M. A. Zwijnenburg, D. J. Adams and A. J. Cowan, *J. Phys. Chem. C*, 2016, **120**, 18479–18486.

164 E. R. Draper, J. R. Lee, M. Wallace, F. Jäckel, A. J. Cowan and D. J. Adams, *Chem. Sci.*, 2016, **7**, 6499–6505.

165 E. R. Draper, L. J. Archibald, M. C. Nolan, R. Schweins, M. A. Zwijnenburg, S. Sproules and D. J. Adams, *Chem. - A Eur. J.*, 2018, **24**, 4006–4010.

166 J. T. Kirner, J. J. Stracke, B. A. Gregg and R. G. Finke, *ACS Appl. Mater. Interfaces*, 2014, **6**, 13367–13377.

167 A. S. Weingarten, R. V. Kazantsev, L. C. Palmer, D. J. Fairfield, A. R. Koltonow and S. I. Stupp, *J. Am. Chem. Soc.*, 2015, **137**, 15241–15246.

168 G. Santosh, E. Shirman, H. Weissman, E. Shimoni, I. Pinkas, Y. Rudich and B. Rybtchinski, *J. Phys. Chem. B*, 2010, **114**, 14389–14396.

169 V. Kunz, V. Stepanenko and F. Würthner, *Chem. Commun.*, 2015, **51**, 290–293.

170 B. H. Farnum, K. R. Wee and T. J. Meyer, *Nat. Chem.*, 2016, **8**, 845–852.

171 N. Singh, M. Tena-Solsona, J. F. Miravet and B. Escuder, *Isr. J. Chem.*, 2015, **55**, 711–723.

172 W. Kim, B. A. McClure, E. Edri and H. Frei, *Chem. Soc. Rev.*, 2016, **45**, 3221–3243.

173 S. Chen, Y. X. Li and C. Y. Wang, *RSC Adv.*, 2015, **5**, 15880–15885.

174 P. Chal, A. Shit and A. K. Nandi, *J. Mater. Chem. A*, 2016, **4**, 16108–16118.

175 F. S. Liu, R. Ji, M. Wu and Y. M. Sun, *Acta. Phys.*, 2007, **23**, 1899–1904.

176 N. J. Hestand, R. V. Kazantsev, A. S. Weingarten, L. C. Palmer, S. I. Stupp and F. C. Spano, *J. Am. Chem. Soc.*, 2016, **138**, 11762–11774.

177 I. Ghosh, L. Marzo, A. Das, R. Shaikh and B. König, *Acc. Chem. Res.*, 2016, **49**, 1566–1577.

178 G. M. Miyake and J. C. Theriot, *Macromolecules*, 2014, **47**, 8255–8261.

179 L. Zeng, T. Liu, C. He, D. Shi, F. Zhang and C. Duan, *J. Am. Chem. Soc.*, 2016, **138**, 3958–3961.

180 M. R. Wasielewski, *Acc. Chem. Res.*, 2009, **42**, 1910–1921.

181 D. Ley, C. X. Guzman, K. H. Adolfsson, A. M. Scott and A. B. Braunschweig, *J. Am. Chem. Soc.*, 2014, **136**, 7809–7812.

182 L. Nian, W. Zhang, S. Wu, L. Qin, L. Liu, Z. Xie, H. Wu and Y. Ma, *ACS Appl. Mater. Interfaces*, 2015, **7**, 25821–25827.

183 J. Balapanuru, G. Chiu, C. Su, N. Zhou, Z. Hai, Q. H. Xu and K. P. Loh, *ACS Appl. Mater. Interfaces*, 2015, **7**, 880–886.

184 Z. Zou, J. Ye, K. Sayama and H. Arakawa, *Nature*, 2016, **704**, 4–7.

185 M. Anpo and M. Takeuchi, *J. Catal.*, 2003, **216**, 505–516.

186 S. H. S. Chan, T. Y. Wu, J. C. Juan and C. Y. Teh, *J. Chem. Technol. Biotechnol.*, 2011, **86**, 1130–1158.

187 U. I. Gaya and A. H. Abdullah, *J. Photochem. Photobiol. C Photochem. Rev.*, 2008, **9**, 1–12.

188 X. Lang, X. Chen and J. Zhao, *Chem. Soc. Rev.*, 2014, **43**, 473–486.

189 S. Chen, P. Slattum, C. Wang and L. Zang, *Chem. Rev.*, 2015, **115**, 11967–11998.

190 R. V. Kazantsev, A. J. Dannenhoffer, A. S. Weingarten, B. T. Phelan, B. Harutyunyan, T. Aytun, A. Narayanan, D. J. Fairfield, J. Boekhoven, H. Sai, A. Senesi, P. I. O'Dogherty, L. C. Palmer, M. J. Bedzyk, M. R. Wasielewski and S. I. Stupp, *J. Am. Chem. Soc.*, 2017, **139**, 6120–6127.

191 E. R. Draper, O. O. Mykhaylyk and D. J. Adams, *Chem. Commun.*, 2016, **52**, 6934–6937.

192 A. S. Weingarten, A. J. Dannenhoffer, R. V. Kazantsev, H. Sai, D. Huang and S. I. Stupp, *J. Am. Chem. Soc.*, 2018, **140**, 4965–4968.

CHAPTER 2

Photocatalytic Hydrogen Evolution using Perylene Bisimides

The work in this chapter has been edited from the published article in the Journal of Materials Chemistry A (RSC) involving the following co-authors:

Michael C. Nolan. James J. Walsh, Laura L. E. Mears, Emily R. Draper, Matthew Wallace, Michael Barrow, Bart Dietrich, Stephen M. King, Alexander J. Cowan and Dave J. Adams*.*[1]

MW was responsible for the NMR diffusion experiments. MB was responsible for the TGA analysis. LLEM, BD and SMK assisted in the collection and analysis of the neutron scattering data. AJC and DJA assisted in the writing of the published manuscript which has been appropriately edited by MN for submission in this thesis.

Acknowledgements

We thank the EPSRC and the University of Liverpool for funding a DTA (MCN). We thank the STFC for funding our time at the ISIS facility (Experiment Number RB1610240)**.** We would also like to thank Ana Castilla-Manjon, Mark Forster, Jonathan Lee and Tom McDonald for their time and help throughout the project. Matthew Wallace would like to thank the EPSRC and Unilever for a Case Award. AJC and DJA thank the EPSRC for Fellowships (EP/K006851/1 and EP/L021978/1 respectively). LLEM, ERD, and BD thank the EPSRC for funding (EP/L021978/1). MB thanks UKRMP for funding (MR/K026739/1). The NMR spectrometers used for this work were funded by the EPSRC (EP/K039687/1 and EP/C005643/1). This work benefited from SasView software, originally developed by the DANSE project under NSF award DMR-0520547.

2.1. Abstract

There is growing interest in the design of supramolecular structures that are photocatalytically active. Perylene bisimides can be self-assembled to produce structures for photocatalytic hydrogen evolution. Herein, we explore the role of pH in controlling self-assembly and photocatalysis. It is shown that self-assembly, which occurs as the pH of the system is decreased, is required for hydrogen evolution to occur.

2.2. Introduction

Photoconductive low molecular weight gelators (LMWGs) are becoming increasingly important due to their tuneable mechanical, electronic and optical properties.[2] In particular, perylene diimide, or perylene bisimide (PBI) derivatives are of interest. In addition to being strongly absorbing in the visible region, many possess n-type semiconductor properties when aggregated,[2–4] which means they have potential use as light harvesting materials in photovoltaics and photocatalysis.[3,5–8] Interestingly, some PBIs are used as LMWGs as they can self-assemble into a wide range of structures as a result of non-covalent interactions including hydrogen bonding, van der Waals interactions and π–π stacking.[9,10] PBIs have also been successfully used as photocatalysts for a range of reactions including hydrogen evolution,[11–17] water oxidation[18] and the reduction of aryl halides.[19,20]

Proton reduction, or the Hydrogen Evolution Reaction (HER), is a widely studied half reaction from the water-splitting process.[21] The HER provides potentially a direct route to storing solar energy in the stable chemical bonds found in H_2.[22] The key to any emerging technology is to provide a cheap and competitive system; LMWGs can be assembled easily at low cost and are comprised only of abundant elements. This warrants their investigation as an alternative to the inorganic materials usually investigated.[23,22] Weingarten *et al.* reported the first work on photocatalytic π-conjugated gels for proton reduction, where the gel phase showed superior activity to that of the solid powder of the same compound,[14,17,24] showing how structuring is key. It is important to understand how a self-assembled network can affect the photocatalytic activity of a LMWG and how subtle changes in molecular packing can affect the photocatalytic ability.[25]

The self-assembly of LMWGs in water can be triggered using several methods, including a solvent switch or a pH switch.[15-17] Recently, PBIs substituted with amino acids in the imide

position, for example as shown in Figure 29a, have been studied for their photoconductive properties as thin films.[28–31] The carboxylic acid functionality on the amino acid side groups allows control over the solubility of the gelator in aqueous solutions at high pH (Figure 29a and b).[28,32] A subsequent decrease in the pH results in the consecutive protonation of the carboxylic acid groups, reducing the solubility and allowing for further self-assembly in solution (Figure 29c).

As mentioned in Chapter 1, Draper et al. have provided studies on the use of amino-acid substituted perylene bisimides as photovoltaic materials.[28,30,33,34] In the studies by Draper et al. both gels and solutions of self-assembled structures are dried down into films and generally show good photoconductivity when self-assembly is present, especially when fibres are aligned. The phenylalanine substituted perylene bisimide, however, has poor performance compared to the alanine substituted perylene bisimides, this is because the structures are less defined when dried down and are not representative of the structures in the wet sample, as recently reported by Mears et al.[35] In this study, the phenylalanine substituted compound is studied in solutions without drying down to help to understand and utilise the conductive nature of free structures in solution. Utilising a wet solution removes the technical processing step of drying down onto a film and allows for a 3D interpretation of self-assembled aggregates in solution.

In this chapter, we show that pH is crucial for controlling the self-assembly of amino-acid functionalised PBIs and that subtle changes in structure can also have a profound effect on the photocatalytic properties of the material. We demonstrate the role of aggregation by showing that we can optimise the rate of hydrogen evolution in water by fine-tuning the pH of the perylene bisimide assemblies.

2.3. Results and Discussion

2.3.1. Preparation and Characterisation of pH-dependant Self-Assembled Perylene Bisimide Solutions

The PBI used here (PBI-F) is substituted with L-phenylalanine on the imide positions (Figure 29a). The synthesis was carried out as described in the Experimental, a scale up to a 3 g synthesis from previous reports was carried out successfully.[28] Aqueous solutions of PBI-F were prepared at a concentration of 10 mg/mL with 20 v/v% methanol and 2 equivalents of

NaOH, resulting in deep red solutions with a pH between 11-12 (Figure 29b). Methanol was added as a sacrificial electron donor in this work for use in the photocatalytic studies.

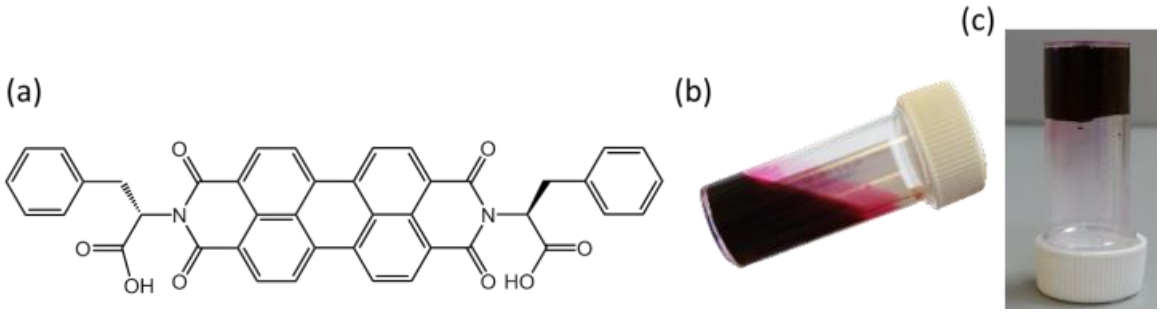

Figure 29. (a) Molecular structure of PBI-F; (b) high pH solution (10 mg/mL PBI-F, 2 eq. NaOH, 20 v/v% methanol); (c) low pH gel (10 mg/mL PBI-F, 2 eq. NaOH, 8 mg/mL GdL, 24 hours).

The pH of PBI-F solutions was lowered, while stirring, by the addition of 10 μL aliquots of 0.1 M HCl to form aggregates in solution. Initial studies showed that PBI-F has two apparent pK_a values (Figure 30) at 8.6 and 5.7, indicated by plateaus in pH. These are related to the consecutive protonations of the carboxylic acid groups. Whilst it might be expected that there is only one pK_a since the two carboxylic acids are apparently identical, these elevated pK_a values can be associated with the pK_a of self-assembled structures.[36] It is therefore expected that structural changes will occur within the solutions at each apparent pK_a.[36,37] For ease, we will describe solutions at pH >8.6, at pH 5.7-8.6, and at pH <5.7 as high, medium, and low pH respectively.

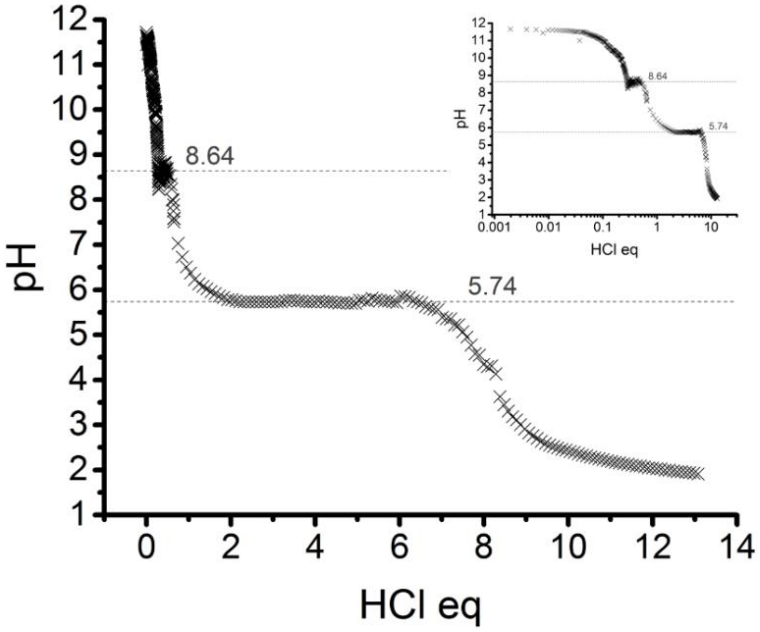

Figure 30. p*K*a titration of PBI-F solution (10 mg/mL) starting from pH 12 and decreasing the pH using 10 μL aliquots of 0.1M $HCl_{(aq)}$. Horizontal lines indicate the two apparent pK_a buffering regions. (Inset) HCl eq. plotted on a log scale to reveal the first apparent pK_a in more detail.

PBI-F solutions can also be gelled by a slow acidification using glucono-δ-lactone (GdL) (Figure 29c, Figure 31).[28,38] The storage modulus, G′, and the loss modulus, G″, evolve in stages as the pH is slowly lowered past the two pK_a values. The strengthening of the gel network, as signified by the increase in the absolute G' value, indicates the formation of a network of self-assembled structures. Although gels are not used in this study, self-assembled structures are still formed in solution when the pH is lowered while being stirred, although this will not form a self-supported gel network it would form a dispersion of aggregates in solution. The stable structures that PBI-F forms in aqueous solutions of 20 v/v% methanol were probed using UV-Vis absorption spectroscopy, viscometry and small angle neutron scattering (SANS) (Figure 32-Figure 36).

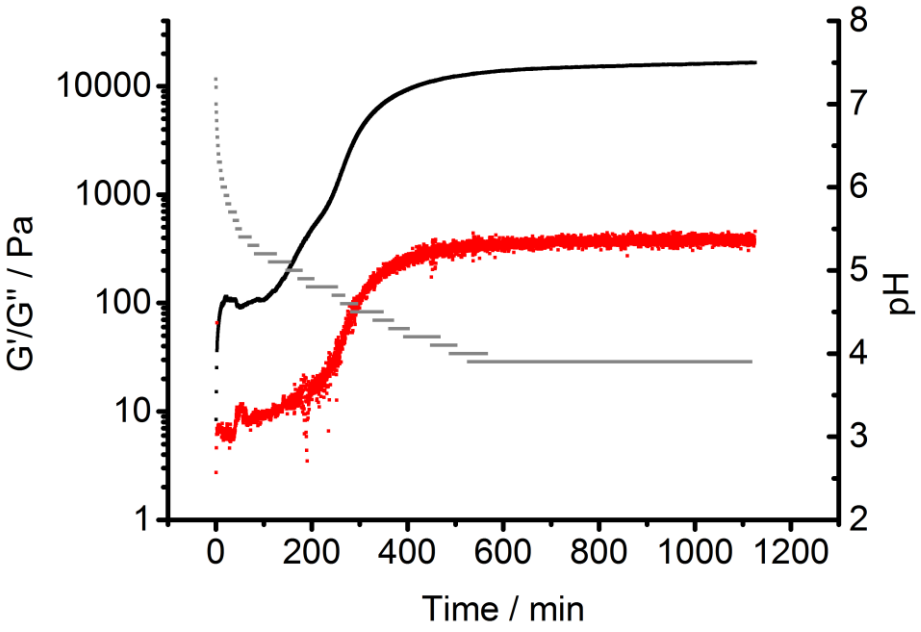

Figure 31. Time sweep for gelation using 8 mg/mL GdL in a PBI-F solution (10 mg/mL) containing 2 molar equivalents $NaOH_{(aq)}$. Grey lines indicate pH (right y-axis) of the gel. Data points indicate G′ (black) and G″ (red) during the evolution of the PBI-F gel over time at a constant frequency. Rheology was performed at 0.5 % strain and 10 rad/s at 25 °C.

Sufficient π -π stacking between perylene cores allows for the formation of PBI fibres and electron transport along these fibres.[18,39] PBIs have characteristic absorption bands at visible wavelengths related to the vibrational transitions of the S_0-S_1 absorption; the intensity, resolution and shift of the absorbance bands are dependent upon the environment around the aromatic core. This allows UV-Vis absorption spectroscopy to be used as a tool for studying aggregation processes.[40] The HOMO and LUMO of the perylene core have a small electronic coupling to the substituents on the peripheral imide positions, due to an orbital node at the imide position.[10,41,42] This allows for diversification in the imide substitutions without largely affecting the energy levels of the molecule's HOMO and LUMO. The orbital energies can instead be manipulated by adding substituents directly onto the perylene core. π-stacking of adjacent molecules can also affect the overall HOMO/LUMO of the system.[41,43,44]

Figure 32 shows the UV-Vis absorption spectra of PBI-F solutions. The higher intensity of absorbance of the 0-1 vibrational transition of the S_0-S_1 absorbance band at 506 nm compared to the 0-0 vibrational transition at 543 nm is an indication of H-type aggregation (Figure 17).[45–50] H-type aggregation describes a face-to-face stacking of the perylene cores of adjacent molecules whereas a J-type aggregation describes a slip-stacked aggregation.[40] The absorption

spectrum of H-aggregates shows a bathochromic shift compared to the spectrum of a monomeric dispersion of PBI in solution.[28] In the case of PBI-F, which has two bulky aromatic groups from the two phenylalanine moieties, we expect a slight rotational displacement in the face-to-face stacking to account for the steric hindrance which would be supported by directional H-bonding of the carboxylic acid groups.[51]

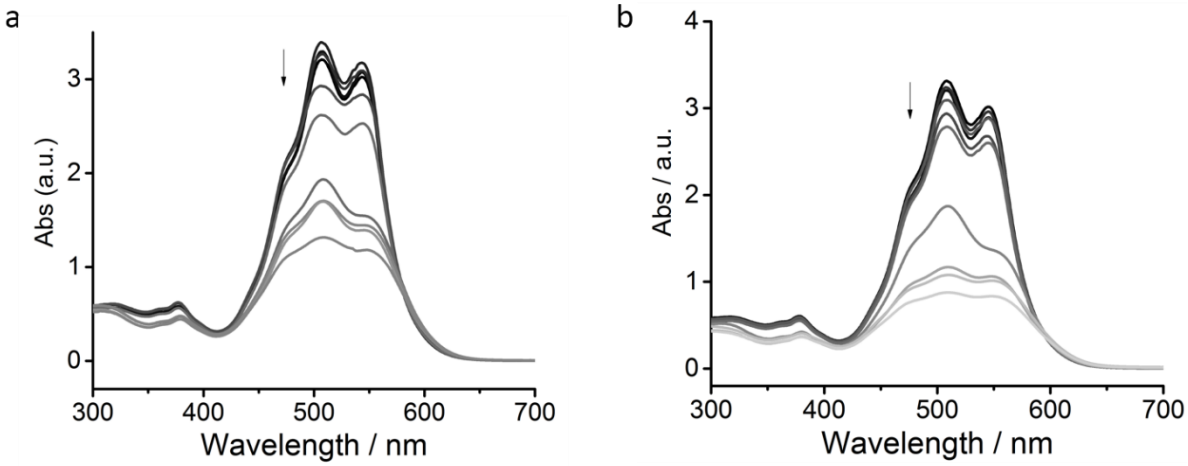

Figure 32. UV-Vis absorption spectra of PBI-F solutions (10 mg/mL) in (a) 20% v/v% methanol$_{(aq)}$ and (b) in H_2O. Arrows indicate the decrease in pH as listed: pH 11, 10, 9, 8, 7, 6, 5, 4, 3, 2.

The solutions in Figure 32a contain 20 v/v% methanol in H_2O at pH 11, 10, 9, 8, 7, 6, 5, 4, 3 and 2, as these are the compositions used for photocatalytic experiments. As methanol has different solvation properties to H_2O, it was also prudent to compare to solutions in H_2O to understand the effect of methanol on the aggregation. The data here suggests that the introduction of 20 v/v% methanol has no major effect as the solutions still exhibit H-aggregation. The reduction in intensity of the bands upon decreasing pH also occurs at similar pHs and to similar intensities between the two solvent mixtures. The decreased intensity of the spectra when the pH is dropped coincides well with the apparent pK_a values (Figure 30), the pH values where the extent of aggregation increases.[52]

SANS is well suited to study LMWGs as neutrons are non-destructive and possess the ability to probe the bulk material. The fitted data provide details of the size and shape of structures in the sample.[53–55] For the SANS experiments, deuterated materials d_4-methanol, D_2O, NaOD and DCl were used to enhance the contrast between the solvent and the molecules.[53] If non-

deuterated solvents are used, then the resulting scatter is dominated by the scattering of the solvent molecules. However, if the scattering length density (SLD) of the molecule and the solvent are matched then the molecule becomes invisible in the scatter.

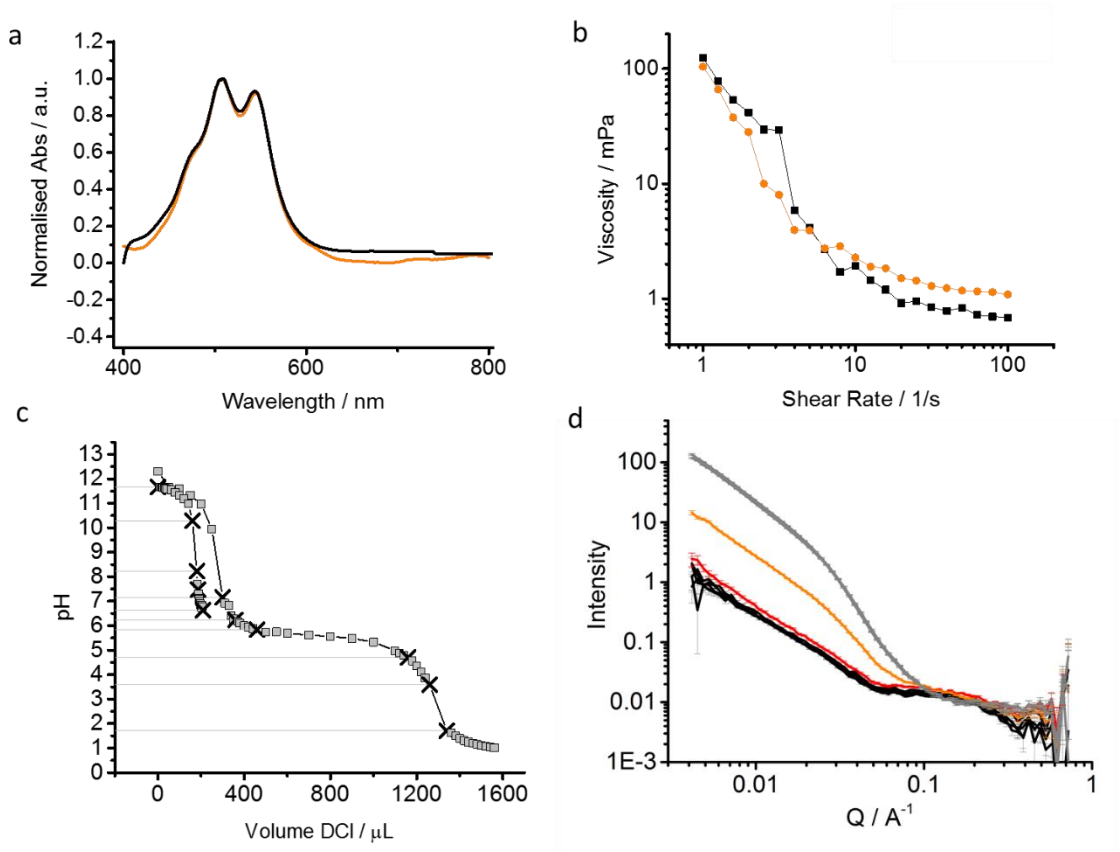

Figure 33. (a) UV-Vis absorbance spectra of PBI-F in 20 v/v % methanol$_{(aq)}$ (black) and deuterated solvents (orange); (b) Viscosity measurements; (c) pH drop, converted from pD,[56] of two stock solutions where crosses indicate where 1 mL aliquots were removed from the starting 20 mL solution for SANS measurements; (d) SANS data collected in a 5 mm pathlength quartz cuvette. pH 11.67, 10.29, 8.40, 7.42, 7.16 (black); pH 6.63 (red); pH 5.84 (orange) and pH 4.64, 3.52, 1.9 (grey).

Samples containing deuterated solvents were measured using UV-Vis absorption spectroscopy and viscometry and compared to the protonated solvents to ensure no unexpected changes would occur. Deuterated samples showed no changes in their absorption spectra or viscometry as compared with the protonated solvents (Figure 33a-b). All pD measurements were converted to pH to allow effective comparison with data collected in pH.[56] The pD of a deuterated solution of PBI-F in 20 v/v% MeOD$_{(aq)}$ was reduced by adding 0.1 M DCl. Aliquots were taken from the solution spanning the whole pD range and a scattering pattern was obtained from each

sample (Figure 33c-d). Here, accurate pH readings are given as these were the aliquots taken during the pH drop.

The scattering data is model-fitted to analytic expressions describing different shapes by using the SasView software (version 3.1.1).[57] For these data, a customised model was created comprising of a (Kratky-Porod) flexible cylinder, a sphere and an absolute power law (Figure 34).[58–60] The Kratky-Porod model depicts a worm-like micellar structure which is expected for this class of PBIs,[28,61,62] the power law (Q^{-m}) accounts for the mass fractal contribution to the scattering intensity and the sphere model represents a sphere.

The composite model formed from the addition of the absolute power law (PL), flexible cylinder (FC) and sphere (Sp) models is summarised by (Equation 4).[57]

$$I = SF_O\{SF_{PL}.P(Q)_{PL} + SF_{FC}.P(Q)_{FC} + SF_{Sp}.P(Q)_{Sp}\} + Background \qquad \text{(Equation 4)}$$

where P(Q) is the relevant scattering form factor and SF is the relevant scale factor and SF_o is the over scale, which was fixed at 1 during fitting. Constant SLD parameters were used: 6.26 x 10^{-6} $Å^{-2}$ for the MeOD/D_2O solvent and 2.17 x 10^{-6} $Å^{-2}$ for the flexible cylinder and sphere. Parameters such as the radius and length of the flexible cylinder and radius of the sphere can be attained from the fits. Uncertainties for parameters were determined by where the model deviated from a visibly good fit. For the longest lengths, only a lower limit can be accurately determined as they move beyond the measurement limits of the instrument. In some instances, this has resulted in flexible cylinder lengths that are beyond the actual measurement limit of the instrument (>150 nm) in the configuration used. This does not invalidate the analysis, it just means that affected values are associated with a greater uncertainty.

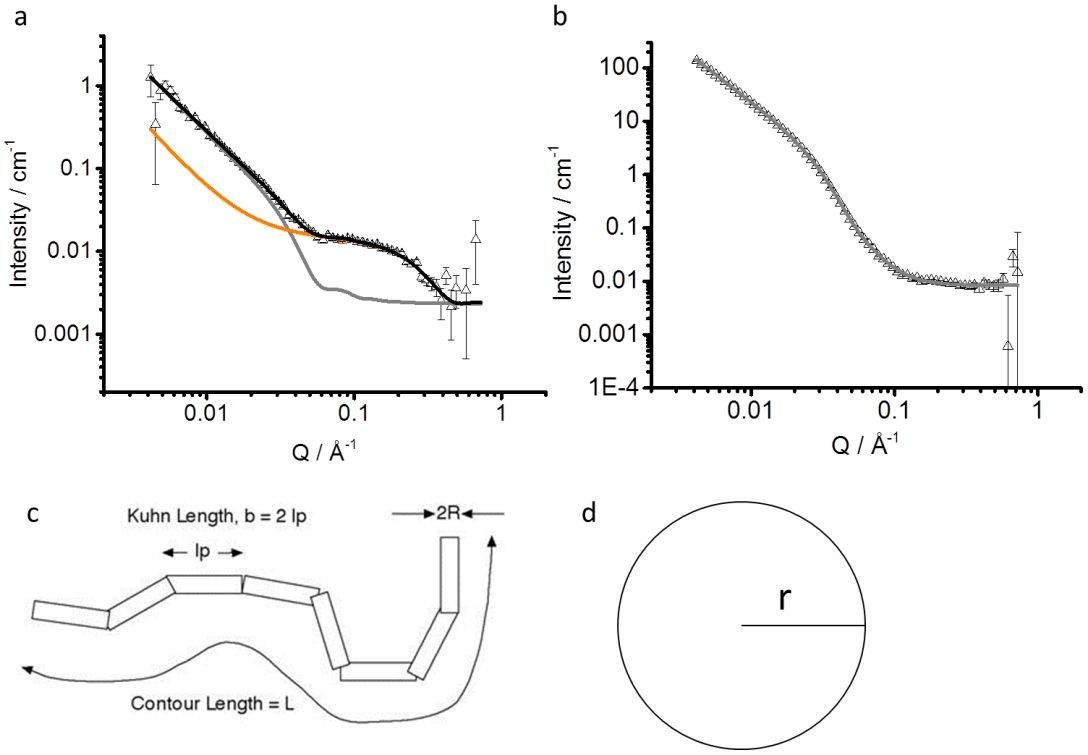

Figure 34. (a) SANS from PBI-F solution at pH 10.6 with fitting lines showing contribution of a flexible cylinder model (grey) and a spherical model (orange) to attain a complete fit (black) of the raw data (triangles with error bars) (b) scattering data from a pH 3.5 solution showing a complete fit to the flexible cylinder model. All models also include a Q^{-m} power law. Schematic representations of (c) the flexible cylinder and (d) sphere.

A clear difference between the curve features of both the sphere and flexible cylinder models are shown in Figure 34a, both shown in combination with an identical power law model. It was impossible to attain a fit of the data using just one model, whereas the combination of the spherical model with the flexible cylinder and power law models provided a convincing fit for all data (Figure 35). The flexible cylinder model revealed that anisotropic structures are present in solutions at both high and low pH (Figure 35-Figure 36), although as will be shown below the relative concentration of these structures is strongly pH dependent. The fitting parameters from the flexible cylinder model (Figure 36) depict the worm-like micelles with radii of 6.2 (± 1.0) nm and a length of 414 (-110, +86.0) nm (where the minimum and maximum error is stated in brackets and plotted in Figure 36). These structures may be described as worm-like micelles at high and medium pH where the PBI still holds a negative charge. However, at low pH, below the second apparent pK_a, there is expected to be little charge on the PBI molecules and we

describe these as fibres. The fibres at low pH have radii of 5.1 (± 1.0) nm and a length parameter >500 nm.

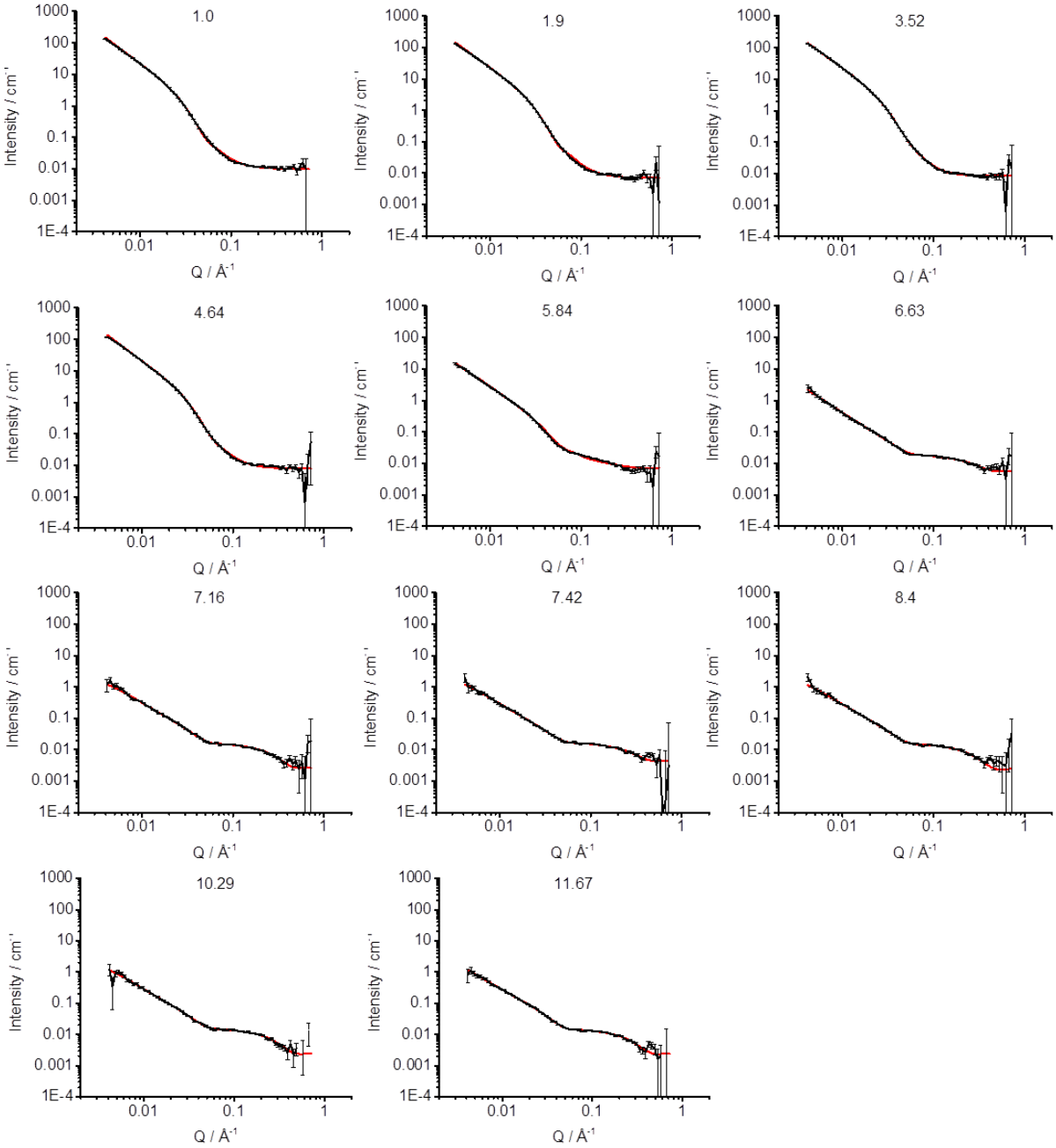

Figure 35. SANS data (black symbols) with model-fitted curves (red lines) of PBI-F (10 mg/mL) in D_2O with 20 v/v % deuterated $methanol_{(aq)}$ at different pD values.

At low pH, the extent of stacking in a single structure is increased (shown by an increase in the power law and flexible cylinder scales, see Figure 36b and d) due to the absence of strong coulombic interactions and the dominance of the weaker intermolecular interactions that promote self-assembly, including π-stacking, H-bonding, Van der Waals and hydrophobic

interactions. The fibres at low pH also have a Kuhn length parameter of 7.8 (-1.0, +7.0) nm compared to 26.3 (-3.00, +4.00) nm for the high pH worm-like micelles (Figure 36e); the Kuhn length is a segment of the flexible cylinder model (Figure 34) and a smaller Kuhn length indicates a more flexible structure.[59,60] For the fibres at low pH, the lack of a supporting hydrated shell of water molecules around the fibre may give rise to the higher flexibility of the structures. The reduced coulombic interactions at low pH may also allow additional interactions between PBI-F molecules *via* the peripheral phenyl rings on the imide groups.

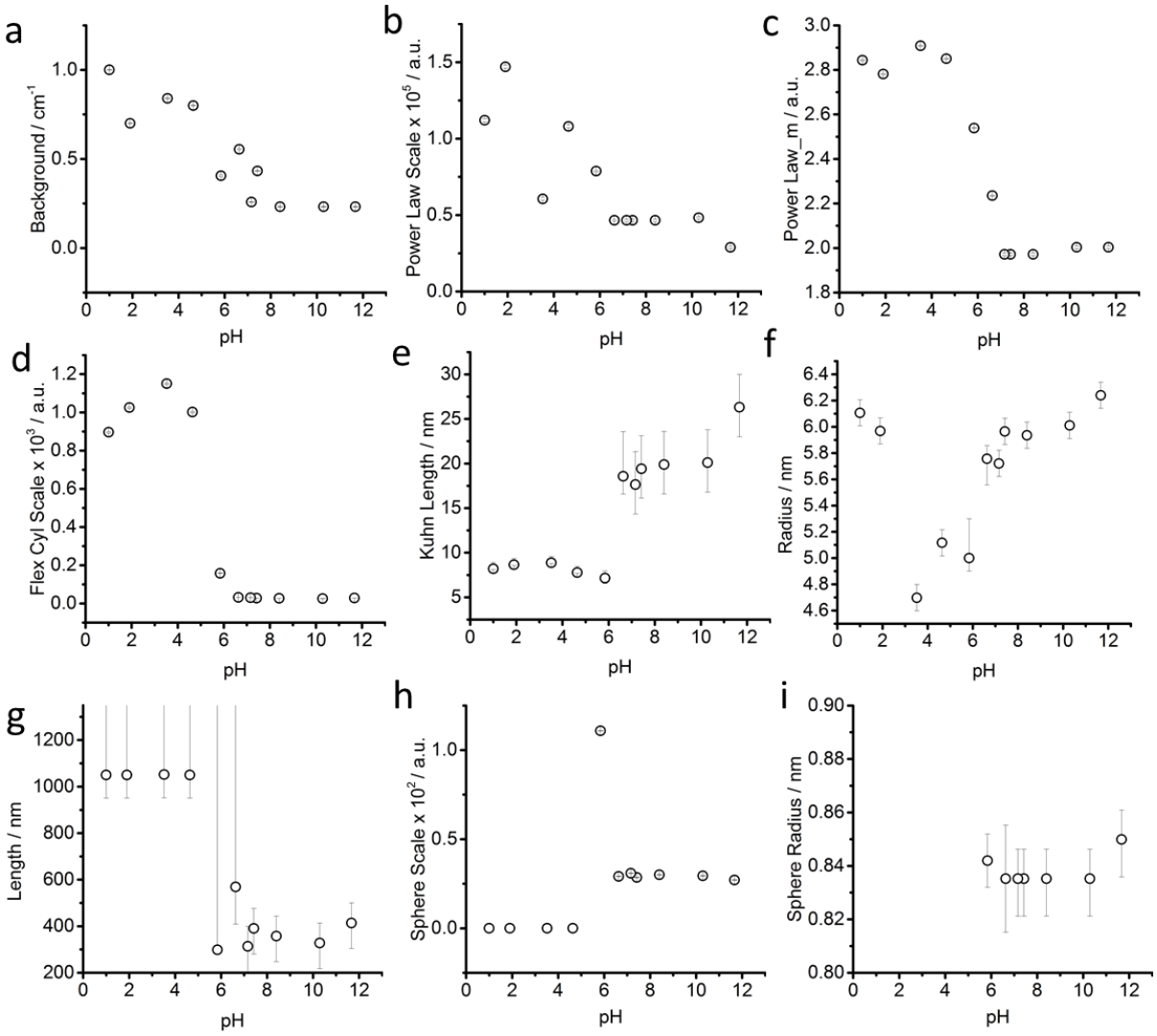

Figure 36. Fitted parameters for the curves shown in Figure 35. (a) background; (b) power law model scale; (c) power law exponent 'm'; (d) flexible cylinder model scale; (e) flexible cylinder Kuhn length; (f) flexible cylinder radii; (g) flexible cylinder length; (h) sphere model scale and (g) sphere radii. Lower and upper uncertainties with the parameters have been investigated and plotted as error bars. Error bars are shown for all points and are sometimes smaller than the scatter circle.

The solutions at high and medium pH also showed an additional type of structure dominating the scattering curve, which exhibits a hump-like feature at around Q = 0.1 $Å^{-1}$ correlating to structures a few nanometres in size (Figure 34 to Figure 36). We hypothesised that free molecules were present in solution above the second apparent pK_a at pH 5.7; in order to test this, diffusion ^{1}H-NMR was carried out on a high pH solution. Broad NMR signals, reduced relaxation times and negative NOEs clearly indicated the presence of aggregated species in solution (Figure 37-Figure 38). However, the observed species were found to possess hydrodynamic radii of only 1.7 (± 0.03) nm. The hump-like feature in the scattering pattern at Q = 0.1 $Å^{-1}$ was found to fit well to the spherical model with a sphere radius of 0.9 (± 0.1) nm. The SANS and NMR data thus strongly suggest the presence of free molecules at high pH, which co-exist with worm-like micelles. The difference between the radii calculated from the two techniques can be related to the uncertainties associated with the fitting and calculation[63,64] as well as solvation effects.

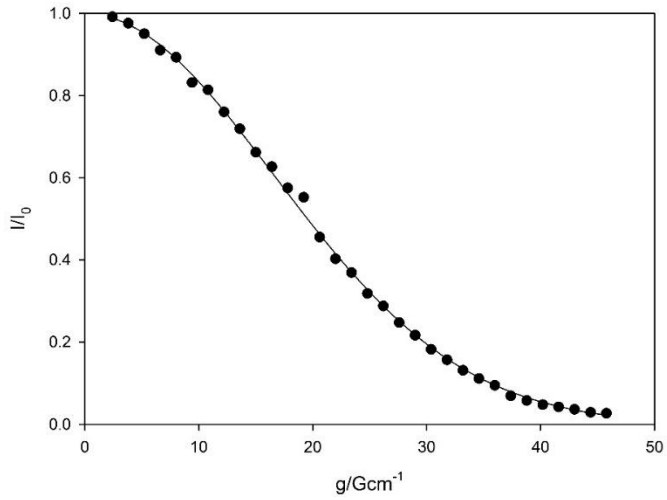

Figure 37. Pulsed-field gradient nuclear magnetic resonance (PFG-NMR) attenuation plot for PBI-F in 20% MeOH, 80% H_2O at pH 11.2. The solid line is a best fit to Equation 5 (see Experimental). Acknowledgement: Matthew Wallace (University of Liverpool)

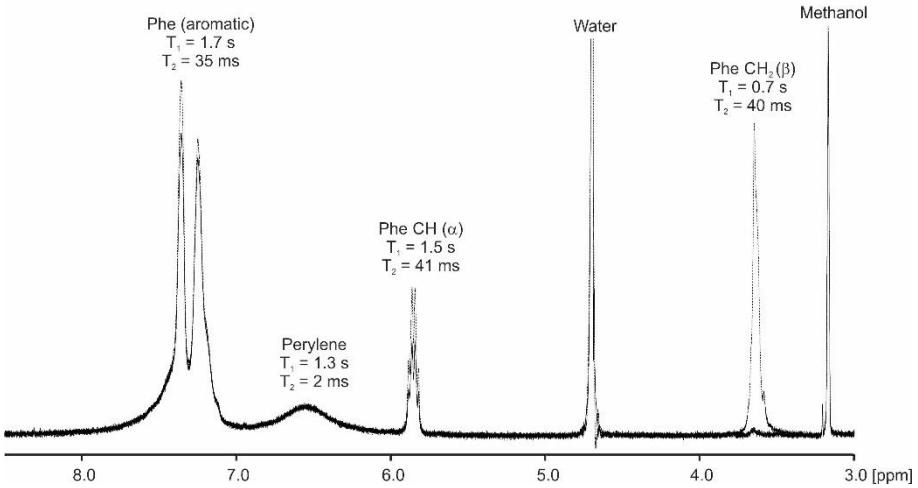

Figure 38. ^{1}H-NMR spectrum of a 10 mg/mL solution of PBI-F in 80 % D_2O, 20% CD_3OD with (solid) and without (dashed) pre-saturation applied to the CH_2 resonances of the phenylalanine (Phe) residues. ^{1}H T_1 and T_2 relaxation times are also indicated. Acknowledgement: Matthew Wallace (University of Liverpool).

We can further our understanding by addressing the contributions of each of the models to the fits (Figure 36). The power law scale factor increases as the pH is lowered showing a corresponding increase in long-range structures. Interestingly, at high pH the spherical model dominates *ca.* 99 %, which is in general agreement with ^{1}H-NMR measurements which show *ca.* 90 % of PBI-F exists as free molecules in solution at high pH. At low pH, the SANS data fits to 100 % flexible cylinder model indicating that the PBI-F molecules are assembled into fibres.

At pH 6.5, the power law scale contribution along with its exponent *m* begins to significantly increase, showcasing the increase in assembly of the molecules into structures which scatter. An increase in the contribution of the flexible cylinder model is also observed at pH 6.0. Importantly, the transition from free molecules to aggregated species at ~pH 6.5 proves to be vital for photocatalysis, as discussed below.

The optical density (O.D.) of the PBI-F samples at 506 nm and the SANS intensity at Q = 0.01 $Å^{-1}$ helps to reveal how aggregation increases as the pH decreases (Figure 40a). As the pH is lowered below the first apparent pK_a at pH 8.6, the O.D. begins to decrease quickly and the scattering intensity increases slowly. At the second pK_a at pH 5.7, the scattering intensity increases at a notably greater rate with not much change thereafter. It is clear that the greatest

change in aggregation occurs as the pH is decreased below pH 5.7; this is where gelation of these materials occurs when the pH is lowered slowly with GδL (Figure 31) and where the formation of longer fibrous structures is observed in SANS for solutions where the pH is lowered using HCl. It is also interesting to note that UV-Vis absorption data shows that aggregation begins to occur below pH 8.6 when the mono-protonated PBI-F starts forming and that SANS indicates the structures begin to change significantly below pH 5.7.

Viscometry was used to identify the extent of networks in the solutions (Figure 39, Figure 40b). Samples were also filtered, using Grade 1 Whatman® filter paper, to collect any solid aggregates present in solution.

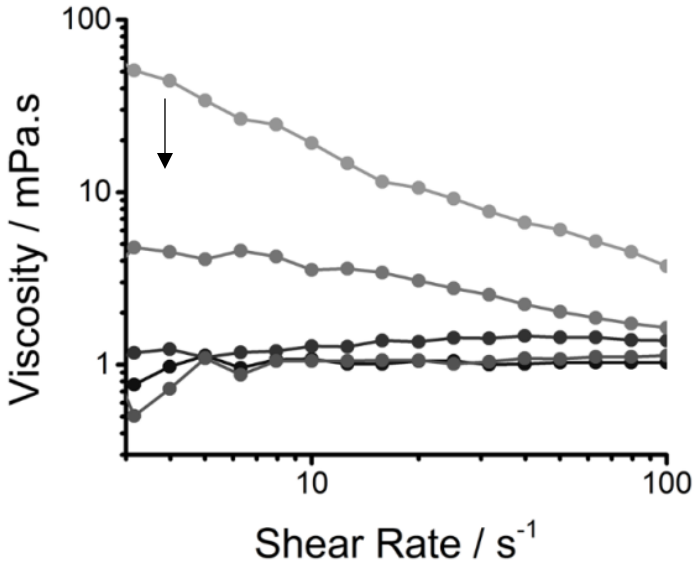

Figure 39. Viscosity of PBI-F (10 mg/mL) solutions in H_2O with 20 v/v% methanol. The viscosity decreases as the pH is increased; data are shown for pH 6.41, 7.68, 8.71, 9.42, 10.1. Arrow indicates reducing viscosity and increasing pH.

Figure 40b shows the percentage of solid collected after filtering 2 mL of a sample compared to the viscosity intensity at a shear rate of 5 s^{-1}. Greater than 95 % solid, compared to the amount of PBI-F added into solution, was collected from the fully protonated solutions below the second apparent pK_a. The dried solutions at high pH and collected solids from low pH were imaged by transmission electron microscopy (TEM) and scanning electron microscopy (SEM) (Figure 41). The microscopy data shows aggregates which are much larger than those observed from SANS. Drying artefacts are highly prevalent in these systems as drying can lead to further aggregation and structural changes.[65] Therefore, the SANS data, which probes the bulk sample, along with UV-Vis spectroscopy and viscometry are better representations of the system used.

Data from SANS, UV-Vis, viscometry and the solid filtration has been summarised in Figure 40 to help clearly show the effect of protonations on the formation of aggregates in solution.

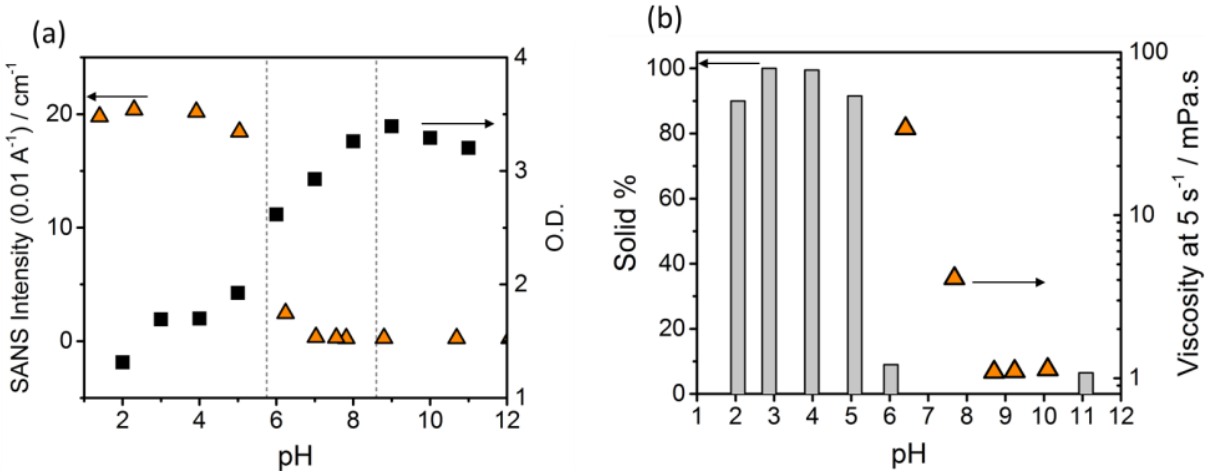

Figure 40. (a) SANS intensity (triangles) from scattering patterns and optical density (O.D., squares) from UV-Vis absorption spectra of PBI-F (10 mg/mL) solutions in 20 v/v% $CH_3OD_{(aq)}$. SANS intensity taken at 0.01 Å-1 and O.D. at 506 nm; Vertical dotted lines indicate pK_a1 (pH 8.6) and pKa2 (pH 5.7) (b) Percentage of PBI-F collected from a solution by filtration (column) and viscosity of solutions at a shear rate of 5 s^{-1} (triangles). Arrows indicate to which axis data correspond.

The viscosity of solutions (Figure 39-Figure 40,) increases greatly between pH 8.6 and 5.7 showing that the singly protonated species promotes the formation of a self-assembled network; this correlates with the broadening of absorption bands in the UV-Vis spectra and changes in the SANS parameters towards longer fibres. The increasing viscosity of the solutions down to pH 5.7 is due to the presence of a higher concentration of worm-like micelles in solution which has been shown in the NMR data.

Hence, we conclude from the UV-Vis, SANS and viscometry data that a low concentration of short, worm-like micelles and a high concentration of free solvated molecules are present in the PBI-F solutions at high pH. The free molecules aggregate to form more worm-like micellar structures below pH 8.6. As the pH approaches 5.7 and the molecules become fully protonated, all the molecules are aggregated into long fibres. The protonation steps lead to intermolecular interactions prevailing over solvating forces, allowing self-assembly on a larger scale to occur.

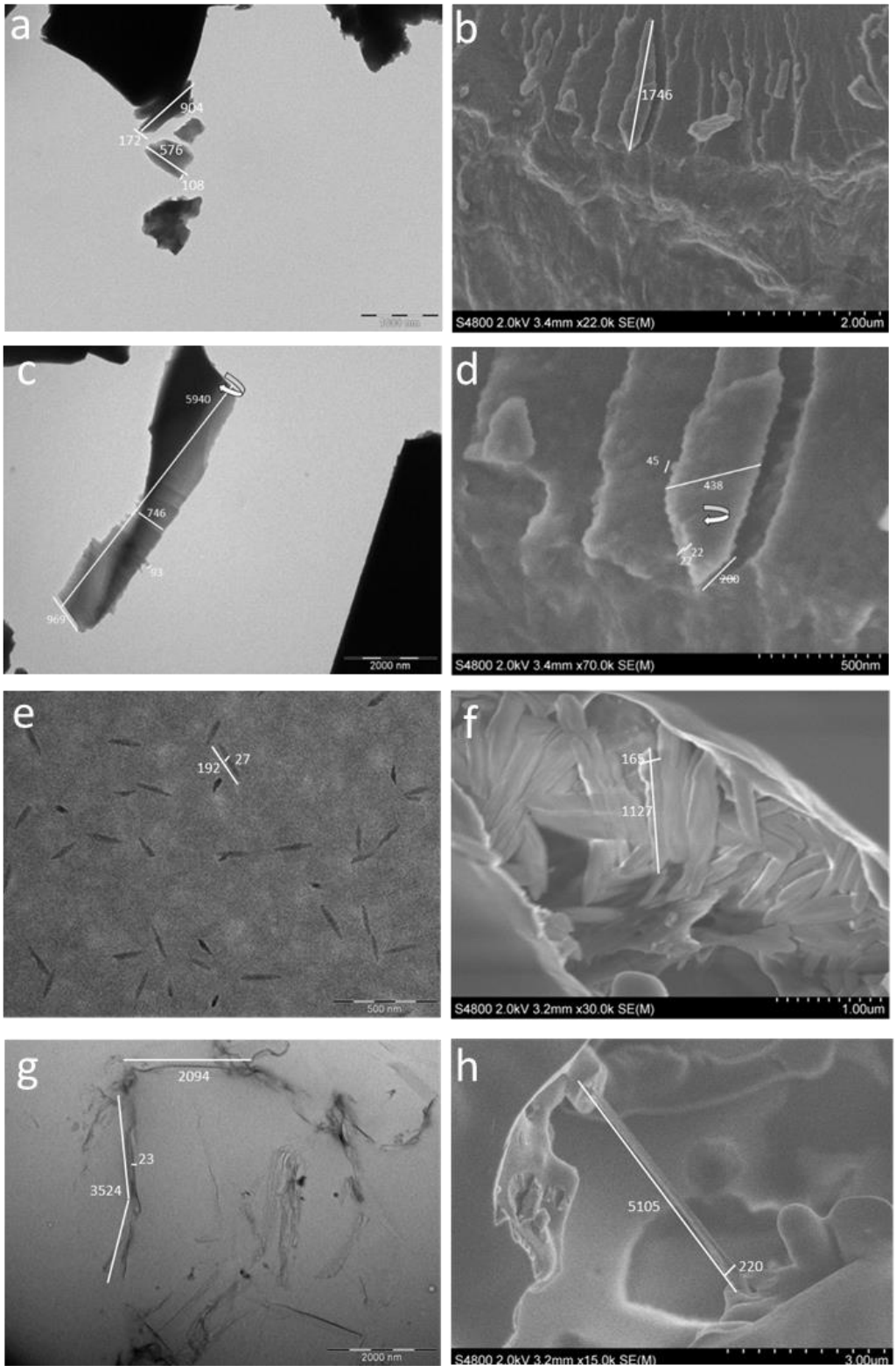

Figure 41. Microscope images of dried aggregates collected from pH 4.5 (a-d) and pH 10.5 (e-h) solutions of PBI-F (10 mg/mL) in 20 v/v% methanol$_{(aq)}$. The left figures being TEM images (a, c, e, g) and the right being SEM (b, d, f, h). Scale bars inset are: (a) 1000 nm; (b) 2000 nm; (c) 2000 nm (d) 500 nm; (e) 500 nm; (f) 1000 nm; (g) 2000 nm; (h) 3000 nm. Acknowledgement for SEM images: Emily Draper (University of Liverpool).

2.3.2. Using Self-Assembled Perylene Bisimide Solutions for Photocatalytic Hydrogen Evolution

Photocatalytic hydrogen evolution was tested at a range of pHs using PBI-F (10 mg/mL) in the presence of polyvinylpyrrolidone (PVP)-capped platinum nanoparticles (1 mol%, *ca.* 8 nm diameter) and methanol (20 v/v%). Methanol is a widely used sacrificial electron donor that induces a minimal pH change upon addition to solution.[66] Platinum has been commonly used as a catalyst for many years.[67] The preparation of platinum nanoparticles has a relatively simple synthesis and characterisation (Figure 42-Figure 45).[67] Altering the type and composition of the hole scavenger and co-catalyst would undoubtedly result in varying photocatalytic activities, but were not examined in this chapter. Preliminary experiments showed that 20 v/v% methanol and PVP-Pt nanoparticles at a concentration of 1 mol% Pt resulted in stable hydrogen evolution rates *ca.* 1 μmol/g/h which, although low, is a detectable amount which can be compared between samples differing in pH and PBI aggregation.

Platinum nanoparticles were prepared by the reduction of salt with potassium bistartrate in the presence of the stabilising agent, PVP.[67] The higher the concentration of PVP, the smaller the size of the nanoparticles.[67] A PVP concentration of 1.0 $wt\%_{(aq)}$ with 1 mM H_2PtCl_6 resulted in monodisperse nanoparticles with an average hydrodynamic radius of 12 nm (Figure 42). Transmission electron microscopy (TEM) images of dried solutions showed aggregation of particles and single particles could not be observed (Figure 43). Thermogravimetric analysis (TGA), where a freeze-dried solution of the nanoparticles was subject to heating, showed that the sample consisted of 7.4% water, 83.7% organic material (PVP) and 7.6% platinum metal.

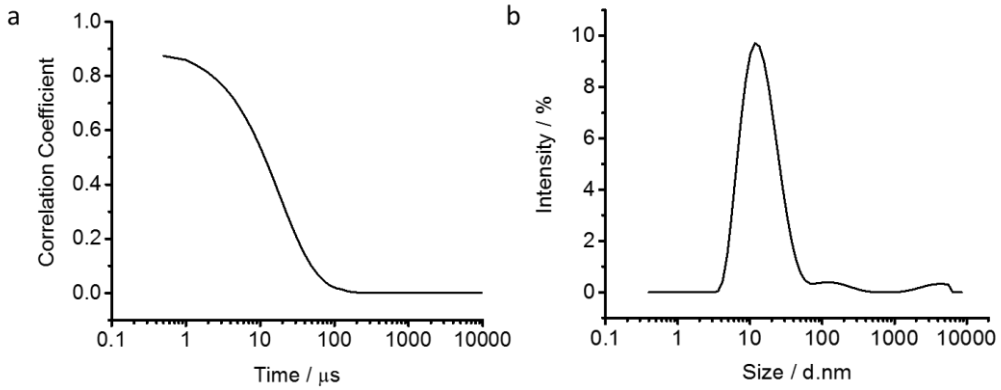

Figure 42. Dynamic Light Scattering (DLS) data of PVP-Pt NPs. (a) Correlogram showing the correlation function where the y-axis is the normalised correlation function and (b) size distribution by intensity calculated using a cumulants fit. Three runs, each with 15 scans, were averaged for the final profile.

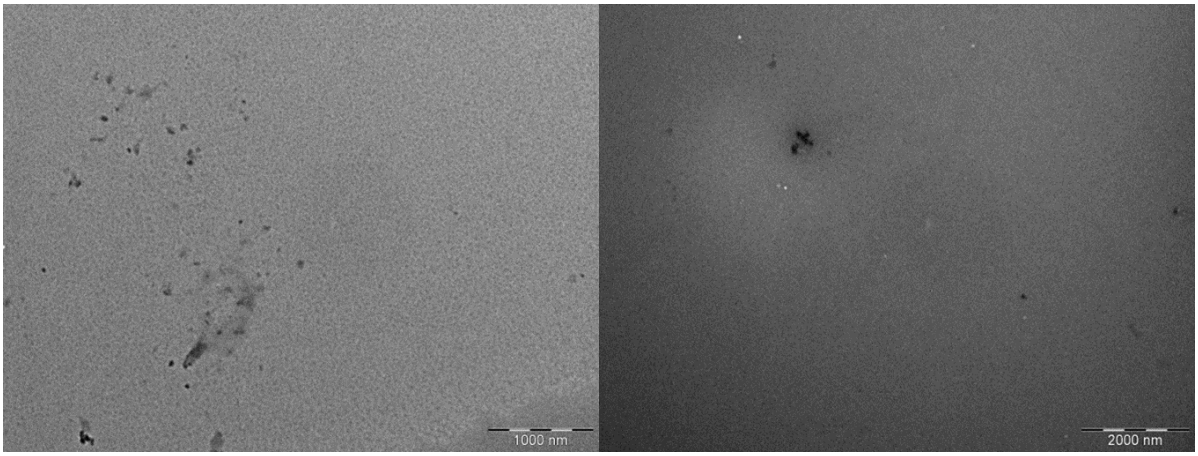

Figure 43. TEM images of PVP-Pt NPs. Samples were dabbed onto a grid and blotted to remove excess water. An accelerating voltage of 120 kV was used. The grids used had a 400 nm mesh copper grid with a carbon formvar coating. Scale bars inset are 1000 nm (left) and 2000 nm (right).

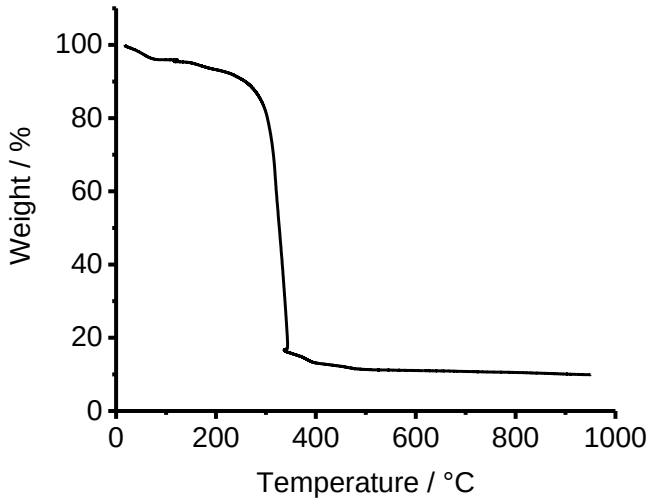

Figure 44. TGA of PVP-Pt NPs. Measurements were carried out on a TA Instruments SDT Q600 TGA machine using a constant air flow of 50 mL/min. Samples were heated up to 120 °C at a heating rate of 20 °C/min and kept at 120 °C for 20 minutes to remove any water, then ramped up to 1000 °C at a heating rate of 10 °C/min.

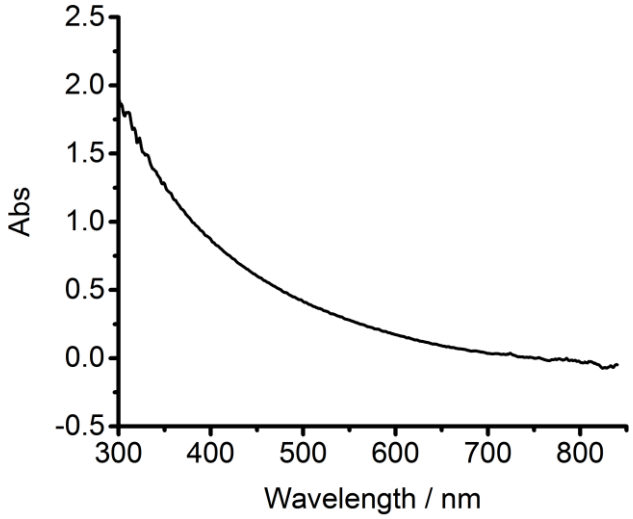

Figure 45. UV-Vis of PVP-Pt NPs. The UV-Vis spectrum was recorded in a quartz cuvette with a 1 cm path length with a Thermo Scientific NanoDrop UV-Vis spectrometer.

Samples of PBI-F, methanol and Pt NPs were irradiated for 4 hours with a white xenon lamp (90 mW cm^{-2}, 300-795 nm (KG1 filter)) while stirring as described in the Experimental and Figure 46-Figure 47. The amount of hydrogen evolved was measured using gas chromatography (GC) via a gas injection from the quartz cuvette headspace.

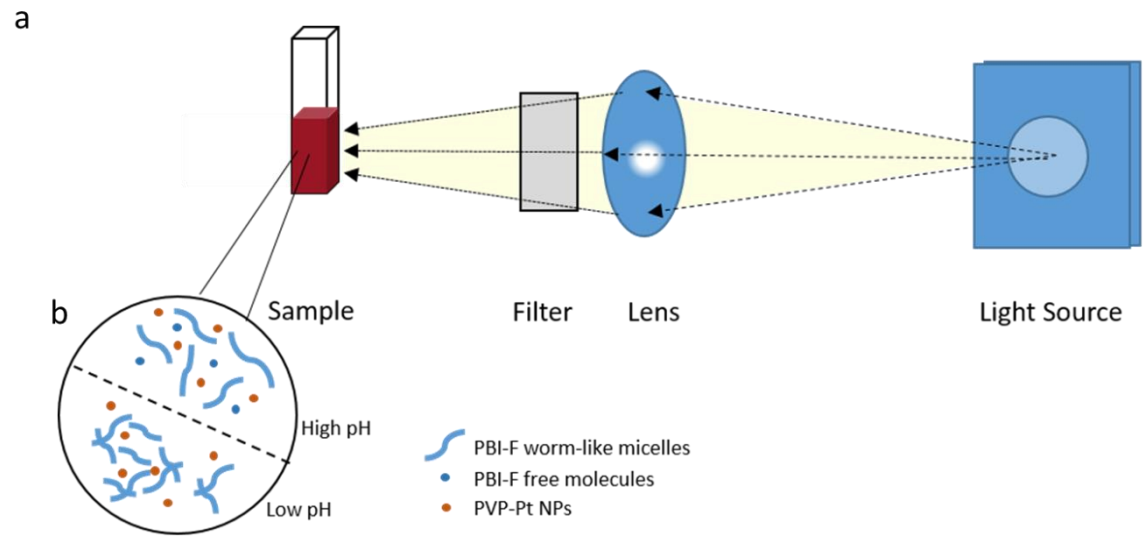

Figure 46. (a) Schematic of the setup used for photocatalytic hydrogen evolution experiments (b) Schematic of the PBI-F fibres, free PBI-F molecules and PVP-Pt NPs in solution at high and low pH. Interactions between PVP-Pt nanoparticles and PBI fibres are not known.

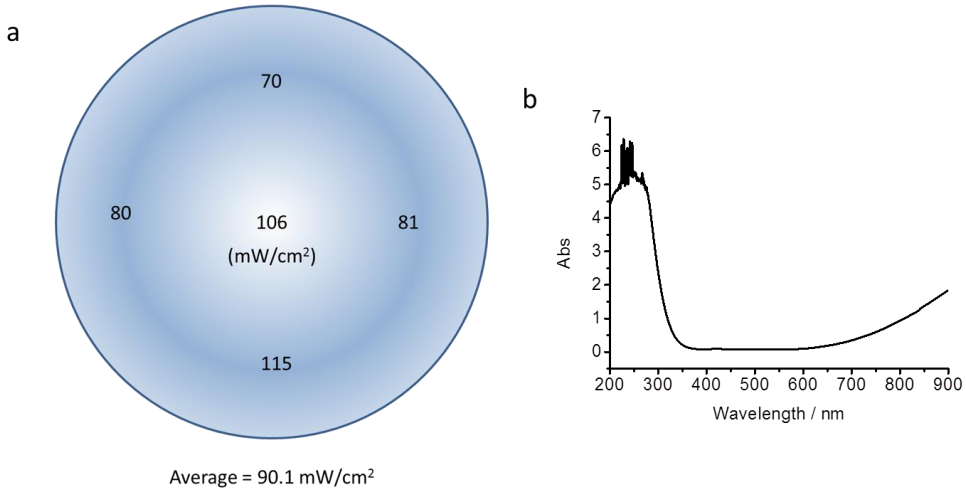

Figure 47. (a) Spectral power distribution of the light beam used to irradiate the sample. (b) The UV-Vis absorption spectrum of the demountable KG1 filter used.

Initial control experiments in the absence of platinum yielded minimal hydrogen. In the absence of methanol, a large amount of CO was evolved during photocatalysis indicating that PBI-F oxidation occurs without the sacrificial donor.[31] The amount of CO evolved was significantly reduced when methanol was present. However, no photodegraded product could

be detected by NMR or FTIR; we note that this would only be present in very small amounts and so might be below the limit of detection.

After 4 hours of irradiation, no hydrogen was evolved at pH values above 8, Figure 48. Between pH 7-5.4 a low rate of hydrogen was produced but repeat experiments to yield error estimates clearly demonstrate the photocatalytic formation of hydrogen. The solution noticeably begins to form a gel-like aggregates at pH 5 which results in a reduced rate of hydrogen production, likely due to the increased viscosity. Below pH 5, the structures appear to aggregate out of solution and are present as a suspension.[68] At pH 4.75, a sharp increase in the rate of H_2 evolution is observed to occur. The hydrogen evolution reaches a maximum at pH 4.5 with a decline at lower pHs. At pH 4.5, our structural characterisation studies (above) show that PBI-F has self-assembled into long fibres and it is proposed that these large aggregates are the photocatalytically active species.

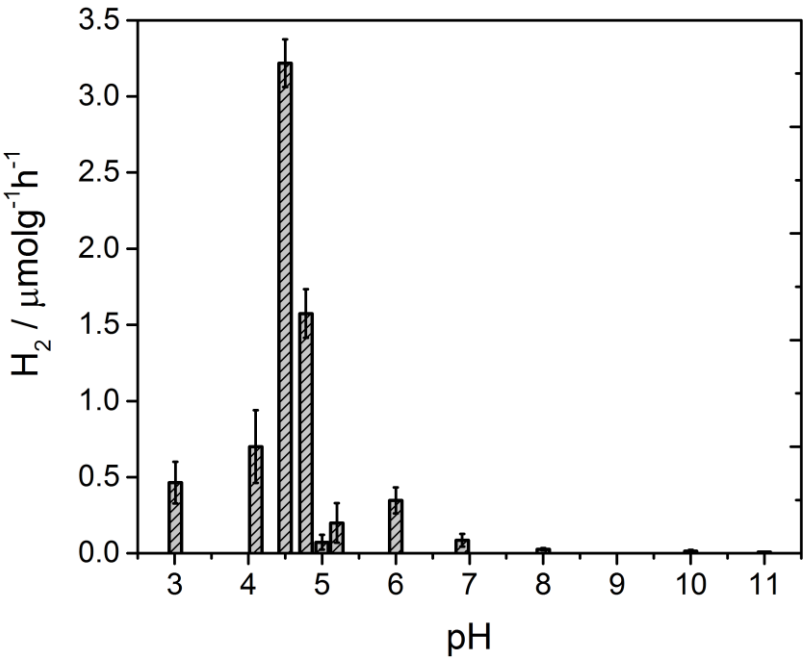

Figure 48. Amount of hydrogen evolved from 4-hour photocatalysis of PBI-F/PVP-Pt/methanol mixtures at different pH values (column with error bars). pH measurements between pH 4-5 are grouped together with +/- 0.2 pH units, all other measurements are grouped up to +/- 0.3 pH units.

The PBI-F solution was stable for up to 13 days (307 hours) of irradiation (Figure 49); the solution became inactive after this time due to the complete evaporation of methanol from the system because of the daily purging of the cell. After 307 hours, a turnover number of 158 per

PVP-Pt NP, or 1.32 x 10^{-2} per Pt atom (see Experimental for calculations), was achieved. The resulting solution was freeze-dried and analysed to try and characterise any products of PBI photodegradation (Figure 50). Again, no product of degradation was detected by NMR or FTIR. This could be due to the low concentration present being below the detectable limit, a significantly lower solubility of the degraded product, or simply that no degradation had occurred. Therefore, it is apparent that PBI-F supramolecular structures show a reasonable degree of photocatalytic stability.

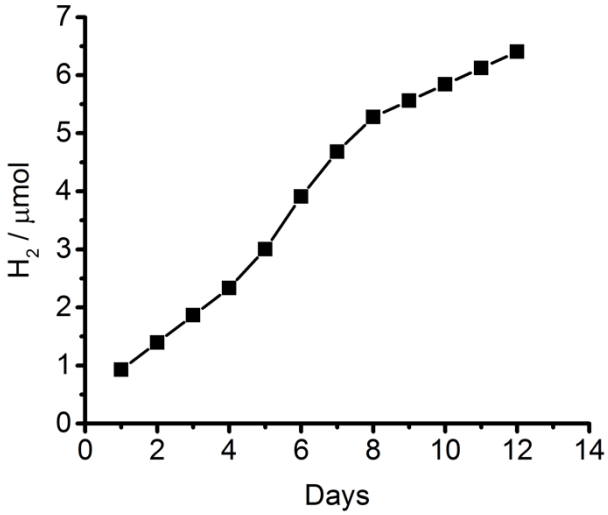

Figure 49. Photocatalytic hydrogen evolution over time of PBI-F/PVP-Pt NPs/20 v/v% methanol$_{(aq)}$ solution at pH 4.5. Each day the septum was replaced and the solution was re-purged for 20 minutes with argon.

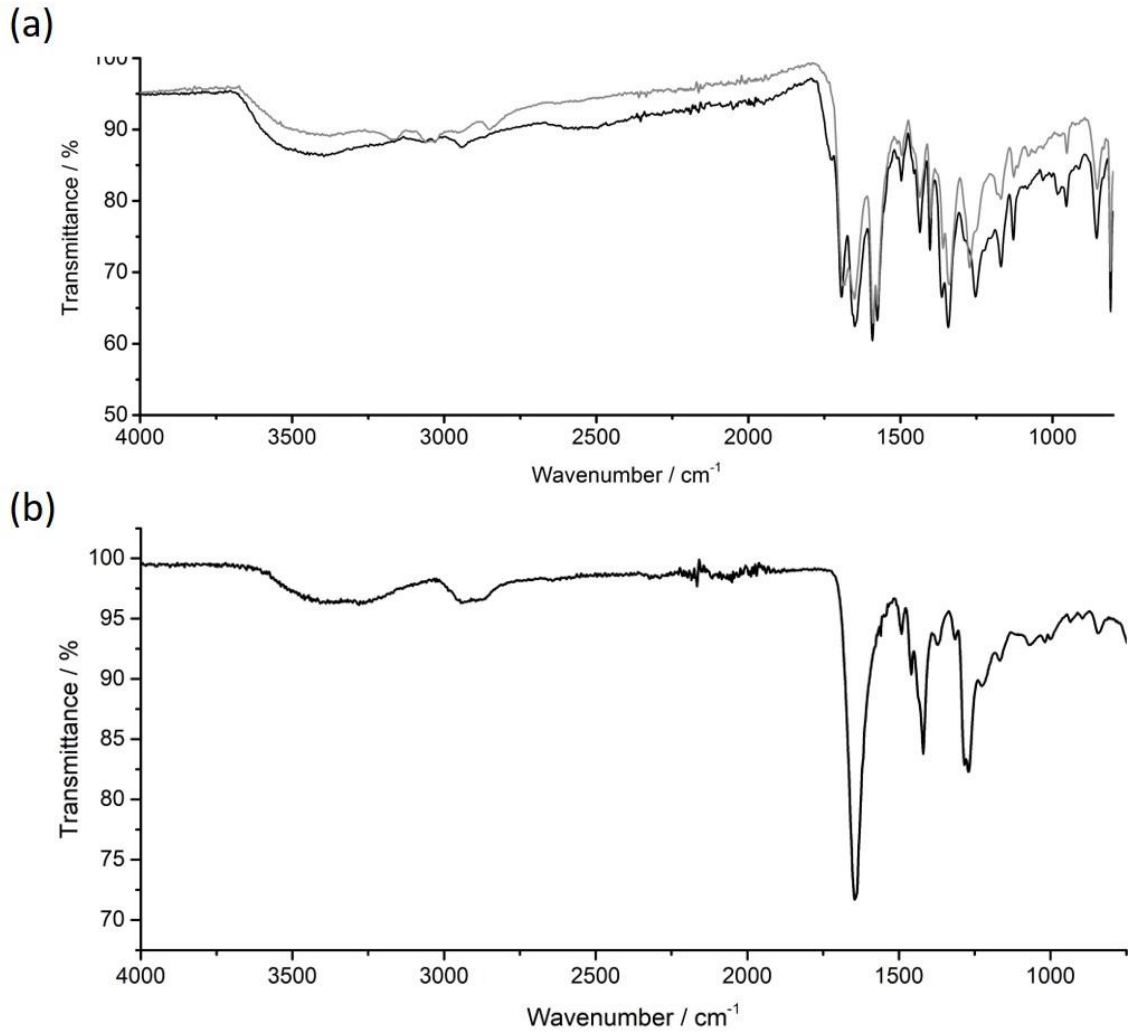

Figure 50. (a) FTIR spectra of freeze-dried photocatalytic solutions (PBI-F/PVP-Pt NPs/20 v/v% methanol$_{(aq)}$) before (grey) and after (black) the long photocatalytic experiment shown in Figure 49. (b) IR spectrum of PVP.

2.3.3. Electrochemical Characterisation of Photocatalytic Solutions

We have explored the mechanism of photocatalytic hydrogen generation and its pH dependence further through electrochemical measurements. PBIs can be chemically, electrochemically and photochemically reduced to form radical anion ($PBI^{\cdot-}$) and dianion (PBI^{2-}) species.[10,28,31,44,69,70] Square wave voltammetry (SWV) (10 mg/mL, 20 v/v% methanol, 0.1 M NaCl, 1 Hz) was carried out at a range of different pHs, Figure 51b. In Figure 51a, the obtained reduction peaks have been plotted against the reversible hydrogen electrode (RHE), describing the potential needed for proton reduction. The potential for proton reduction changes at different pH when plotted against the reversible hydrogen electrode as the concentration of

protons in solution changes the equilibrium, and this potential is plotted as a dotted line in Figure 51a.

In Figure 51a, although the aggregation of PBI-F changes with pH, the reduction potentials remain unchanged and the activity only becomes thermodynamically viable due to the changing potentials of the RHE. Furthermore, the current intensity of all reductions in Figure 51b reduces as the pH is lowered below the first and second pK_a values. These reductions are in line with the increasing aggregation of the PBI solutions, as detected by UV-Vis, viscometry and SANS, and may be an indication that the electrochemistry is only measuring the smaller worm-like micelles or freely solvated molecules in solution and is not detecting the larger fibres forming at the lower pH.

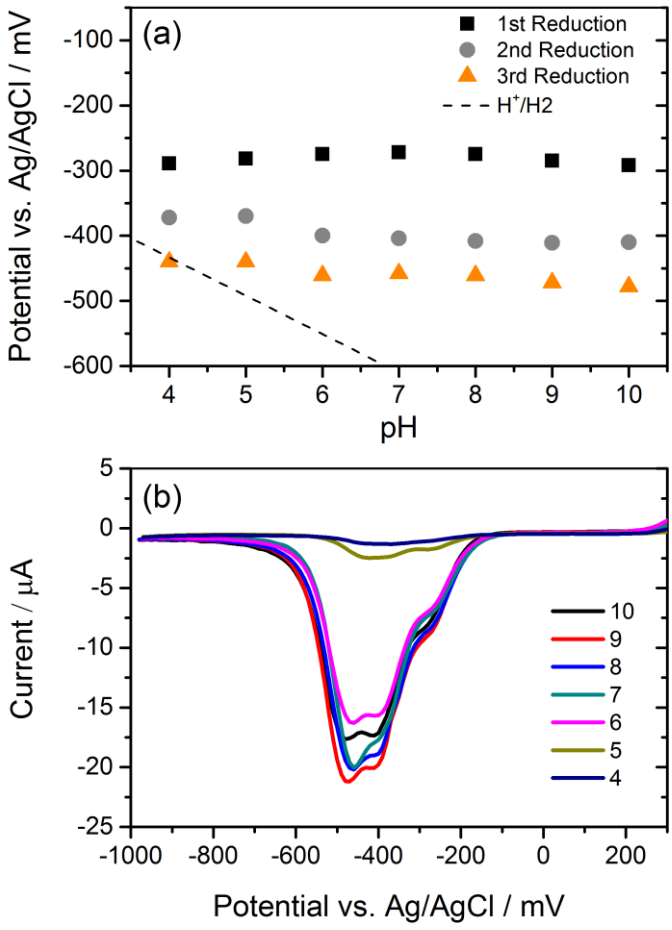

Figure 51. (a) Reduction potentials of PBI-F (10 mg/mL) in 20 v/v% methanol at various pHs. Reduction peaks were picked from SWV measurements shown in (b) which shows three reductions. The dotted line indicates the energy required for hydrogen evolution – reduction potentials which lie underneath this line can feasibly drive hydrogen evolution. (b) SWVs of

PBI-F (10 mg/mL) at pH 10-4 in 20 v/v % methanol(aq). Measured using Ag/AgCl electrode with a scan rate of 1 Hz. The SWVs were scaled in the y-axis (μA) to roughly the same size.

The characteristic absorbances of the PBI radical anion ($PBI^{\cdot-}$) at 725 nm and dianion (PBI^{2-}) at 610 nm in the UV-Vis absorption spectra allow for them to be identified by UV-Vis absorption spectroscopy.[69] As three reductions are observed in the voltammogram, spectroelectrochemistry (SEC) was used to help determine the nature of each reduction (Figure 52). Due to the high molar absorption coefficient of the PBI, a 1 mg/mL solution was used for SEC measurements to attain a full absorption spectrum. A complex voltammogram was obtained with three close lying reductions, labelled x, y and z (-0.285, -0.411 and -0.472 $V_{Ag/AgCl}$, respectively).

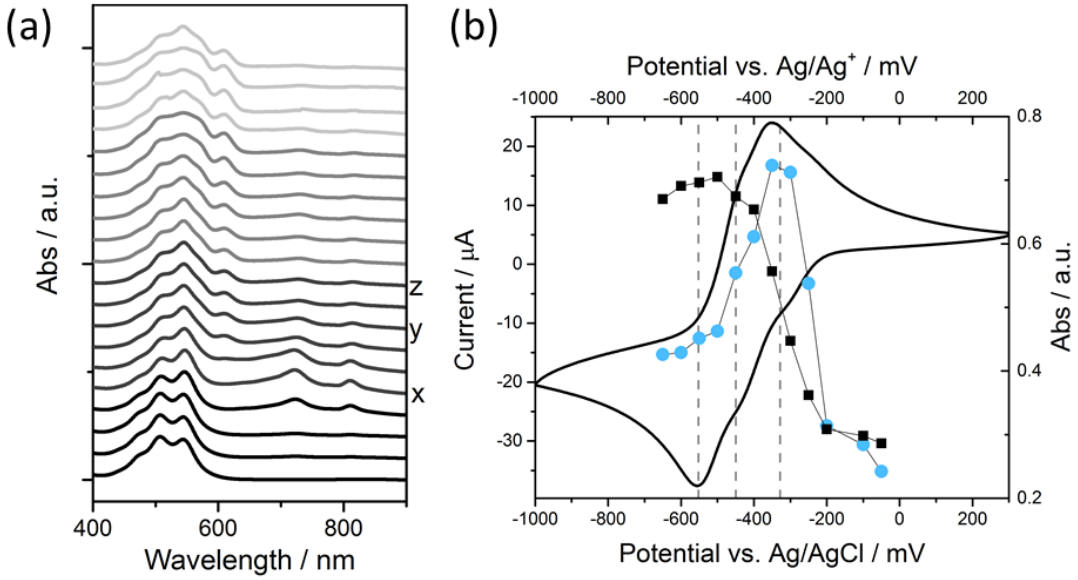

Figure 52. (a) UV-Vis absorption spectra of PBI-F (1 mg/mL, 20 v/v% $methanol_{(aq)}$) from thin layer spectroelectrochemical (SEC) measurements. The voltage applied through the cell during data collection was (from bottom to top): -0.05, -0.1, -0.2, -0.25, -0.3 (x), -0.35, -0.4, -0.45 (y), -0.5, -0.55 (z), -0.6, -0.65, -0.7, -0.8, -0.9, -0.95, -1.1, -1.15, -1.2, -1.25 V vs. Ag wire. x = -328; y = -450; z = -552 mV vs. Ag wire. (b) Cyclic Voltammogram (CV) of PBI-F (line, mV vs. Ag/AgCl) overlaid with the UV-Vis absorption intensity at 725 nm ($PBI^{\cdot-}$, circles, mV vs. Ag/Ag^{+}) and 610 nm (PBI^{2-}, squares, mV vs. Ag/Ag^{+}). Vertical dotted lines from right to left correspond to x, y, z in (a).

Prolonged reduction (1 min) at potentials close to the first reduction potential, x, gives rise to partial conversion of the PBI to $PBI^{\cdot-}$ with an increase in the 725 nm absorbance. As the potential is increased, we observe PBI^{2-} forming with the increase of a new absorption band at 610 nm, related to the dianion, as the $PBI^{\cdot-}$ band at 725 nm decreases. The dianion band grows as the 2nd reduction potential is reached, but does not complete until the most negative reduction potential is reached. Due to closely lying reduction potentials, the overlapping of the bands makes it difficult to assign the middle reduction band. It is therefore proposed that the first and third reduction features at -0.285 and -0.472 $V_{Ag/AgCl}$ can be assigned to the $PBI/PBI^{\cdot-}$ and $PBI^{\cdot-}/PBI^{2-}$ couples. The SEC measurements indicate that the reduction at -0.411 $V_{Ag/AgCl}$ also appears to be related to the $PBI^{\cdot-}/PBI^{2-}$ couple. The presence of this additional reduction peak is tentatively ascribed to the presence of multiple PBI-F environments in the assembled structures or may also be due to the formation of states with charge delocalised across the aggregated structure.[71]

All three reductions are found to show minimal pH dependence between pH 10-4 with a < 50 mV difference between pH 6 and 4 for all reductions, Figure 51. Notably only the 3rd reduction of the solution PBI ($PBI^{\cdot-}/PBI^{2-}$) at a pH of approximately 5 and lower is predicted to be sufficiently reducing for hydrogen evolution to occur (Figure 51a). However, it should again be noted that this electrochemical analysis seems to only focus on soluble species and does not measure the larger fibres formed at low pH. At low pH, the increasing viscosity of the solution (Figure 40) and the gradual formation of insoluble aggregates hampers studies and attempts to electrochemically characterise the collected solid are to date unsuccessful. As we measure photocatalytic hydrogen production at pH 7, a pH where we would not anticipate $PBI^{\cdot-}/PBI^{2-}$ in solution to be active for H_2 production on the basis of Figure 48, it is likely that the active species are the large aggregated structures which begin to be present in significant levels at these pH values.

2.3.4. Wavelength Dependence of Photocatalytic Solutions

To explore if $PBI^{\cdot-}$ or PBI^{2-} generation is required for hydrogen evolution, UV-Vis absorption spectroscopy was used to probe the formation of radical anion and dianion species after visible (470 nm) and UV (365 nm) irradiation (Figure 53). For samples at pH 9.5, 6 and 4.5, the radical anion is formed under 470 nm irradiation. Under 365 nm irradiation, a decreased yield of $PBI^{\cdot-}$ is observed and a new UV/Vis absorption at ~610 nm is present, assigned to PBI^{2-}. These data

are supported with a wavelength-dependant photocatalytic study, where if samples can photocatalytically produce hydrogen evolution with different activities at 365 and 470 nm then the active reduced species can be identified (Figure 53-Figure 54).

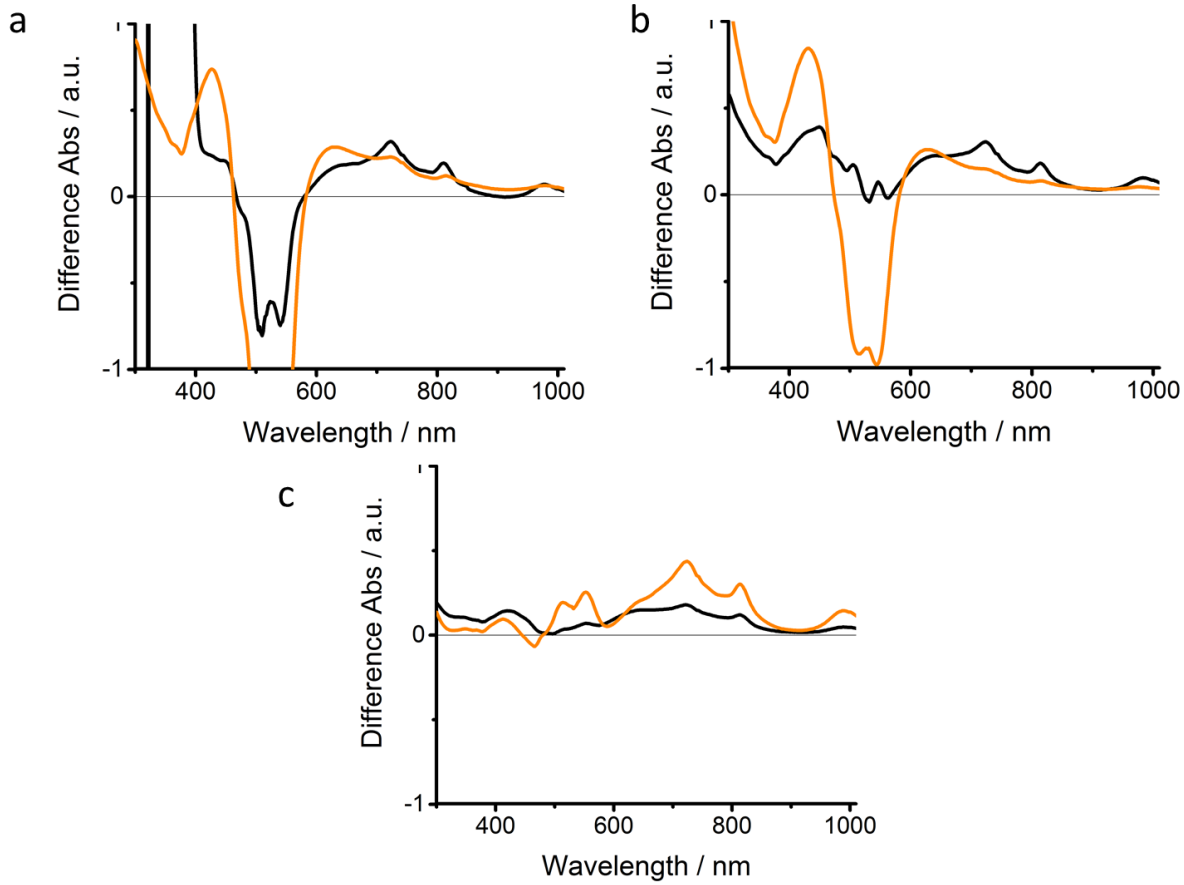

Figure 53. Difference absorption spectra of PBI-F (10 mg/mL) solutions in H_2O with 20 v/v% methanol with 1 mol% PVP-Pt NPs. Samples were irradiated with 470 nm (black lines) and 365 nm (orange lines) LEDs for one hour while solutions were housed in a sealed demountable 0.1 mm quartz cuvette. Three different pHs were measured; (a) pH 9.5 (b) pH 6 and (c) pH 4.5. For the pH 4.5 measurement, the heating from UV irradiation may have altered the aggregation which resulted in an increase in the absorbance between 400-600 nm. Visible hydrogen bubbles were also observed in this sample which may have affected the resulting spectrum. (a) is shown on the same y-axis scale as others to show clearly the difference in absorption between 600-900 nm which is of most importance.

The wavelength dependence study of a pH 4.5 sample for hydrogen evolution activity (Table 1, Figure 54) shows that activity is only observed during UV irradiation. Here, the irradiation wavelength overlaps with the UV absorption band of the S_0-S_2 transition and coincides with the formation of the dianion species. These results suggest that PBI^{2-} is generated during

photocatalysis and is the active species for hydrogen evolution in this system. An apparent quantum efficiency of 0.018 % was obtained from 365 nm irradiation, calculated for a two-electron reduction of H^+ to H_2. These findings are in agreement with other work where <400 nm irradiation induces conductivity and photocatalytic activity.[13,28,31] Although this value is low compared to many inorganic semiconductors, it is in-line with comparable perylene-based systems.[13,14,17] Here, it is important to note that the aim of this work is to understand the relationship between supramolecular structure and photocatalytic activity and not to optimise activity.

λ / nm	E (= hυ/λ) x10^{-19} / mWcm^{-2}	Ratio of E_λ vs E_{365nm}	E irradiated onto sample / mWcm^{-2}
365	5.44	1	5
400	4.97	0.91	4.56
420	4.73	0.87	4.35
450	4.41	0.81	4.06
465	4.27	0.78	3.92
470	4.23	0.78	3.88
523	3.80	0.70	3.49
528	3.76	0.69	3.46
590	3.37	0.62	3.09
617	3.22	0.59	2.96
624	3.18	0.58	2.92

Table 1. Calculation of normalised power outputs onto the sample from LEDs of various wavelengths, accounting for the number of photons supplied by each wavelength. Values used for the wavelength dependence hydrogen evolution study.

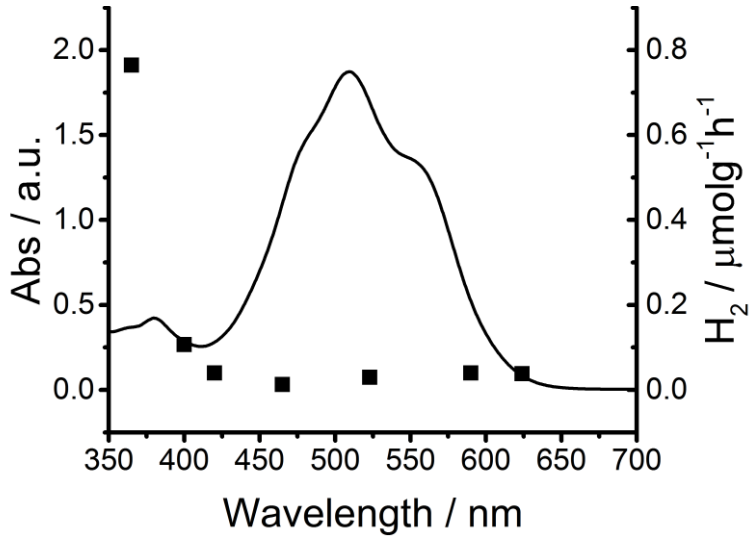

Figure 54. Wavelength dependence of hydrogen evolution (scatter) of a pH 4.5 solution of PBI-F (10 mg/mL), PVP-Pt NPs (1 mol%) with 20 v/v% methanol$_{(aq)}$. Overlaid is the UV-vis absorption spectrum of the solution without irradiation for reference (line).

We have therefore demonstrated that PBI-F solutions become photochemically active for H_2 production at low pH with a maximum hydrogen evolution rate being observed at pH 4.5. Characterisation of the PBI-F samples demonstrates that at the potentials where hydrogen evolution occurs, long self-assembled fibres are present. Notably, we begin to observe hydrogen evolution at around pH 7, the point at which the SANS experiment indicates that an increased amount of assembled structures begins to form. Strikingly, we also find that at this pH the potential of the $PBI^{\cdot-}/PBI^{2-}$ couple in solution is not sufficiently reducing for proton reduction to occur and indicates that a larger aggregated structure, which could not be measured electrochemically, is responsible for the activity towards proton reduction.

2.3.5. Neutron Scattering Characterisation Utilising *in-situ* Irradiation

Ultra-small angle scattering (USANS) was combined with SANS as a tool to try and discover if there are any changes in the short or longer range order of the solutions during and after irradiation. For this experiment, a new sample environment was used; a 365 nm light source was combined with a fibre optic cable to direct a collimated beam of light onto the sample (Figure 55). The light was held outside of the neutron beam so that samples could be irradiated in situ while scattering data was collected. The light could be turned on and off as part of the computerised scripting involved in queuing samples for the data collection.

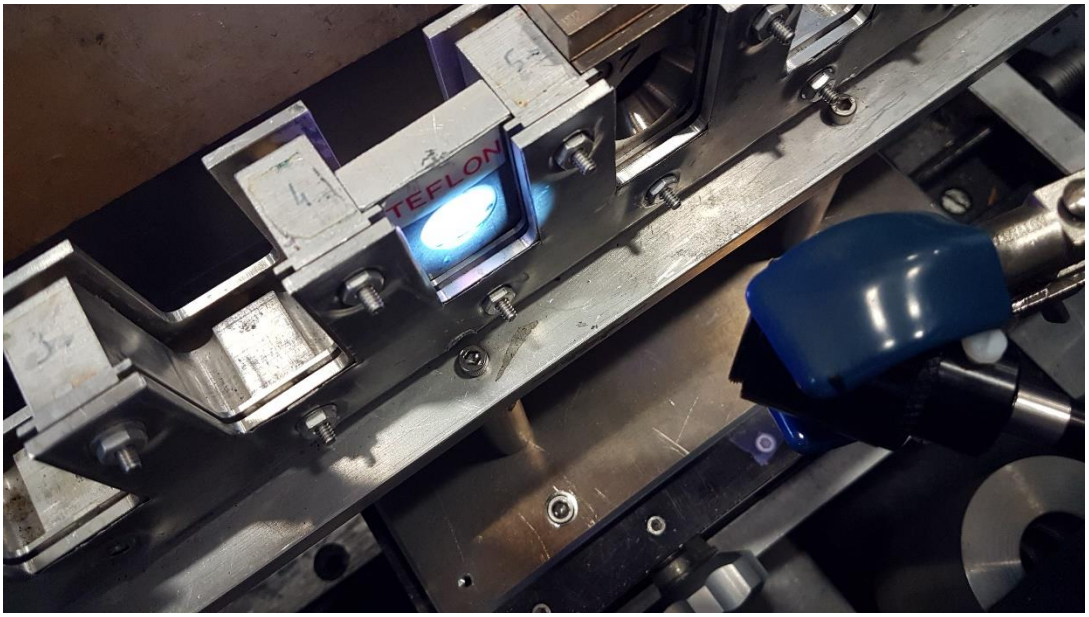

Figure 55. Photo of a sample cell in the sample holder with a 365 nm LED using the BT5 beamline instrument at the NIST Center for Neutron Research (NCNR).

USANS data reaches to lower Q values than just SANS alone. Due to instrument limitations, the lower Q values of the USANS regime (0.01-0.0006 nm^{-1}) were collected on a different beam line to the SANS data (0.01-5 nm^{-1}). An overlap of several points was collected around 0.01 nm^{-1} to account for any discrepancies between the intensities collected from the two instruments to allow the data to be combined accurately.

PBI-F solutions containing 20% methanol with deuterated solvents were prepared at pH 6.0, 4.5 and 2.0. Scattering data was collected before, during and after 30 minutes of irradiation (Figure 56). The USANS scattering intensity was very low for pH 6 showing no long-range order at these pHs. As the pH is lowered the intensity of the scattering in the USANS regime increases significantly showing the formation of a long-range order in the solutions. Importantly, the in-situ irradiation induces no change in the SANS or USANS for the pH 2 sample however a noticeable drop in scattering is observed in the USANS regime for pH 4.5 during irradiation. Interestingly the scattering recovers fully as soon as the light is turned off and can be repeated reversibly for several runs. At this stage only a broad view of the underlying structure change is understood which is that the long-range order is lost during irradiation of the pH 4.5 sample which quickly recovers. This is the first time that information like this has been attained during irradiation for low molecular weight photocatalysts and could give an indication that a rearrangement of the long-range order occurs when there is a residual charge on the fibres.

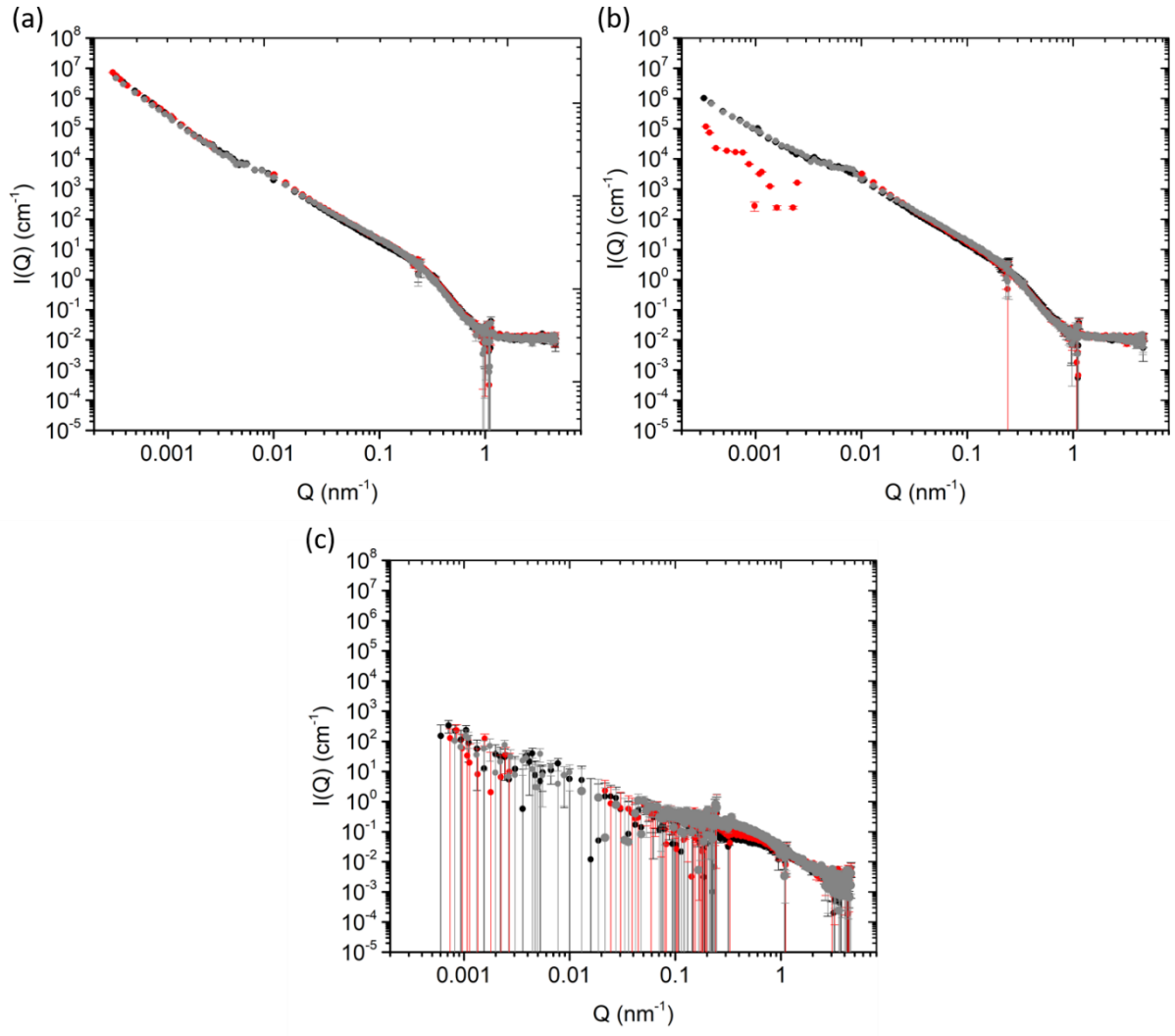

Figure 56. Neutron scattering data on PBI-F/20% d^4-methanol solutions before (black), during (red) and after (grey) irradiation at 365 nm. (a) pH 2.0, (b) pH 4.5 and (c) pH 6.0.

2.4. Conclusions

Our observations strongly suggest that hydrogen evolution is catalysed by the self-assembled structures and not from free molecules in solution. The large increase in hydrogen evolution rate is in line with the structural changes and the point at which we observe the highest concentration of the self-assembled fibrous structures. It is likely that the formation of these fibrous structures, which are known to be effective for long-range electron transport,[28] are vital in enabling photoelectron transfer to the sites of the platinum co-catalysts. The rationale for the subsequent decrease in hydrogen evolution rate at lower pH may be a result of a loss of charge on the fibres but this is not yet clear. It is likely that activity is a product of a delicate balance

between aggregate size, self-assembled structure, charge state and availability of edges in the material.

Through a combination of pH-dependent electrochemical and photocatalytic studies, we have shown the importance of the self-assembly of a perylene bisimide on its photocatalytic activity. Currently, there are very few reported examples of self-assembled materials for H_2 evolution and our focus on understanding the pH-induced structural changes of perylene bisimides provides important new insights for the field. This work provides a route to open a wealth of opportunities for the optimisation of self-assembled PBIs for photocatalytic applications.

2.5. Experimental

2.5.1. Synthetic Procedures

The synthesis of PBI-F was scaled up from a previously described synthesis.[28] In a 100 mL Schlenk flask, Perylenetetracarboxylic dianhydride (PTCDA) (3.0 g, 7.62 mmol), imidazole (10.42 g, 152.94 mmol) and L-phenylalanine (2.43 g, 15.3 mmol) were mixed and purged with nitrogen for 10 minutes. Once purged, the mixture was heated up to 120 °C and the resulting molten solution was stirred for 5 hours at 120 °C under nitrogen. The reaction was then cooled to 90 °C and 5 mL of deionised water was added. The reaction was stirred at 90 °C for 1 hour and then cooled to room temperature before filtering to remove unreacted PTCDA. The pH of the filtrate was then adjusted to 2-3 using 2 M HCl (*ca.* 100 mL). The resulting mixture was stirred at 60 °C for 8 hours. The precipitate was collected via vacuum filtration and washed thoroughly with acidified H_2O. The final compound was analysed by NMR spectroscopy, mass spectroscopy and FTIR spectroscopy (Figure 57-Figure 59).

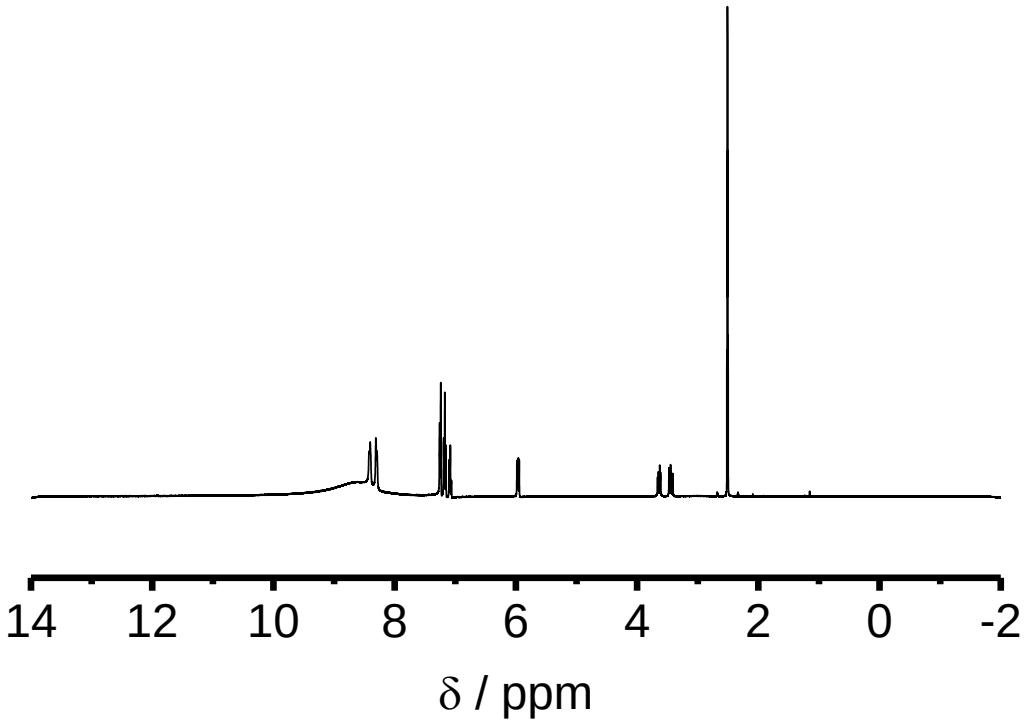

Figure 57. ^{1}H-NMR spectrum of PBI-F recorded in DMSO with a drop (*ca.* 5 μL) of TFA to aid solubility.

^{1}H NMR 400 MHz, (DMSO-d^{6}, 25 ˚C): δ (ppm) = 11.89 (s, 2H; -O<u>H</u>, CH(COO<u>H</u>)CH$_2$Phe); 8.15 (m, 8H, Perylene Core); 7.18 (m, 10H, -<u>Phe</u>); 5.97 (dd, 2H, J = 9.74, 5.62, C<u>H</u>(COOH)CH$_2$Phe); 4.51 (s, H$_2$O), 3.55 (m, C<u>H$_2$</u>-Phe), 2.50 (q, DMSO).

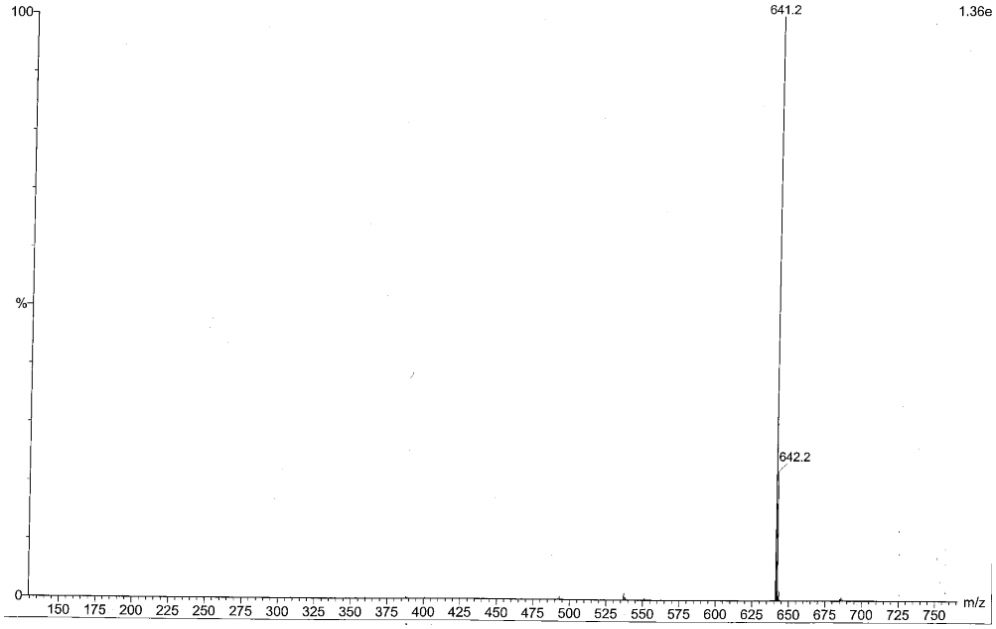

Figure 58. Mass Spectrum of PBI-F.

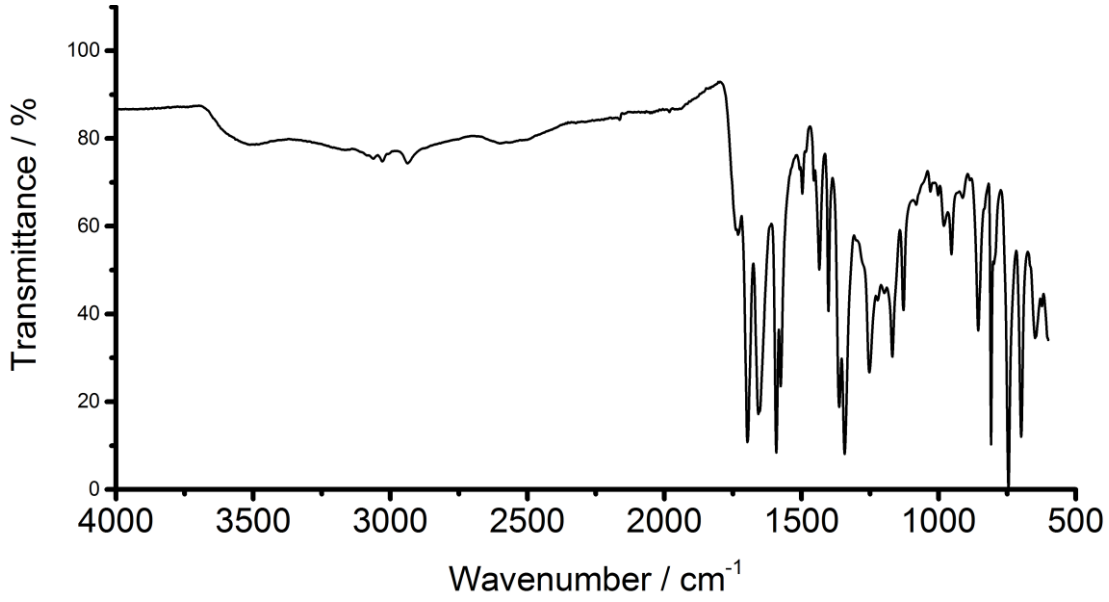

Figure 59. ATR FTIR spectrum of powdered PBI-F.

PVP-capped Pt nanoparticles

The preparation of PVP-Pt NPs was carried out using a previously described method.[67] A 20 mL aqueous solution of potassium *L*-tartrate monobasic (0.5 wt%) was brought to reflux (ca. 100 °C). Then, 20 mL of an aqueous solution of H_2PtCl_6 (1 mM Pt) and PVP (1.0 wt%) was added into the vortex of the stirring reflux solution and left to reflux for 60 minutes. A dark brown solution formed after 5 minutes, with no further visible change thereafter. The solution was cooled to room temperature and then spin filtered by distributing across 3x20 mL Corning® Spin-X® UF concentrators containing a polyethersulfone membrane with a 50k molecular weight filter. The solutions were centrifuged for 3x30 minutes at 5000 rpm and then re-dispersed in ultra-pure water to a total volume of 20 mL and 1.0 mM Pt. The PVP-Pt NPs were characterised by dynamic light scattering (DLS), TEM, thermogravic analysis (TGA) and UV-Vis absorption spectroscopy (Figure 42-Figure 45).

2.5.2. Instruments and Procedures

Preparation of LMWG solutions

7 mL solutions of PBI-F were prepared by weighing out 70 mg PBI-F (10 mg/mL) into 14 mL vials then, while stirring, adding 4.58 mL deionised H_2O, 1.02 mL 0.2M $NaOH_{(aq)}$ (2 eq.) and 1.4 mL methanol (20 v/v %). The solutions were stirred overnight and pH was adjusted the next day by adding 0.1M HCl dropwise to the solution while stirring and measuring the pH.

For those solutions where platinum nanoparticles are present, some of the water is substituted for a platinum nanoparticle solution in the ratio of 1 mol% nanoparticles to PBI. The solutions were stirred for another 30 minutes and the pH was checked and adjusted if needed before use. Any aggregates of PBI in solution were present as a suspension. The solutions were not stirred during UV-Vis absorption spectroscopy, electrochemistry, and SANS measurements.

pH measurements

A FC200 pH probe from HANNA instruments with a 6 mm x 10 mm conical tip was used for pH measurements. pD measurements were collected with the same probe and corrected with a constant offset of pH = pD – 0.4.[56]

Dynamic Light Scattering (DLS) Measurements

DLS measurements were performed on a Malvern Zetasizer Nano ZS using non-invasive backscatter optics with a He-Ne laser source at 633 nm. Measurements were collected at room temperature using 3 runs of 25 scans. The correlation data were fitted within the software using a cumulants fit which showed a fit with low error due to the singular modality of the distribution.

Thermogravic Analysis (TGA) Measurements

Acknowledgement: Michael Barrow (University of Liverpool)

TGA measurements were carried out by Michael Barrow on a TA Instruments SDT Q600 TGA machine using a constant air flow of 100 mL/min. Samples were heated up to 120 °C at a heating rate 10 °C/min. The samples were kept at 120 °C for 20 minutes to remove any water, then ramped to 200 °C at a heating rate of 10 °C/min.

Nuclear Magnetic Resonance (NMR) Spectroscopy

Diffusion NMR

Acknowledgement: Matthew Wallace (University of Liverpool)

Diffusion NMR (PFG-NMR) experiments were performed using a modified double stimulated echo sequence based on that of Jerschow and Muller[72] (Bruker pulse program library dstegp3s). The sequence was modified to include pre-saturation of the methanol resonance during the relaxation delay (5 s) and a double-echo WATERGATE sequence of Liu *et al.*[73] (Bruker pulse program library ZGGPW5) after the PFG-NMR sequence to supress the H_2O resonance. Spectra were recorded as a function of the gradient amplitude, g, in 32 steps and 16 scans from

2.4 to 45.6 G/cm. The diffusion delay, Δ, was set at 0.2 s while the gradient pulse length, δ, was set at 2.9 ms. The delay between successive hard pulses in the selective WATERGATE train was set at 250 μs, corresponding to a 4000 Hz separation between the null points. The sample was maintained at a constant temperature of 298±0.5 K, the deviation in temperature during the experiment being less than 0.1 K. The aromatic resonances of PBI-F (7-8 ppm) were integrated and fitted to (Equation 5) to obtain the diffusion coefficient, D:

$$\frac{I}{I_0} = exp\left[-\gamma^2 g^2 \delta^2 D\left(\Delta - \frac{5\delta}{3} - \tau\right)\right] \qquad \text{(Equation 5)}$$

where: I and I_0 are integrals with and without an applied gradient, γ is the gyromagnetic ratio of ^{1}H and τ is a short delay during the pulse sequence (200 μs). From this, D was obtained as (1.55±0.02) x 10^{-10} m^2s^{-1} (uncertainty obtained using method of Brown et al.[74]). Applying the Einstein-Stokes equation (Equation 6)

$$R_h = \frac{k_B T}{6\pi\eta D} \qquad \text{(Equation 6)}$$

where k_B is Boltzmann's constant and T is the absolute temperature and using a viscosity (η) of 0.821 mPa.s,[75] we obtain a hydrodynamic radius (R_h) for the diffusing entities of 1.72±0.03 nm.

Quantification of amount of PBI-F visible by NMR

A 10 mg/mL solution of PBI-F was prepared in 80 % D_2O, 20% CD_3OD at a pD 10.4. The CH_2 resonances of the phenylalanine residues were integrated against the resonance of a 30 mM solution of TSP (3-(trimethylsilyl)-propionic-2,2-3,3-d_4 acid sodium salt) in an internal glass capillary. The integrals corresponded to 92% of a theoretical 10 mg/mL solution of PBI-F. The spectrum was acquired using a 30° flip angle, an acquisition time of 4 s and a relaxation delay of 20 s. 32 scans were recorded.

The CH_2 resonances of the phenylalanine residues were irradiated for 8 s using a train of 157 Gaussian pulses, each 50 ms in duration with a peak power of 24 Hz, followed by a 30° hard pulse and signal acquisition (4 s). 8 scans were acquired. The other resonances of the phenylalanine residues are attenuated (negative NOE). The resonances are also much broader

and display reduced T_1 and T_2 relaxation times compared to what would be expected for a freely-dissolved molecule of similar size. These results are all consistent with the NMR-visible PBI-F being in exchange with large aggregates.[76,77] T_1 and T_2 relaxation times were measured using the inversion-recovery and CPMG sequences respectively. For T_1, the signal intensity was acquired using sixteen delay values from 1 ms to 20 s. For T_2, the spacing between the π pulses was kept fixed at 2 ms and the number of pulses varied from 2 to 180 in sixteen steps.

Mass Spectrometry

Mass Spectroscopy measurements were carried out using a Micromass LCT Mass Spectrometer +40 V in methanol. Measurements were carried out courtesy of the University of Liverpool mass spectrometry service.

UV-Vis Absorption Spectroscopy

UV-Vis absorption spectra were taken using a Shimadzu UV-2600 spectrometer and a 0.1 mm demountable quartz cuvette (Starna). For irradiation experiments an LED (RS Electronics) was pointed at the sample and the spectrometer covered with a blackout cloth.

Fourier Transformed Infra-Red (FTIR) Spectroscopy

FTIR was carried out on a BrukerVertex instrument with a CaF_2 IR cell with a 0.1 mm pathlength.

Neutron Scattering Measurements

Neutron scattering is an effective technique for the structural characterisation of networks.[78] In these experiments, a neutron facility is required which can provide a neutron source whose beam is directed to a crystal which filters neutrons of certain wavelengths towards a sample.[79] When the neutrons collide with atoms in a sample they are scattered and are then recorded on detectors. Elastic scattering is commonly used for structure determination, where neutrons change course after colliding with a nucleus but do not lose energy. If the neutrons interact with the nucleus then they can change in both direction and energy, this is inelastic scattering and is used for studying dynamics. The low scattering angle of small angle neutron scattering (SANS) along with neutron wavelengths on the magnitude of smaller structures, ~1 nm, allows for structures of the nanometre scale to be analysed. The highly penetrating nature of neutrons also allow for samples to be analysed in bulk and solutions can be analysed, even in low

concentrations of material such as in LMWG materials which typically contain <1 wt% gelator. The nuclei of different elements scatter neutrons differently; for example, protons scatter neutrons strongly, quantified as the scattering length density (SLD), due to the presence of unpaired electron spins, the deuterium isotope which has no unpaired electrons is invisible to the measurements. The substitution to deuterated solvents can maximise the contribution of the other elements to the scattering pattern. In addition, the SLD of the material you want to characterise can be matched to the solvent, a method called contrast matching, this can allow for selective removal of parts of structures to blend into the solvent scattering allowing for the hierarchical nature of networks to be elucidated by a methodical approach. Another approach is to modify the structures themselves by substituting hydrogen with deuterium to remove this species from the scattering pattern, this method is particularly useful with organic materials if a multicomponent system is used, each component can be individually characterised in the mixture and then compared to the overall non-deuterated scattering.

Experimental methods of neutron scattering measurements are wide and varied. Samples can be measured while being manipulated in various ways such as during flow, shear,[54,80,81] changing temperature and pressure and while being irradiated with light. The diversity of this technique allows for many experiments to be designed.

Modelling the scattering curves requires knowledge of the various models which can be used.[53] Software packages such as SasView and Igor Pro[82] provide a range of model functions for fitting, including sphere-based, cylinder-based,[55] ellipsoid-based and lamellar-based functions amongst others. Shape-independent functions are also used, including the Porod model describing surface roughness and the Absolute Power Law describing the fractal structure of the network. Each model contains dimensional parameters which can be computationally fitted to the scattering curve within the software. A shape-independent function such as the power law is a main component of the scatter for almost all gel networks; the continuous hierarchical structure, whether homogeneous or not, will provide a fractal pattern with an exponent of approximately -1 to -4.[83] When plotted on a double logarithmic scale, the various length scales of the scatter may show different exponents related to the hierarchical nature of the materials; the crossover points of these lines can change depending on the contrast of the material within the solution, indicating that this is indeed related to the hierarchical relationship within the networks. There have been many examples of fitting SANS data for low molecular weight gelators in several forms, such as when aggregates are suspended in solution, when self-

supporting hydrogel networks are formed and on dried films.[35,65,84–87] Less commonly, ultra-small angle neutron scattering (USANS) is used.[80,88–90] This is a relatively new technique which can provide data on the length scales of 0.1-50 microns revealing more detail about the long-range order, and larger domains, of the networks which SANS alone cannot provide.

Small Angle Neutron Scattering (SANS) Measurements

SANS measurements of the gelator solutions were performed using the SANS2D instrument (STFC ISIS Pulsed Neutron Source, Oxfordshire, UK). A simultaneous Q-range [$Q = 4\pi\sin(\theta/2)/\lambda$, where θ is the scattering angle] of 0.005 to 0.7 $Å^{-1}$ was achieved using an incident wavelength (λ) range of 1.75 to 16.5 Å and employing a sample-to-detector distance of 4 m, with the 1 m^2 detector offset vertically 60 mm and sideways 100 mm. Samples were housed in 5 mm quartz cuvettes and measured for ~30 minutes. Scattering data were normalized for the sample transmission and background corrected using a quartz cell with 20 v/v% MeOD in D_2O and also corrected for the linearity and efficiency of the detector response using the Mantid framework.[91] The scattering data were then fitted in the SasView software (version 3.1.1)[57] to a customised model comprising of a (Kratky-Porod) flexible cylinder, a sphere and an absolute power law.[58–60] The power law (Q^{-m}) accounts for the mass fractal contribution to the scattering intensity which is combined with the flexible cylinder and sphere models (Figure 34).

Ultra Small Angle Neutron Scattering (USANS) Measurements

USANS measurements of the gelator solutions were performed using the BT5 instrument (NIST Center for Neutron Research (NCNR), National Institute for Standards and Technology (NIST), Gaithersburg, MD, USA). A Q-range [$Q = 4\pi \sin(\theta/2)/\lambda$, where θ is the scattering angle] of 0.00003 to 0.0011 $Å^{-1}$ was achieved using a Bonse-Hart type double crystal diffractometer with a wavelength (λ) of 2.4Å ($\Delta\lambda/\lambda$=6%) in the standard geometry.[92] Samples were housed in 5 mm quartz cuvettes and measured for 4 hours each. Scattering data were normalized for the sample transmission and background corrected using a quartz cell containing D_2O.[82] The data was reduced using IGOR Pro.[82] The reduced data were then fitted in the SasView software (version 4.1.1)[57] to a customised model comprising of a (KratkyPorod) flexible cylinder and an absolute power law.[58–60] The power law (Q^{-m}) accounts for the mass fractal contribution to the scattering intensity which is combined with the flexible cylinder model. As there was no overlap between the USANS and SANS data, the USANS data and fits

were manually offset in the y-axis for visual representation. Data were fitted before any post-modification was applied.

Rheological Measurements

Viscosity measurements were performed on an Anton Paar Physica MCR301 rheometer utilising a 75 mm cone and plate geometry. 1.0 mL of solutions were pipetted onto the plate and left to stabilise for 2 minutes before measurements. Experiments were run at 25 °C. The viscosity of each solution was recorded under the rotation, with the shear rate varying from 1 to 100 s^{-1}.

The rheological time sweep was carried out by mixing 2 mL of gelator solution with 16 mg GdL and pipetted onto the stationary bottom plate of the rheometer. A 50 mm cone plate was lowered onto the sample and mineral oil was places around the outside of the plate to prevent drying. Measurements were taken at 0.5 % strain and 10 rad/s at 25 °C. Meanwhile, a repeat gel was made in a 5 mL Sterilin vial with a pH probe submersed in the solution, with measurements taken in intervals over the course of gelation. All data was overlaid together.

Electrochemical Measurements

Cyclic Voltammetry Cyclic voltammetry (CV) measurements were collected using a three-electrode system and a PalmSens1 potentiostat. All systems were measured in aqueous conditions using 5 mL of sample. 0.1 M sodium chloride (NaCl) was used as the electrolyte, glassy carbon as the working electrode (d = 3 mm, BASi), a Pt mesh as a counter electrode and an Ag/AgCl electrode with a double junction as the reference electrode. CVs were measured from 1.0 V to -1.0 V then back to 1.0 V and repeated over a range of scan rates: the most successful in observing the desired peaks was 0.01 V/s. All samples were purged with argon for 30 minutes before a measurement was run.

Square Wave Voltammetry (SWV) SWV measurements were collected using a three-electrode system and a Dropsens potentiostat with a glassy carbon working electrode, a Pt wire counter electrode and a Ag/AgCl reference electrode. The supporting electrolyte was 0.1 M NaCl. The measurements were scanned from 0.3 V to – 1.0 V at a rate of 1 Hz.

Spectroelectrochemistry Spectroelectrochemical experiments were carried out on 1 mg/mL samples of PBI-F using a thin layer SEC cell containing a Pt counter electrode and an Ag wire

pseudo-reference electrode. The cell was placed inside a Shimadzu UV-2600 spectrometer. The current through the sample was monitored while a chosen potential was applied across the cell and a UV-Vis absorption spectrum was recorded when the current reached a plateau. This took approximately 1 minute due to the slow diffusion through the cell.

Photocatalytic Experiments

Photocatalytic experiments were carried out using a 75 W Xe lamp, a lens and 2 x KG1 filters to achieve an output of 100 $mWcm^{-2}$ onto the sample (Figure 46 to Figure 47). Solutions tested for photocatalysis were stirred in a 1 cm pathlength quartz cuvette with a 25 mL headspace sealed with a rubber septum. Solutions were pre-purged for 30 minutes with N_2, and H_2 was measured via gas chromatography at t=0 and after 4 hours of irradiation.

For wavelength dependence studies, a similar setup was used and the lamp exchanged for an LED. A photodiode was used to monitor the power output of the LEDs onto the sample and the power was altered accordingly to ensure all samples received a matching irradiance as 5 $mWcm^{-2}$ at 365 nm (Table 1).

Gas Chromatography Analysis

GC headspace analysis was performed using an Agilent 6890N employing N6 helium as the carrier gas (5 $mLmin^{-1}$). A 5 Å molecular sieve column (ValcoPLOT, 30 m length, 0.53 mm ID) and a pulsed discharge detector (D-3-I-HP, Valco Vici) were employed. H_2 peak areas were quantified with multiple calibrant gas injections.

TON Calculation

(1) Moles of Pt in 5 mL sample: 4.8×10^{-4}

(2) Number of Pt atoms in 5 mL sample: 2.92×10^{20}

(3) Volume of Pt NPs with a 4 nm Pt core radius (measured via TEM): 267.95 nm^3

(4) Pt atom volume:[93] 0.0225 nm^3

(5) Number of Pt atoms in one NP [(3) / (4)]: 11909

(6) Number of Pt NPs in sample [((1) / (5)) * 6.022 x 1023 mol-1) : 2.448×10^{16}

(7) Molecules of Hydrogen evolved in pH 4.5 sample after 307 hours (Experimental): 3.86×10^{18} mol

(8) TON per Pt atom ((2) / (7)): 1.32×10^{-2} (9) TON per Pt NP ((6) / (7)): 158

2.6. References

1 M. C. Nolan, J. J. Walsh, L. L. E. Mears, E. R. Draper, M. Wallace, M. Barrow, B. Dietrich, S. M. King, A. J. Cowan and D. J. Adams, *J. Mater. Chem. A*, 2017, **5**, 7555–7563.

2 C. Li and H. Wonneberger, *Adv. Mater.*, 2012, **24**, 613–636.

3 F. Würthner, C. R. Saha-Moller, B. Fimmel, S. Ogi, P. Leowanawat and D. Schmidt, *Chem. Rev.*, 2016, **116**, 962–1052.

4 J. Choi, H. Song, N. Kim and F. S. Kim, *Semicond. Sci. Technol.*, 2015, **30**, 064002.

5 J. T. Kirner, J. J. Stracke, B. A. Gregg and R. G. Finke, *ACS Appl. Mater. Interfaces*, 2014, **6**, 13367–13377.

6 J. Roncali, P. Leriche and P. Blanchard, *Adv. Mater.*, 2014, **26**, 3821–3838.

7 F. Fernández-Lázaro, N. Zink-Lorre and Á. Sastre-Santos, *J. Mater. Chem. A*, 2016, **4**, 9336–9346.

8 J. López-Andarias, M. J. Rodriguez, C. Atienza, J. L. López, T. Mikie, S. Casado, S. Seki, J. L. Carrascosa and N. Martín, *J. Am. Chem. Soc.*, 2015, **137**, 893–897.

9 R. V Ulijn and A. M. Smith, *Chem. Soc. Rev.*, 2008, **37**, 664–675.

10 F. Würthner, *Chem. Commun.*, 2004, **14**, 1564–1579.

11 S. Chen, C. Wang, B. R. Bunes, Y. Li, C. Wang and L. Zang, *Appl. Catal. A Gen.*, 2015, **498**, 63–68.

12 F. S. Liu, R. Ji, M. Wu and Y. M. Sun, *Acta. Phys.*, 2007, **23**, 1899–1904.

13 S. Chen, Y. X. Li and C. Y. Wang, *RSC Adv.*, 2015, **5**, 15880–15885.

14 A. S. Weingarten, R. V Kazantsev, L. C. Palmer, M. McClendon, A. R. Koltonow, A. P. S. Samuel, D. J. Kiebala, M. R. Wasielewski and S. I. Stupp, *Nat. Chem.*, 2014, **6**, 964–970.

15 S. Chen, D. L. Jacobs, J. Xu, Y. Li, C. Wang and L. Zang, *RSC Adv.*, 2014, **4**, 48486–48491.

16 T. Abe, Y. Tanno, N. Taira and K. Nagai, *RSC Adv.*, 2015, **5**, 46325–46329.

17 A. S. Weingarten, R. V. Kazantsev, L. C. Palmer, D. J. Fairfield, A. R. Koltonow and S. I. Stupp, *J. Am. Chem. Soc.*, 2015, **137**, 15241–15246.

18 J.-X. Li, Z.-J. Li, C. Ye, X.-B. Li, F. Zhan, X.-B. Fan, J. Li, B. Chen, Y. Tao, C.-H. Tung and L.-Z. Wu, *Catal. Sci. Technol.*, 2016, **6**, 672–676.

19 I. Ghosh, T. Ghosh, J. I. Bardagi and B. König, *Science*, 2014, **346**, 725–728.

20 L. Zeng, T. Liu, C. He, D. Shi, F. Zhang and C. Duan, *J. Am. Chem. Soc.*, 2016, **138**,

3958–3961.

21 H. Ahmad, S. K. Kamarudin, L. J. Minggu and M. Kassim, *Renew. Sustain. Energy Rev.*, 2015, **43**, 599–610.

22 K. Maeda and K. Domen, *J. Phys. Chem. Lett.*, 2010, **1**, 2655–2661.

23 R. S. Sprick, J. X. Jiang, B. Bonillo, S. Ren, T. Ratvijitvech, P. Guiglion, M. A. Zwijnenburg, D. J. Adams and A. I. Cooper, *J. Am. Chem. Soc.*, 2015, **137**, 3265–3270.

24 N. J. Hestand, R. V. Kazantsev, A. S. Weingarten, L. C. Palmer, S. I. Stupp and F. C. Spano, *J. Am. Chem. Soc.*, 2016, **138**, 11762–11774.

25 D. Liu, J. Wang, X. Bai, R. Zong and Y. Zhu, *Adv. Mater.*, 2016, **28**, 7284–7290.

26 J. Raeburn, A. Zamith Cardoso and D. J. Adams, *Chem. Soc. Rev.*, 2013, **42**, 5143–56.

27 J. Raeburn, C. Mendoza-Cuenca, B. N. Cattoz, M. A. Little, A. E. Terry, A. Zamith Cardoso, P. C. Griffiths and D. J. Adams, *Soft Matter*, 2015, **11**, 927–935.

28 E. R. Draper, J. J. Walsh, T. O. McDonald, M. A. Zwijnenburg, P. J. Cameron, A. J. Cowan and D. J. Adams, *J. Mater. Chem. C*, 2014, **2**, 5570–5575.

29 E. R. Draper, J. R. Lee, M. Wallace, F. Jackel, A. J. Cowan and D. J. Adams, *Chem. Sci.*, 2016, **7**, 6499–6505.

30 E. R. Draper, O. O. Mykhaylyk and D. J. Adams, *Chem. Commun.*, 2016, **52**, 6934–6937.

31 J. J. Walsh, J. R. Lee, E. R. Draper, S. M. King, F. Jäckel, M. A. Zwijnenburg, D. J. Adams and A. J. Cowan, *J. Phys. Chem. C*, 2016, **120**, 18479–18486.

32 E. Kozma, G. Grisci, W. Mróz, M. Catellani, A. Eckstein-Andicsovà, K. Pagano and F. Galeotti, *Dye. Pigment.*, 2016, **125**, 201–209.

33 E. R. Draper, J. R. Lee, M. Wallace, F. Jäckel, A. J. Cowan and D. J. Adams, *Chem. Sci.*, 2016, **7**, 6499–6505.

34 E. R. Draper, L. J. Archibald, M. C. Nolan, R. Schweins, M. A. Zwijnenburg, S. Sproules and D. J. Adams, *Chem. - A Eur. J.*, 2018, **24**, 4006–4010.

35 L. L. E. Mears, E. R. Draper, A. M. Castilla, H. Su, Zhuola, B. Dietrich, M. C. Nolan, G. N. Smith, J. Doutch, S. Rogers, R. Akhtar, H. Cui and D. J. Adams, *Biomacromolecules*, 2017, **18**, 3531–3540.

36 C. Tang, A. M. Smith, R. F. Collins, R. V. Ulijn and A. Saiani, *Langmuir*, 2009, **25**, 9447–9453.

37 D. J. Adams, L. M. Mullen, M. Berta, L. Chen and W. J. Frith, *Soft Matter*, 2010, **6**, 1971–1980.

38 D. J. Adams, M. F. Butler, W. J. Frith, M. Kirkland, L. Mullen and P. Sanderson, *Soft*

Matter, 2009, **5**, 1856.

39 A. T. Haedler, K. Kreger, A. Issac, B. Wittmann, M. Kivala, N. Hammer, J. Köhler, H.-W. Schmidt and R. Hildner, *Nature*, 2015, **523**, 196–199.

40 S. Yagai, T. Seki, T. Karatsu, A. Kitamura and F. Würthner, *Angew. Chem. Int. Ed.*, 2008, **47**, 3367–3371.

41 H. Langhals, S. Demmig and H. Huber, *Spectrochim. Acta Part A Mol. Spectrosc.*, 1988, **44**, 1189–1193.

42 H. Langhals, *Heterocycles*, 1995, **40**, 477–500.

43 F. Würthner and A. Sautter, *Chem. Commun.*, 2000, **2**, 445–446.

44 S. K. Lee, Y. Zu, A. Herrmann, Y. Geerts, K. Müllen and A. J. Bard, *J. Am. Chem. Soc.*, 1999, **121**, 3513–3520.

45 J. Sung, P. Kim, B. Fimmel, F. Würthner and D. Kim, *Nat. Commun.*, 2015, **6**, 8646.

46 U. Rosch, S. Yao, R. Wortmann and F. Wurthner, *Angew. Chem. Int. Ed.*, 2006, **45**, 7026–7030.

47 X.-Q. Li, V. Stepanenko, Z. Chen, P. Prins, L. D. a Siebbeles and F. Würthner, *Chem. Commun.*, 2006, **37**, 3871–3873.

48 C. W. Struijk, A. B. Sieval, J. E. J. Dakhorst, M. Van Dijk, P. Kimkes, R. B. M. Koehorst, H. Donker, T. J. Schaafsma, S. J. Picken, A. M. Van de Craats, J. M. Warman, H. Zuilhof and E. J. R. Sudholter, *J. Am. Chem. Soc.*, 2000, **122**, 11057–11066.

49 F. Meinardi, M. Cerminara, A. Sassella, R. Bonifacio and R. Tubino, *Phys. Rev. Lett.*, 2003, **91**, 247401.

50 Y. Che, A. Datar, K. Balakrishnan and L. Zang, *J. Am. Chem. Soc.*, 2007, **129**, 7234–7235.

51 J. Seibt, P. Marquetand, V. Engel, Z. Chen, V. Dehm and F. Würthner, *Chem. Phys.*, 2006, **328**, 354–362.

52 P.-A. Plötz, S. Polyutov, S. D. Ivanov, F. Fennel, S. Wolter, T. A. Niehaus, Z. Xie, S. Lochbrunner, F. Würthner and O. Kuehn, *Phys. Chem. Chem. Phys.*, 2016, **53**, 1689–1699.

53 J.-B. Guilbaud and A. Saiani, *Chem. Soc. Rev.*, 2011, **40**, 1200–1210.

54 V. Croce, T. Cosgrove, C. A. Dreiss, S. King, G. Maitland and T. Hughes, *Langmuir*, 2005, **21**, 6762–6768.

55 C. A. Dreiss, *Soft Matter*, 2007, **3**, 956–970.

56 A. Kręzel and W. Bal, *J. Inorg. Biochem.*, 2004, **98**, 161–166.

57 SasView - Small Angle Scattering Analysis, http://www.sasview.org, (accessed 1

October 2016).

58 A. Guinier and G. Fournet, *John Wiley Sons, Inc., New York*, 1955, 1–19.

59 J. S. Pedersen and P. Schurtenberger, *Macromolecules*, 1996, **29**, 7602–7612.

60 W. R. Chen, P. D. Butler and L. J. Magid, *Langmuir*, 2006, **22**, 6539–6548.

61 R. Van Der Weegen, P. A. Korevaar, P. Voudouris, I. K. Voets, T. F. A. De Greef, J. A. J. M. Vekemans and E. W. Meijer, *Chem. Commun.*, 2013, **49**, 5532–5534.

62 A. Arnaud, J. Belleney, F. Boué, L. Bouteiller, G. Carrot and V. Wintgens, *Angew. Chem. Int. Ed.*, 2004, **43**, 1718–1721.

63 R. Evans, Z. Deng, A. K. Rogerson, A. S. McLachlan, J. J. Richards, M. Nilsson and G. A. Morris, *Angew. Chem. Int. Ed.*, 2013, **52**, 3199–3202.

64 D. K. Wilkins, S. B. Grimshaw, V. Receveur, C. M. Dobson, J. A. Jones and L. J. Smith, *Biochemistry*, 1999, **38**, 16424–16431.

65 A. Z. Cardoso, L. L. E. Mears, B. N. Cattoz, P. C. Griffiths, R. Schweins and D. J. Adams, *Soft Matter*, 2016, **12**, 3612–3621.

66 F. Guzman, S. S. C. Chuang and C. Yang, *Ind. Eng. Chem. Res.*, 2013, **52**, 61–65.

67 Y. Tan, X. Dai, Y. Li and D. Zhu, *J. Mater. Chem.*, 2003, **13**, 1069–1075.

68 M. Wallace, J. A. Iggo and D. J. Adams, *Soft Matter*, 2015, **11**, 7739–7747.

69 R. O. Marcon and S. Brochsztain, *J. Phys. Chem. A*, 2009, **113**, 1747–1752.

70 T. H. Reilly, A. W. Hains, H. Y. Chen and B. A. Gregg, *Adv. Energy Mater.*, 2012, **2**, 455–460.

71 F. Schlosser, M. Moos, C. Lambert and F. Würthner, *Adv. Mater.*, 2013, **25**, 410–414.

72 N. M. Alexej Jerschow, *J. Magn. Reson.*, 1997, **375**, 372–375.

73 M. Liu, X. Mao, C. Ye, H. Huang, J. K. Nicholson and J. C. Lindon, *J. Magn. Reson.*, 1998, **132**, 125–29.

74 R. J. W. Lambert, I. Mytilinaios, L. Maitland and A. M. Brown, *Comput. Methods Programs Biomed.*, 2012, **107**, 155–163.

75 B. Gonzalez, N. Calvar, E. Gomez and A. Dominguez, *J. Chem. Thermodyn.*, 2007, **39**, 1578–1588.

76 V. J. Nebot, B. Escuder, J. F. Miravet, J. Smets and S. Fernández-Prieto, *Langmuir*, 2013, **29**, 9544–9550.

77 B. Escuder, M. LLusar and J. F. Miravet, *J. Org. Chem.*, 2006, **71**, 7747–7752.

78 M. Shibayama, *Polym. J.*, 2011, **43**, 18–34.

79 R. K. Heenan, S. M. King, D. S. Turner and J. R. Treadgold, *17th Meet. Int. Collab. Adv. Neutron Sources*, 2005, 1–6.

80 J. P. Schneider, D. J. Pochan, B. Ozbas, K. Rajagopal, L. Pakstis and J. Kretsinger, *J. Am. Chem. Soc.*, 2002, **124**, 15030–15037.

81 C. Yan, A. Altunbas, T. Yucel, R. P. Nagarkar, J. P. Schneider and D. J. Pochan, *Soft Matter*, 2010, **6**, 5143–5156.

82 S. R. Kline, *J. Appl. Crystallogr.*, 2006, **39**, 895–900.

83 A. Y. Cherny, E. M. Anitas, V. A. Osipov and A. I. Kuklin, *J. Appl. Crystallogr.*, 2014, **47**, 198–206.

84 S. A. Jamieson, K. W. K. Tong, W. A. Hamilton, L. He, M. James and P. Thordarson, *Langmuir*, 2014, **30**, 13987–13993.

85 K. L. Morris, L. Chen, J. Raeburn, O. R. Sellick, P. Cotanda, A. Paul, P. C. Griffiths, S. M. King, R. K. O'Reilly, L. C. Serpell and D. J. Adams, *Nat. Commun.*, 2013, **4**, 1480.

86 C. Colquhoun, E. R. Draper, R. Schweins, M. Marcello, D. Vadukul, L. C. Serpell and D. J. Adams, *Soft Matter*, 2017, **13**, 1914–1919.

87 E. R. Draper, B. J. Greeves, M. Barrow, R. Schweins, M. A. Zwijnenburg and D. J. Adams, *Chem*, 2017, **2**, 716–731.

88 D. W. Schaefer and M. M. Agamalian, *Curr. Opin. Solid State Mater. Sci.*, 2004, **8**, 39–47.

89 H. R. Ramay, M. C. Branco, P. Schneider and D. J. Pochan, *Faraday Discuss.*, 2008, **139**, 251–264.

90 M. A. Iannuzzi, R. Reber, D. M. Lentz, J. Zhao, L. Ma and R. C. Hedden, *Polymer*, 2010, **51**, 2049–2056.

91 O. Arnold, J. C. Bilheux, J. M. Borreguero, A. Buts, S. I. Campbell, L. Chapon, M. Doucet, N. Draper, R. Ferraz Leal, M. A. Gigg, V. E. Lynch, A. Markvardsen, D. J. Mikkelson, R. L. Mikkelson, R. Miller, K. Palmen, P. Parker, G. Passos, T. G. Perring, P. F. Peterson, S. Ren, M. A. Reuter, A. T. Savici, J. W. Taylor, R. J. Taylor, R. Tolchenov, W. Zhou and J. Zikovsky, *Nucl. Instruments Methods Phys. Res. Sect. A Accel. Spectrometers, Detect. Assoc. Equip.*, 2014, **764**, 156–166.

92 A. R. Drews, J. A. Barker, C. J. Glinka and M. Agamalian, *Phys. B*, 1998, **241**–**243**, 189–191.

93 A. Bondi, *J. Phys. Chem.*, 1964, **68**, 441–451.

CHAPTER 3

High Throughput Screening of Photocatalytic Hydrogen Evolution using Perylene Bisimides

This work involved supervision from Professor Dave Adams and Dr Alex Cowan. High throughput experiments were undertaken at the Centre for Materials Discovery at the University of Liverpool with assistance from Rob Clowes and Dr Ben Alston, with thanks to Professor Andy Cooper. Some preliminary hydrogen evolution and UV-Vis data were collected by Ben Coles for his undergraduate project and by Maelle Loyer on an Erasmus scheme project, both supervised by MN. Acknowledgements for data collection are found within figure captions.

3.1. Abstract

As Chapter 2 has shown, a phenylalanine-substituted perylene bisimide dye exhibits interesting properties for its use as a photocatalyst for the hydrogen evolution reaction.[1] The study has been expanded to explore other parameters which may increase the photocatalytic activity of the solutions; (1) different amino acid substituents onto the PBI core have been investigated as this alters the molecular packing,[2] (2) lower PBI concentrations have been studied as this will lower the solution viscosity and increase the light penetration through the solution, (3) differing methanol concentrations have been studied to see the effect on PBI solubility and the use of excess sacrificial electron donor, and (4) differing pH values have been studied to optimise the conditions for each solution as the previous study has shown pH is crucial to the photocatalytic activity. High-throughput instrumentation has been implemented to increase the experimental output as the photocatalytic experiments are time consuming and require repeat experiments to provide error bars, this has allowed the many parameters to be investigated.

3.2. Introduction

The nature of the self-assembled aggregates are affected by the structure of the PBI monomers.[3] Different structures can possess varying photocatalytic activities due to their differing physical properties. As the photocatalytic performance of PBI molecules have been shown to be highly dependent on pH it is clear that subtle changes in the morphology of the self-assembled structure can have a critical effect on the activity for photocatalytic hydrogen evolution.[4] Supramolecular assembly is important for the conductivity of the fibres and the amount of radical anion formed.[5]

The general focus of the published literature in the area of perylene photocatalysts is showcasing the different ways PBIs can be used in photocatalytic cells and the differing experimental conditions, such as how to best combine with metal co-catalysts.[6] These investigations are key for the advancement of the area of dye-sensitized photocatalysis, however there is limited focus on the effect of altering the self-assembled structures themselves. A study such as this requires an intrinsic comparison between various structures to elucidate the effect of the self-assembly on photocatalytic activity. This work intends to examine the effects of self-assembly on hydrogen evolution from platinum nanoparticles by systematically changing the material composition.

3.3. Results and Discussion

3.3.1. Photocatalytic hydrogen evolution using self-assembled PBI derivatives under UV irradiation

The photocatalytic activity of solutions containing perylene bisimides and platinum nanoparticles in methanol and water are dependent on pH and the nature of the self-assembled structure of the PBI photocatalyst (see Chapter 2).[1] Each amino acid investigated has differing steric properties and a different level of hydrophobicity[7] and when substituted at the imide position on PBI influences the way the molecules pack together and their self-assembled structures;[5,8,9] therefore, eight different PBIs have been screened to compare their activity as photocatalysts for the hydrogen evolution reaction. The amino acids used are alanine (A), phenylalanine (F), histidine (H), leucine (L), serine (S), valine (V), tryptophan (W) and tyrosine (Y) (see Figure 60). The compounds were synthesised as reported in Chapter 2 or attained from other works within the group by Draper et al.[5] All compounds have been shown to contain worm-like micelles in solutions,[5,9] however the extent of the self-assembly and the types of structures present have not been studied in detail. An extensive analysis such as that carried out in in Chapter 2 would be required to understand the types of structures present and attain useful data. The study in this chapter will focus on attaining experimental information about the use of the different PBIs and conditions in a photocatalytic setting which may reveal avenues for a more detailed analysis in the future.

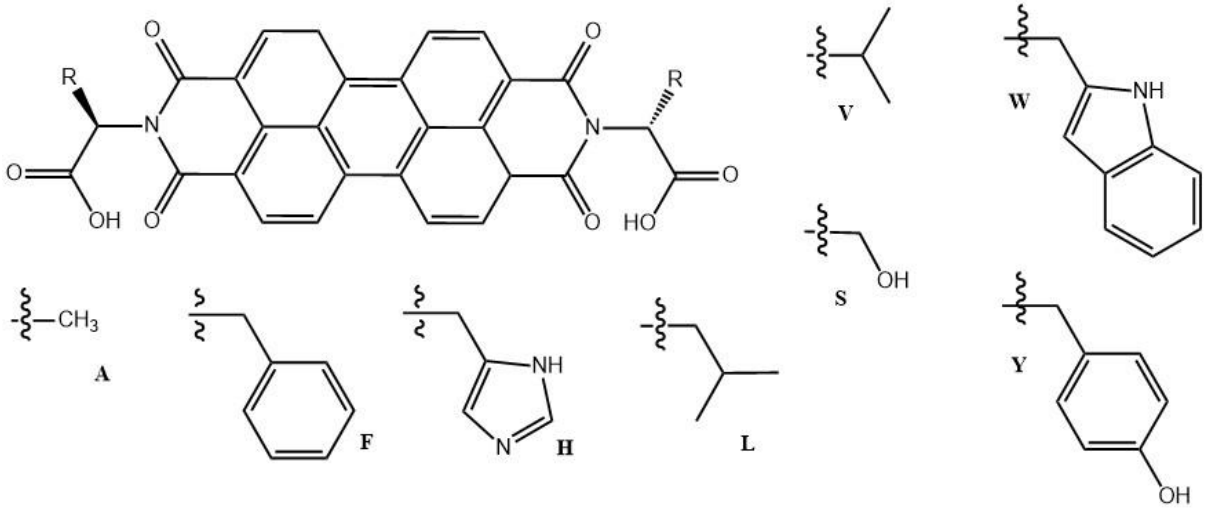

Figure 60. Structure and abbreviations of the PBI amino acid derivatives which have been investigated in this work.

A sample environment housing three UV LEDs in parallel was developed which allowed up to three samples to be irradiated and stirred simultaneously with reproducible results, this allowed more in-depth preliminary studies to be carried out.

Solutions of each PBI were prepared with 10 mg/mL PBI, 20 vol% methanol and platinum nanoparticles (1 mol % Pt). The solutions were prepared with 2 equivalents of sodium hydroxide and then the pH lowered to pH 6, 4.5 or 2 by adding 0.1M HCl dropwise. Photocatalytic experiments were carried out on the solutions as explained in Chapter 2, where 5 mL of solution was purged in a sealed quartz cell with a headspace and then irradiated for 4 hours and GC analysis carried out on the gas composition in the headspace to monitor evolved hydrogen, however in this case UV LEDs were used for irradiation rather than the Xe lamp. The pH of the solutions remained stable after irradiation.

Figure 61 shows the amount of hydrogen evolved from the hydrogen evolution experiments using the range of substituents as shown in Figure 60. This data reveals that a careful choice of photocatalyst is needed in this system as each PBI shows a different overall activity for hydrogen evolution, despite exhibiting absorbances in the visible spectrum (Figure 62). The changes may be closely linked to the extent and type of aggregation and the amount of radical anion which each supramolecular assembly forms.[9] The general trend for pH activity is similar for each PBI however the optimal pH is different. Each amino acid has differing sterics and hydrophobicity was has shown to result different extents of aggregation which may be the cause of different optimal pHs in solution.[8–10] There is a correlation between pH and photocatalytic activity for the PBIs, as shown in Chapter 2 for PBI-F. Some PBIs show higher activity, such as PBI-A, F and V, and some yield little to no hydrogen like PBI-H and PBI-W. Although structure is likely to be an important factor, there is also the possibility that the amino acid can be oxidised and affect the activity by acting as a hole trap. For example, the oxidation potentials of the amino acid alanine (ca. 0.4-0.65 $V_{Ag/AgCl}$) would allow for the amino acid to act as an electron donor.[10]

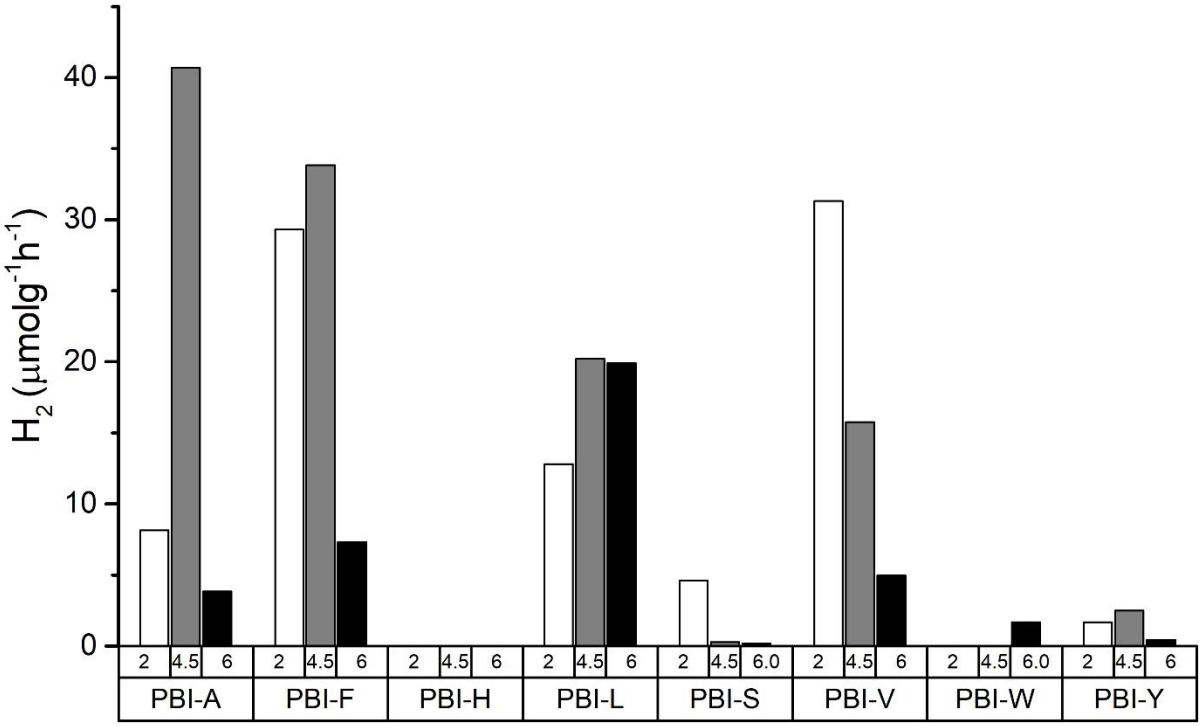

Figure 61. The amount of hydrogen evolved after irradiating PBI/Pt NPs/Methanol solutions of different pH for 4 hours with a 365 nm LED. PBI concentration was 5 mg/mL, methanol concentration at 20 vol % and co-catalyst at 1 mol% Pt. Secondary x-axis labels indicate pH.

3.3.2. Understanding the electronic and optical properties of self-assembled perylene bisimide derivatives

The highest occupied molecular orbital (HOMO) energy and the lowest occupied molecular orbital (LUMO) energy of compounds are important when considering their use in optoelectronics.[11] For a compound to reach an excited state the energy gap between the HOMO and LUMO, known as the band gap, must be overcome for the donation of an electron from the HOMO into the LUMO.[11] Perylene bisimides can accept electrons into the LUMO to form a reduced species; this is regularly displayed in dye based photovoltaics.[12] The relative energies of the HOMO and LUMOs of p and n-type materials should be carefully considered when designing materials for optoelectronic applications. It is possible that the energy levels can be optimised by considering the molecular structure as well as the geometries of adjacent molecules.[13–15] The HOMO and LUMO can be estimated calculated by using experimental data from cyclic voltammetry (CV) and UV-Vis absorption spectroscopy. Therefore, UV-Vis and cyclic voltammetry studies were carried out on aqueous PBI solutions at high pH. As the self-assembly of the PBI is different in various solutions, different solvents were also compared, aqueous solutions at high pH were compared with DMF solutions. (Figure 62-Figure 65, Table

4-Table **6**). The HOMO and LUMO values estimated from these data are in line with literature values of similar materials.[16–20]

The higher intensity of the 0-0 vibrational transition at 534 nm is an indication that the PBI species is less aggregated in the organic solvents (Figure 63), on the other hand the aqueous solutions show the typical absorption intensities related to H-aggregation (Figure 62).[21] Additionally, the aqueous solutions were irradiated with a UV light for 5 minutes and the spectra recorded afterwards to reveal the reduction peaks of the radical anion species at 710, 810 and 980 nm, and dianion species found within the shoulder at 620 nm.[22] The absorption spectra before irradiation for gelators PBI-F, W and Y have a different shape to the others. These three gelators contain bulky hydrophobic groups on the peripherals of the compounds which may be directing the molecules into a distinctly different shape to those with the smaller groups.

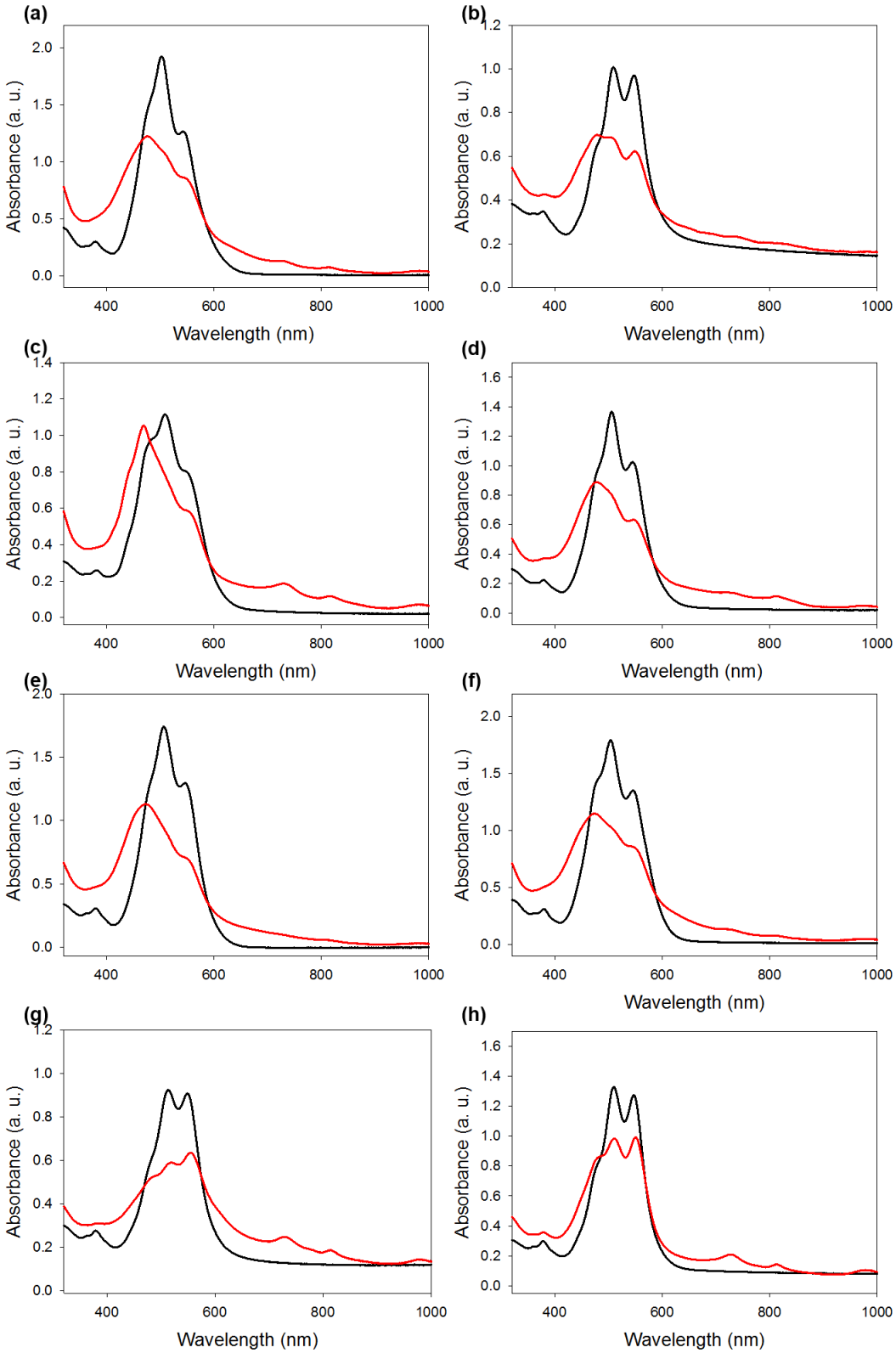

Figure 62. UV-Vis absorption spectrum in high pH solution at 5 mg/mL in a 0.1 mm quartz cuvette for (a) PBI-A, (b) PBI-F, (c) PBI-H, (d) PBI-L, (e) PBI-S, (f) PBI-V, (g) PBI-W and (h) PBI-Y. The black data is before irradiation and the red data is after irradition with 365 nm LED.

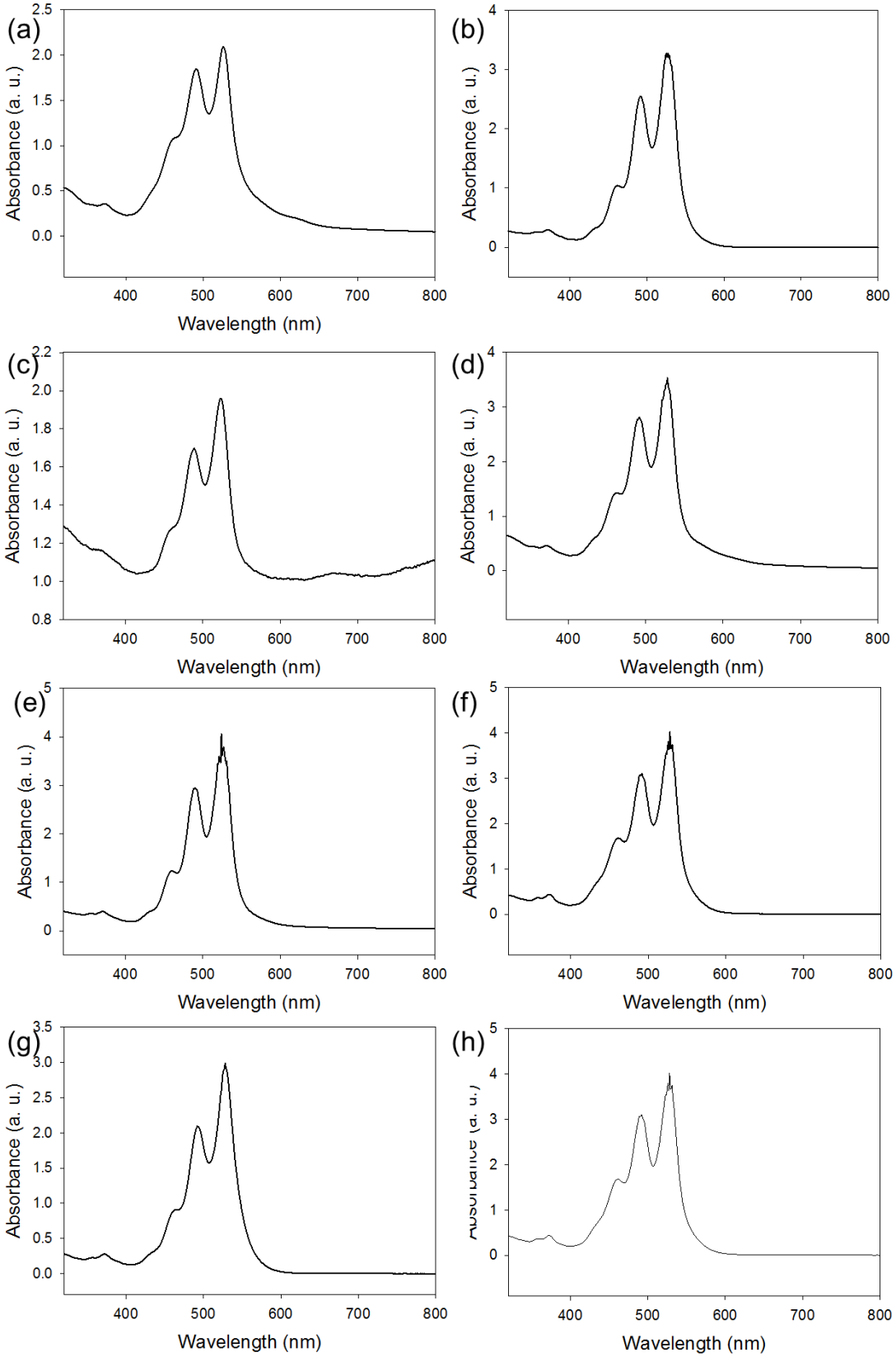

Figure 63. UV-vis absorption spectra at 5 mg/mL in DMF in a 0.1 mm quartz cuvette (a) PBI-A, (b) PBI-F, (c) PBI-H, (d) PBI-L, (e) PBI-S, (f) PBI-V, (g) PBI-W and (h) PBI-Y.

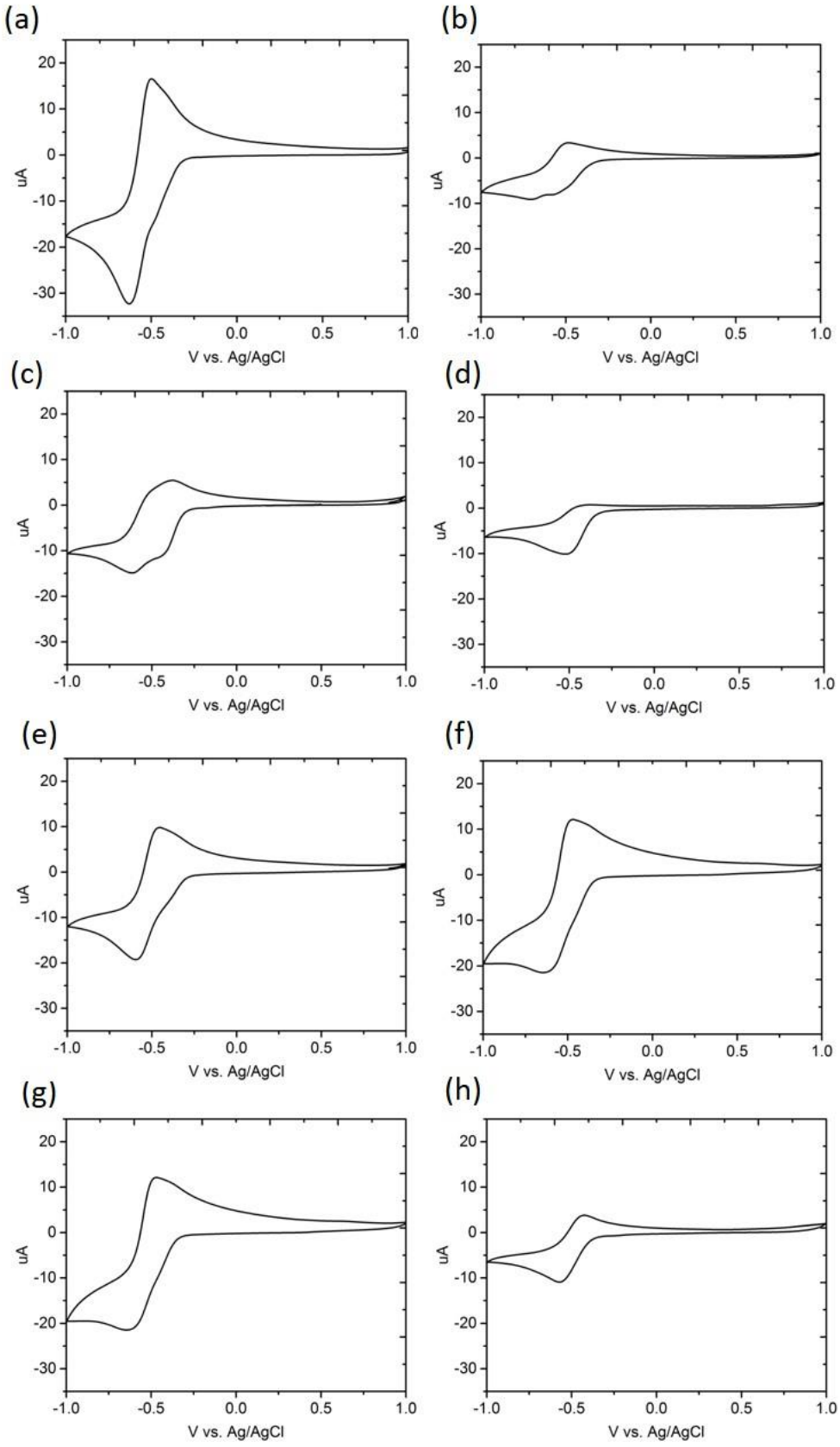

Figure 64. Cyclic voltammagram of high pH solutions of (a) PBI-A, (b) PBI-F, (c) PBI-H, (d) PBI-L, (e) PBI-S, (f) PBI-V, (g) PBI-W and (h) PBI-Y. Graphs have been scaled to the same values to compare all the data. 0.1 M NaCl was added as the electrolyte.

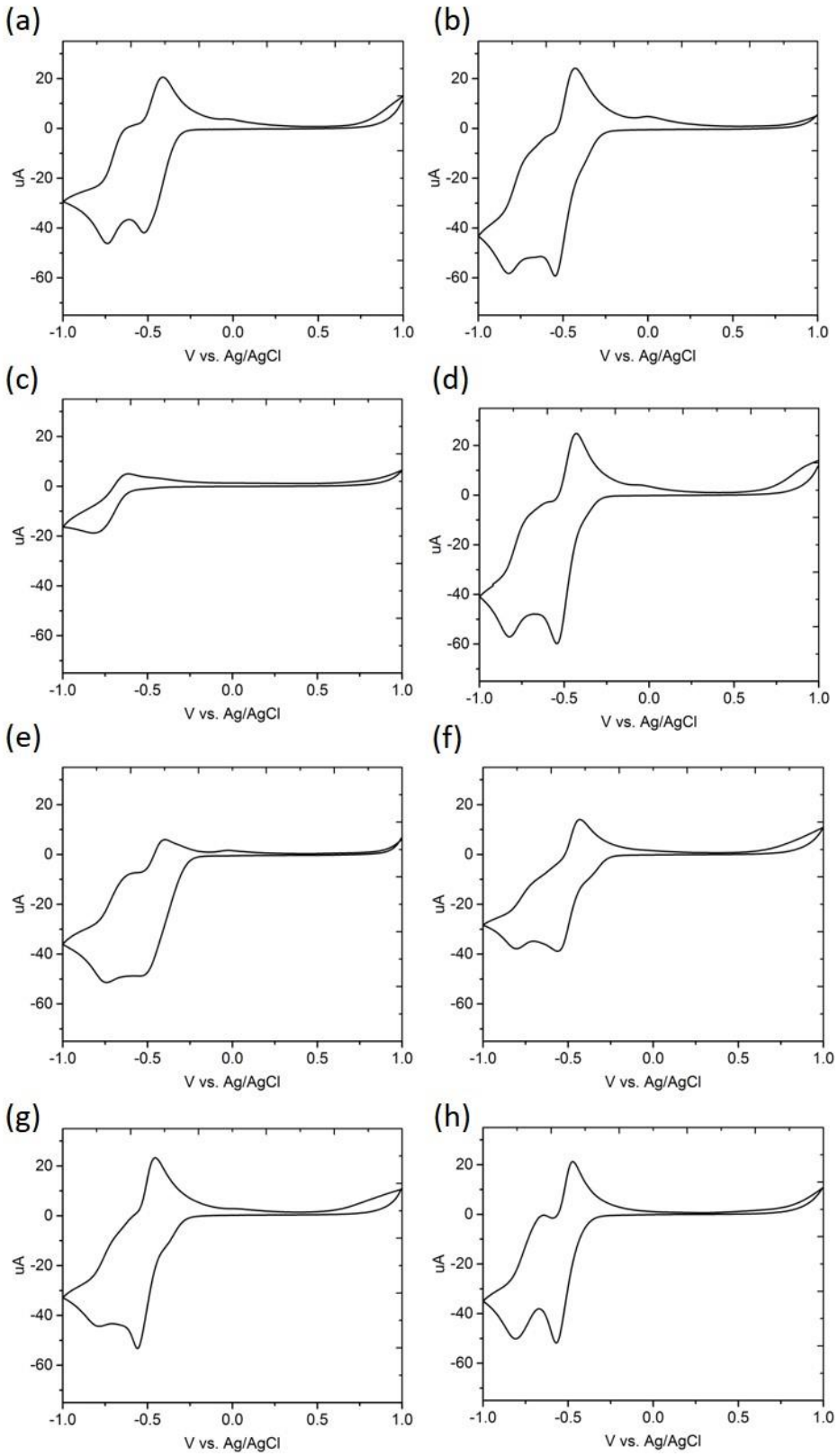

Figure 65. Cyclic voltammagram of DMF solutions of (a) PBI-A, (b) PBI-F, (c) PBI-H, (d) PBI-L, (e) PBI-S, (f) PBI-V, (g) PBI-W and (h) PBI-Y. Graphs have been scaled to the same values to compare all the data. 0.1 M of tetrabutylammonium hexafluoroborate (TBAHFB) was used as the electrolyte.

In both aqueous and organic solutions a quasi-reversible reduction is observed (Figure 64-Figure 65) as although the peak separation is < 59 mV the anodic current does not always equal the cathodic current. The peak separation could arise for several reasons such as surface adsorption onto the electrode or cross comparison between peak pairs. The reductions are broader and less defined in the aqueous solutions compared to the organic, however the reduction values are unchanged. This could be a strong indication that self-assembly does not have a direct effect on the reduction values, that the CVs are only measuring molecularly dissolved species in solution, or that the aggregates are only contributing slightly to the CV trace. To test this, a scan rate dependence study was carried out on a PBI-A solution (Figure 66-Figure **67**). The reduction and oxidation values are unchanged when the scan rate is changed (Figure 66). The square root of the scan rate is proportional to the current response (Figure 67) indicating a reversible process. If the electron transfer is through the larger self-assembled aggregates, then changing the scan rate would reveal a diffusion limitation.

The Randles-Sevcik equation describes the effect of scan rate on peak current and can determine the diffusion coefficient of the electroactive species (Table 2), however as the reduction potentials are overlapping then analysis should be approached with caution.[23] The Stokes-Einstein equation can be used to predict the radius of the reductive species (Table 3). The first and second reductions show remarkably different behaviours from each other. The calculated radius of the measured species is unchanged for reduction 2 and increases at slower scan rates for reduction 1. The first reduction is dependent on scan rate showing a diffusion limitation, possibly related to measuring the aggregate; as the scan rate is lowered, the calculated radius increases to 51 nm as the slower scan rates increases the diffusion layer thickness due to a diffusion limitation. The second reduction seems independent from the scan rate, as the free molecule is much smaller and more conductive. It seems that the self-assembled aggregates are sometimes measured as part of the first reductive peak and that the most prominent peak, the maximum reduction peak, is the solvated species. This analysis, however, is to be taken with caution as several factors could be affecting the current potentials such as the overlapping potentials and the possible presence of a chemical step following the reduction process.

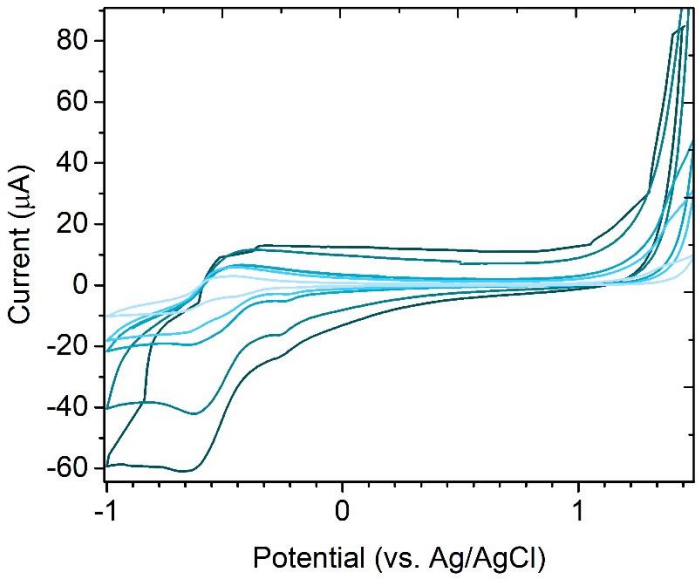

Figure 66. Scan Rate Dependant CVs of PBI-A (5 mg/mL) at high pH. Solutions were measure at scan rates of 1, 0.5, 0.1, 0.05, 0.01 V/s (dark blue to light blue traces).

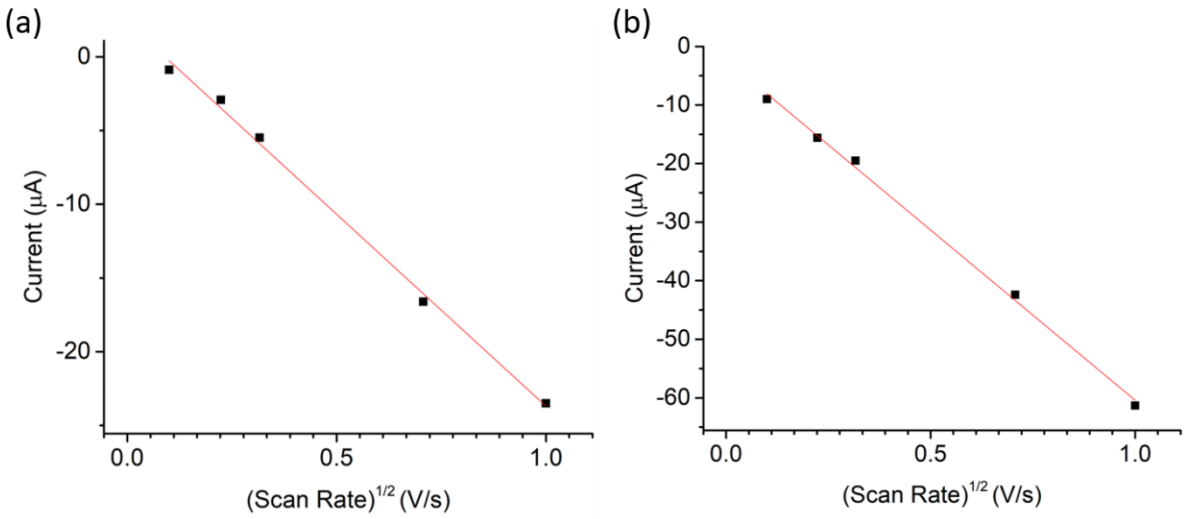

Figure 67. Analysis of the current responses from the maximum of reductions 1 (a) and 2 (b) from the scan rate dependence scans in Figure 66.

The HOMO and LUMO values of the species observed in the solutions when using the most reductive peak are summarised in Table 4-Table 6 and Figure 68. Although the most reductive species is related to the solvated species, it is the clearest peak to decipher in all spectra and so this has been used for the HOMO and LUMO determination. The optical band gap, E_g, of all PBI species are around 1.8 eV in aqueous solutions and 2.0 eV in DMF solutions with little

difference between the various amino acid derivatives. The bathochromic shift of the UV-Vis data from DMF to high pH solutions is around 20 nm indicating the presence of H-aggregation. Across the whole series of solutions of PBI derivates the HOMO and LUMO values vary only slightly (Figure 68), however this could be different if the LUMO can be calculated electrochemically from the self-assembled species in solution.

Table 2. Diffusion coefficient values of PBI-A (5 mg/mL) in aqueous solutions calculated from the Randles Sevcik equation.

Scan Rate / Vs^{-1}	Diffusion Coefficient (Reduction 1) (x 10^{-8}) cm^2s^{-1}	Diffusion Coefficient (Reduction 2) (x 10^{-8}) cm^2s^{-1}
1.0	1.70	1.44
0.5	1.69	1.38
0.1	0.92	1.46
0.05	0.52	1.87
0.01	0.23	3.13

Table 3. Diffusion radius calculated from the Stokes-Einstein equation.

Scan Rate / Vs^{-1}	Radius (Reduction 1) / nm	Radius (Reduction 2) / nm
1.0	7.00	8.23
0.5	7.01	8.60
0.1	12.87	8.13
0.05	22.82	6.35
0.01	51.07	3.80

Table 4. Calculation of the optical band gap using the UV-Vis absorption spectra in DMF and at high pH solution.

	λ_{max} S_0-S_1 0-0 (nm)			λ_{onset} (nm)		Optical Band Gap, E_g (eV)	
Gelator	**High pH**	**DMF**	**Bathochromic shift**	**High pH**	**DMF**	**High pH**	**DMF**
PBI-A	542	527	15	690	692	1.80	1.79
PBI-F	548	527	21	697	626	1.78	1.98
PBI-H	552	524	28	698	614	1.78	2.02
PBI-L	548	528	21	702	669	1.77	1.86
PBI-S	545	525	20	678	633	1.83	1.96
PBI-V	543	529	15	696	624	1.78	1.99
PBI-W	550	528	21	703	613	1.77	2.03
PBI-Y	549	529	21	692	624	1.80	1.99

Table 5. Electrochemical values from CVs of PBIs in DMF and high pH solution.

	Reduction$_{max}$ (V vs. Ag/AgCl)		Oxidation$_{max}$ (V vs. Ag/AgCl)		$E_{1/2}$ (V vs. Ag/AgCl)	
Gelator	**High pH**	**DMF**	**High pH**	**DMF**	**High pH**	**DMF**
PBI-A	-0.62	-0.52	-0.50	-0.41	-0.56	-0.47
PBI-F	-0.72	-0.55	-0.50	-0.43	-0.61	-0.49
PBI-H	-0.62	-0.51	-0.39	-0.62	-0.50	-0.56
PBI-L	-0.53	-0.54	-0.41	-0.43	-0.47	-0.49
PBI-S	-0.59	-0.53	-0.48	-0.40	-0.53	-0.46
PBI-V	-0.64	-0.56	-0.49	-0.43	-0.57	-0.50
PBI-W	-0.63	-0.56	-0.49	-0.46	-0.56	-0.51
PBI-Y	-0.57	-0.56	-0.43	-0.41	-0.50	-0.49

Table 6. Approximated HOMO/LUMO values using CV for the solutions at high pH and in DMF.

	LUMO (eV vs. vacuum)				HOMO (eV vs. vacuum)			
Gelator	**High pH[a]**	**DMF[a]**	**High pH[b]**	**DMF[b]**	**High pH[a]**	**DMF[a]**	**High pH[b]**	**DMF[b]**
PBI-A	-3.91	-4.04	-4.07	-4.20	-5.72	-5.83	-5.88	-5.99
PBI-F	-3.96	-4.06	-4.12	-4.22	-5.74	-6.05	-5.90	-6.21
PBI-H	-3.86	-4.13	-4.02	-4.29	-5.64	-6.16	-5.80	-6.32
PBI-L	-3.82	-4.06	-3.98	-4.22	-5.59	-5.92	-5.75	-6.08
PBI-S	-3.89	-4.03	-4.05	-4.19	-5.72	-6.00	-5.88	-6.16
PBI-V	-3.92	-4.07	-4.08	-4.23	-5.71	-6.06	-5.87	-6.22
PBI-W	-3.91	-4.08	-4.07	-4.24	-5.68	-6.11	-5.84	-6.27
PBI-Y	-3.85	-4.06	-4.01	-4.22	-5.65	-6.05	-5.81	-6.21

[a] using the value SHE vs. vacuum = 4.28 eV[24]

[b] using the value SHE vs. vacuum = 4.44 eV[25]

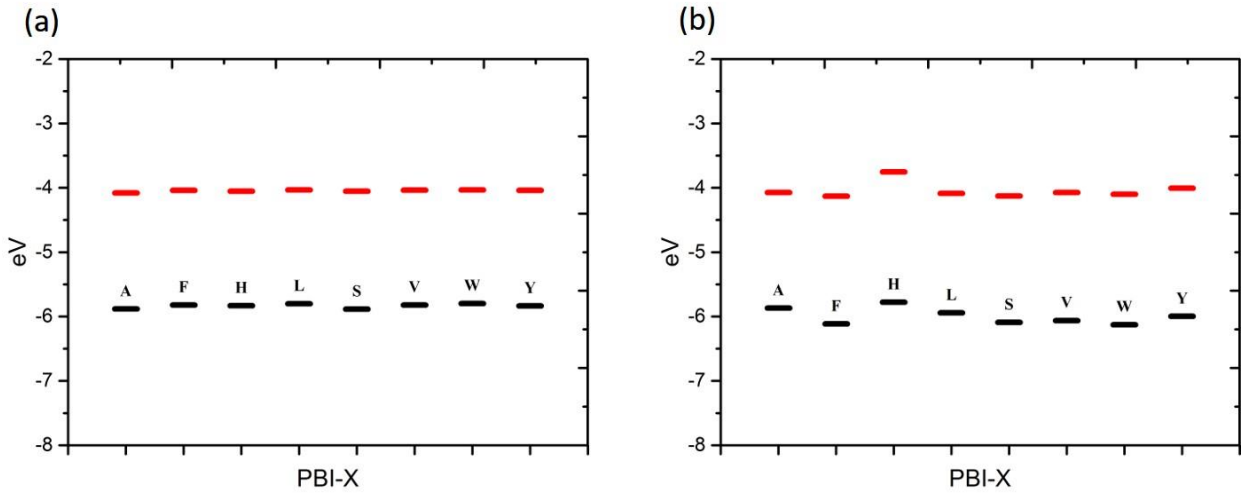

Figure 68. Summary of the experimentally approximated HOMO and LUMO values of the amino acid substituted PBI derivatives at (a) high pH in H_2O and (b) in DMF.

Although the experimentally calculated HOMO and LUMO values of the PBI derivatives are similar, the preliminary hydrogen evolution study (Figure 61) still shows that the different PBI derivatives have different activities. The CVs were analysed further, and the maximum current capacity was measured from the reductions and oxidations (Figure 69), here distinct differences between the PBIs were observed. Differences in supramolecular structure, such as more closely packed fibres, would result in more efficient charge transfer, this would result in a more conductive solution. PBI-A showed the largest current output in H_2O followed by PBI-V, whereas PBI-L and F show the smallest current outputs. Compared with the hydrogen evolution data, these four PBIs were the main active PBIs out of the whole group and each show a pH dependence. However, it seems clear that each have a unique pH maximum where the differences are possibly related to their different hydrophobicity. In DMF the largest current outputs are found in PBI-F and L solutions whereas the minimal current output is PBI-H. Again, although PBI W, Y and S show good conductivity in solutions, it may be the self-assembled species which isn't measured here which may be the main contributor to the photocatalytic hydrogen evolution. It is again important to note that the inconsistencies in these trends may, through the process of elimination, provide contributing evidence that the self-assembled species are the photocatalytic active species in this system. A general photocatalytic scheme has been depicted in Figure 70.

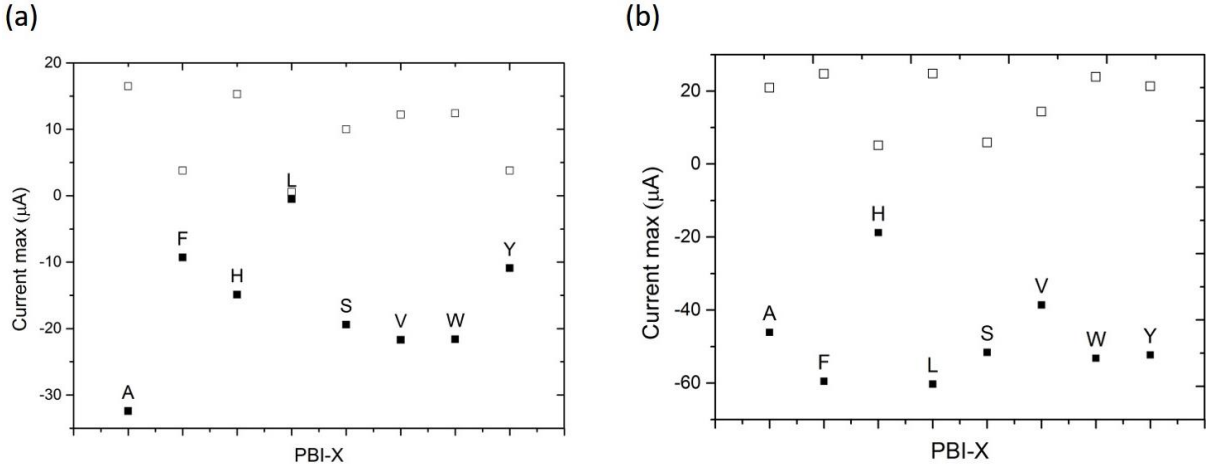

Figure 69. The maximum and minimum current values from the oxidations (open squares) and reductions (closed squares) from the CV studies of the PBIs in at (a) high pH in H_2O and (b) in DMF.

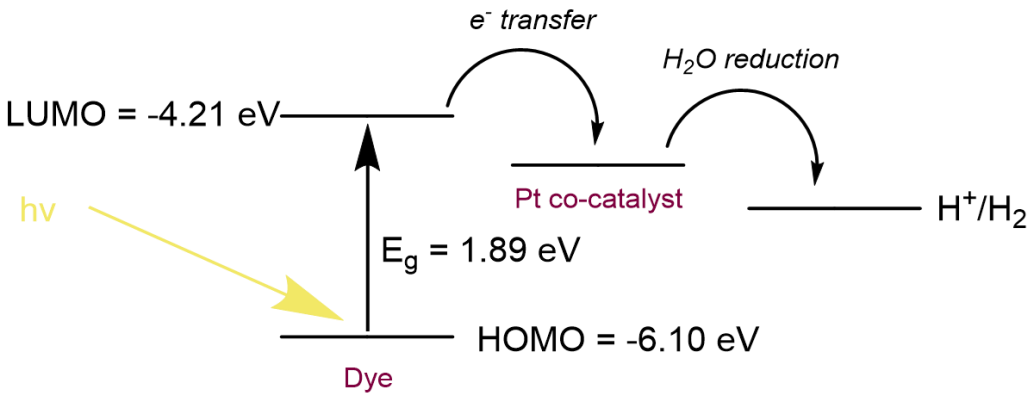

Figure 70. Schematic energy level diagram for dye-sensitised H_2 production from water using 0.5 mg/mL PBI-V with a platinum co-catalyst and methanol. The LUMO values were determined from CVs, optical band gap (E_g) value estimated from the onset of absorption from UV-Vis spectrum and the HOMO value was calculated from the LUMO and optical band gap values. Acknowledgement: Ben Coles.

3.3.3. The effect of PBI-V concentration on photocatalytic hydrogen evolution under UV irradiation.

Solutions with lower concentrations of PBI have several different characteristics which can change the photocatalytic activity; reduced photocatalyst concentration, reduce opacity and a decreased photocatalyst:co-catalyst ratio, these would result in more efficient mixing, increased light penetration an increase in photocatalyst and co-catalyst interactions, respectively. These factors are in competition with the reduced photocatalyst amount. PBI-V was investigated further at various concentrations of PBI. Firstly, control studies for PBI-V at pH 4.5 indicated that the perylene and the platinum co-catalyst needed to be present for hydrogen evolution to occur. However, methanol is not needed in this mixture for hydrogen evolution to occur. It is hypothesised that the PVP capping ligands on the platinum nanoparticles are able to act as electron donors under the right conditions.[25]

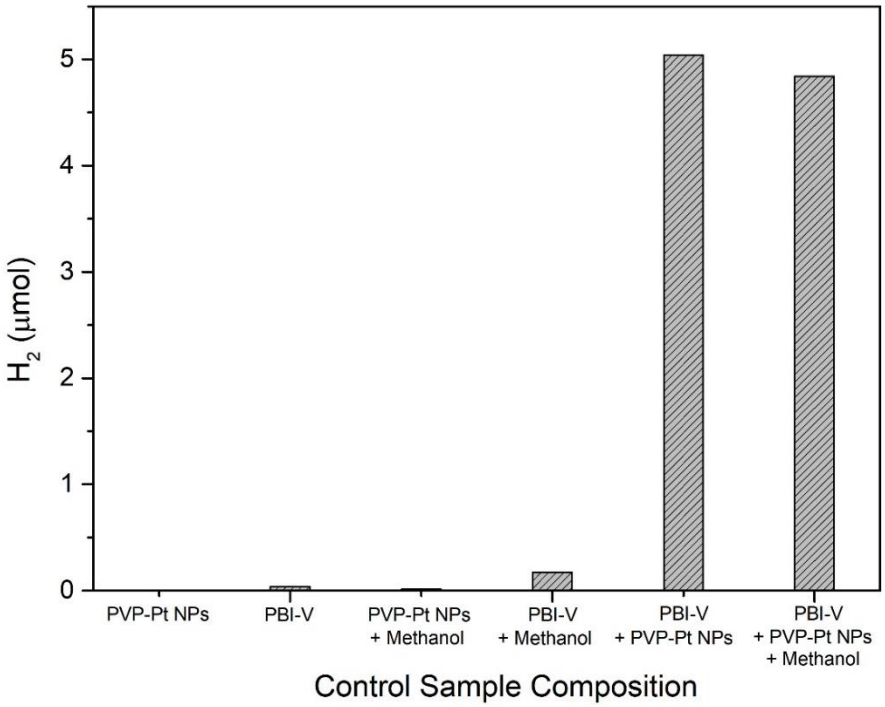

Figure 71. Control photocatalysis runs of PBI-V at 1 mg/mL with/without PVP-Pt nanoparticles and with/without methanol. All solutions were at pH 4.5 and irradiated with UV LEDs for 4 hours.

Figure 72 shows a relationship between the concentration of photocatalyst and the amount of hydrogen produced. Samples of PBI, Pt NPs and 20% methanol were regulated to pH 4.5. Five different concentrations of PBI-V solutions were prepared: 10, 5, 1, 0.5 and 0.1 mg/mL. The solutions were then irradiated for 4 hours using the LED photocatalytic system. Interestingly, halving the concentration of PBI-V from 10 mg/mL to 5 mg/mL resulted in a more than two-fold increase in evolved H_2 (inset, Figure 72). Lowering the concentration down to 1 and 0.5 mg/mL results in no further change in evolved H_2, however lowering to 0.1 mg/mL causes a dramatic reduction in H_2. The reduction in activity at lower concentrations may also be attributed to the critical aggregation concentration, where below this concentration aggregation is not dominant but above this concentration the assemblies are formed and could be in more compact assemblies.[26] The critical aggregation concentration is for these solutions is unknown however it would appear that being above this concentration is necessary for photocatalytic performance. Notably, when the PBI concentration is lowered and the evolved H_2 remains unchanged, the rate of H_2 is increased. There seems to be an optimal PBI concentration between 0.1-1.0 mg/mL. This could be a result of a combination of parameters; the viscosity and mixing of the solutions, the opacity and light penetration for PBI activation and the ratio of photocatalyst to co-catalyst. Here, the amount of platinum is kept constant despite the changing

concentration of photocatalyst, this allows for observations to be made against the PBI concentration; however the changing ratio of photocatalyst to co-catalyst must still be appreciated in any observations and this ratio is instead analysed independently later.

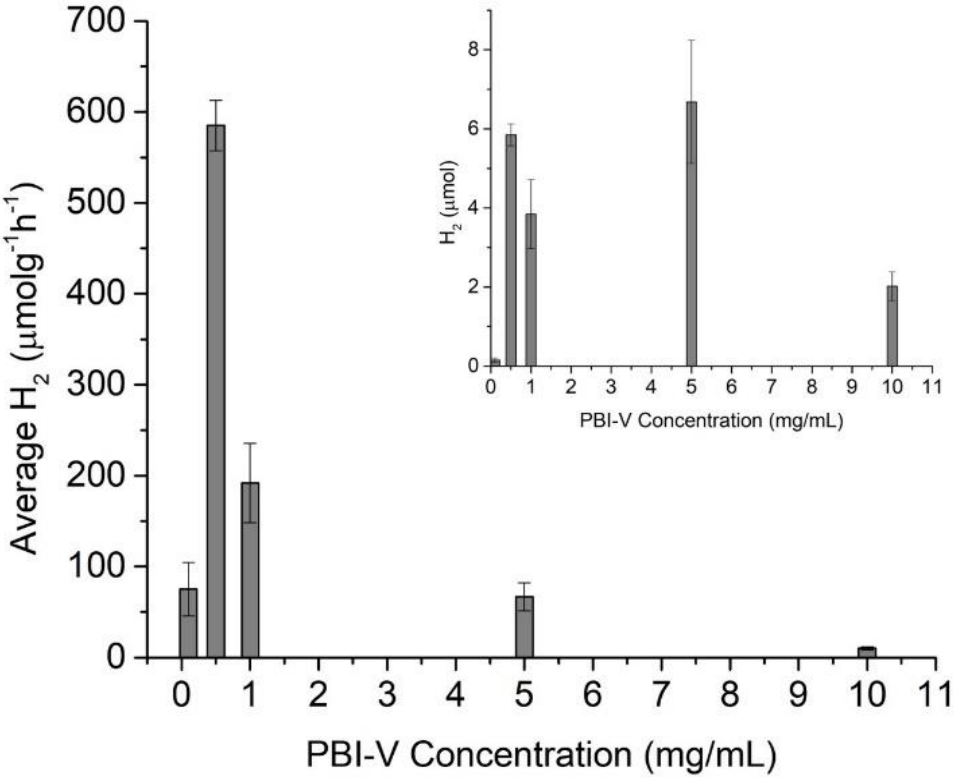

Figure 72. Rate of photocatalytic hydrogen evolution for PBI-V/20% methanol/Pt NPs solutions at different PBI concentrations, irradiated for 4 hours with a 365 nm LED. Inset: μmoles of hydrogen produced. Acknowledgement: Ben Coles (University of Glasgow).

The UV-Vis spectra of the PBI solutions were analysed before and after irradiation. These data were collected in a 1 mm pathlength cuvette which is smaller than the 1 cm pathlength cuvette used in the photocatalysis, the data can still be correlated as the suspensions formed in the solutions remain the same and the effects of the different suspensions can be observed. Difference spectra helps to reveal the extent of the radical anion formation for each PBI concentration. The intensity of the radical anion peak at 727 nm was compared to find the concentration of the active reduced species being formed for each solution (Figure 73). The amount of radical anion formed increases substantially between 0.1 and 1 mg/mL but increases only slowly upon a further increase of concentration up to 5 and 10 mg/mL. The lack of increase

in the steady state concentration of radical anion at higher concentrations could be explained by the increased electron recombination occurring because of increased PBI concentration and may be a reason why increasing the PBI concentration above 1 mg/mL has no further effect on the amount of hydrogen evolved during photocatalysis.

As the concentration of the gelator increases from below the critical aggregation concentration, the type and extent of self-assembly may be changing. As the concentration continues to increase this could be undergoing further changes. An optimal assembly for reduces species to form and survive may be formed between 1-5 mg/mL. Figure (d) in Figure 73 is reminiscent of a T_{gel} (sol-gel transition temperature) vs. concentration plot which indicates that increasing concentration further has no major physical effects on the gel.

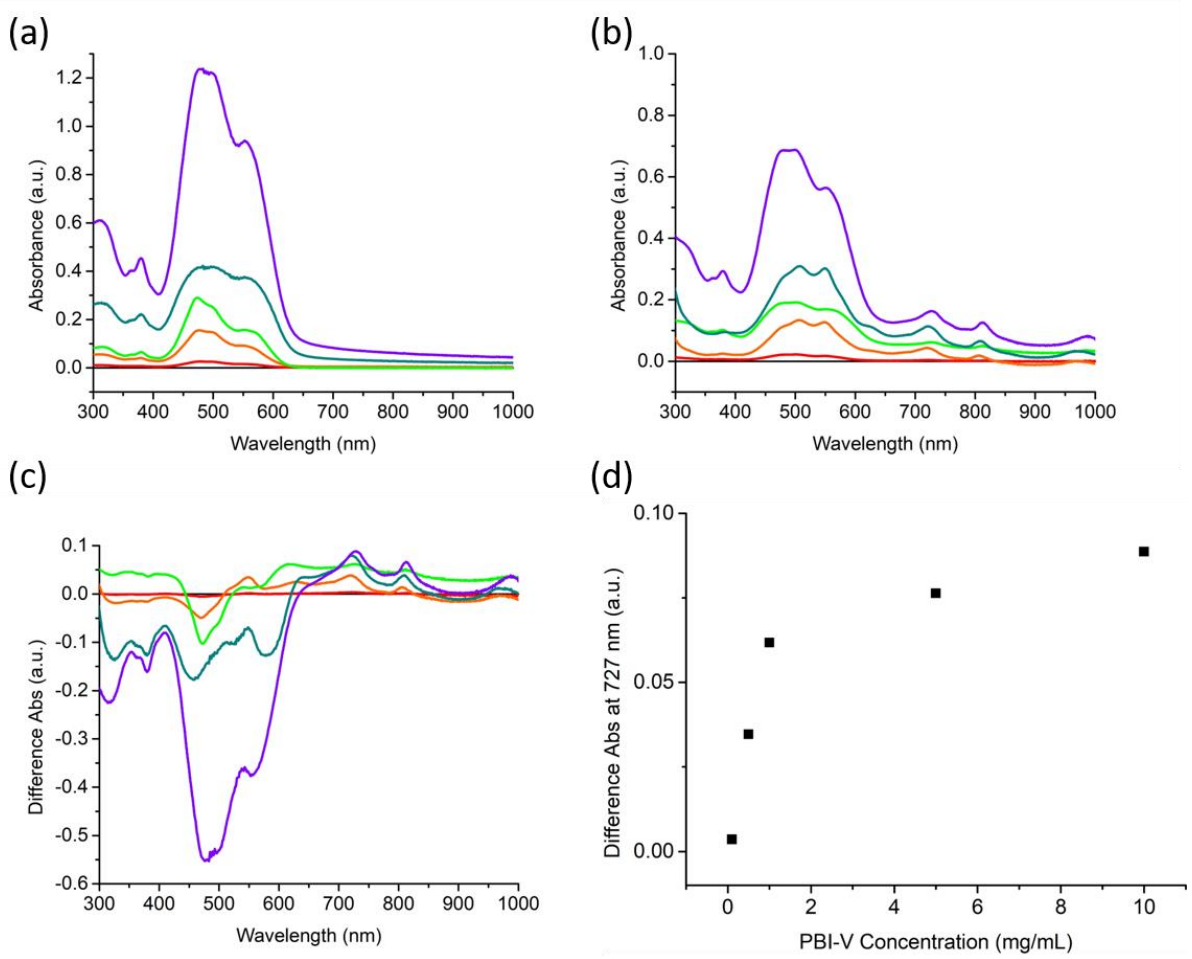

Figure 73. UV-Vis spectra of PBI-V/Pt NPs/20% methanol (a) before irradiation, (b) after 5 minutes of irradiation at 365 nm, (c) the difference spectra obtained from (a) and (b), and (d) the difference results at 727 nm summarised as a function of concentration. Colours indicate

10 mg/mL (purple), 5 mg/mL (dark green), 1 mg/mL (light green), 0.5 mg/mL orange and 0.1 mg/mL red.

3.3.4. Expansion to High-Throughput Photocatalysis

PBI-V and PBI-F were investigated in further detail using high throughput instrumentation which allows 48 samples to be run simultaneously under a solar simulator lamp. As shown by Figure 74, the spectrum of a perylene bisimide closely resembles that of the solar simulator which could allow for a strong utilization of the full wavelength of light.

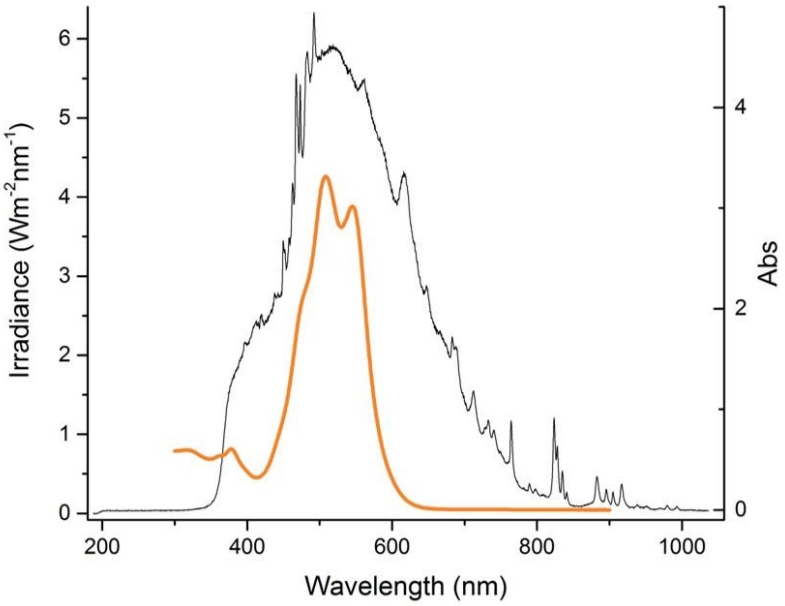

Figure 74. UV-Vis spectrum of the solar simulator (black, irradiance) overlaid with a spectrum of PBI-F solution (orange, absorbance) at high pH.

PBI-F and PBI-V have been chosen for the high throughput study as the data collected from PBI-F solutions can be corroborated with previous results and PBI-V had shown promising results in the preliminary experiments. The high throughput equipment used is described in the experimental. The data collected from the high throughput study cannot be directly compared to other results as the solar simulator provides a different spectrum of light than other sources (Xe lamp source in Chapter 2, 365 nm LED in Chapter 3 Figure 61) but data can be compared and correlated.

Solutions of PBI-F, PVP-Pt NPs and methanol were irradiated using the solar simulator and compared with previous data collected in Chapter 2 using the Xe lamp (Figure 75). Both

experimental setups resulted in similar trends along the pH scale. The optimum rate of hydrogen evolution was around pH 4-5 in both cases, the solar simulator setup showed a threefold increase in activity due to the higher intensity of light. For the following results presented using the solar simulator, any values close to zero may sometimes show a negative number due to the calibration fit not passing through zero.

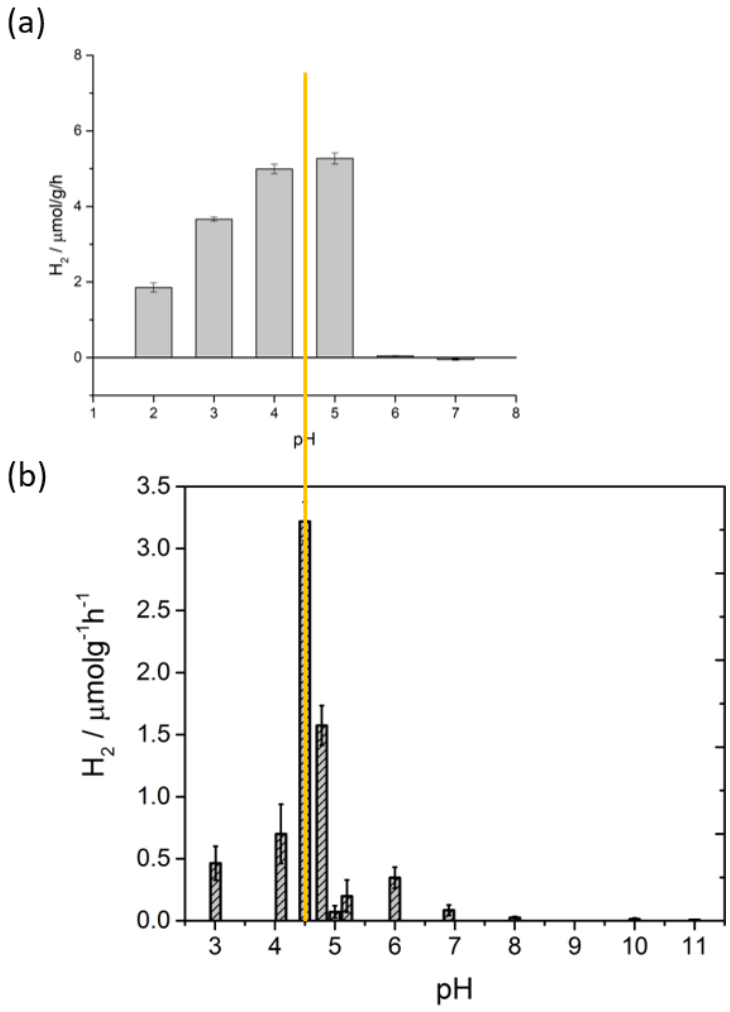

Figure 75. PBI-F/Pt NPs/20% Methanol solutions at different pHs irradiated for 4 hours and the amount of hydrogen measured via GC headspace analysis. (a) irradiated using solar simulator and (b) previous data from Chapter 2 irradiated using a Xe lamp. Orange line extrapolates the optimal pH 4.5 results from (b) to where it would show in (a) to show the results are correlated.

Photocatalysis of PBI-V showed a similar trend to PBI-F under the solar simulator conditions (Figure 76) although this was different from the data observed in preliminary experiments (Figure 61) where the optimal hydrogen evolution for PBI-V increased at lower pHs, rather than at pH 4-5. Although the light sources are different in the two experiments the differences

could be more aptly explained by considering the mixing; in the preliminary experiments the cuvettes were taller with a small stirrer bar driving the mixing from the bottom whereas under the solar simulator the vials were laid on their side and rolled evenly on a roller mixer. Studies have shown that photocatalysis is highly dependent on the environment and mixing parameters. In general, the high throughput experiments showed much smaller error bars which may be due to a more reproducible control over the mixing parameters.

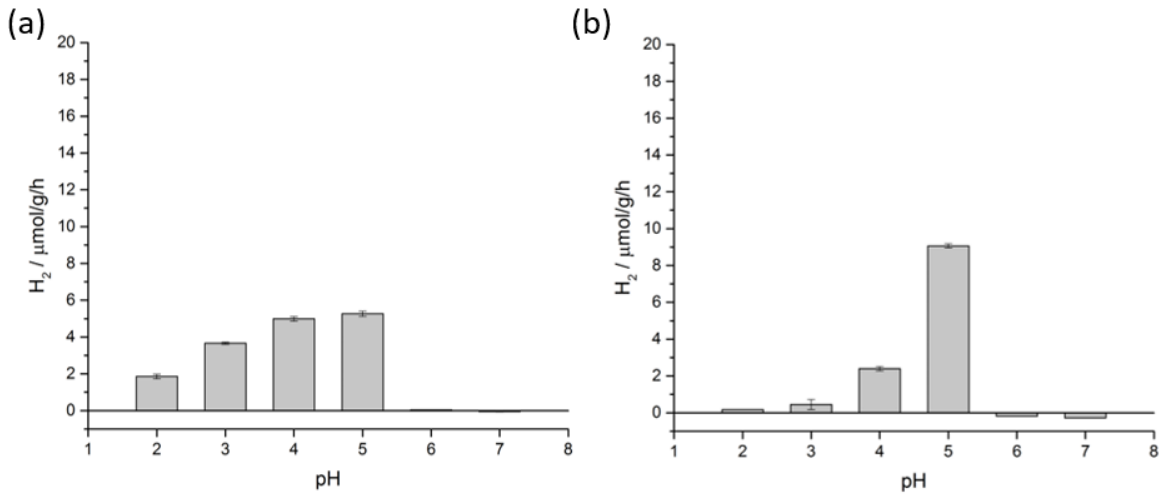

Figure 76. Rate of photocatalytic hydrogen evolution for (a) PBI-F and (b) PBI-V at 10 mg/mL from pH 7-2.

The concentration of PBI-F and PBI-V was reduced to 5 mg/mL with promising results (Figure 77). As mentioned previously, reducing the concentration of the photocatalyst could be expected to reduce the amount of hydrogen evolved by half, however in Figure 77 the amount of hydrogen produced stays roughly the same and so the rate of hydrogen per gram of photocatalyst is doubled. Here this is shown for both PBI-F and PBI-V showing that this trend is not confined to a singular PBI. This shows the importance of optimising the PBI concentration in these systems, as the 10 mg/mL solutions must not be utilising all the PBI molecules.

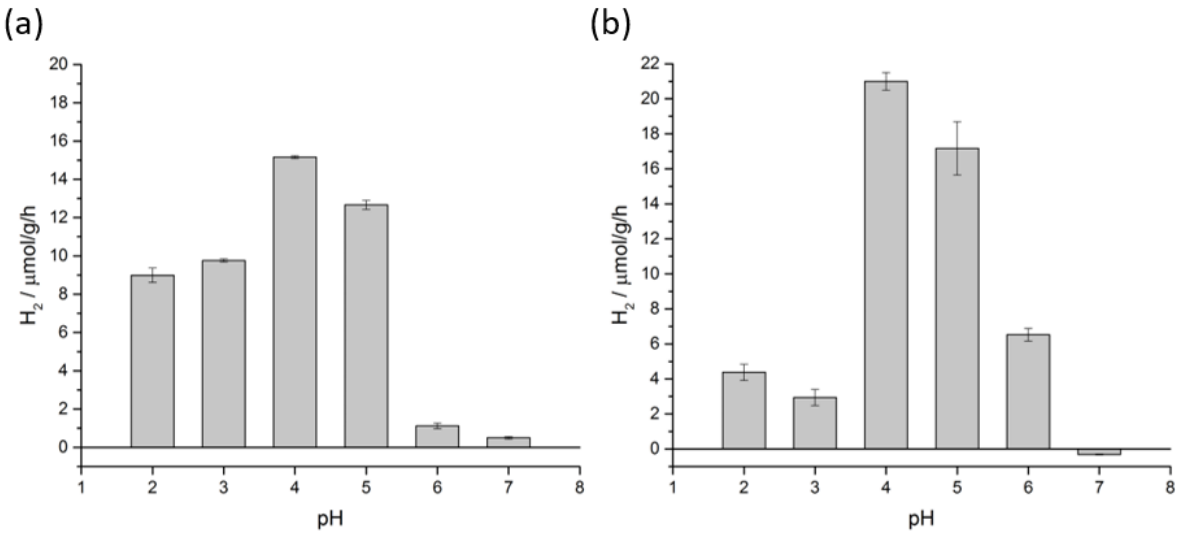

Figure 77. Rate of photocatalytic hydrogen evolution for (a) PBI-F and (b) PBI-V at 5 mg/mL from pH 7-2.

3.3.5. Effect of pH on the yield of the PBI radical anion

Spectroscopy studies show a strong relationship between yield of PBI radical with pH, where the maximum amount of radical anion formed is at pH 5 which is also the pH to yield the highest amount of H_2 (Figure 78). UV-Vis spectra were collected on 5 mg/mL PBI-V solutions before and after 5 minutes of UV irradiation (Figure 78) and the radical anion peaks were analysed to see if pH changes the amount of reduced species formed (Figure 79). The UV-Vis data shows a clear trend against pH where the most radical anion formed is at pH 5, shown with the largest increase in the absorbance bands at 720 and 980 nm. Although the band at 720 nm show a rising inflection in the absorbance to the main absorbance bands between 400-600 nm, the band at 980 nm is not influenced by this rising inflection and still confirms the same trend in the data from 720 nm.

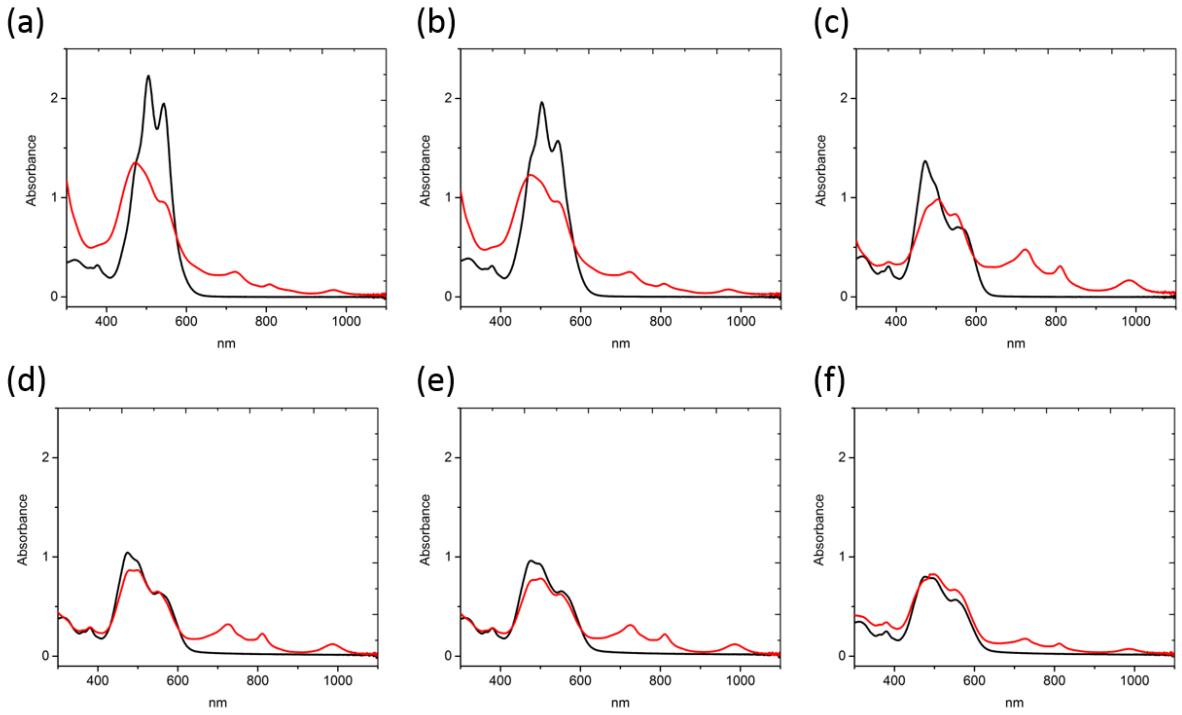

Figure 78. UV-Vis absorbance data of PBI-V/20 vol% methanol/Pt solutions at pH (a) 7, (b) 6, (c) 5, (d) 4, (e) 3 and (f) 2. Black lines are before irradiation and red lines are after 5 minutes of UV irradiation.

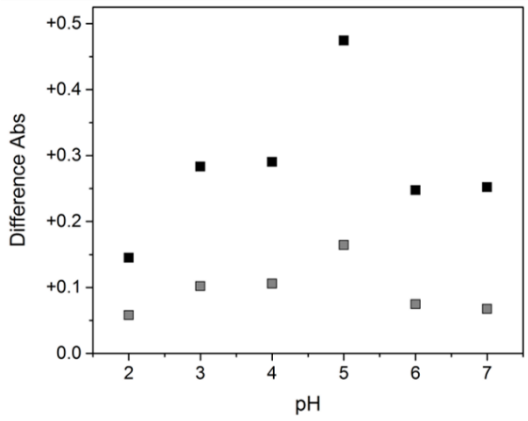

Figure 79. UV-Vis data of PBI-V/20 vol% methanol/Pt solutions using the raw data from Figure 78. The y-axis indicates the difference in the absorbance at 725 nm (black) and 980 nm (grey) after 5 minutes of UV irradiation.

Scan rate dependant cyclic voltammograms were collected to understand the reduction processes at these pH values and the current response was studied as a function of the square root of the scan rate Figure 80. All solutions show a linear relationship showing the electron transfer process is fast and the reaction is limited by diffusion.

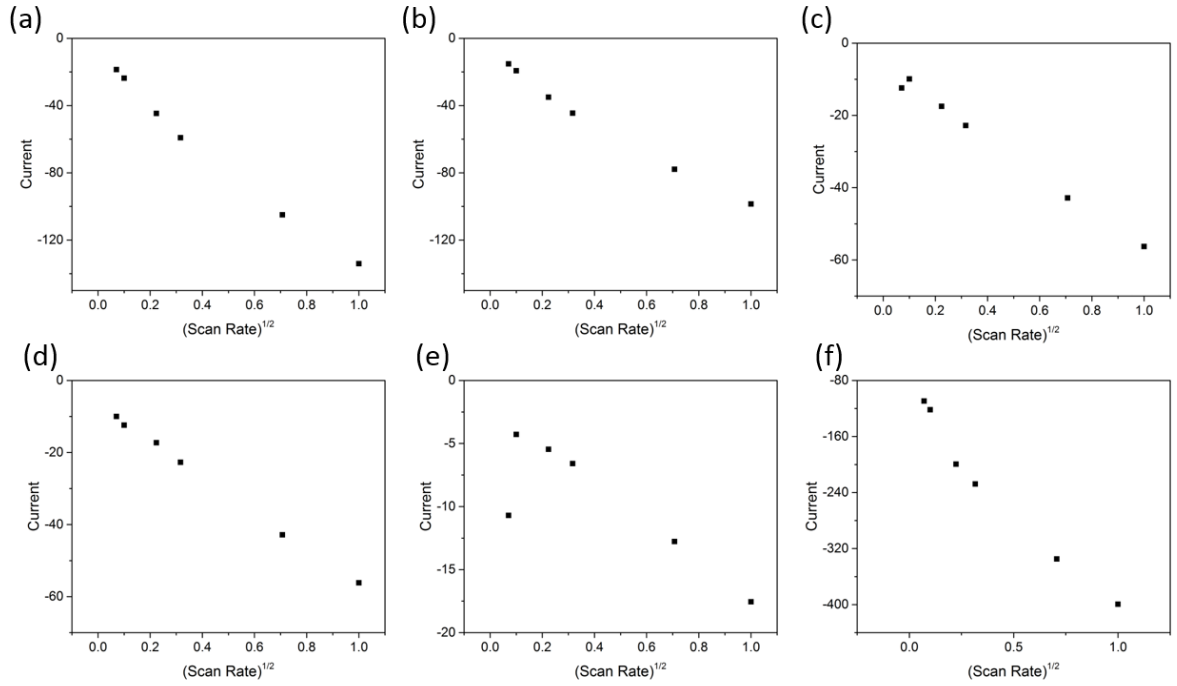

Figure 80. Scan rate dependence of the maximum reduction for solutions at pH (a) 7, (b) 6, (c) 5, (d) 4, (e) 3, (f) 2.

Dynamic thin-layer spectroelectrochemistry was used to analyse the growth of the reduced species by UV-Vis spectroscopy as the applied potential is slowly scanned to more negative potentials (Figure 81). Here, a CV was run at a slow scan rate of 0.05 V/s and the UV-Vis spectra collected at 620 nm, 720 nm, 810 nm and 984 nm. For pH's 6 and 7, 968 nm was measured instead of 984 nm. The sharp reduction at around 0 V is the reduction of the platinum nanoparticles in solution. The first reduction potential observed at -0.4 V (vs. Ag/AgCl) is not related to the formation of the radical anion or the colour change, however this reduction peak is regularly observed in solutions. Further control investigations need to be carried out to assign these peaks, such as applying a constant potential for a longer period of time and measuring the evolution of any related reduction peaks in the UV-Vis spectra. This peak may be due to the presence of a unique self-assembled species which hasn't been identified or could be the platinum nanoparticles in solution. The increase of the absorbances at 720, 810 and 984/968 nm, related to the radical anion, occur at -0.48 V (vs. Ag/AgCl). This is followed quickly by the increase in absorbance at 620 nm, related to the presence of the dianion. This data proves that although one broad peak is regularly observed in the CVs that this is in fact a two-electron process. Importantly, however, there seems to be no large difference in the CV traces between

the different pHs. As previously mentioned, the electrochemistry processes measured in solution may not be measuring the larger aggregates present and this may be why there is no visible difference when comparing these measurements.

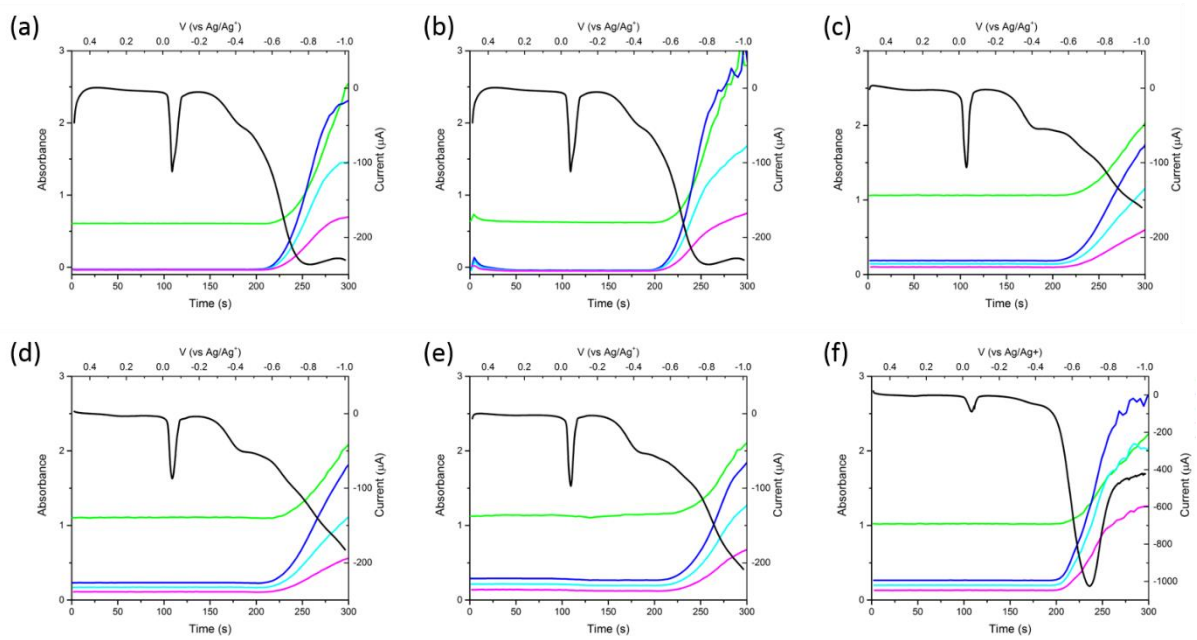

Figure 81. Dynamic thin-layer spectroelectrochemistry of PBI-V/Pt/20% methanol solutions at 5 mg/mL PBI at pH's (a) 7 (b) 6 (c) 5 (d) 4 (e) 3 and (f) 2. Black lines are the current response from the applied potential (top x, right y). Coloured lines indicate the absorbance over time, which correlates to the potential applied at that time. Wavelengths measured are 620 nm (green), 720 nm (dark blue), 810 nm (cyan) and 984 nm (pink). For pH's 6 and 7, 968 nm was measured instead of 984 nm.

3.3.6. Effect of solvent on molecular packing and H_2 evolution

The methanol concentration at each pH was also altered. It was hypothesised that changing the methanol concentration will have two effects; the solubility of the PBI will change which may further help realise a structure-activity relationship and the use of methanol as an electron donor may mean an excess of methanol is needed to efficiently drive the reactions.

UV-Vis spectra were obtained of PBI-F solutions at pH 6 with 0, 10, 20, 30, 40, 50, 60, 70, 80, 90 and 100 vol% methanol to help elucidate the effect of methanol on molecular packing (Figure 82). Photographs of dilute PBI solution with different concentrations of methanol also result in different colours showing the optical properties and assemblies seem to differ between

solutions (Figure 83). The absorbance bands broadened upon increasing methanol concentration indicating an increase in molecular packing within the solutions. An additional absorbance band at 630 nm became increasingly strong upon increasing methanol concentrations. As aggregates were present in the solution when methanol was present these were then centrifuged out and UV-Vis spectra were collected on the supernatant. A clear difference was observed, where the remaining solution had sharp bands and no band at 630 nm. Methanol introduces a solvent-trigger aggregation which may affect the charge transport properties of the material.

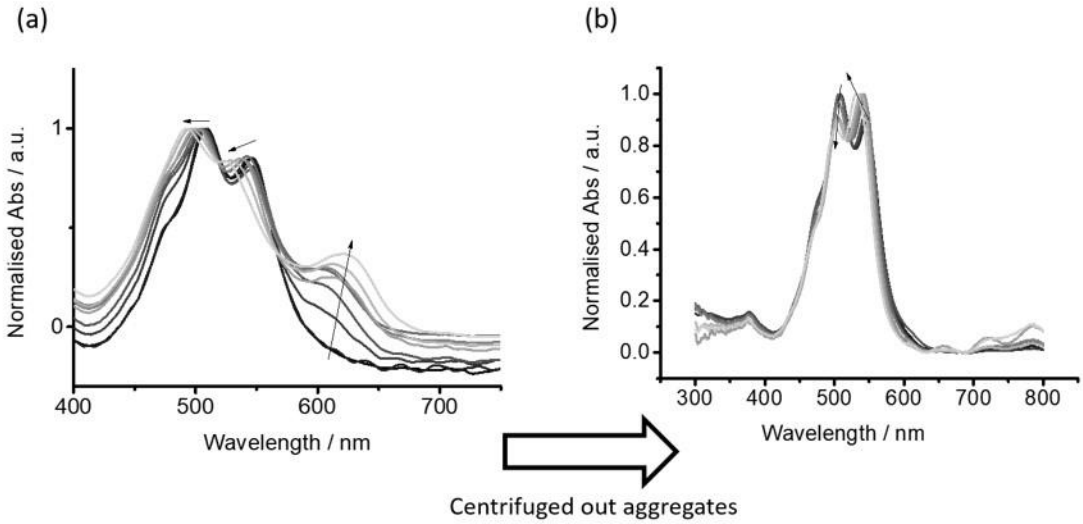

Figure 82. UV-Vis spectra of PBI-F and methanol solutions containing 0, 10, 20, 30, 40 50, 60, 70 80, 90 and 100% methanol (lines, black to grey). (a) solutions containing aggregates and (b) the supernatant of solutions after centrifuging out aggregates. Arrows indicate the changing of peaks upon increasing methanol concentration.

Figure 83. Solutions of PBI-F 0.1 mg/mL solutions at high pH with (left to right) 0, 20, 40, 60, 80 and 100% methanol$_{(aq)}$.

It can be elucidated from Figure 84-Figure **87** that changing methanol concentration in solution has a minimal effect on the amount of hydrogen evolved from irradiation when the pH is set at pH 4. It is assumed that this is the most stable pH where self-assembly is the strongest. Deviations from this pH result in reduced activity, as expected, but the sensitivity to methanol concentration also increases; this could be a strong indication that the most stable PBI assemblies form at a specific pH which can help give increased conductivity and photocatalytic activity. If indeed the PBI aggregates are required for the higher levels of hydrogen evolution, then the most stable aggregates will remain in solution providing a higher concentration of active species.

As will be discussed in Chapter 4 and is the discussion of various published literature,[27] the addition of an anti-solvent to prepare gels results in a spherical-type aggregation. The use of methanol in the PBI solutions may indeed have a similar effect where spherical-type aggregates are formed. Although not studied in this work, this work would benefit from structural analysis, such as the in-depth analysis in Chapter 2, to help understand the difference in structures between solutions which may reveal an important comparison of activity between spherical and fibre assemblies.

Interestingly, at pH 6, where less self-assembly is present as it is above the second pK_a, increasing the methanol concentration increases the photocatalytic activity. As methanol reduces the solubility of PBI the increased activity could be related to the increase in self-assembled catalytic structures. At pH lower than 4, increasing the methanol concentration has a detrimental effect on the hydrogen evolved. As assemblies at the low pH are already formed from the pH-switch, increase the concentration of anti-solvent will affect the structures formed and decrease the photocatalytic activity. In conclusion, when comparing self-assembly between a solvent switch and a pH-switch, the pH-switch provides stable and more photocatalytically active structures. If the methanol addition indeed promotes spherical assembly in these solutions, then the formation of these can increase photocatalytic performance of non-structured solutions indicating self-assembly is important. However, when comparing between the possible spherical micelles and fibres, the fibres are much more active as photocatalysts.

The summary of each methanol concentration for each pH is showed in the contour plots in Figure 88 which show that the PBI-V at 5 mg/mL shows the highest amount of hydrogen but with a smaller optimal pH window compared to the PBI-F.

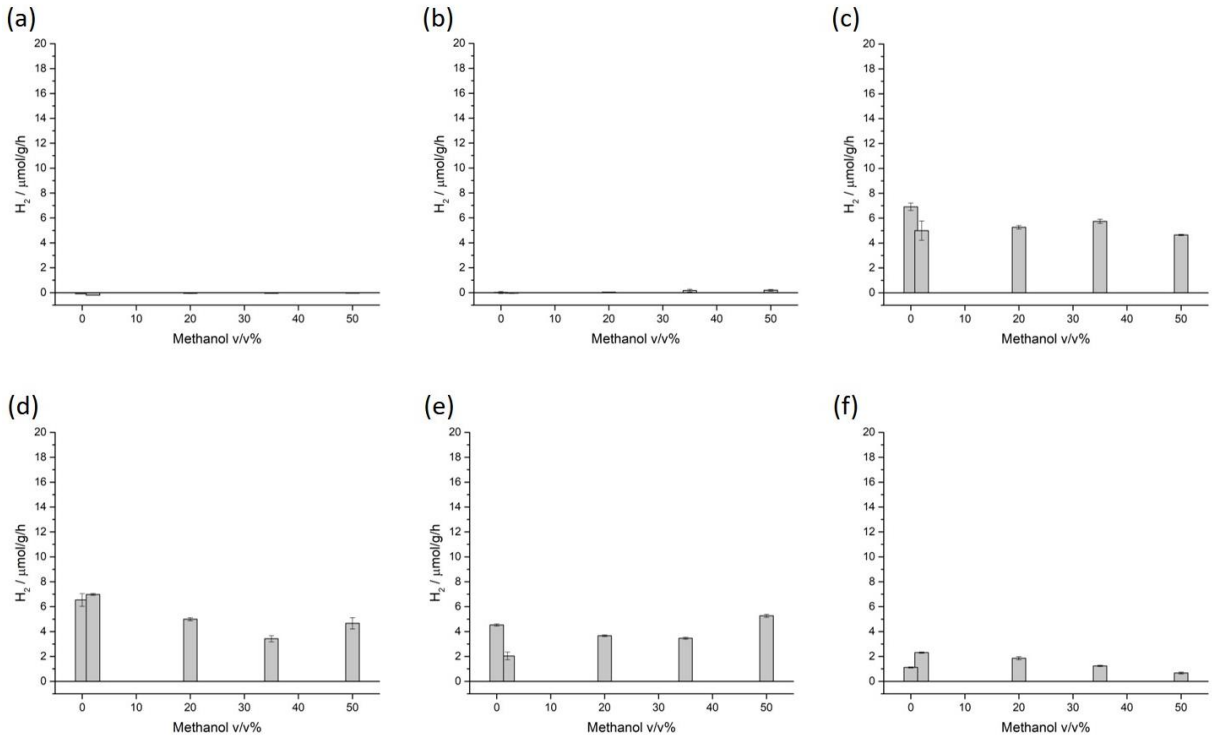

Figure 84. Hydrogen evolution of PBI-F (10 mg/mL) and Pt solutions with various methanol concentrations. The pH of solutions were altered using HCl to a final pH of (a) 7, (b) 6, (c) 5, (d) 4, (e) 3 and (f) 2.

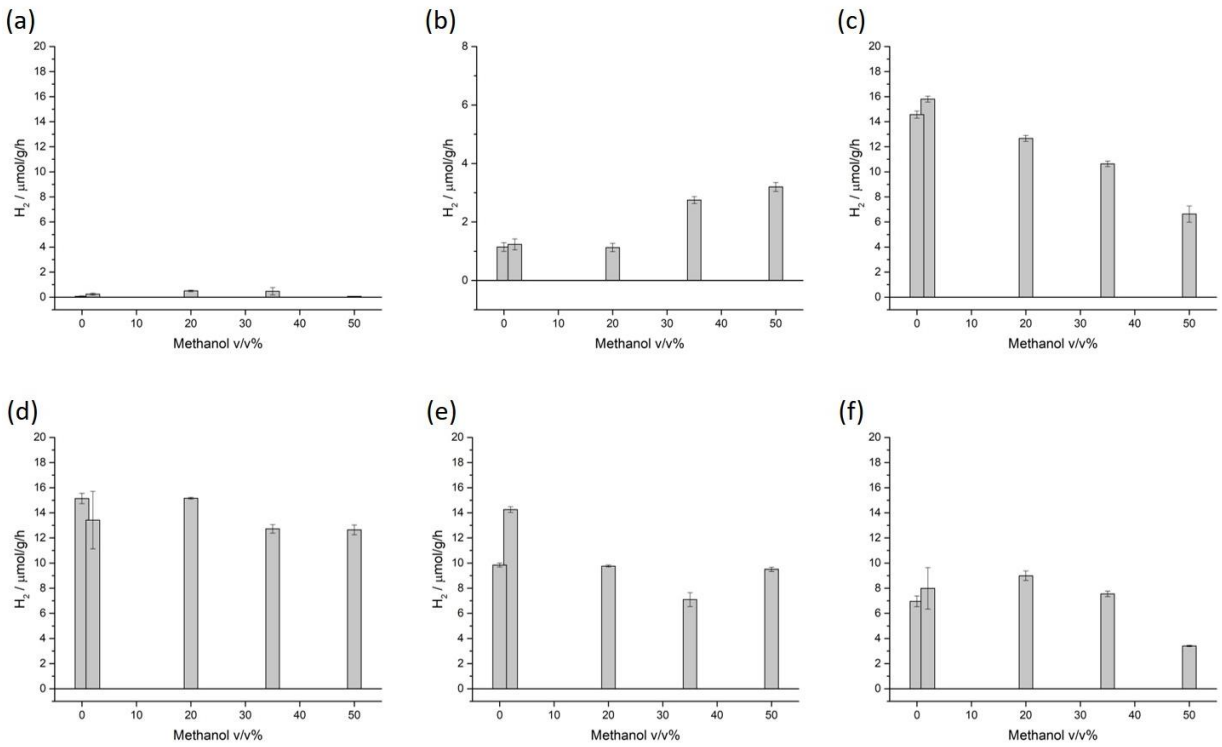

Figure 85. Hydrogen evolution of PBI-F (10 mg/mL) and Pt solutions with various methanol concentrations. The pH of solutions were altered using HCl to a final pH of (a) 7, (b) 6, (c) 5, (d) 4, (e) 3 and (f) 2.

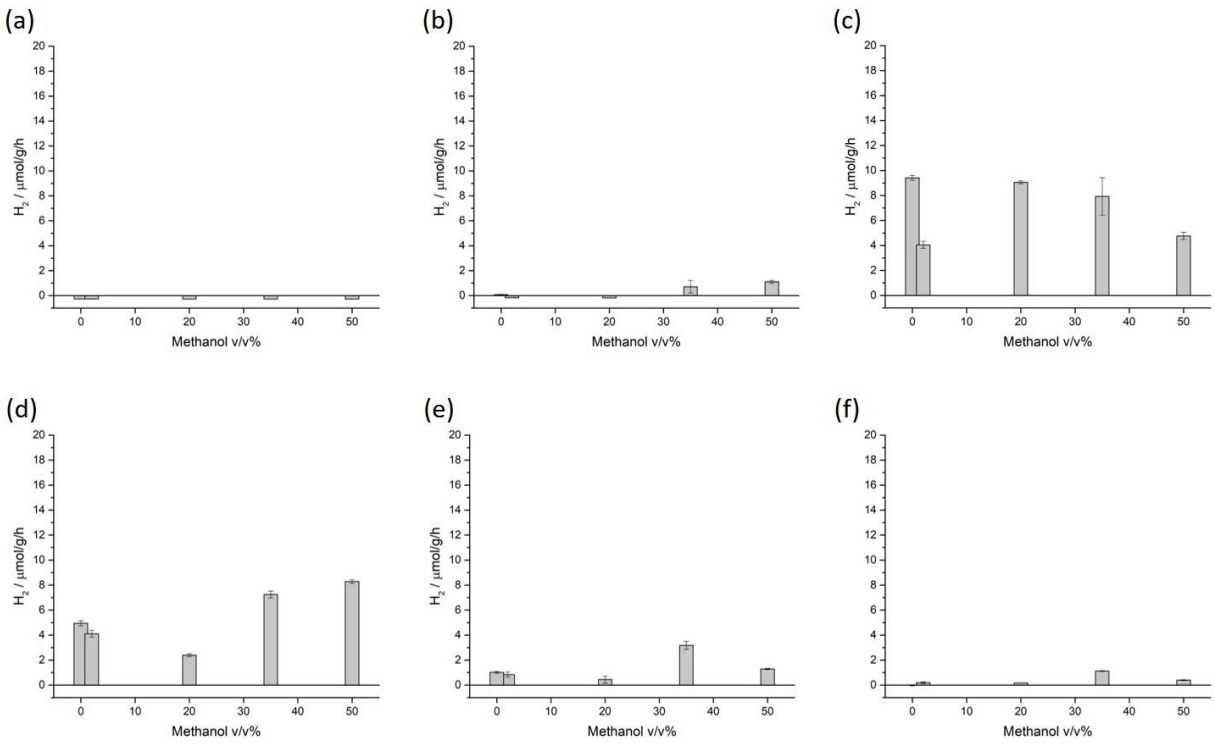

Figure 86. Hydrogen evolution of PBI-V (10 mg/mL) and Pt solutions with various methanol concentrations. The pH of solutions were altered using HCl to a final pH of (a) 7, (b) 6, (c) 5, (d) 4, (e) 3 and (f) 2.

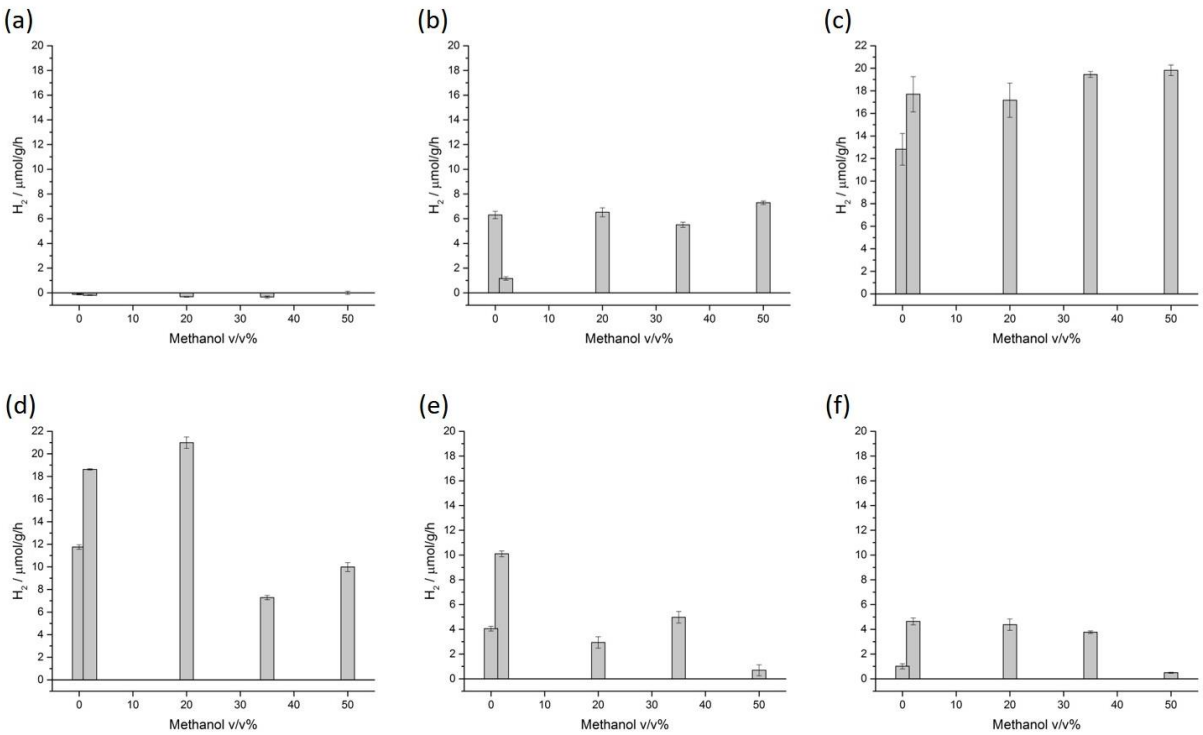

Figure 87. Hydrogen evolution of PBI-F (5 mg/mL) and Pt solutions with various methanol concentrations. The pH of solutions were altered using HCl to a final pH of (a) 7, (b) 6, (c) 5, (d) 4, (e) 3 and (f) 2.

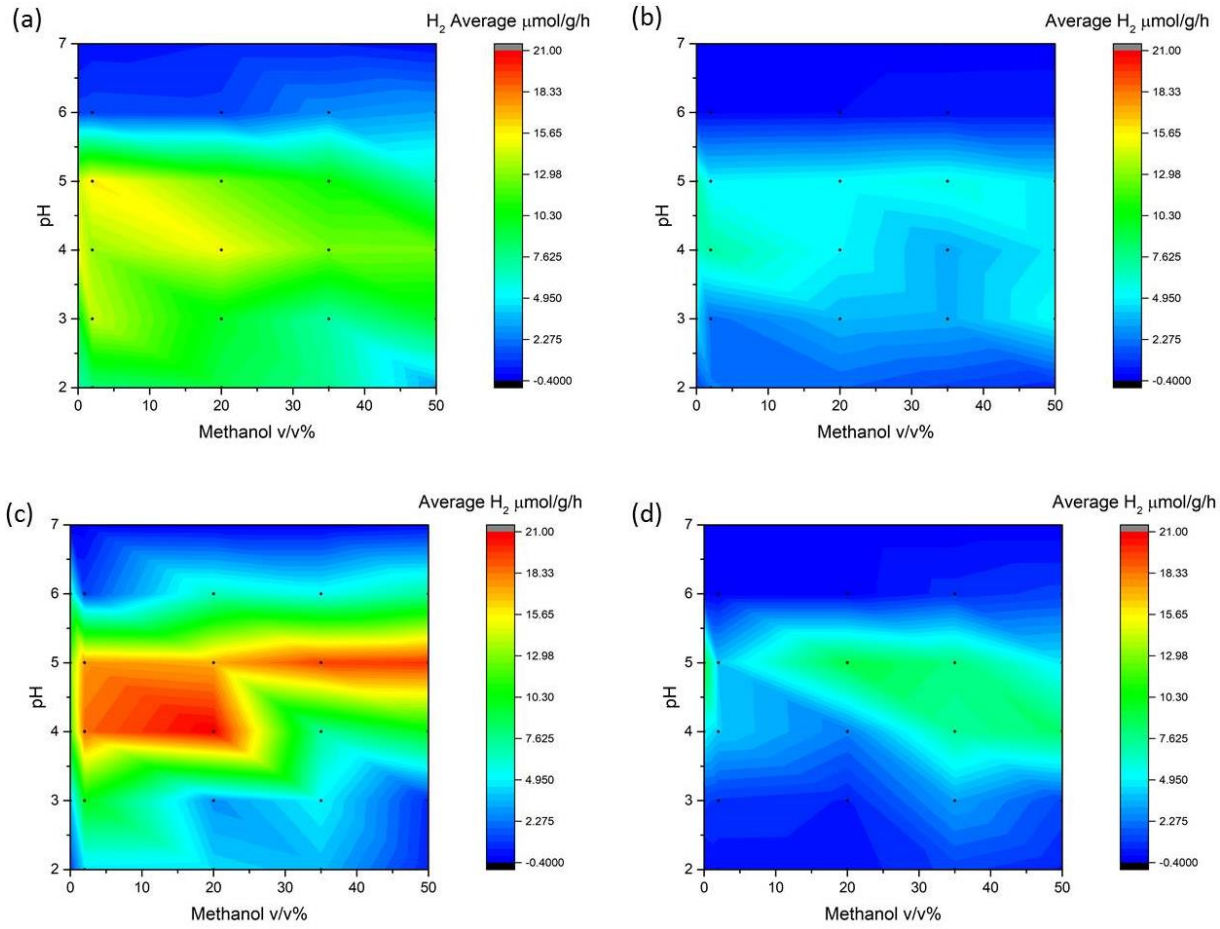

Figure 88. Summary contour colour charts showing the average rate of hydrogen evolution for (a) PBI-F 5 mg/mgL(b) PBI-F 10 mg/mL (c) PBI-V 5 mg/mL (d) PBI-V 10 mg/mL a different pHs and methanol concentrations. All solutions contain 1 mol% PVP-Pt NPs.

3.3.7. Effect of concentration of PBI derivatives on photocatalytic hydrogen evolution utilizing high throughput instrumentation

The concentration studies were expanded to a range of PBIs; here PBI-F, L, V and Y were tested (Figure 89-Figure **92**). Similar results comparable to those in Figure 72 were found with the overall activity for each gelator, which also agrees with the preliminary studies in Figure 61. When comparing the concentrations of perylene as a photocatalyst one must consider both the amount of hydrogen produced but also understand the amount of perylene needed to produce that amount. For example, if a 0.1 mg/mL produced the same amount of hydrogen as a 1 mg/mL solution then the 0.1 mg/mL solution is more efficient. The maximum amount of H_2 was produced using PBI-F, producing 1.1 µmol H_2 in 4 hours. The least amount of hydrogen produced was from PBI-Y. PBI-V proved to be active at very low concentrations, 0.3 µmols of H_2 was produced at 0.1 mg/mL giving rise to a much-improved rate of 150 µmol/g/h, which

is measured per gram of photocatalyst. So, although PBI-F has provided the most hydrogen, PBI-V is able to work efficiently at low concentrations.

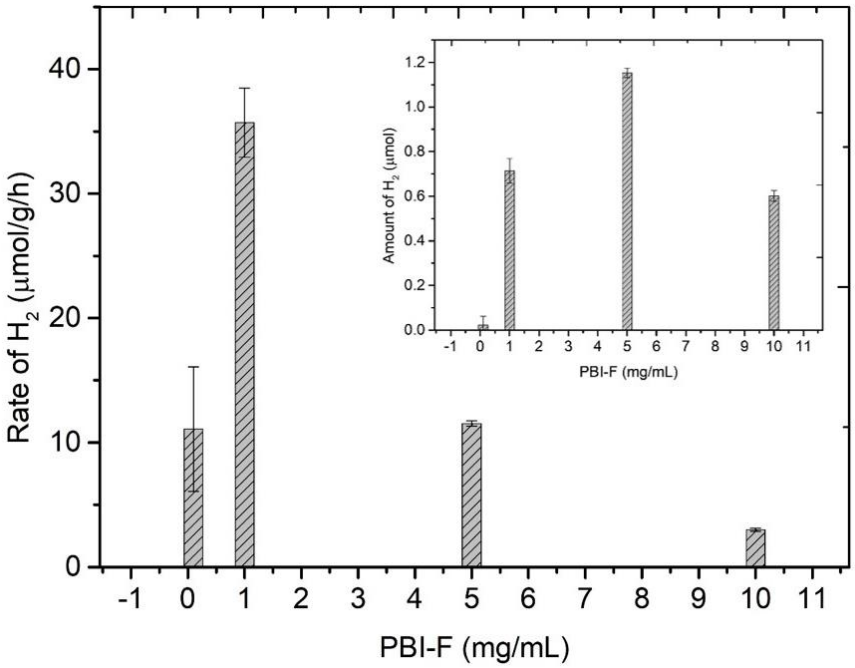

Figure 89. Rate of photocatalytic hydrogen evolution for PBI-F/20% methanol/Pt NPs solutions at different PBI concentrations, irradiated for 4 hours using the high throughput equipment and solar simulator. Results are shown for 10, 5, 1 and 0.1 mg/mL. Inset: μmoles of hydrogen produced.

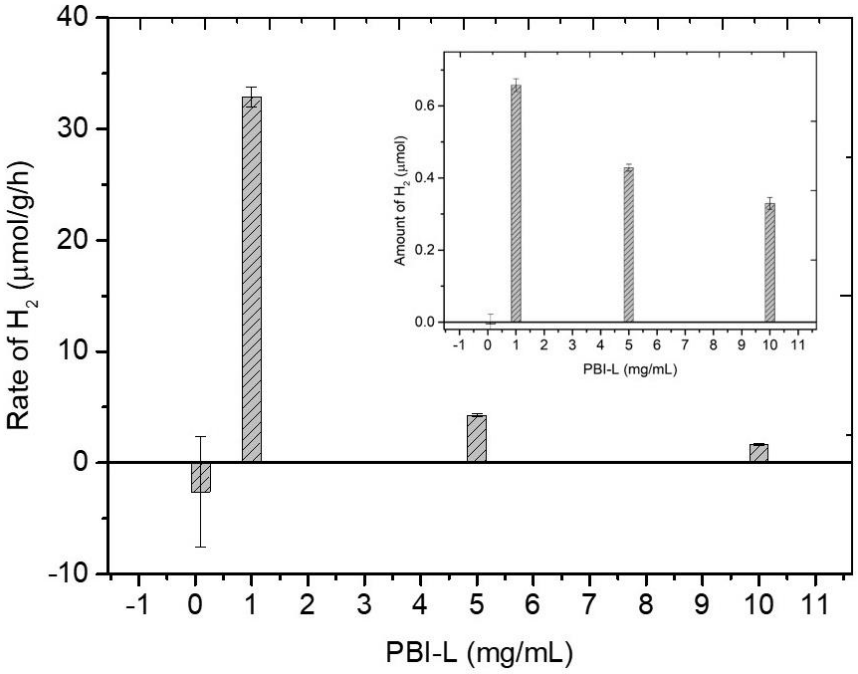

Figure 90. Rate of photocatalytic hydrogen evolution for PBI-L/20% methanol/Pt NPs solutions at different PBI concentrations, irradiated for 4 hours using the high throughput equipment and solar simulator. Results are shown for 10, 5, 1 and 0.1 mg/mL. Inset: μmoles of hydrogen produced.

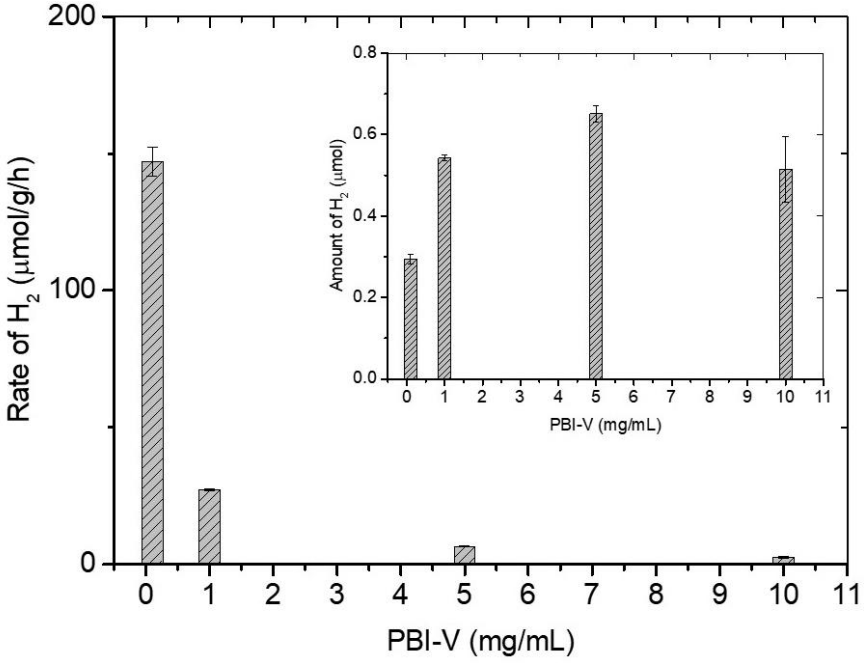

Figure 91. Rate of photocatalytic hydrogen evolution for PBI-V/20% methanol/Pt NPs solutions at different PBI concentrations, irradiated for 4 hours using the high throughput equipment and solar simulator. Results are shown for 10, 5, 1 and 0.1 mg/mL. Inset: μmoles of hydrogen produced.

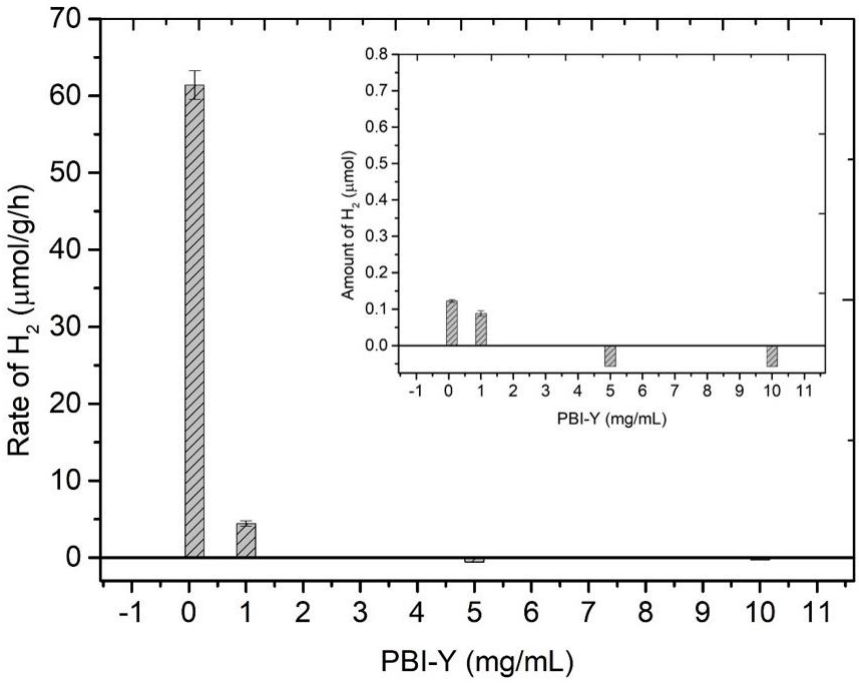

Figure 92. Rate of photocatalytic hydrogen evolution for PBI-Y/20% methanol/Pt NPs solutions at different PBI concentrations, irradiated for 4 hours using the high throughput equipment and solar simulator. Results are shown for 10, 5, 1 and 0.1 mg/mL. Inset: μmoles of hydrogen produced.

As stated above, there are several properties which are altered when only changing the photocatalyst concentration. An important factor to consider further is the concentration of the platinum co-catalyst. It is likely there is a subtle relationship describing the interactions between the PBI fibres and the platinum co-catalyst, if the interactions are optimised further than this may result in increased electron transfer from the PBI to the catalyst, reducing electron recombination mechanisms. In some cases, excess Pt co-catalyst has been shown to cause a plateau in activity for photocatalytic hydrogen evolution.[28]

3.3.8. Effect of the ratio of PBI:Pt on photocatalytic hydrogen evolution

When only the PBI concentration is decreased, the ratio of PBI:Pt is increased. In Figure 93-Figure 96 the Pt concentration was altered for different concentrations of PBI-F, L, V and Y and used in the high throughput photocatalysis setup. For ease of comparison the amount of Pt used has been normalised; the amount of platinum added into a 10 mg/mL PBI concentration has been normalised to 1, this relates to 1 mol % Pt at this PBI concentration. In Figure 93-Figure 96 an amount of '1' was tested for each concentration along with 1, 0.1, 0.01 mol% Pt,

the samples tested are summarized in Table 7. Inaccuracies in the weighing of small amounts of PBI rendered the experiments for 0.01 mg/mL PBI invalid and data are not shown.

Table 7. PBI and Pt concentrations used in high throughput photocatalysis for PBI-F, PBI-L, PBI-V and PBI-Y. All samples contain 20 v/v% methanol.

PBI concentration / mg/mL	Pt NPs / (a.u.) Normalised	Pt NPs / mol% Pt
10	1	1
10	0.1	0.1
10	0.01	0.01
5	1	2
5	0.5	1
5	0.05	0.1
5	0.005	0.01
1	1	10
1	0.1	1
1	0.01	0.1
1	0.001	0.01
0.1	1	100
0.1	0.01	1
0.1	0.001	0.1
0.1	0.0001	0.01
0.01	1	1000
0.01	0.001	1
0.01	0.0001	0.1
0.01	0.00001	0.01

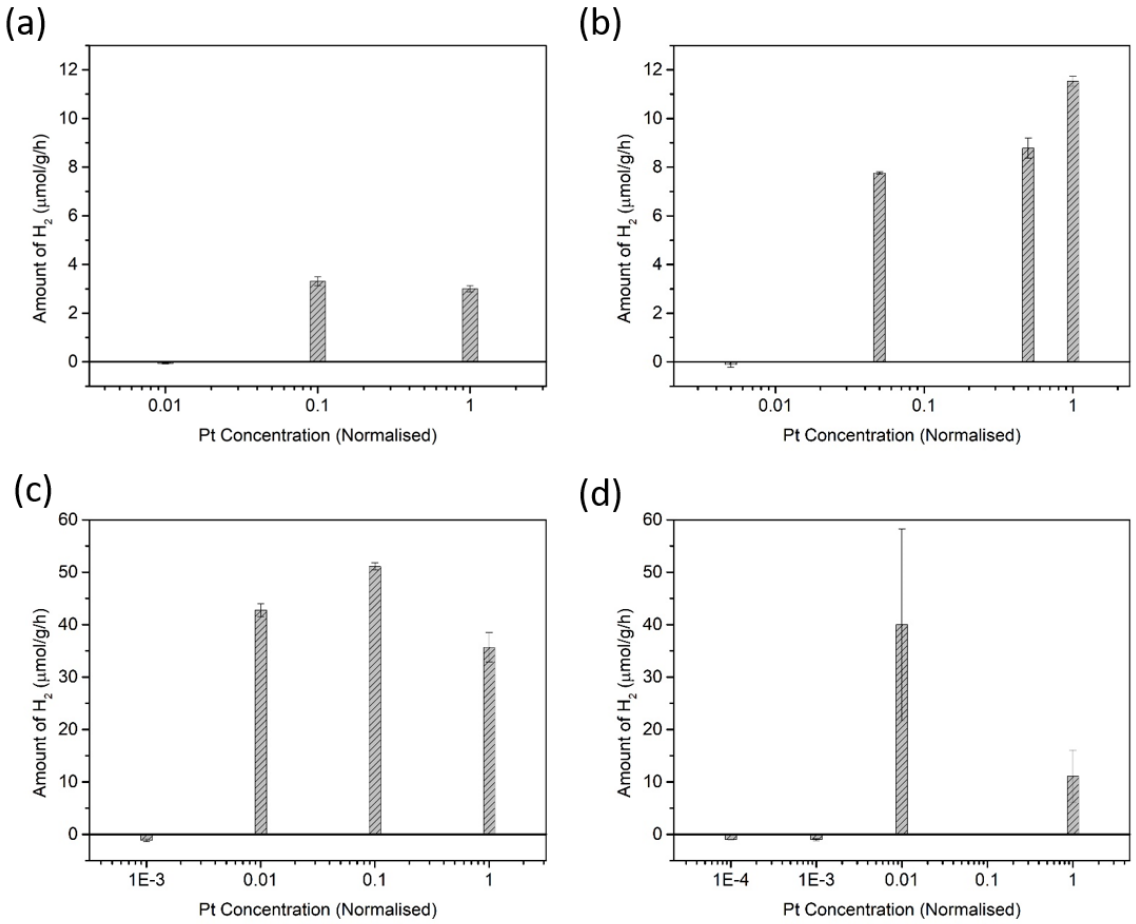

Figure 93. Rate of hydrogen evolution from high throughput photocatalytic experiments using PBI-F/20% methanol/PVP-Pt nanoparticles with varying amounts of Pt. PBI concentration is varied; (a) 10 mg/mL, (b) 5 mg/mL, (c) 1 mg/mL, (d) 0.1 mg/mL. The concentration of Pt is normalised where 1 = 1 mol% Pt at 10 mg/mL PBI.

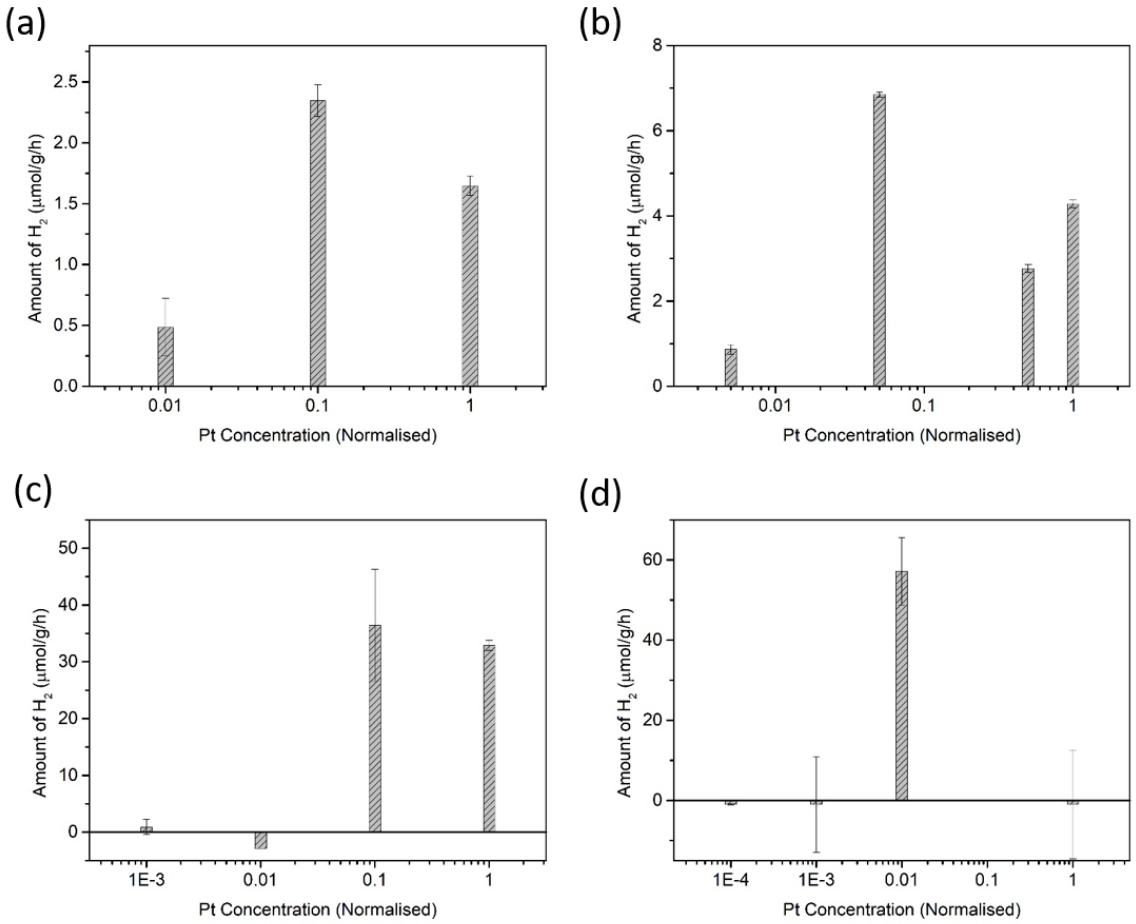

Figure 94. Rate of hydrogen evolution from high throughput photocatalytic experiments using PBI-L/20% methanol/PVP-Pt nanoparticles with varying amounts of Pt. The concentration is normalised where 1 = 1 mol% Pt at 10 mg/mL PBI. PBI concentration is varied; (a) 10 mg/mL, (b) 5 mg/mL, (c) 1 mg/mL, (d) 0.1 mg/mL. The concentration of Pt is normalised where 1 = 1 mol% Pt at 10 mg/mL PBI.

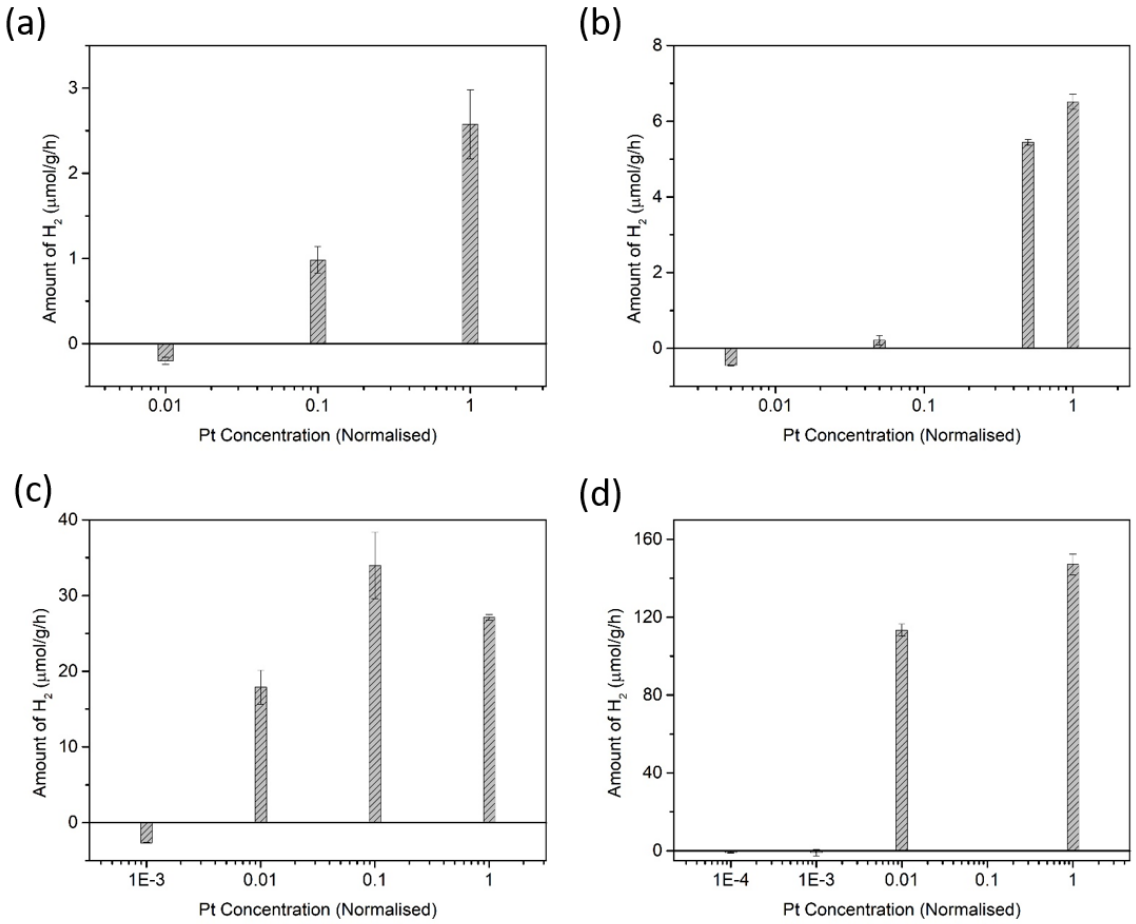

Figure 95. Rate of hydrogen evolution from high throughput photocatalytic experiments using PBI-V/20% methanol/PVP-Pt nanoparticles with varying amounts of Pt. The concentration is normalised where 1 = 1 mol% Pt at 10 mg/mL PBI. PBI concentration is varied; (a) 10 mg/mL, (b) 5 mg/mL, (c) 1 mg/mL, (d) 0.1 mg/mL. The concentration of Pt is normalised where 1 = 1 mol% Pt at 10 mg/mL PBI.

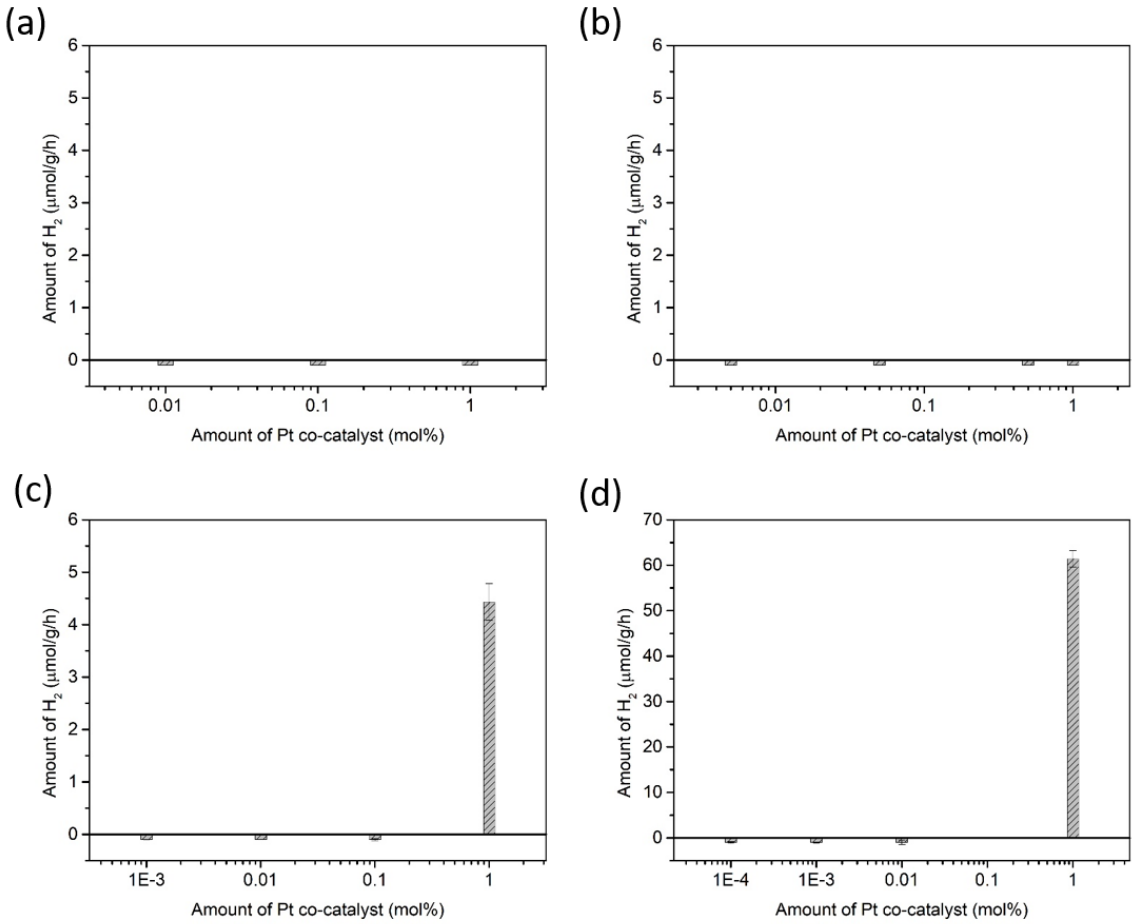

Figure 96. Rate of hydrogen evolution from high throughput photocatalytic experiments using PBI-Y/20% methanol/PVP-Pt nanoparticles with varying amounts of Pt. The concentration is normalised where 1 = 1 mol% Pt at 10 mg/mL PBI. PBI concentration is varied; (a) 10 mg/mL, (b) 5 mg/mL, (c) 1 mg/mL, (d) 0.1 mg/mL. The concentration of Pt is normalised where 1 = 1 mol% Pt at 10 mg/mL PBI.

Approximately 1 mol% Pt is needed for the optimal hydrogen evolution to occur. Modifying the Pt concentration away from 1 mol%, either higher or lower, results in a reduced rate of photocatalytic hydrogen production.

3.4. Conclusions

In summary, high throughput instrumentation has allowed a number of different parameters to be studied in the PBI-based photocatalytic system which would otherwise have not been able to be tested due to the time-consuming nature of the experiments. Chapter 2 observed that pH is critical for the activity of PBI-F solutions. Here, a similar pH trend has been observed across eight different amino acid substituents. The trend across the PBIs is similar with slightly different optimal pHs, the changes may be a result of the differing sterics and hydrophobicity between the groups which affects the packing arrangements of the molecules, depending on the charge in the environment. The overall activity between the PBIs also varies greatly; published data already shows that the packing arrangements affects the amount of reduced species being formed.[5] The percentage of radical anion produced also decreases at high photocatalyst concentrations which coincides with a decrease in photocatalytic hydrogen production. Increasing the PBI concentration results in a linear increase of radical anion formation until the concentration is raised too high where solutions become too opaque and viscous which decreases light penetration, increases electron recombination mechanisms and reduces the efficiency of photocatalytic hydrogen evolution. An investigation into changing the solvent mixture revealed that the addition of methanol results in aggregation behaviour at high pH. At the pHs which show low photocatalytic activity, where there is a low concentration of aggregates, the solvent-induced aggregation results in a turn on in photocatalytic activity. The formation of fibre aggregates through a pH switch, as was measured in Chapter 2, results in a turn on in photocatalytic activity compared to worm-like micelles present at high pH. However, a more thorough structure analysis of the solvent switch may reveal the presence of active but less optimal spherical aggregates. The ratio of photocatalyst PBI to co-catalyst Pt can be optimised and should be investigated whenever a component in the system is changed. For this system, 1 mol % Pt was optimal.

The optimised rate of activity from the LED system is greater than the solar simulator system, where ~200 μmol/g/h of PBI-V at 1 mg/mL was observed under 4 hours of strong UV irradiation compared to ~33 μmol/g/h for the same sample under solar simulator irradiation. This indicates the importance of the light source in cross-comparison between experiments. Importantly, this work shows that some samples can be correlated across different light sources. It is common that published results use different light sources. Unless the exact spectra and sample environments can be matched then the absolute value of the photocatalysis results

cannot be compared. However, in this instance the internal trends within the dataset can be directly correlated and understood.

3.5. Experimental

^{1}H-NMR Analysis for PBI gelators

Acknowledgements for analysis: Dr Bart Dietrich, University of Glasgow.

PBI-A

δ_H (400 MHz, DMSO-d_6) 8.27-8.16 (8H, m, $\underline{H}_{Ar}$), 5.58 (2H, q, *J* 6.94, C$\underline{H}^{*}$), 1.67 (6H, d, *J* 6.92, C$\underline{H}_3$).

PBI-F

δ_H (400 MHz, DMSO-d_6) 13.02 (2H, br, COO$\underline{H}$), 8.69 (2H, d, *J* 7.56, $\underline{H}_{Ar}$), 8.43 (2H, d, *J* 7.04, $\underline{H}_{Ar}$), 7.21 (4H, d, *J* 7.23, $\underline{H}_{Ar}$), 7.14 (4H, t, *J* 7.50, $\underline{H}_{Ar}$), 7.08-7.04 (2H, m, $\underline{H}_{Ar}$), 5.93 (2H, dd, *J* 9.90, 5.78, C$\underline{H}^{*}$), 3.61 (4H, dd, *J* 14.14, 5.10, PhC$\underline{H}_2$).

PBI-L

δ_H (400 MHz, DMSO-d_6) 12.88 (2H, br, COO$\underline{H}$), 8.75 (4H, m, $\underline{H}_{Ar}$), 8.49-8.44 (4H, m, $\underline{H}_{Ar}$), 5.61 (2H, dd, *J* 8.66, 5.10, C$\underline{H}^{*}$), 2.17-2.04 (4H, m, CH*C$\underline{H}_2$), 1.67-1.57 (2H, m, C$\underline{H}$(CH$_3$)$_2$), 1.01-0.93 (12H, m, CH(C$\underline{H}_3$)$_2$).

PBI-V

δ_H (400 MHz, DMSO-d_6) 12.80 (2H, br, COO$\underline{H}$), 8.92 (4H, d, *J* 8.16, $\underline{H}_{Ar}$), 8.60 (4H, d, *J* 7.96, $\underline{H}_{Ar}$), 5.20 (2H, d, *J* 9.24, C$\underline{H}^{*}$), 2.77-2.68 (2H, m, C$\underline{H}$(CH$_3$)$_2$), 1.26 (6H, d, *J* 6.52, CH(C$\underline{H}_3$)$_2$), 0.77 (6H, d, *J* 6.88, CH(C$\underline{H}_3$)$_2$).

PBI-Y

δ_H (400 MHz, DMSO-d_6) 13.06 (2H, br, COO$\underline{H}$), 9.07 (2H, d, *J* 1.92, O$\underline{H}$), 8.40-8.35 (8H, m, $\underline{H}_{Ar}$), 7.02 (4H, d, *J* 8.32, $\underline{H}_{Ar}$), 6.55 (4H, d, *J* 8.44, $\underline{H}_{Ar}$), 5.90 (2H, dd, *J* 9.98, 5.50, C$\underline{H}^{*}$), 3.58-3.46 (4H, m, CH*C$\underline{H}_2$).

Preparation of LMWG solutions

Solutions of PBI-X were prepared by adding H_2O, 2 molar equivalents of 0.1M NaOH and stirred until the PBI is dissolved. The methanol and PVP-Pt NPs were then added and the pH regulated by adding 0.1M HCl dropwise while stirring. PVP-Pt NPs were prepared as described in Chapter 2. The pH was measured using a Hanna pH probe as described in Chapter 2.

LED Photocatalysis

Photocatalytic experiments were performed using LedEngin UV LEDs with an irradiance of 90 mW cm^{-2} at 365 nm (Figure 97). The irradiance at the samples was measured using a Thor Labs Power Meter with a Si Photodiode sensor. Photocatalytic solutions were stirred in a 1 cm pathlength quartz cuvette with a 25 mL headspace, sealed with a rubber septum. Solutions were pre-purged for 30 minutes with Argon then irradiated for 4 hours. H_2 production was quantified using gas chromatography, headspace analysis was performed by taking 500 μL of gas from the headspace using a gas-tight syringe and transferring to a Shimadzu GC-2010 Plus, employing a barrier discharge ionisation detector (BID-2010 Plus). Daily injections of a known gas composition were performed daily for calibration purposes.

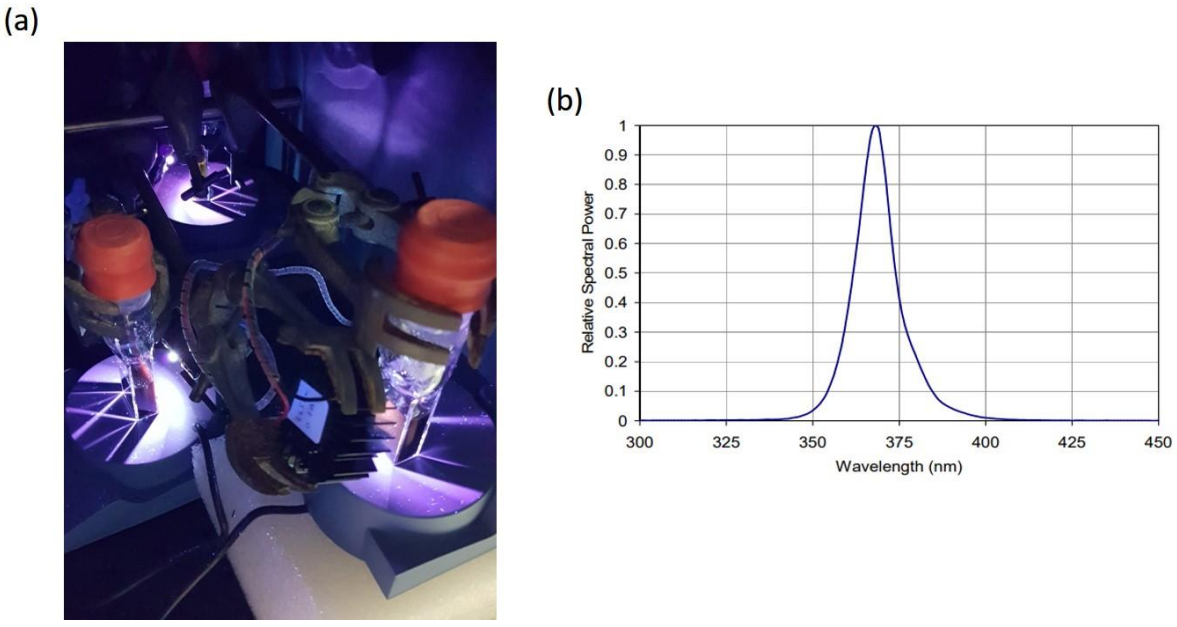

Figure 97. (a) Photograph of the LED photocatalysis setup where three cuvettes are stood on stirrer plates and irradiated with UV LEDs. (b) UV-Vis spectrum of the UV LEDs.

High Throughput Photocatalysis

For high throughput photocatalysts, 48 samples of 5 mL photocatalytic solutions were prepared in 14 mL glass GC vials and purged for 4 hours under N_2 using a ChemSpeed system (Figure 98a). The samples were then placed on a roller mixer and illuminated with a 300 W Newport Xe light-source (Model: 6258, Ozone free) for 4 hours (Figure 98b). Headspace gas analysis was measured automatically using a Bruker 450-GC gas chromatograph (Figure 98c). Hydrogen was detected with a thermal conductivity detector and calibrated with a standard of known concentration.

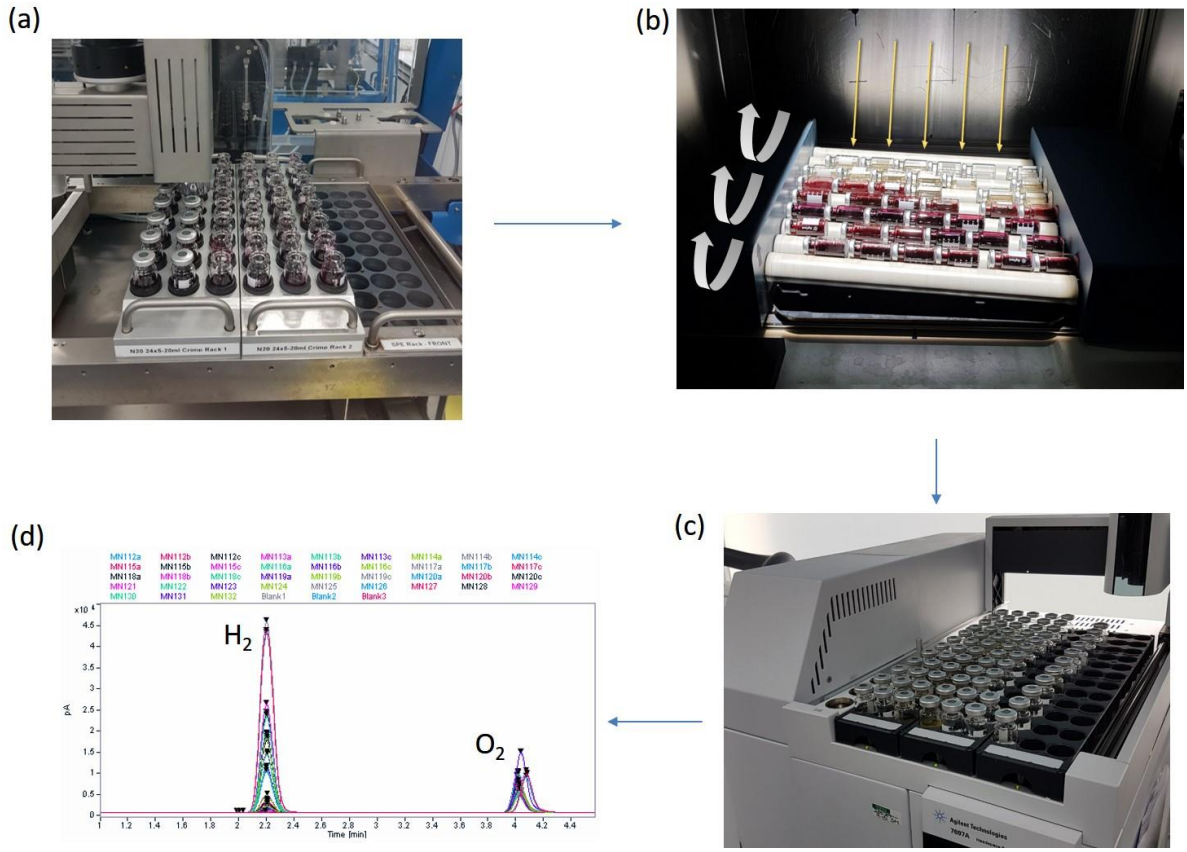

Figure 98. (a) Nitrogen purging of the headspace and automated capping of 48 samples, (b) samples rotated on a roller mixer while being irradiated from a solar simulator, (c) headspace analysis using gas chromatography and an auto sampler, (d) chromatograph showing hydrogen concentration.

Cyclic Voltammetry

CVs were collected using a three-electrode system and a Dropsens potentiostat with a glassy carbon working electrode, a Pt wire counter electrode and an Ag/AgCl reference electrode. The supporting electrolyte was 0.1 M NaCl in water and 0.1 M tetrabutylammonium

hexafluoroborate (TBAHFB) in DMF. The measurements were scanned from 1.0 V to – 1.0 V, firstly 5 times at a scan rate of 0.5 V/s and a step value of 0.01 V, then 5 scans were collected at 0.05 V/s with a step of 0.005 V. The broadness and resolution of the CVs sometimes changed between scans (assumed to be due to the high viscosity of solutions) although the absolute response and potential of the peaks did not change. Therefore, the clearest scan from the 5 scans at 0.05 V/s was selected for analysis.

For calibration, the $E_{1/2}$ for the ferrocene-ferrocenium redox couple (Fc/Fc^+) in DMF was measured at 0.479 V vs. Ag/AgCl. Although not used for calibration, the $E_{1/2}$ for the ferrocene carboxylic acid redox couple (Fc-COOH/Fc^+-COOH) in water was measured at 0.616 V vs. Ag/AgCl.

Spectroelectrochemistry

Spectroelectrochemical experiments were carried out using a thin layer SEC cell containing a Pt counter electrode and an Ag wire pseudo-reference electrode. The cell was placed inside an Agilent Cary 60 spectrophotometer. A CV was measured at a scan rate of 0.05 V/s while the absorbance was measured at different wavelengths. As the electrochemistry has a time unit and the two measurements were started simultaneously, both the measurements were able to be aligned.

Scan Rate Dependent Cyclic Voltammetry

Scan rate dependent cyclic voltammetry was run on solutions using the CV method stated above, measuring at scan rates 1, 0.5, 0.1, 0.05, 0.01 V/s consecutively. The Randles-Sevkic equation was used and the peak current vs (scan rate)$^{0.5}$ was plotted to reveal either a linear or non-linear line, where a non-linear trend shows there is a diffusion limitation. A diffusion limitation would mean the current changes when more time is allowed for the measurement which could be due to the presence of larger aggregated species or a more viscous solution.

The Randles-Sevcik equation was used as follows:

$$i_p = 0.4463\, nFAC \left(\frac{nF\nu D}{RT}\right)^{0.5} \qquad \text{(Equation 7)}$$

Where i_p is the current maximum in amps, n is the number of electrons transferred, A is the electrode area in cm^2, F is the Faraday Constant in $Cmol^{-1}$, D is the diffusion coefficient in cm^2s^{-1}, C is the concentration in $molcm^{-3}$, v is the scan rate in Vs^{-1}, R is the gas constant in $JK^{-1}mol^{-1}$ and T is the temperature in K.

The Stokes-Einstein equation and the Diffusion Coefficient from the Randles-Sevcik equation can be used to calculate radii of the electrochemically measured species in solution. The Stokes-Einstein equation was used as follows:

$$R_h = \frac{k_B T}{6\pi\eta D} \qquad \text{(Equation 8)}$$

where k_B is Boltzmann's constant and T is the absolute temperature and using a viscosity (η) of 0.821 mPa.s,[29] we obtain a hydrodynamic radius R_h for the diffusing entities.

UV-Vis Spectroscopy

UV-Vis absorption spectra were obtained using an Agilent Cary 60 spectrophotometer scanning from 800-300 nm at a medium scan rate. Samples were housed in a 0.1 mm quartz demountable cuvette. For the irradiated samples, a UV LED was placed inside the spectrometer and samples irradiated for 5 minutes and the UV-Vis absorption spectrum was recorded.

HOMO/LUMO calculations

For the determination of the Lowest Unoccupied Molecular Orbital (LUMO) energy level, the reduction maximum for the first reduction potential vs. Ag/AgCl was obtained from the CV data. For calculating the LUMO energy in eV, potentials were then converted to vs. Fc/Fc^+ using an experimental value (+0.479 V), then to vs. SCE (+0.47 V), then to vs. SHE (-0.24 V), then to vs. vacuum (-4.28 V or -4.44 V) by using known literature conversions.[24,25] Therefore, the final calculation was:

$$E_{LUMO}\ (eV) = (Red_{max} + 0.479\ V + 0.470\ V - 2.4\ V - (4.28\ V \text{ or } 4.44\ V))$$

For the aqueous solutions measured in the experiment, the solvent window for water (water oxidation) was reached at potentials > 0.9 V vs Ag/AgCl. Therefore, the oxidation of PBI expected to be around 1.5 V vs Ag/AgCl was inaccessible in aqueous solutions.

As the PBI materials in this study are used in photovoltaics, it was also deemed suitable to use the optical band gap to approximate the HOMO energy levels.[19,30]

The Highest Occupied Molecular Orbital (HOMO) energy was approximated by subtracting the optical band gap, E_g, from the LUMO energy. E_g was calculated by using the onset of absorption from the UV-Vis spectrum (λ_{onset}) and converted to eV using the equation:

$$E_g\ (eV) = 1242/\lambda$$

The approximate HOMO energy was then calculated using the equation E_{HOMO} (eV) = E_{LUMO} - E_g.

The HOMO and LUMO energies from solutions of PBI-X in both high pH water and dimethylformamide (DMF) were measured in order to compare the differences between the aggregated and dissolved material.

3.6. References

1 M. C. Nolan, J. J. Walsh, L. L. E. Mears, E. R. Draper, M. Wallace, M. Barrow, B. Dietrich, S. M. King, A. J. Cowan and D. J. Adams, *J. Mater. Chem. A*, 2017, **5**, 7555–7563.

2 K. Balakrishnan, A. Datar, T. Naddo, J. Huang, R. Oitker, M. Yen, J. Zhao and L. Zang, *J. Am. Chem. Soc.*, 2006, **128**, 7390–7398.

3 F. Würthner, *Chem. Commun.*, 2004, **14**, 1564–1579.

4 S. Chen, P. Slattum, C. Wang and L. Zang, *Chem. Rev.*, 2015, **115**, 11967–11998.

5 E. R. Draper, L. J. Archibald, M. C. Nolan, R. Schweins, M. A. Zwijnenburg, S. Sproules and D. J. Adams, *Chem. - A Eur. J.*, 2018, **24**, 4006–4010.

6 M. R. Wasielewski, *Acc. Chem. Res.*, 2009, **42**, 1910–1921.

7 Z. Chen, V. Stepanenko, V. Dehm, P. Prins, L. D. A. Siebbeles, J. Seibt, P. Marquetand, V. Engel and F. Würthner, *Chem. - A Eur. J.*, 2007, **13**, 436–449.

8 E. R. Draper, B. J. Greeves, M. Barrow, R. Schweins, M. A. Zwijnenburg and D. J. Adams, *Chem*, 2017, **2**, 716–731.

9 E. R. Draper, J. J. Walsh, T. O. McDonald, M. A. Zwijnenburg, P. J. Cameron, A. J. Cowan and D. J. Adams, *J. Mater. Chem. C*, 2014, **2**, 5570–5575.

10 J. J. Walsh, J. R. Lee, E. R. Draper, S. M. King, F. Jäckel, M. A. Zwijnenburg, D. J.

Adams and A. J. Cowan, *J. Phys. Chem. C*, 2016, **120**, 18479–18486.

11 F. Würthner, C. R. Saha-Moller, B. Fimmel, S. Ogi, P. Leowanawat and D. Schmidt, *Chem. Rev.*, 2016, **116**, 962–1052.

12 T. Aytun, L. Barreda, A. Ruiz-Carretero, J. A. Lehrman and S. I. Stupp, *Chem. Mater.*, 2015, **27**, 1201–1209.

13 J. L. Bredas, J. P. Calbert, D. A. da Silva Filho and J. Cornil, *Proc. Natl. Acad. Sci.*, 2002, **99**, 5804–5809.

14 Y. Geng, J. Wang, S. Wu, H. Li, F. Yu, G. Yang, H. Gao and Z. Su, *J. Mater. Chem.*, 2011, **21**, 134–143.

15 A. S. Weingarten, A. J. Dannenhoffer, R. V. Kazantsev, H. Sai, D. Huang and S. I. Stupp, *J. Am. Chem. Soc.*, 2018, **140**, 4965–4968.

16 E. Zhou, K. Tajima, C. Yang and K. Hashimoto, *J. Mater. Chem.*, 2010, **20**, 2362–2368.

17 X. Zhang, Y. Wu, J. Li, F. Li and M. Li, *Dye. Pigment.*, 2008, **76**, 810–816.

18 P. Chal, A. Shit and A. K. Nandi, *J. Mater. Chem. A*, 2016, **4**, 16108–16118.

19 J. T. Kirner, J. J. Stracke, B. A. Gregg and R. G. Finke, *ACS Appl. Mater. Interfaces*, 2014, **6**, 13367–13377.

20 W. S. Shin, H. H. Jeong, M. K. Kim, S. H. Jin, M. R. Kim, J. K. Lee, J. W. Lee and Y. S. Gal, *J. Mater. Chem.*, 2006, **16**, 384–390.

21 D. Görl, X. Zhang and F. Würthner, *Angew. Chem. Int. Ed.*, 2012, **51**, 6328–6348.

22 R. O. Marcon and S. Brochsztain, *J. Phys. Chem. A*, 2009, **113**, 1747–1752.

23 A. J. Bard and L. R. Faulkner, *Electrochemical Methods: Fundamentals and Applications*, John Wiley & Sons, NY, 1944.

24 A. A. Isse and A. Gennaro, *J. Phys. Chem. B*, 2010, **114**, 7894–7899.

25 S. Trasatti, *Pure Appl. Chem.*, 1986, **58**, 955–966.

26 A. Z. Cardoso, L. L. E. Mears, B. N. Cattoz, P. C. Griffiths, R. Schweins and D. J. Adams, *Soft Matter*, 2016, **12**, 3612–3621.

27 J. Raeburn, A. Z. Cardoso and D. J. Adams, *Chem. Soc. Rev.*, 2013, **42**, 5143–56.

28 E. P. Melián, C. R. López, A. O. Méndez, O. G. Díaz, M. N. Suárez, J. M. Doña Rodríguez, J. A. Navío and D. Fernández Hevia, *Int. J. Hydrogen Energy*, 2013, **38**, 11737–11748.

29 B. Gonzalez, N. Calvar, E. Gomez and A. Dominguez, *J. Chem. Thermodyn.*, 2007, **39**, 1578–1588.

30 S. Admassie, O. Ingan, E. Perzon and M. R. Andersson, *Synth. Met.*, 2006, **156**, 614–623.

CHAPTER 4

Optimising Low Molecular Weight Hydrogels for Automated 3D Printing

The work in this chapter has been edited from the published article in Soft Matter (RSC) involving the following co-authors:

Michael C. Nolan, Ana M. Fuentes Caparrós, Bart Dietrich, Michael Barrow (MB), Emily R. Cross, Markus NMN Bleuel (MNB), Stephen M. King and Dave J. Adams

AMFC and MB were responsible for preliminary work testing the 3D printing for hydrogel extrusion. BD was responsible for the experimental set up and maintenance of the 3D printer. ERC, MNB and SMK assisted in the collection and analysis of the neutron scattering data. DJA supervised the project and assisted in drafting the final published manuscript.

Acknowledgements

We thank the EPSRC and the University of Liverpool for funding a DTA (MCN). DJA thanks the EPSRC for a Fellowship (EP/L021978/1). AMFC acknowledges an Erasmus traineeship. MB thanks UKRMP for funding (MR/K026739/1). BD thanks the EPSRC for funding (EP/L021978/1). The EPSRC are thanked for funding the confocal microscope used in this project (EP/J004790/1 and EP/N007417/1). ERC thanks the University of Glasgow for funding. MCN would also like to thank Emily Draper for helpful comments throughout the project. We thank Finlay Walton (University of Glasgow) for help setting up the confocal microscopy. We thank the STFC for funding our time at the ISIS facility (Experiment Number RB1710066). This work also utilized the BT-5 USANS instrument and facilities of the Center for High Resolution Neutron Scattering, supported in part by the National Science Foundation under Agreement No. DMR-1508249.50 This work benefitted from SasView software, originally developed by the DANSE project under NSF award DMR-0520547.51 SasView also contains code developed with funding from the EU Horizon 2020 programme under the SINE2020 project Grant No. 654000. Certain commercial equipment, instruments, or materials are identified in this paper to foster understanding. Such identification does not imply recommendation or endorsement by the National Institute of Standards and Technology, nor does it imply that the materials or equipment identified are necessarily the best available for the purpose.

4.1. Abstract

Hydrogels prepared from low molecular weight gelators (LMWGs) are formed as a result of hierarchical intermolecular interactions between gelators to form fibres, and then further interactions between the self-assembled fibres via physical entanglements, as well as potential branching points. These interactions can allow hydrogels to recover quickly after a high shear rate has been applied. There are currently limited design rules describing which types of morphology or rheological properties are required for a LMWG hydrogel to be used as an effective, printable gel. By preparing hydrogels with different types of fibrous network structures, we have been able to understand in more detail the morphological type which give rise to a 3D-printable hydrogel using a range of techniques, including rheology, small angle scattering and microscopy. We also demonstrate the printability of perylene bisimide gels for photocatalytic applications.

4.2. Introduction

The controlled shaping and delivery of hydrogels has many potential applications such as tissue engineering,[1] drug delivery,[2–6] and optoelectronics.[7,8] 3D printers can allow for the reproducible, controlled and automatic delivery of materials within a 3D space without the need for moulds.[9] 3D printing technology has improved dramatically over recent years with the development of high resolution techniques using a range of materials and delivery mechanisms.[10–12] Extrusion-based 3D printers are now cheap and readily accessible to small scale laboratories and can be adapted for specific needs.[13] This has led to a vast increase in investigations into printing new materials with interesting applications. Extrusion printing is generally used for viscous materials and can result in a continuous 3D network if the material and printing parameters are optimised.[14] There has been extensive research in the extrusion of peptides and polymer blends using precursor solutions which form hydrogels after extrusion *via* processes such as UV curing,[15–18] addition of crosslinking salts,[17] the submersion into a gel or solution,[19] and changing the temperature.[20] However, 3D printing of hydrogels prepared from low molecular weight gelators (LMWGs) is far less common, and understanding and developing the processing techniques for these materials can have significant potential applications in forming complex hierarchical structures for tissue engineering.[21,22]

A supramolecular gel network formed *via* non-covalent interactions would allow for the reversible breaking and recovery of the network.[23] The process of forming a gel inside a syringe

and then extruding relies on both thixotropy and the recovery of the mechanical properties of the gel which, in turn, greatly relies on the microstructure of the gel network.[24,25] Huang et al. have shown that the recovery after shear in organogel systems can depend on the gel microstructure, which in turn depends on the conditions under which gelation is carried out.[26] Similarly, Pochan and co-workers studied hydrogel behaviour during and after flow and showed that planar domains of the gel network break apart to allow the gel to flow.[24] Using a preformed gel that recovers quickly reduces the need for the additional treatment of the extruded precursor solution to form a gel. This approach opens up opportunities to encapsulate drugs, catalysts and other materials inside the gel which will not leak from the network if the network recovers quickly after extrusion.[24,27] Using hydrogels as cell carriers has also been shown to improve cell viability during bio-printing.[28]

Most reported examples of hydrogels suitable for printing have been discovered through serendipity. In general, why some gels are thixotropic and others are not is not well understood. There is a need to understand the link between the microstructure of the gel network and its printability, where the ability to print the gel is considered as the ability to recover a continuous gel network with a reasonable resolution after extrusion. The challenge is to be able to develop design rules to guide the selection of the correct LMWG and network type to attain the desired printed gel properties.

Hydrogels formed from LMWGs can be prepared under different conditions to give different mechanical properties.[29–33] To improve the recovery of hydrogels after extrusion, it is common to increase the gelator concentration to increase the concentration of fibres and crosslinking.[9] However, it is also understood that using different gelation triggers, such as a pH change or the addition of an anti- solvent, leads to different mechanical properties due to the formation of different gel microstructures.[29,34] In this study, the recoverability and printability of different gel microstructures are compared. Our aim is to form an understanding as to which gel microstructures are desirable when developing printable low molecular weight hydrogels.

4.3. Results and Discussion

4.3.1. Preparation of Recoverable Low Molecular Weight Gels

To create a comprehensive study on LMWG hydrogel recoverability, four carefully selected gels were studied. As previously mentioned, LMWG which form printable hydrogels are usually found by trial and error. Therefore, initially, we carried out a broad study on the recovery of mechanical properties within our library of gelators. A range of gelators were tested along with the three different gelation triggers using solvent, salt and pH switches (Figure 99). The names of gelators given are internal references for the gelators, where '1ArFF' is a 1-naphthol is appended with two phenylalanine groups (see gelator **(1)** nomenclature below). Interestingly, the 1ArFF gelator showed different recovery properties depending on the method used for gelation.

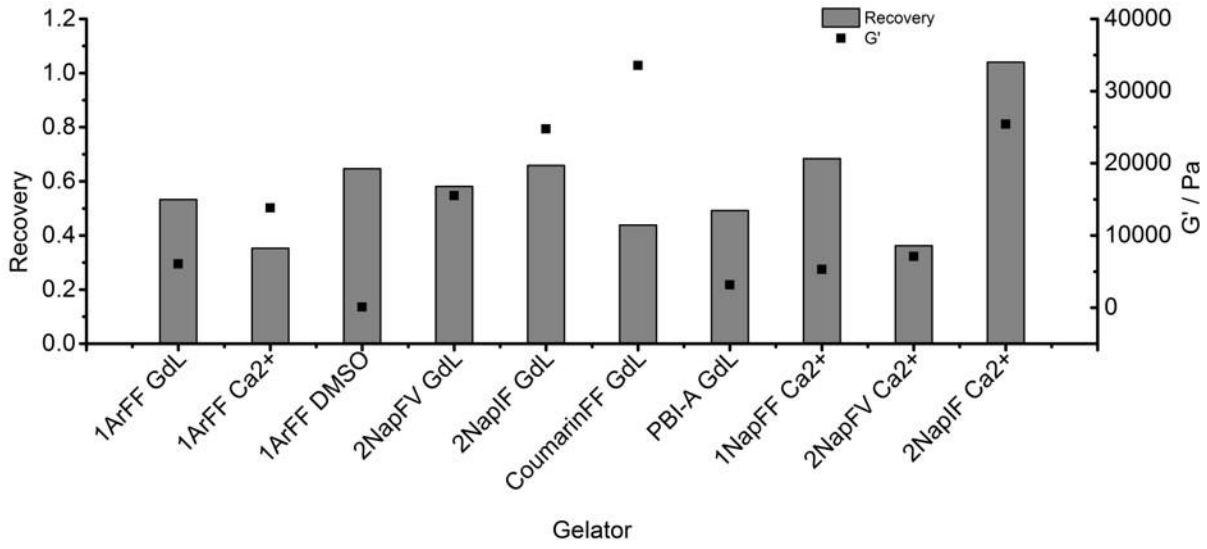

Figure 99. Rheological tests of gelators gelled in various ways. The G′ in the LNR is recorded (black squares) alongside the ratio of G′ after high strain was applied (columns).

The recovery properties were measured using rheometry with a vane and cup geometry in which a high shear rate was applied and the recovery of the storage modulus, G′, was monitored. The ratio of the G' before and after was measured and recorded. This revealed several gelators which formed gels that could possibly be printed due to their good recovery. To move forwards with the investigation, gelators were chosen due to their largely different recovery properties from their gels formed from different gelation methods. This would allow for structural analysis of printed gels between the various gelation methods formed from the

same compound. The two gelators for this study were '1ArFF', 3-phenyl-2-[3-phenyl-2-[2-(5,6,7,8-tetrahydronaphthalen-1-yloxy)acetamido] propanamido]propanoic acid (**1**) and '1NapFF', Fmoc-diphenylalanine (**2**), Scheme 1.[35] The synthesis of these gelators and the materials used are described in the Experimental.

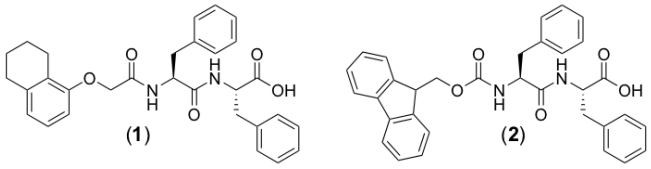

Scheme 1. The structures of LMWG 1 and 2.

Two different methods were used to form hydrogels from these LMWGs. In the first method, the LMWG was dissolved in DMSO to a concentration of 16.7 mg/mL. Water was then added to provide a final concentration of the LMWG of 5 mg/mL, a volume percentage of DMSO of 30 vol% and a final pH of 5.9. This solvent-triggered approach[33,36,37] provided gels **1a** and **2a** respectively from the two LMWG. Alternatively, solutions of the LMWGs at pH 11.8 for **1** and pH 9.9 for **2** were prepared by the careful addition of sodium hydroxide solution to a dispersion of the LMWGs in water (here, in the case of **2**, it is necessary to carefully control the pH as deprotection of the Fmoc group occurs at high pH). The pH of these solutions was then lowered by the addition of glucono- δ-lactone (GdL). GdL hydrolyses slowly in solution which results in a slow homogeneous acidification of the solution to form the gel at pH 3.6.[38,39] This pH-triggered approach afforded gels **1b** and **2b** from the two LMWGs respectively. The different gelation triggers are expected to result in the formation of different microstructures of the gel network which we expected to show different recovery properties when extruded from a syringe.[14,25,33] All gels were formed directly inside 10 mL polypropylene syringes. The salt-triggered gel was not able to be formed with volumes in excess of 5 mL so was not studied in more detail as larger volumes were required for this study. Salt-triggered gels were prepared by adding 2 equivalents of Ca^{2+} from a 200 mg/mL $CaCl_2$ solution to the stationary gelator solution in water.

4.3.2. Extrusion Flow Properties of pH-triggered and Solvent-triggered Gels

When gels are extruded from a syringe, a range of properties need to be considered and evaluated. First, the rheological properties of the gels should be tested to see if the gel is able to recover after the gel is exposed to a high shear rate. Oscillatory rheology can be used as a tool for understanding if gels are able to recover upon an oscillatory shear, however this may not be fully representative of the type of shear found inside a syringe during extrusion.[24] Other structural characterisation techniques such as microscopy and small angle neutron scattering (SANS) have proven useful in observing the structure of gels and can be used in conjunction with rheology to gain a thorough understanding of the materials before and after extrusion.[24,40] Here, we have characterised the gels using rheological, microscopy, and scattering techniques, to understand the effect of extrusion on the gels.

The 3D printer used here is described in detail in the Experimental. The shear rate the gel encounters as it is extruded from the syringe can be calculated using Equation 9,[24,41] where $\dot{\gamma}$ is the shear rate (in s^{-1}), V is the volume of extruded gel (in m^3), r is the radius of the nozzle (in m^3) and t is the time taken to extrude the volume of gel (in s).

$$\text{Shear Rate, } \dot{\gamma} = \frac{(4 \cdot V)}{\pi \times r^3 \times t}$$

Equation 9. Equation for the shear rate through the syringe nozzle.

A typical extrusion rate using the 3D printer in this configuration is 835 μL/s through the nozzle of a syringe with an internal diameter of 0.8 mm, resulting in a shear rate of *ca.* 16,000 s^{-1}. The automation of the 3D printer allowed for accurate control over the flow rate of the gel during extrusion and Equation 9 was used to relate all prints to a known shear rate. The gelator solutions were added to a syringe, allowed to gel for 18 hours and then extruded automatically using a 3D printer (Figure 100). A stronger or more viscous material will require a higher shear rate to extrude from the syringe and the stress applied to the gel will have an impact on the resulting structure. Lines of 6 cm length were printed of gels **1a, 1b** and **2a, 2b** by extruding 200 μL and 400 μL of gel.

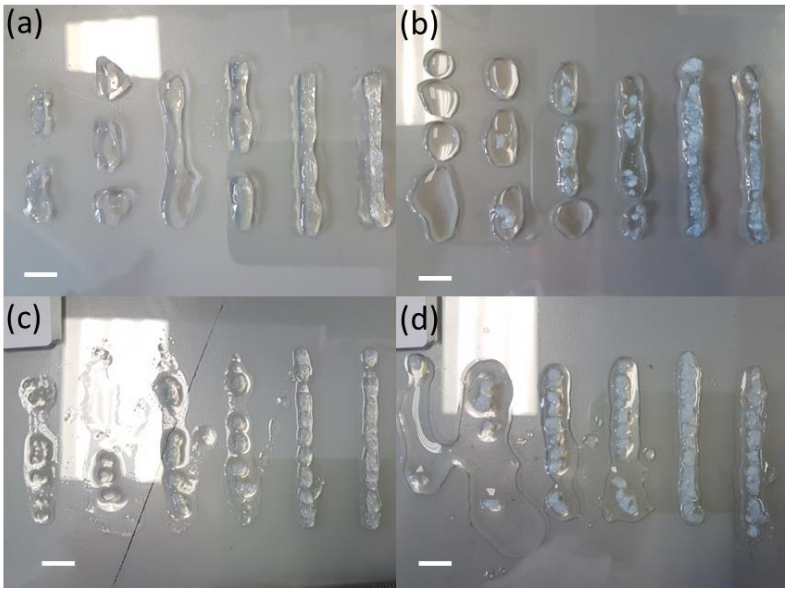

Figure 100. Automatically extruded lines of gels (a) **1a**; (b) **1b**; (c) **2a**; (d) **2b** at set shear rates. pH-triggered gels **1b** and **2b** gels were extruded with double the shear rate. Lines are (left to right) 1094, 1094, 3322, 3322, 16612 and 16612 s^{-1} for (a) and (c) and 2208, 2208, 6645, 6645, 33224 and 33224 s^{-1} for (b) and (d). Lines in (a) and (c) contain 200 μL gel and lines in (b) and (d) contain 400 μL gel. Scale bar 1 cm in all cases.

It quickly became clear that the pH-triggered gels (**1b** and **2b**) needed a higher shear rate to be successfully extruded from the syringe, which was achieved by extruding 400 μL of gel instead of 200 μL. The printing of a 6 cm line took 0.24 seconds and at lower shear rates only solution is extruded from the gel. This observation agrees with compression tests on Fmoc-dipeptide hydrogels, which showed that solution is expelled from the gel when a slowly increasing force is applied, however the gel undergoes a brittle break when compressed quickly which could allow the gel to flow.[42] As the solvent-triggered gels **1a** and **2a** could be extruded using lower shear rates this resulted in more continuous and reproducible lines of prints. Different concentrations of gels of **2a** were also prepared and their prints optimised (Figure 101, Table 8).

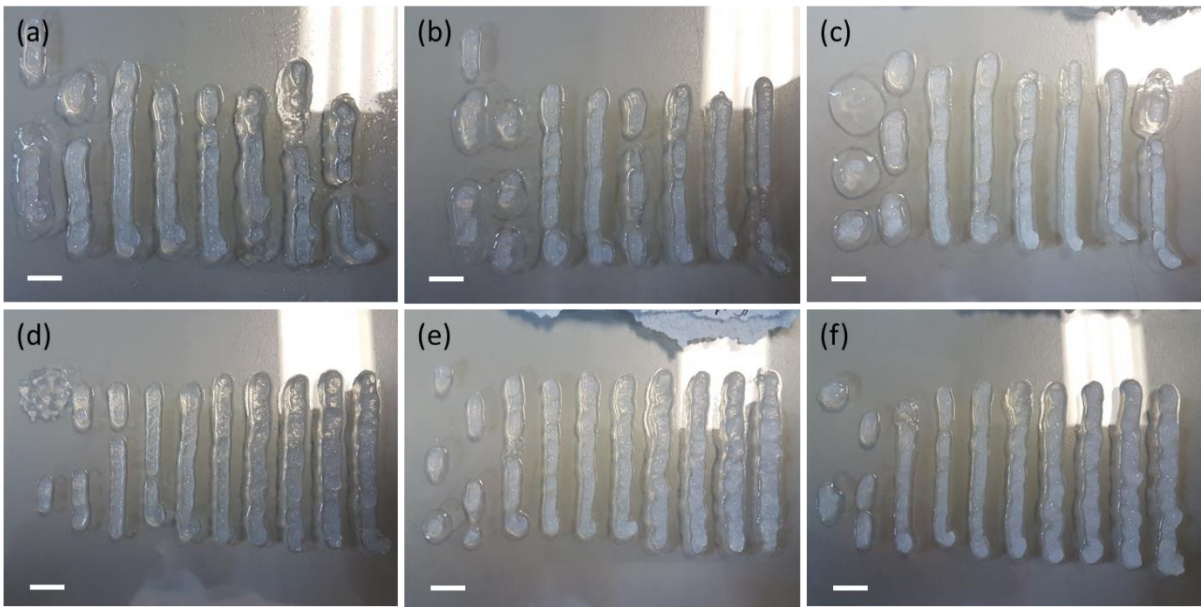

Figure 101. Photographs of lines of **2a** at (a, d) 5, (b, e) 7.5 and (c, f) 10 mg/mL concentrations printed using different parameters to find the optimal line. (a-c) Constant volume of 40 μL/cm and, from left to right, speeds of 10k, 10k, 15k, 15k, 20k, 20k, 25k and 25k mm/min. (d-f) Constant speed of 15k mm/min and, from left to right, volumes of 10, 20, 30, 40, 50, 60, 70, 80, 90 and 100 μL/cm. Scale bars are 1cm in all cases.

(a)

Print speed x10^3 / mm/min	10	15	20	25
Shear rate at a constant volume of 40 μL/cm	13,263	19,894	26,526	34,105

(b)

Volume of gel / μL/cm	10	20	30	40	50	60	70	80	90	100
Shear rate at a constant print speed of 15,000 mm/min	4,974	9,947	14,921	19,894	24,868	29,842	34,815	39,789	44,762	49,736

Table 8. Shear rate of the extruded gels from the concentration study in Figure 101. (a) Constant volume prints from Figure 101a-c, (b) Constant speed prints from Figure 101d-f.

The 3D printer has several parameters which can be optimised for printing the gels (the volume of the gel to extrude, the speed of the extrusion, the height of the accessory from the printing bed and the speed the printing accessory moves along the axes during printing).[43] Each parameter was systematically changed and optimised for each gel. The printing parameters were optimised by extruding a constant volume of 40 μL/mm at speeds of 5, 10, 15, 20 and 25k mm/min. The optimal speed was defined as the line of the thinnest continuous gel. Then, lines were printed using a constant optimal speed and volumes of 1-10 μL/mm and the thinnest

continuous line chosen. A line of each gel was printed using the optimal conditions for each gel and photographed (Figure 102a-d). The optimal resolution for the printed gels was 4x4x1 mm in the x, y and z axes. The optimal printing parameters are shown in Table 9.

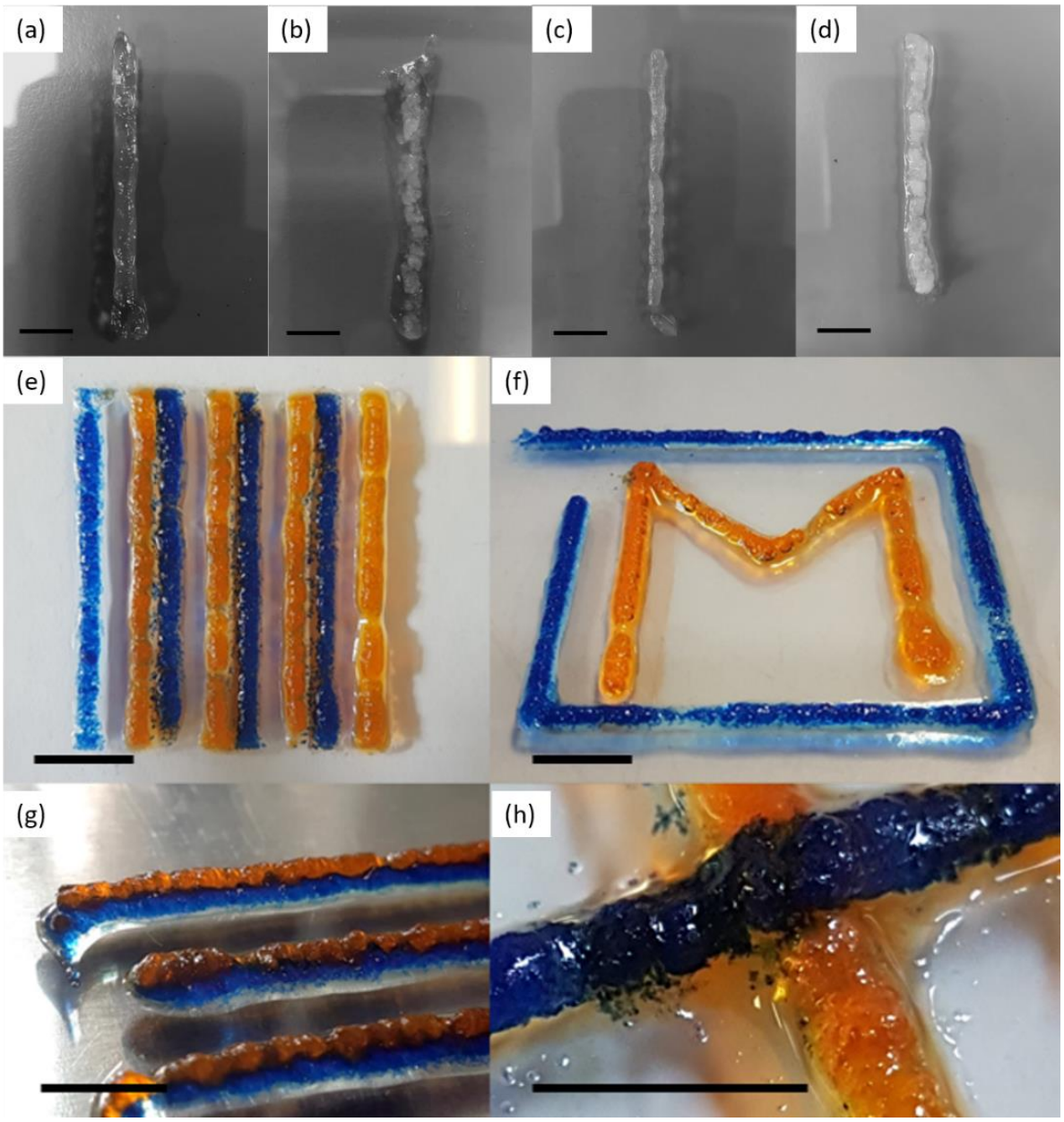

Figure 102. Photographs of optimised 3D printed gels of (a) 1a, (b) 1b, (c) 2a, and (d) 2b. 3D printed gels of **2a** mixed with dyes Nile Blue (0.5 mg/mL) or Methyl Orange (0.25 mg/mL) and printed side by side ((e) and (f)) and one on top of the other ((g) and (h)). The scale bar represents 1 cm in all cases.

Gel	Volume / μm/cm	Speed / mm/min	Time taken to print a 5 cm line / s	Shear Rate / s^{-1}
1a	40	15,000	0.24	19,894
1b	80	15,000	0.24	39,789
2a	40	15,000	0.24	19,894
2b	80	15,000	0.24	39,789

Table 9. Optimal parameters for printing gels 1a, 1b, 2a and 2b as shown in Figure 102.

When comparing lines printed using the optimised parameters, more continuous gel structures were observed using the solvent-triggered gels **1a** and **2a** compared to the pH-triggered gels **1b** and **2b**. Gel **2a** was then mixed with dyes (Nile Blue or Methyl Orange) and printed side by side to show the versatility of the printing method in printing pre-programmed structures (Figure 102e-h). Additionally, we were able to print gels of 3-6 layers, which could be removed from the plate and manipulated (Figure 103a-f). Here, the layers acted as if they were fused together and the colours stayed in well-defined regions. Only the colour on the bottom layer became less defined due to the weight of the structure on top. The close interaction of the dye molecules with the gelator fibres is demonstrated in the confocal microscopy measurements (Figure 104).

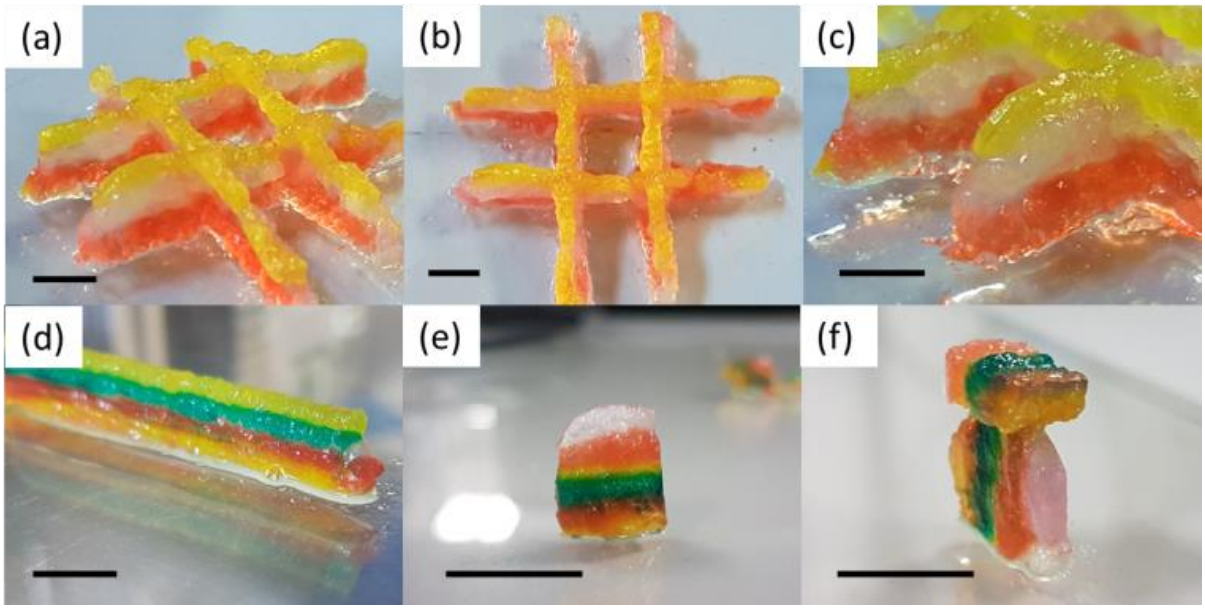

Figure 103. Photographs of 3D printed gels of **2a** with dyes mixed in to show the different layers. (a-c) A three-layered structure; (d-f) a six-layered structure. Sections were removed using a scalpel and oriented in different ways (e-f). Scale bar represents 1cm in all cases.

4.3.3. Morphology of Extruded Gels

A key question is why gels formed by the different triggers can be printed with different success. To explain this, we first turned to confocal microscopy (Figure 104). Although the resolution of this technique is not suitable for examining the individual fibres that lead to gelation, it is possible to probe the gel microstructure.[30] We examine the differences before and after extrusion. Before extrusion, the solvent-triggered gels show the presence of spherulitic domains, in keeping with our previous reports.[33,44] The domains were much smaller for **1a** as compared to **2a**. After extrusion, similar domains were observed, although in both cases there was an increase in domain size. Pochan and co-workers reported that bundles of fibres, described as fibrils, have a random orientation during gel flow.[24]

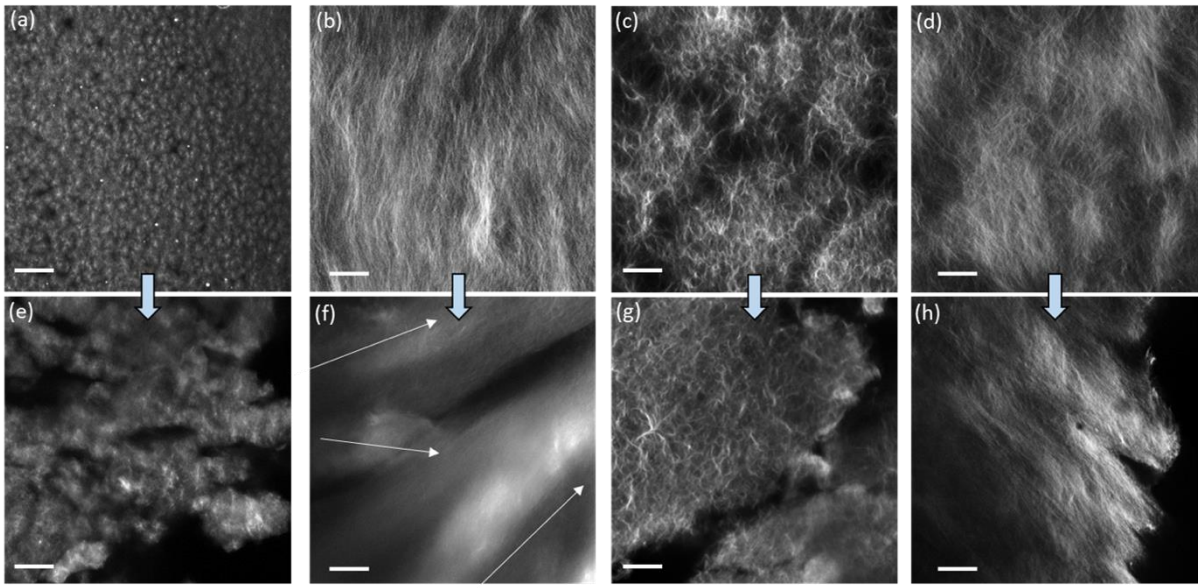

Figure 104. Confocal microscope images of (a) **1a**; (b) **1b**; (c) **2a**; (d) **2b**. (e)-(h) are images of the gels after extrusion from a syringe. Gelator solutions were stained with Nile Blue before gels were formed. The arrows in (f) are a suggestion of different orientations of structures inside the gel. The scale bars represent 20 μm.

Similarly, Huang et al. have shown that spherulitic structures result in thixotropic gels.[26] Tomasini and co-workers also commented that hydrogels with denser fibrous networks are affected to a greater extent by the application of high shear.[25] Therefore, we suggest that the spherical-like domains of **1a** and **2a** formed from the solvent-triggered gelation method can greatly reduce the effect of the random orientations during flow and hence allow these gels to be effectively printed. The pH-triggered gels before extrusion have greater uniformity than the

solvent-triggered gels, which again is consistent with our data elsewhere.[31] After extrusion however, there is a significant decrease in homogeneity. The data for **1b** especially shows a significant change in the apparent ordering of the underlying fibres and changes in the gel microstructure. Similar effects are observed for **2b**. These changes can be linked to the loss of homogeneity of the gel after extrusion in the microscopy.

The confocal microscopy data were supported with small angle neutron scattering (SANS) and ultra-small angle neutron scattering (USANS) data. The raw data was reduced using IGOR Pro.[45] The reduced data were then fitted (Figure 105) in the SasView software (version 4.1.1)[46] to a customized model comprising of a (Kratky-Porod) flexible cylinder and an absolute power law.[47–49]

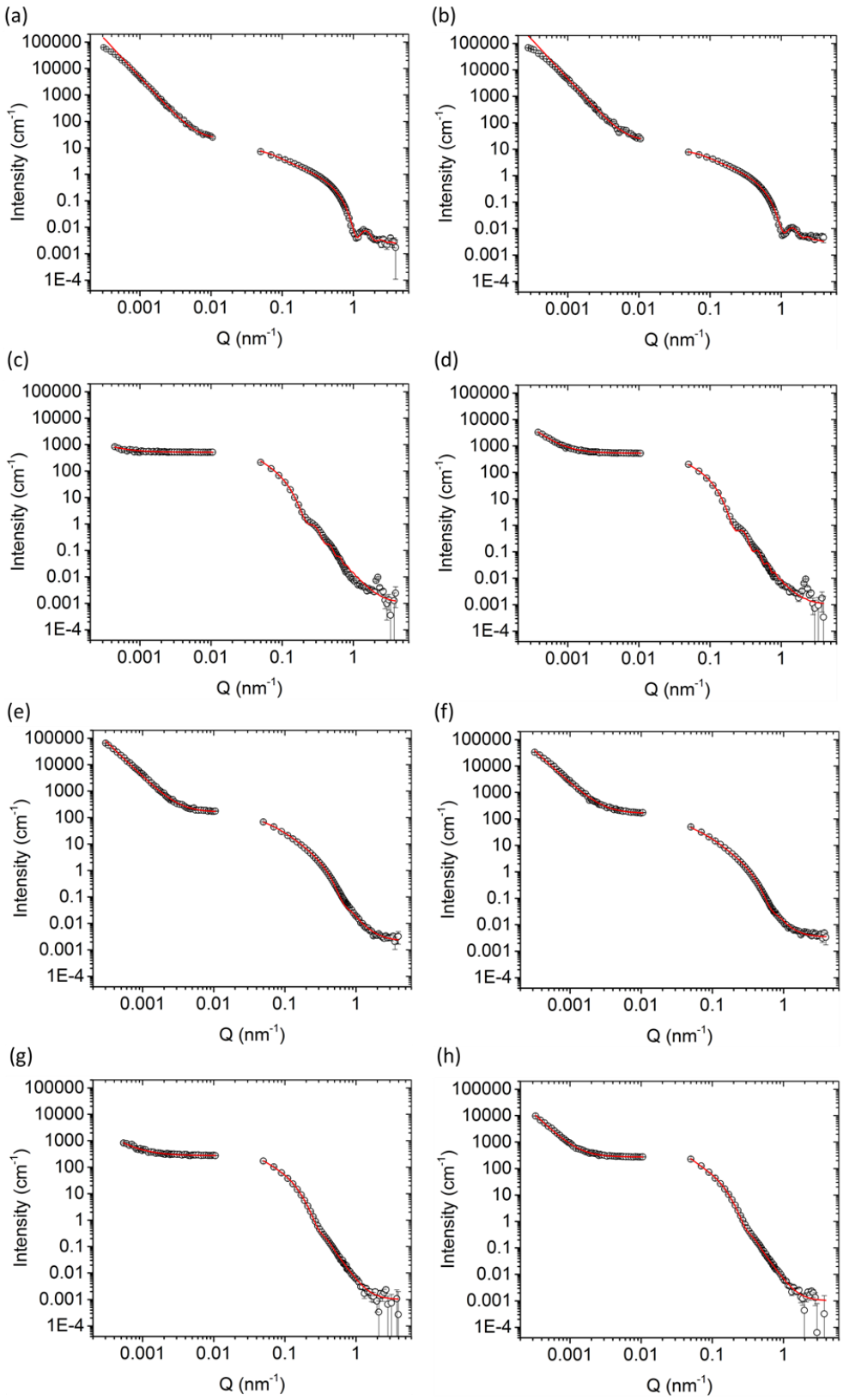

Figure 105. SANS and USANS data of (a) **1a**; (b) **1a** after extrusion; (c) **1b**; (d) **1b** after extrusion; (e) **2a**; (f) **2a** after extrusion; (g) **2b**; (h) **2b** after extrusion. The scatter with error indicates the scattering data and the red lines are the modelled fits of the data where SANS and USANS were fitted separately. Y-axis can also be referred to as I(Q).

The Kratky-Porod model has been used to fit scattering data for similar hydrogels.[30,31,50–52] The power law (Q^{-m}) accounts for the mass fractal contribution to the scattering intensity which is combined with the flexible cylinder model. As there was no overlap between the USANS and SANS data, the USANS data and fits were manually offset in the y-axis by +20 for **1a**, +500 for **1b**, +150 for **2a** and +250 for **2b** for visual representation, however data were fitted before any post-modification was applied. The fitted data is shown in Figure 105. Scattering data of each gel before and after extrusion has been overlaid for a closer comparison of the changes (Figure 106).

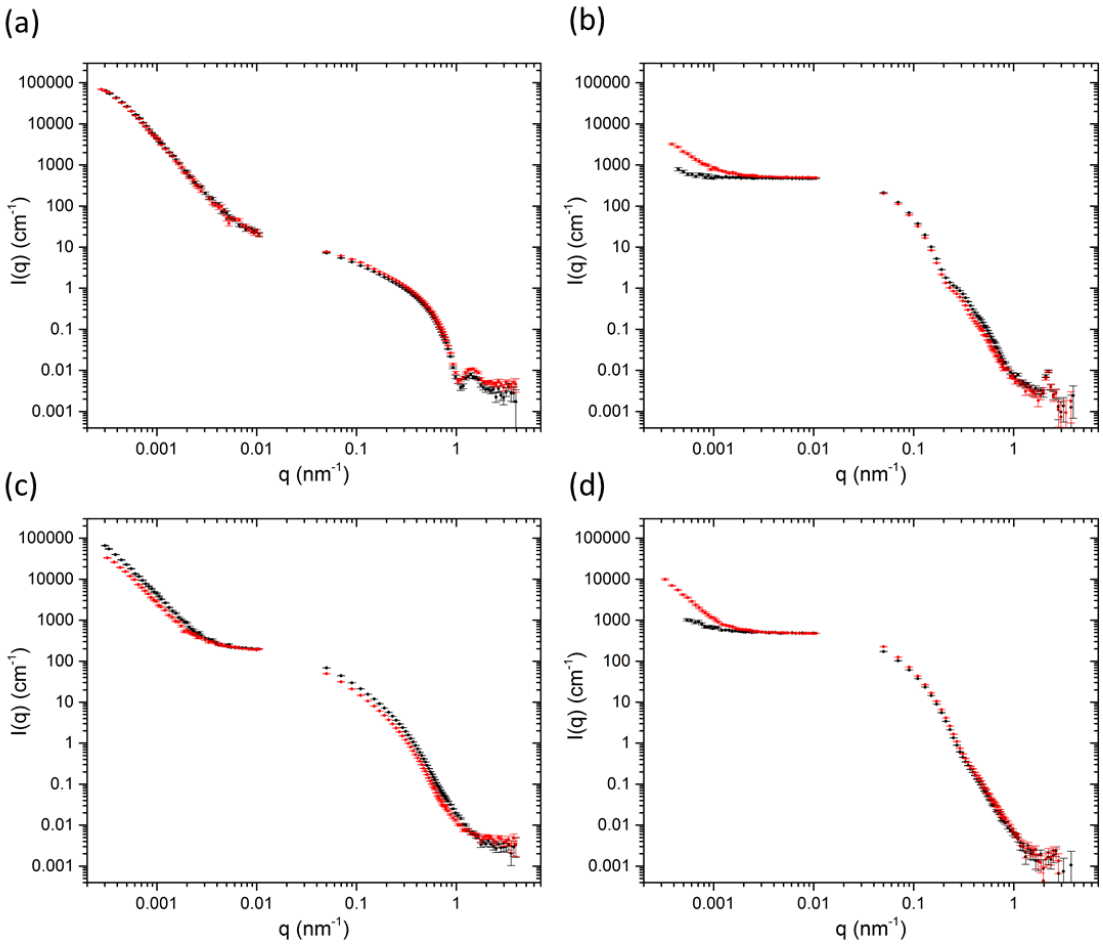

Figure 106. Ultra-small angle neutron scattering and small angle neutron scattering data of gels (a) **1a**; (b) **1b**; (c) **2a**; (d) **2b**. Black data are for the gels before extrusion and the red data are for the gels after extrusion.

For the gels here, the scattering in the SANS regime at Q = 4 nm^{-1} to 0.06 nm^{-1} suggest cylinder-like structures on the nanoscale, such as fibres and fibrils, which remain unchanged after extrusion. The survival of the primary fibre structure is also inferred by the confocal

microscopy where similar sizes of fibres are observed across all samples when comparing them before and after extrusion (see Figure 104). Parameters of all fits are shown in Table 10a-b.

(a)

	USANS							
	1a	1a Extruded	1b	1b Extruded	2a	2a Extruded	2b	2b Extruded
p1_background (cm^{-1})			0.002	0.002	0.002	0.002	0.002	0.002
p1_kuhn_length (nm)			10	10	10	10	10	10
p1_length (nm)			100	100	100	100	100	100
p1_radius (nm)			2	2	2	2	2	2
p1_scale ($x10^{-3}$)	0	0	**0.04**	**0.091**	0.04	0.04	0.078	0.075
p1_sld ($x10^{-6}$ Å^{-2})			2.17	2.17	2.17	2.17	2.17	2.17
p1_sld_solvent ($x10^{-6}$ Å^{-2})			6.27	6.27	6.27	6.27	6.27	6.27
p2_power	3.9	3.9	**2.72**	**3.1**	**3.57**	**3.44**	**2.8**	**3.5**
p2_scale ($x10^{-4}$)	1.70E-09	1.70E-09	**1.00E-06**	**1.80E-07**	**2.50E-08**	**5.10E-08**	**1.25E-06**	**8.00E-09**
scale_factor			1	1	1	1	1	1
Radius PD			0	0	0	0	0	0

(b)

	SANS							
	1a	1a Extruded	1b	1b Extruded	2a	2a Extruded	2b	2b Extruded
p1_background (cm^{-1})	0.002	0.002	0.00101	0.00101	0.0021	0.0034	0.00101	0.00101
p1_kuhn_length (nm)	50	50	36	36	12	12	26	26
p1_length (nm)	**90**	**70**	100	100	230	230	100	100
p1_radius (nm)	3.4	3.5	18	18	5.5	5.5	13	13
p1_scale ($x10^{-3}$)	**1.85**	**2.15**	1.45	1.45	**2.40**	**1.50**	**1.80**	**2.00**
p1_sld ($x10^{-6}$ Å^{-2})	2.17	2.17	2.17	2.17	2.17	2.17	2.17	2.17
p1_sld_solvent ($x10^{-6}$ Å^{-2})	6.27	6.27	6.27	6.27	6.27	6.27	6.27	6.27
p2_power	1	1	2.9	2.9	**2.3**	**2.5**	**3.3**	**3.4**
p2_scale ($x10^{-4}$)	**2**	**5**	**0.14**	**0.07**	**0.3**	**0.13**	0.01	0.01
scale_factor	1	1	1	1	1	1	1	1
Radius PD	0	0	0	0	0.2	0.2	0.2	0.2

Table 10. Derived fit parameters for (a) USANS and (b) SANS data fitted to the Kratky-Porod flexible cylinder (contribution p1) plus power law (contribution p2) model. For details of the meaning of the parameters the reader is referred to the SasView model documentation at www.sasview.org. The data shown in bold is to clarify where changes were made in the fits between the original and extruded counterparts of each gel. Polydispersity is abbreviated to PD.

For gels **2a** and **2b**, a larger radius was used for fitting the flexible cylinder model. We hypothesise that it is the bundles of fibres that are responsible for the larger radius (and less pronounced oscillations in the SANS). Consequently, a radius polydispersity factor (=standard deviation/mean) of 0.2 was needed to fit the feature in the scattering at 0.6 nm^{-1}, suggesting a range of radii are present from various fibril sizes. The fits using polydispersity are displayed

in Figure 107. As is clear from these fits, the oscillations in the model fits are a close match to the smaller oscillations in the scatters, and that polydispersity of the radius parameter is used only to lower the intensity of these oscillations, thus providing a convincing fit of the data.

The more significant differences in this study are observed in the USANS regime at lower Q which provides details about the microstructure of the gels on the micron scale.[23,24,53,54] For the solvent-triggered gels **1a** and **2a**, the features in the scattering in the USANS regime (100 nm – 10 μm) for 2 x 10^{-4} nm^{-1} < q < 0.001 nm^{-1} remain largely unchanged after extrusion. These data agree with the microscopy, where **1a** and **2a** both show spherical-type domains containing localised networks of the primary fibres before extrusion, with **2a** exhibiting a network of larger spherical domains. The rising inflection of the scattering at low Q for **2a** compared to **1a** is representative of the larger scattering domains and pores as observed in the microscopy.[53] The power law exponent for **1a** is 3.9 in the USANS, consistent with spherical structures. In contrast the power exponent for **2a** is 3.57, but here the flexible cylinder model contributes more to the fit (Table 10). The power law contribution to the scattering intensity from **2a** after extrusion decreases at low Q which suggests that there is a reduction in the number of scattering domains. The power law exponent also decreases from 3.57 to 3.44 which suggests a move from the spherical-type morphology towards a more typical network-like structure.

It seems that the extrusion process pushes the larger domains in **2a** together into a more continuous network. Again, these data agree with the microscopy, which shows that the spherical domains seem to become more tightly packed after extrusion. Although the same process seems to be happening with gel **1a**, this gel has much smaller spherical domains initially, so we suggest that the changes are more indistinguishable on the USANS scale compared to those of **2a**.

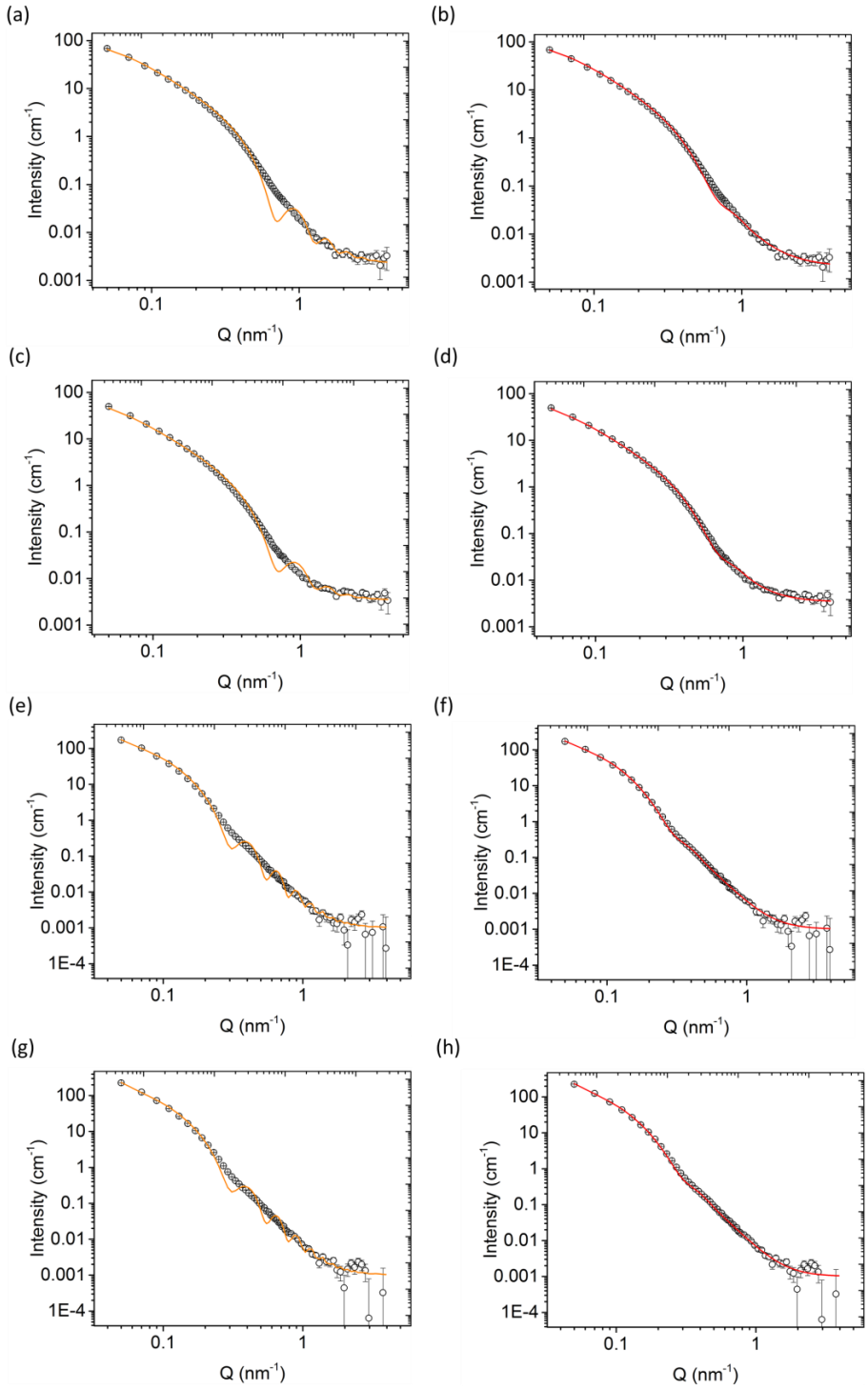

Figure 107. SANS data and fits showing the use of radius polydispersity (pd) in the fits of **2a** and **2b**, before and after extrusion. Defining features in the scatter were fitted first with no polydispersity, then pd(radius)=0.2 was added to broaden the features from the model. (a) **2a** pd(radius)=0; (b) 2a pd(radius)=0.2; (c) **2a** after extrusion pd(radius)=0; (d) **2a** after extrusion pd(radius)=0.2; (e) **2b** pd(radius)=0; (f) **2b** pd(radius)=0.2; (g) **2b** after extrusion pd(radius)=0; (h) **2b** after extrusion pd(radius)=0.2. Scatters are data with y errors and lines are model fits.

The pH-triggered gels **1b** and **2b**, however, show significant changes in scattering upon extrusion. Initially, the power law exponent is 2.7 and 2.8 for **1b** and **2b** respectively which increases to 3.1 and 3.5 after extrusion. As described above, the microscopy images show a continuous, dense fibrous network initially which breaks down into randomly oriented domains after extrusion. Before extrusion, the gels show weak USANS scattering, which is almost indistinguishable from the empty cell. This agrees with the observation that the gels are more homogeneous than the solvent-triggered gels. After extrusion, however the intensity, I(Q), of the USANS scatter increases by an order of magnitude suggestive of the formation of larger scale inhomogeneities. For these gels, the microscopy shows randomly orientated domains which would be the likely cause of this increase in scattering.

Hence, from these data, it appears that gels with different microstructures can be printed with differing degrees of efficiency. Whilst it is clearly of interest to be able to print such gels, an important question is how the rheological properties of the gels are affected by the printing process.

Strain and frequency sweeps of the original gels were collected using a parallel plate geometry (Figure 108) and compared to the gels after extrusion (Figure 108-Figure 110). Slices and moulds of gels were used for analysis. Importantly, gels with similar initial rheological properties (storage and loss moduli, G′ and G″ respectively) were chosen for the study to make a fair comparison between the different microstructures present.

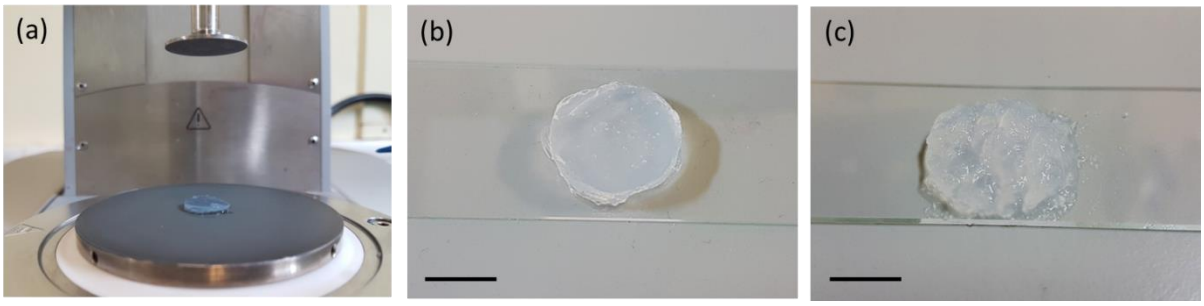

Figure 108. (a) Photograph of a slice of the gel **1a** on the rheometer plate with the pp25/s measuring system ready to be lowered. For recovery strain tests, the bottom plate was covered with sandpaper to prevent wall slipping. (b) Original gel and (c) extruded gel examples on glass slides before rheology tests. Scale bar 1cm in all cases.

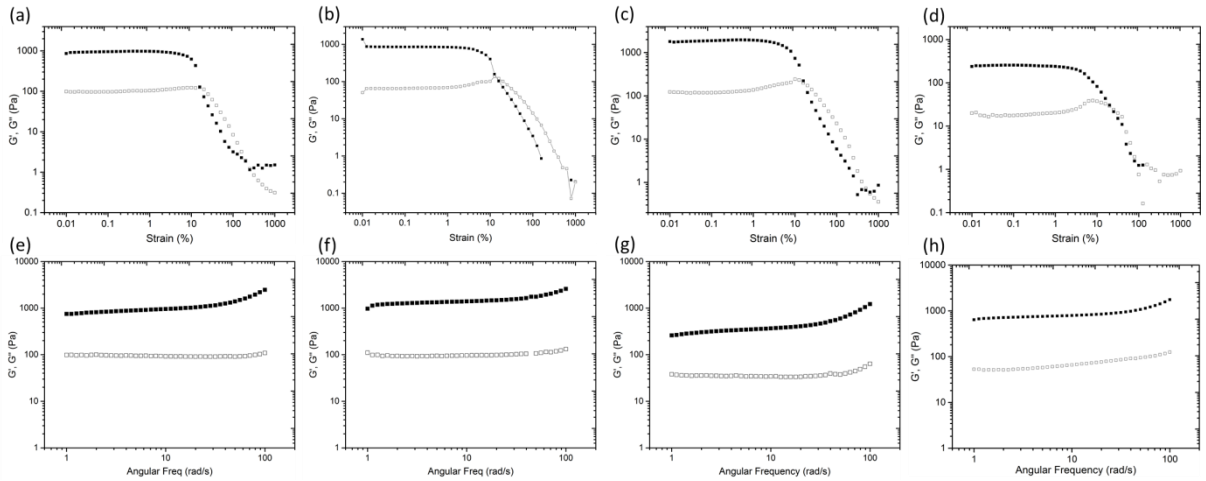

Figure 109. Strain (a-d) and frequency (e-h) sweeps of gels before extrusion (a, e) **1a**; (b, f) **1b**; (c, g) **2a**; (d, h) **2b**. Frequency sweeps were run at a strain of 0.2 %. Open circles represent G″ and solid circles represent G′.

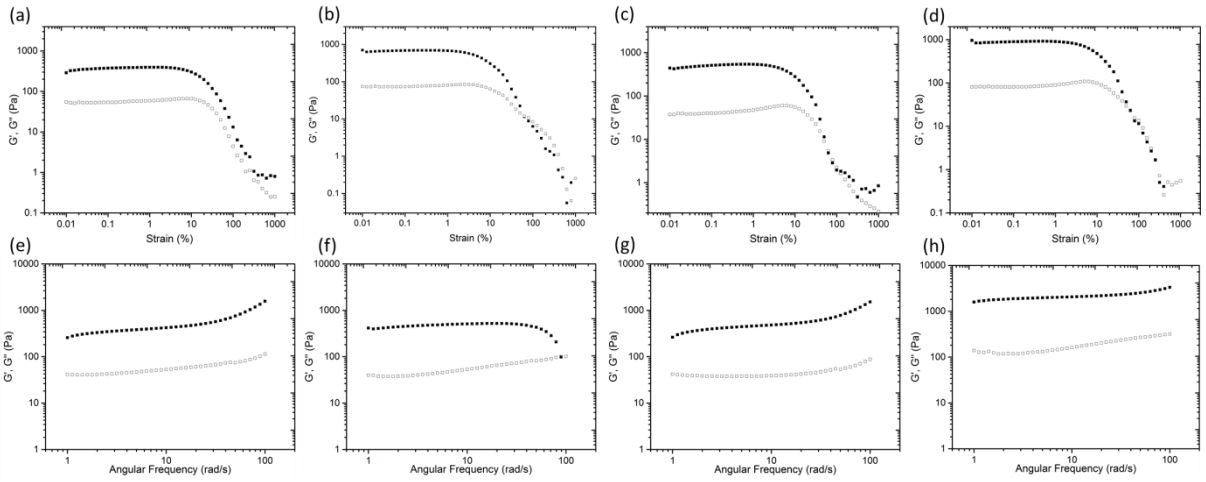

Figure 110. Strain (a-d) and frequency (e-h) sweeps of gels after extrusion (a, e) **1a**; (b, f) **1b**; (c, g) **2a**; (d, h) **2b**. Frequency sweeps were run at a strain of 0.2 %. Open circles represent G″ and solid circles represent G′.

The original gels all break at a strain of around 10-20%, shown by where G′ falls below G″ in the strain sweep. The shear rates the gels are exposed to during extrusion are much higher than the strains measured during rheology and it is fair to assume therefore that the gels are fully broken during extrusion. Figure 100-Figure 103 show visually recovered gels upon very high shear rates where the gels have fully broken during extrusion (1000 - 33,000 s^{-1}).

The absolute G′ value in the linear viscoelastic region (LVR) was similar before and after extrusion for all gels showing that the absolute moduli of the networks have not changed. Wall slippage was an issue when measuring the extruded gels and can be observed in the strain sweep of **1a** where G′ does not drop below G″ (Figure 110a). The breaking of the gel network is measured by the point where G′ falls below G″. All gels break at a higher strain after extrusion. G′ initially begins to drop at the same strain for all gels however as the extruded gels break at a higher strain this results in a longer flow region before breaking, this could be a result of the extruded gels having breaks on the macro scale (the inner diameter of the syringe tip is 0.8 mm).

Pre-compression of the gel inside the syringe also leads to a strengthening of the network with an increase in G′ and the breaking point (Figure 111). This observation is consistent with our previous data on pH-triggered gels which show that a compression of the gel results in a non-reversible strengthening of the network.[42] A compression sweep was also carried out on the rheometer where the gap distance of the measuring system was lowered by 10 μm/s while a frequency of 10 rad/s was applied and the G′ and G″ were measured. This is shown as a function of normal force, N, in Figure 112. This showed in real time that compression of the gel resulted in a strengthening of the network and may have a gradient effect on the printing results if one is printing large volumes of gel from a single syringe.

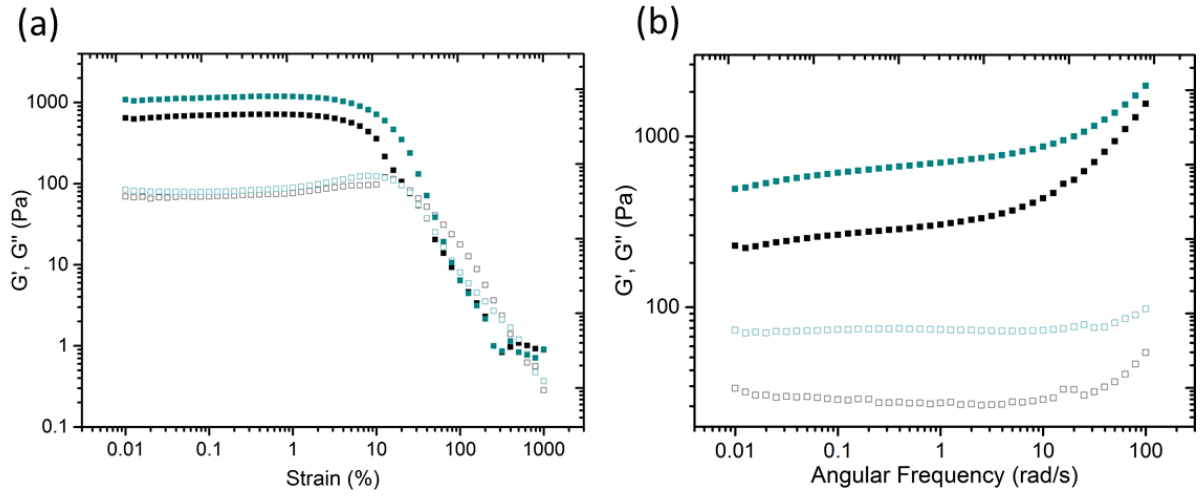

Figure 111. (a) Strain sweeps and (b) frequency sweeps of **2a** before (black) and after compression during printing (blue). Frequency sweeps were run at a constant strain of 0.2 %. Open circles represent G″ and solid circles represent G′.

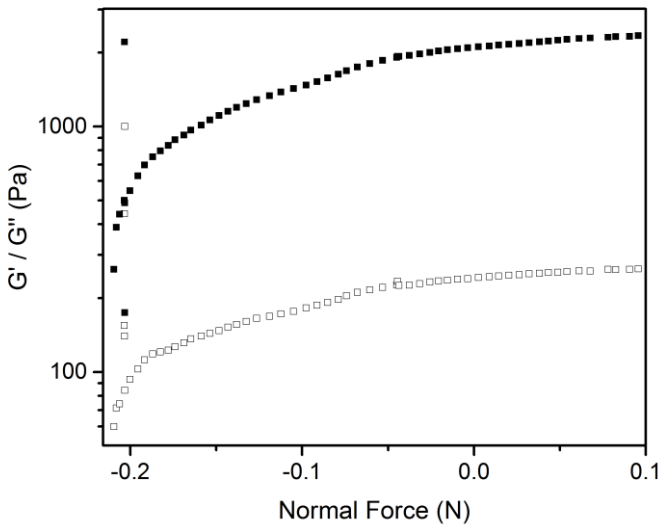

Figure 112. Compression sweep on gel **2a** where the gap between the parallel plate measuring system and base plate was decreased by 10 μm/s while applying a constant strain of 0.2 %. Open circles represent G″ and solid circles represent G′.

The presence of DMSO may be a limitation for some applications. However, we note that we have previously shown that the DMSO can be removed by iterative washing (although this is clearly not always possible or appropriate).[30] It is also possible in some cases to use other solvents such as ethanol which can be removed by evaporation.[30]

Published data shows that gel fibrils have a random orientation during flow and that gel structures with a rough orientation show better thixotropic properties than smooth gels with dense fibrous networks.[24,25] Indeed, it can be assumed that solvent-triggered gels containing localised spherical domains of fibres and fibrils allows the gel to flow more freely without destroying the microstructure of the network (see Scheme 2).

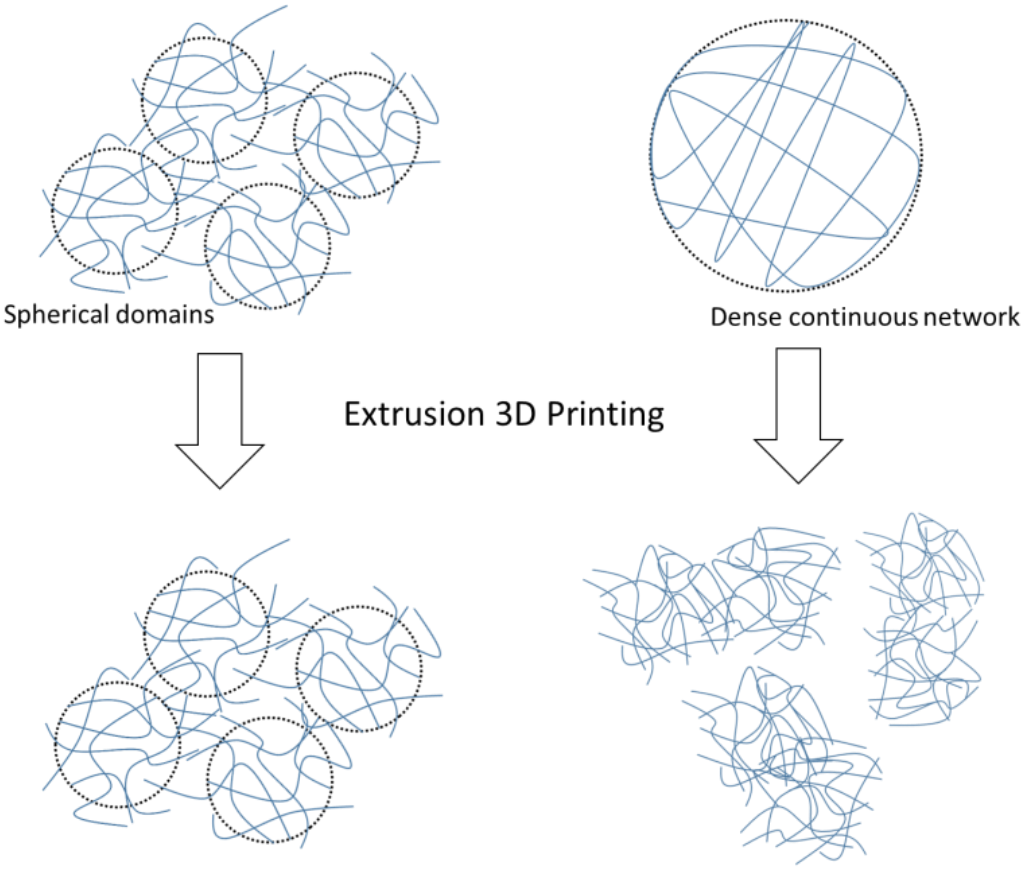

Scheme 2. Schematic showing the recovery of spherical gel domains compared to a dense continuous network of fibres after extrusion.

4.3.4. 3D Printing of Photocatalytic Perylene Bisimide Gels

Perylene bisimide dyes have been shown to be active photocatalysts in driving the hydrogen evolution reaction (Chapter 2 and 3). One main advantage of using LMWG as photocatalysts is their ease of processing. For example, a self-assembled dispersion of photocatalytic fibres is simple to prepare in aqueous solution and does not require any lengthy syntheses or a high level of technical expertise. If gels of perylene bisimides could be easily prepared and then automatically printed, this could provide another justification for the investigation of these materials for photocatalytic applications.

USANS and SANS data were collected on gels of PBI-A, L and V formed via the GdL pH switch (Figure 113). As mentioned above, the GdL switch results in a homogeneous gel with a dense fibrous network. We have shown the extrusion of these types of networks result in a more random orientation compared to the spherulitic structures from the DMSO switch. pH-

switch PBI gels have been used for extrusion here as these have already shown they have photoconductive properties and have been studied in detail (see Chapter 2 and 3).

The pH-switch gels were prepared in cuvettes for neutron scattering, a ‘dark’ scattering measurement was taken (black scatters, Figure 113) and then gels were irradiated in-situ with a UV LED for 40 minutes, after 20 minutes of irradiation a ‘light’ scattering measurement was taken (red scatters, Figure 113) then a ‘dark’ measurement was taken 20 minutes after irradiation (grey scatters, Figure 113). Gels were also prepared inside a syringe, as used for the 3D printing, and extruded into the neutron scattering cuvettes. As with previous studied on other gels earlier in the chapter, the gels are reformed after extrusion. The dark and light measurements were also taken on the extruded samples to explore the effect of extrusion on their stability during irradiation.

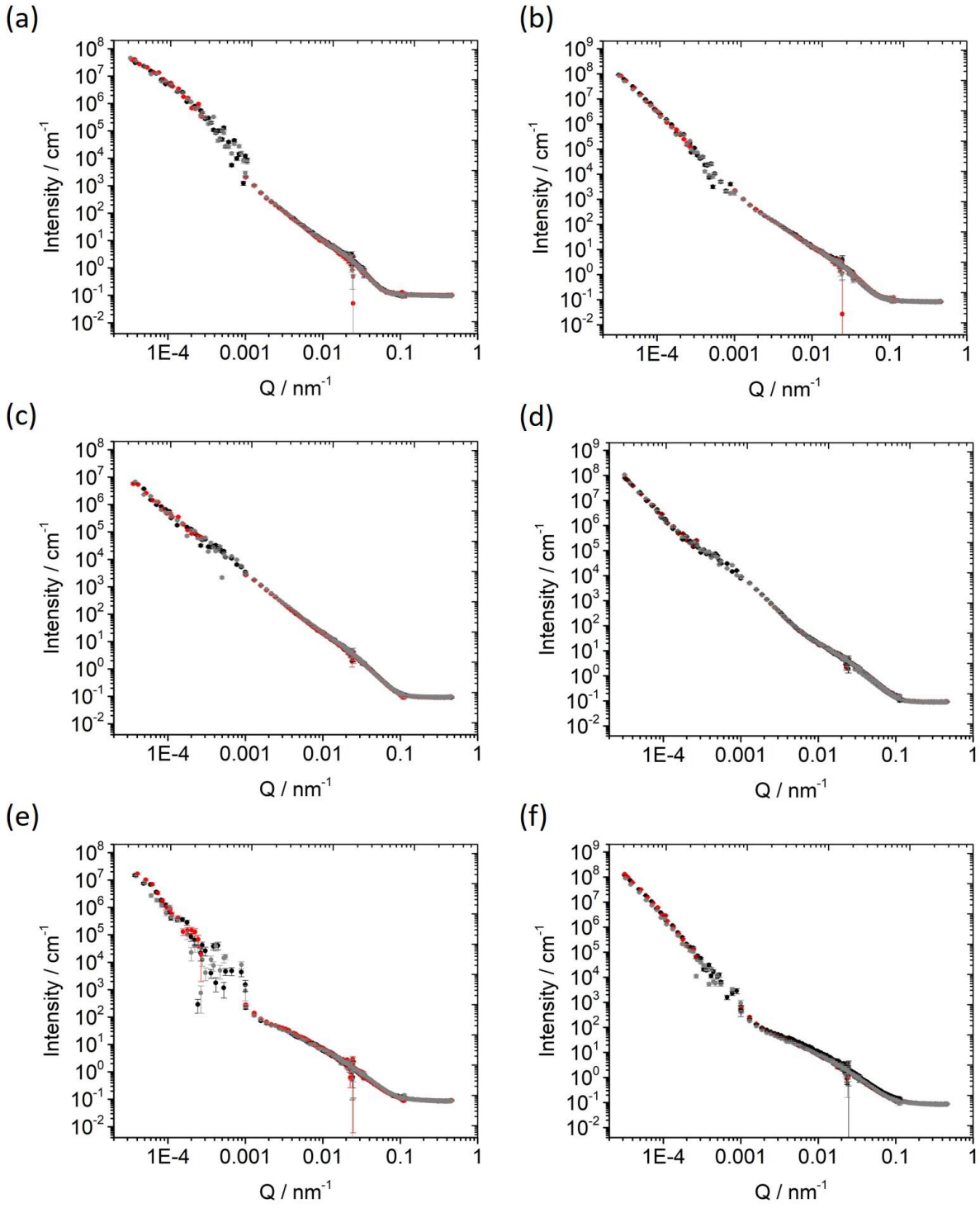

Figure 113. Neutron scattering range spanning the SANS and USANS regimes of gels prepared via a pH switch; (a) PBI-A, (b) extruded PBI-A, (c) PBI-L, (d) extruded PBI-L, (e) PBI-F and (f) extruded PBI-F. A 'dark' scattering measurement was taken (black scatters) and then gels were irradiated in-situ with a UV LED for 40 minutes, after 20 minutes of irradiation a 'light' scattering measurement was taken (red scatters) then a 'dark' measurement was taken 20 minutes after irradiation (grey scatters).

After extrusion, the scattering in the USANS regime increases in intensity due to the loss of homogeneity and the presence of more scattering structures. This correlates to the scattering and microscopy data shown with gels **1b** and **2b** where gel domains of a few 100 μm in diameter show a more random orientation compared to before extrusion. The scattering in the SANS regime, related to the primary fibres, remains unchanged showing that the changes occurring are on the larger scale. Before extrusion, the scattering of all gels is stable during and after irradiation which shows promise for their use as photoconductive materials. When extruded, the scattering intensity in the USANS regime increases, which implies a loss of the homogeneity in the structures, likely due to the gels being formed via a pH switch which from the dense network. This property is not desirable for their use as 3D printable electronic materials which would be an interesting application for these materials and so other gel preparation methods such as a solvent switch must be considered when considering the use of PBIs as 3D printable materials. Positively, the extruded gels remain stable before, during and after irradiation. In comparison with the solutions measured in a similar way in Chapter 2, the gels show much more stability with no in-situ change during irradiation.

4.4. Conclusions

We have shown that solvent-triggered gels which form spherical domains composed of tightly packed primary fibres and fibrils can be printed effectively from a syringe. The gels can be 3D printed into an array of layered designs depending on the desired application. The quality of the prints of the solvent-triggered gels surpasses those made *via* a pH trigger, which instead contain a continuous smooth fibrous network before extrusion. We think these are substantial and transferable observations which have already been demonstrated across a range of gelators including several Fmoc derivatives gelled using different triggers. We have previously shown in detail how the microstructure can be strongly affected by the method of gel formation.[29] The spherulitic microstructure needed can be achieved using a solvent-trigger to form the hydrogels. We have shown that this microstructure can be achieved for a range of LMWG, and from a range of initial solvents including DMSO (as used here), ethanol, and hexafluoroisopropanol.[30] It is also possible to vary the ratio of organic solvent to water in the final gel, and so we anticipate that it should be possible to prepare gels that can be printed with a range of properties. Importantly, the solvent-triggered gels with spherical domains were able to be 3D printed with good resolution to form a continuous fibrous network which showed superior recovery properties to those gels with different microstructures as shown by visual

examination of printed gels and microscopy along with the stability of scattering data. Finally, PBI gels have been extruded and their stability to irradiation have been measured via neutron spectroscopy. The pH switch gels have shown the predicted change upon extrusion, as seen for the other gels, and the gel networks show no change during and after irradiation. Chapter 2 describes solutions of PBIs whose networks are altered during irradiation, however as these gels have survived extrusion they are able to withstand these changes. We hope that these observations will be taken into consideration in the future when developing hydrogels for 3D printing and extrusion applications.

4.5. Experimental

4.5.1. Instruments and Procedures

3D Printer

Acknowledgements: Dr Bart Deitrich (University of Glasgow)

The 3D-printer was assembled and optimised by Bart Dietrich (University of Glasgow), for full experimental details on the setup please see the published manuscript on this work.

The 3D printing of gels was carried out on a RepRap Ormerod 2 3D printer version 528.4 (https://reprappro.com/documentation/ormerod-2/) running David Crocker's dc42 firmware version 1.09k (https://github.com/dc42/RepRapFirmware). The hot end and extruder drive of the printer were replaced with a paste extruder designed by Richard Horne (http://richrap.blogspot.co.uk/2012/04/universal-paste-extruder-ceramic-food.html). The printer was controlled *via* a modified version of Christian Hammacher's Duet Web Control user interface version 1.06 (https://github.com/chrishamm/DuetWebControl). A number of modifications to the printer's startup configuration file were necessary to accommodate the paste extruder. The hardware is shown in Figure 114.

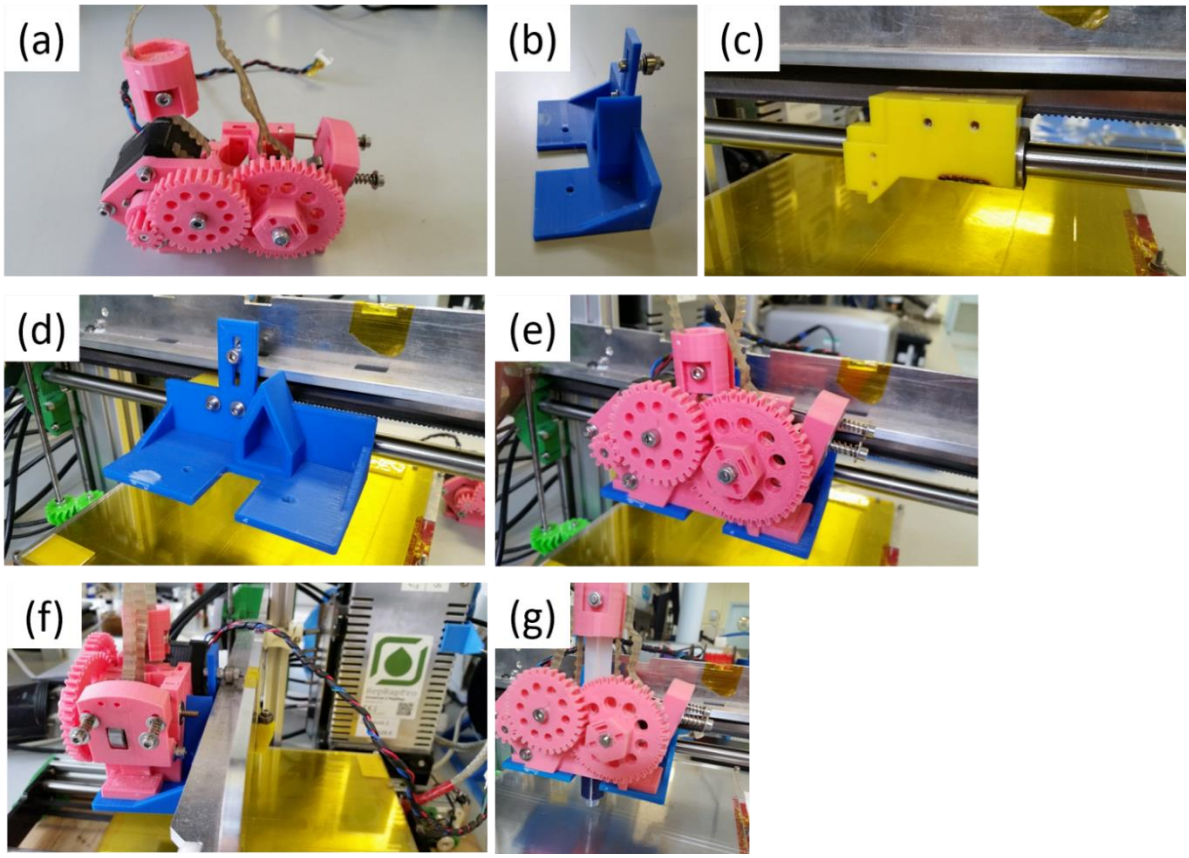

Figure 114. (a) The paste extruder, (b) Paste extruder caddy, (c) Bare x-axis carriage with hot end, infrared sensor board, and nozzle mount removed, (d) Caddy mounted to the x-axis carriage, (e) Paste extruder mounted on caddy, (f) Caddy runner bearing riding atop x-axis rib (left of vertical x-axis arm) and x-axis carriage runner bearing (right or x-axis arm), (g) The syringe and gel loaded into the paste ready to be extruded onto the printing bed.

Preparation of LMWG solutions and gels

The two LMWGs were synthesized as described previously.[38,55] Low molecular weight gelator solutions were prepared in different ways depending on their gelation trigger. The gelator solutions for the pH switch gels were prepared by weighing out 25 mg of gelator (5 mg mL^{-1}) into 14 mL vials then, while stirring, adding deionised H_2O and $NaOH_{(aq)}$ (1 eq.) to a total volume of 5 mL and stirring overnight. Then, glucono-δ-lactone (GdL) was preweighed into 10 mL polypropylene syringes (8 mg/mL). The gelator solutions were transferred in through the nozzle of the syringes via a needle and the syringes were left standing upright to gel overnight. The pH-triggered gels reached a final pH of 3.6. The gelator solutions for the solvent switch gels were prepared by weighing out 25 mg of gelator (5 mg/mL) into 14 mL vials then adding 1.5 mL dimethyl sulfoxide (DMSO). The DMSO gelator solution was sonicated in an ultrasonic bath for a few minutes until the gelator was dissolved. The DMSO solution was then

transferred to a 10mL polypropylene syringe and 3.5 mL H_2O at pH 6 was then added to the DMSO solution and left to gel overnight. The solvent-triggered gels had a final pH of 6.0.

pH measurements

A FC200 pH probe from HANNA instruments with a 6 mm × 10 mm conical tip was used for pH measurements. pH measurements were carried out on the solutions prior to gelation and on the gels post-measurement.

Rheological measurements

Rheological measurements were performed on an Anton Paar Physica MCR301 rheometer utilising a 25 mm sandblasted parallel plate geometry. Sand paper was attached to the bottom plate to prevent wall slippage for the recovery tests where a higher shear rate was applied. 3 mm thick slices of gels were carefully removed from the syringe they had formed in and then transferred to the rheometer. For the rheological measurements of extruded gels, gels were manually extruded at a rate of 1 mL/s directly onto the rheometer plate into a circular mould. In all cases the rheometer plate was lowered to the top of the gel which was a gap of approximately 3 mm.

For shear sweep measurements, a constant frequency of 10 rad/s was applied and the shear rate (s^{-1}) was ramped from 0 to 100. For frequency sweeps a shear rate of 0.02 s^{-1} was used which was within the linear viscoelastic region of the strain sweeps and the angular frequency was ramped from 1 to 100 rad/s. For compressions tests a constant shear rate of 0.02 s^{-1} as applied while the gap distance decreased at a constant rate of 10 μm/s.

Confocal Microscopy

Confocal Microscopy images were taken using a Zeiss LSM 710 confocal microscope with a LD EC Epiplan NEUFLUAR 50x (0,55 DIC) objective. Samples were stained with Nile Blue and excited at 634 nm using a He-Ne laser with the emission detected between 650 and 710 nm. Gels were prepared in disposable Greiner Bio-One CELLviewTM 35 mm plastic cell culture dishes with a glass bottom. Extruded gels were prepared in a syringe then extruded into the cell culture dish shortly before imaging. To stain the pH switch gels with Nile Blue, a 0.1 wt% Nile Blue solution was prepared and added to the gelator solution at 2 μL/mL. To stain the solvent switch gels the Nile Blue was mixed with the water and added to the DMSO gelator solution to a final Nile Blue concentration of 2 μL/mL.

Small Angle Neutron Scattering (SANS)

SANS measurements of the gelator solutions were performed using the SANS2D time-of-flight diffractometer (STFC ISIS Pulsed Neutron Source, Oxfordshire, UK).[56] A simultaneous Q-range [$Q = 4\pi \sin(\theta/2)/\lambda$, where θ is the scattering angle] of 0.005 to 0.7 Å−1 was achieved using an incident wavelength (λ) range of 1.75 to 16.5 Å and employing a sample-to-detector distance of 4 m, with the 1 m^2 detector offset vertically 60 mm and sideways 100 mm. The incident neutron beam was collimated to 8 mm diameter. Samples were housed in 2 mm pathlength quartz cuvettes and measured for 60 minutes each. The 'raw' scattering data were normalized to the incident neutron wavelength distribution, corrected for the linearity and efficiency of the detector response and the measured neutron transmission (*i.e.*, absorbance) using the Mantid framework.[57,58] They were then placed on an absolute scale by comparison with the expected scattering from a partially-deuterated polystyrene blend of known composition and molecular weights in accordance with established procedures.[59] The background scattering from a quartz cell containing the deuterated solvent and was then subtracted. The resulting 'reduced' scattering data were then fitted to a customized model comprising of a (Kratky-Porod) flexible cylinder and an absolute power law in the SasView software (version 4.1.1).[47–49] The power law (Q^{-m}) accounts for the mass fractal contribution to the scattering intensity which is combined with the flexible cylinder and sphere models.

The SANS measurements for Figure 113 were performed using the NG7SANS instrument (NCNR, NIST, Gaithersburg, MD, USA). The Q-range [$Q = 4\pi \sin(\theta/2)/\lambda$, where θ is the scattering angle] of 0.001 to 0.5 $Å^{-1}$ was achieved using standard 3 detector geometries (1m with an 0.25m detector offset, 4m,13m) with 6 Å neutrons and the neutron lens setting at 8.13Å neutron wavelength. The samples were housed in 5 mm standard cell holders with quartz windows and measured for 60 minutes before and after irradiation, and for 20 minutes during irradiation. Counting times and scattering data points were adjusted accordingly to reduce data collection time for in-situ measurements. Scattering data were normalized for the sample transmission and background corrected using a quartz cell with D_2O and also corrected for the linearity and efficiency of the detector response using the NCNR Igor macros.

Ultra Small Angle Neutron Scattering (USANS)

USANS measurements of the gelator solutions were performed using the BT5 instrument (NIST Center for Neutron Research (NCNR), National Institute for Standards and Technology

(NIST), Gaithersburg, MD, USA). A Q-range [$Q = 4\pi \sin(\theta/2)/\lambda$, where θ is the scattering angle] of 0.00003 to 0.0011 $Å^{-1}$ was achieved using a Bonse-Hart type double crystal diffractometer with a wavelength (λ) of 2.4Å ($\Delta\lambda/\lambda$=6%) in the standard geometry.[60] Samples were housed in 5 mm quartz cuvettes and measured for 4 h each if the full scatter was taken. Scattering data were normalized for the sample transmission and background corrected using a quartz cell containing the deuterated solvent.[45]

For irradiation samples, a new environment setup was used where a fiber optic light was focused onto the sample while house in the beam line (Figure 115). The light was switched on and off using a digital script which also controlled the measuring of the scattering, this allowed for an accurate kinetics analysis of samples before, during and after irradiation.

The UV sample series were measured with half the counting time for standard samples and, in order to scan for the time dependence of the sample change, three additional shorter scans were performed for each sample. The full scans at the beginning and end of each sample irradiation covered a Q-range of 0.00003 to 0.0011 $Å^{-1}$ in approximately 105 minutes and the shorter scans covered approximately one order of magnitude in q (0.00003 to 0.00027 $Å^{-1}$) lasting approximately 26 minutes each.

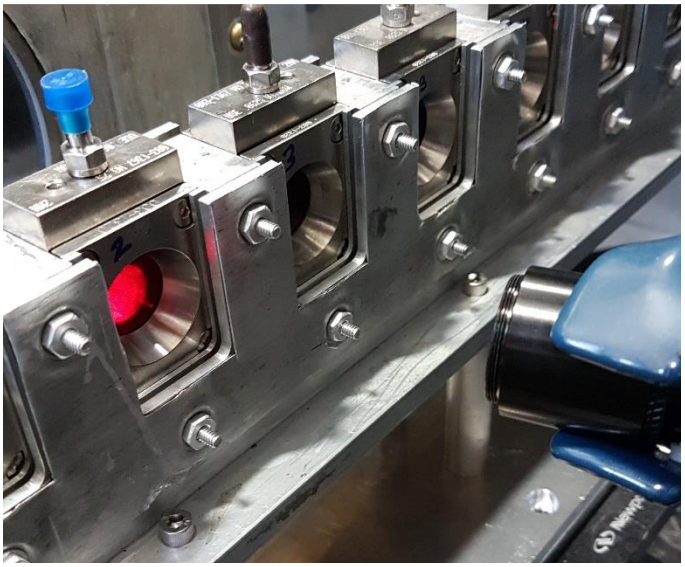

Figure 115. Photograph of the sample environment at the SANS beamline showing the focussing of the UV light onto the area of the sample to be measured during scattering.

4.6. References

1 J. L. Drury and D. J. Mooney, *Biomaterials*, 2003, **24**, 4337–4351.

2 M. Rodrigues, A. C. Calpena, D. B. Amabilino, M. L. Garduño-Ramírez and L. Pérez-García, *J. Mater. Chem. B*, 2014, **2**, 5419.

3 S. Gupta, M. Singh, A. R. M., P. S. Yavvari, A. Srivastava and A. Bajaj, *RSC Adv.*, 2016, **6**, 19751–19757.

4 K. J. Skilling, F. Citossi, T. D. Bradshaw, M. Ashford, B. Kellam and M. Marlow, *Soft Matter*, 2014, **10**, 237–56.

5 X. Li, Y. Wang, C. Yang, S. Shi, L. Jin, Z. Luo, J. Yu, Z. Zhang, Z. Yang and H. Chen, *Nanoscale*, 2014, **6**, 14488–14494.

6 Y. Zhou and X. Li, *Chin. Chem. Lett.*, 2017, **28**, 1835–1840.

7 T. Billiet, M. Vandenhaute, J. Schelfhout, S. Van Vlierberghe and P. Dubruel, *Biomaterials*, 2012, **33**, 6020–6041.

8 S. V. Murphy, A. Skardal and A. Atala, *J. Biomed. Mater. Res. - Part A*, 2013, **101 A**, 272–284.

9 T. Jungst, W. Smolan, K. Schacht, T. Scheibel and J. Groll, *Chem. Rev.*, 2016, **116**, 1496–1539.

10 A. Carlson, A. M. Bowen, Y. Huang, R. G. Nuzzo and J. A. Rogers, *Adv. Mater.*, 2012, **24**, 5284–5318.

11 S. Ji and M. Guvendiren, *Front. Bioeng. Biotechnol.*, 2017, **5**, 1–8.

12 T. J. Hinton, Q. Jallerat, R. N. Palchesko, J. H. Park, M. S. Grodzicki, H.-J. Shue, M. H. Ramadan, A. R. Hudson and A. W. Feinberg, *Sci. Adv.*, 2015, **1**, 1–10.

13 J. A. Reid, P. A. Mollica, G. D. Johnson, R. C. Ogle, R. D. Bruno and P. C. Sachs, *Biofabrication*, 2016, **8**, 025017.

14 K. Hölzl, S. Lin, L. Tytgat, S. Van Vlierberghe, L. Gu and A. Ovsianikov, *Biofabrication*, 2016, **8**, 032002.

15 L. Ouyang, C. B. Highley, C. B. Rodell, W. Sun and J. A. Burdick, *ACS Biomater. Sci. Eng.*, 2016, **2**, 1743–1751.

16 L. Ouyang, C. B. Highley, W. Sun and J. A. Burdick, *Adv. Mater.*, 2017, **29**, 1604983.

17 L. Shi, H. Carstensen, K. Hölzl, M. Lunzer, H. Li, J. Hilborn, A. Ovsianikov and D. A. Ossipov, *Chem. Mater.*, 2017, **29**, 5816–5823.

18 L. C. Hsiao, A. Z. M. Badruddoza, L.-C. Cheng and P. S. Doyle, *Soft Matter*, 2017, **13**, 921–929.

19 C. B. Highley, C. B. Rodell and J. A. Burdick, *Adv. Mater.*, 2015, **27**, 5075–5079.

20 R. Suntornnond, J. An and C. K. Chua, *Macromol. Mater. Eng.*, 2017, **302**, 1600266.

21 A. M. Pekkanen, R. J. Mondschein, C. B. Williams and T. E. Long, *Biomacromolecules*, 2017, **18**, 2669–2687.

22 I. Donderwinkel, J. C. M. van Hest, N. R. Cameron, M. Duocastella, B. Pippenger, S. Bellance, R. Bareille, M. Remy, L. Bordenave, J. Amedee, F. Guillemot, P. Strippoli, S. Canaider, A. Tamayol, A. Khademhosseini, M. R. Dokmeci, A. Atala, A. Khademhosseini, G. H. Zhu, X. Y. Jin, S. R. Shin, M. R. Dokmeci and A. Khademhosseini, *Polym. Chem.*, 2017, **31**, 7250–7256.

23 J. P. Schneider, D. J. Pochan, B. Ozbas, K. Rajagopal, L. Pakstis and J. Kretsinger, *J. Am. Chem. Soc.*, 2002, **124**, 15030–15037.

24 C. Yan, A. Altunbas, T. Yucel, R. P. Nagarkar, J. P. Schneider and D. J. Pochan, *Soft Matter*, 2010, **6**, 5143–5156.

25 N. Zanna, S. Focaroli, A. Merlettini, L. Gentilucci, G. Teti, M. Falconi and C. Tomasini, *ACS Omega*, 2017, **2**, 2374–2381.

26 X. Huang, S. R. Raghavan, P. Terech and R. G. Weiss, *J. Am. Chem. Soc.*, 2006, **128**, 15341–15352.

27 B. Raphael, T. Khalil, V. L. Workman, A. Smith, C. P. Brown, C. Streuli, A. Saiani and M. Domingos, *Mater. Lett.*, 2017, **190**, 103–106.

28 B. A. Aguado, W. Mulyasasmita, J. Su, D. Ph, K. J. Lampe, D. Ph, S. C. Heilshorn and D. Ph, *Tissue Eng. Part A*, 2012, **18**, 806–815.

29 J. Raeburn, A. Zamith Cardoso and D. J. Adams, *Chem. Soc. Rev.*, 2013, **42**, 5143–56.

30 J. Raeburn, C. Mendoza-Cuenca, B. N. Cattoz, M. A. Little, A. E. Terry, A. Zamith Cardoso, P. C. Griffiths and D. J. Adams, *Soft Matter*, 2015, **11**, 927–935.

31 C. Colquhoun, E. R. Draper, R. Schweins, M. Marcello, D. Vadukul, L. C. Serpell and D. J. Adams, *Soft Matter*, 2017, **13**, 1914–1919.

32 F. Tantakitti, J. Boekhoven, X. Wang, R. V. Kazantsev, T. Yu, J. Li, E. Zhuang, R. Zandi, J. H. Ortony, C. J. Newcomb, L. C. Palmer, G. S. Shekhawat, M. O. De La Cruz, G. C. Schatz and S. I. Stupp, *Nat. Mater.*, 2016, **15**, 469–476.

33 J. Raeburn, G. Pont, L. Chen, Y. Cesbron, R. Lévy and D. J. Adams, *Soft Matter*, 2012, **8**, 1168–1174.

34 M. D. Segarra-Maset, V. J. Nebot, J. F. Miravet and B. Escuder, *Chem. Soc. Rev.*, 2013, **42**, 7086–7098.

35 L. Chen, S. Revel, K. Morris, L. C. Serpell and D. J. Adams, *Langmuir*, 2010, **26**,

13466–13471.

36 A. Mahler, M. Reches, M. Rechter, S. Cohen and E. Gazit, *Adv. Mater.*, 2006, **18**, 1365–1370.

37 N. A. Dudukovic and C. F. Zukoski, *Langmuir*, 2014, **30**, 4493–4500.

38 D. J. Adams, M. F. Butler, W. J. Frith, M. Kirkland, L. Mullen and P. Sanderson, *Soft Matter*, 2009, **5**, 1856–1862.

39 Y. Pocker and E. Green, *J. Am. Chem. Soc.*, 1973, **95**, 113–119.

40 J. Gao, C. Tang, M. A. Elsawy, A. M. Smith, A. F. Miller and A. Saiani, *Biomacromolecules*, 2017, **18**, 826–834.

41 R. Darby, *Chemical Engineering and Fluid Mechanics*, Marcel Dekker Inc, 1996.

42 D. J. Adams, L. M. Mullen, M. Berta, L. Chen and W. J. Frith, *Soft Matter*, 2010, **6**, 1971–1980.

43 S. Kyle, Z. M. Jessop, A. Al-Sabah and I. S. Whitaker, *Adv. Healthc. Mater.*, 2017, DOI: 10.1002/adhm.201700264.

44 L. Chen, J. Raeburn, S. Sutton, D. G. Spiller, J. Williams, J. S. Sharp, P. C. Griffiths, R. K. Heenan, S. M. King, A. Paul, S. Furzeland, D. Atkins and D. J. Adams, *Soft Matter*, 2011, **7**, 9721–9727.

45 S. R. Kline, *J. Appl. Crystallogr.*, 2006, **39**, 895–900.

46 SasView - Small Angle Scattering Analysis, http://www.sasview.org, (accessed 1 October 2016).

47 A. Guinier and G. Fournet, *John Wiley Sons, Inc., New York*, 1955, 1–19.

48 J. S. Pedersen and P. Schurtenberger, *Macromolecules*, 1996, **29**, 7602–7612.

49 W. R. Chen, P. D. Butler and L. J. Magid, *Langmuir*, 2006, **22**, 6539–6548.

50 K. L. Morris, L. Chen, J. Raeburn, O. R. Sellick, P. Cotanda, A. Paul, P. C. Griffiths, S. M. King, R. K. O'Reilly, L. C. Serpell and D. J. Adams, *Nat. Commun.*, 2013, **4**, 1480.

51 A. Z. Cardoso, L. L. E. Mears, B. N. Cattoz, P. C. Griffiths, R. Schweins and D. J. Adams, *Soft Matter*, 2016, **12**, 3612–3621.

52 M. C. Nolan, J. J. Walsh, L. L. E. Mears, E. R. Draper, M. Wallace, M. Barrow, B. Dietrich, S. M. King, A. J. Cowan and D. J. Adams, *J. Mater. Chem. A*, 2017, **5**, 7555–7563.

53 M. A. Iannuzzi, R. Reber, D. M. Lentz, J. Zhao, L. Ma and R. C. Hedden, *Polymer*, 2010, **51**, 2049–2056.

54 H. R. Ramay, M. C. Branco, P. Schneider and D. J. Pochan, *Faraday Discuss.*, 2008, **139**, 251–264.

55 J. Gupta, D. J. Adams and N. G. Berry, *Chem. Sci.*, 2013, **7**, 1–3.

56 ISIS Neutron and Muon Source, http://isis.stfc.ac.uk/, (accessed 10 February 2016).

57 O. Arnold, J. C. Bilheux, J. M. Borreguero, A. Buts, S. I. Campbell, L. Chapon, M. Doucet, N. Draper, R. Ferraz Leal, M. A. Gigg, V. E. Lynch, A. Markvardsen, D. J. Mikkelson, R. L. Mikkelson, R. Miller, K. Palmen, P. Parker, G. Passos, T. G. Perring, P. F. Peterson, S. Ren, M. A. Reuter, A. T. Savici, J. W. Taylor, R. J. Taylor, R. Tolchenov, W. Zhou and J. Zikovsky, *Nucl. Instruments Methods Phys. Res. Sect. A Accel. Spectrometers, Detect. Assoc. Equip.*, 2014, **764**, 156–166.

58 Mantid Project, http://www.mantidproject.org/, (accessed 8 February 2016).

59 G. D. Wignall and F. S. Bates, *J. Appl. Crystallogr.*, 1987, **20**, 28–40.

60 A. R. Drews, J. A. Barker, C. J. Glinka and M. Agamalian, *Phys. B*, 1998, **241**–**243**, 189–191.

CHAPTER 5

Summary, Conclusions and Future Work

The overall aim of the work in this Thesis was to investigate how the self-assembled structures of low molecular weight gelators can be optimised to attain desirable photocatalytic and recovery properties. Importantly the work shows the importance of the supramolecular structure exhibiting the properties rather than the results being driven from the starting molecule itself. The first application studied was the photocatalytic activity for hydrogen evolution. Self-assembled aggregates of perylene bisimides were prepared using a pH switch and the supramolecular assemblies in solution were irradiated with light in the presence of methanol and a platinum co-catalyst. Upon irradiation, the perylene bisimides become reduced, forming a radical anion which can be transported across the π-orbitals of adjacent molecules. A phenylalanine-substituted PBI (PBI-F) was dissolved at high pH and self-assembly was promoted via a slow pH drop using acid. The pH was carefully controlled, and the specific structures present in the solutions of different pH were characterised using neutron scattering, spectroscopy and rheology. This study showed that PBI-F self-assembles into H-aggregated structures in solution which become longer and more numerous as the pH is lowered below each of the two apparent pK_a values, which were found at pH 8.6 and pH 5.7. Samples at each pH were irradiated with white light for 4 hours in the presence of methanol and platinum and the amount of hydrogen produced was measured. The activity for hydrogen evolution turned on in-line with the formation of self-assembled structures, providing good evidence that the self-assembled gelator is more active as a photocatalyst than the molecularly dissolved species. Electrochemical studies showed that the radical anion and dianion species were generated in the solutions, and that the turn-on in hydrogen production coincided with the dianion species having enough energy to drive the reaction. There are many possible explanations as to why the aggregates are more active than the dissolved species; efficient electron transport along a conductive fibre can help promote the charge transfer of free charge carriers which can then donate to a co-catalyst, the longer fibres can also help increase the interactions between the photocatalyst and co-catalyst. The key to this work was to provide a link between the type of supramolecular assembly and the activity for hydrogen evolution and this link was made.

Photocatalytic experiments are time consuming and require repeat measurements for more accurate results. Therefore, high throughput instrumentation was utilised to expand the photocatalysis study. A library of amino-acid substituted perylene bisimide compounds were prepared and studied, each of which exhibited differing activities and electronic behaviour. The PBIs prepared were PBI-A, F, H, L, S, V, W and Y. The high throughput instrumentation

allowed for many parameters to be considered including concentration, co-catalyst ratio, pH and the use of co-solvents.

All PBIs provided some activity for hydrogen evolution however some, such as PBI-V and PBI-F, were more active. The concentration played a key role in both the amount and the rate of hydrogen evolution where an optimal concentration of 0.1 mg/mL was observed for PBI-V solutions which reached a hydrogen evolution rate of 150 $\mu molg^{-1}h^{-1}$. Electronic considerations showed that the amount of radical anion produced reached a plateau for PBI-V concentrations above 5 mg/mL. A UV-Vis spectroscopy study on the pH of PBI-V also revealed that solutions at pH 5 contained the highest concentration of radical anion and dianion during irradiation and this solution was also the most active for hydrogen production. The addition of an antisolvent methanol, as described in Chapter 4, promotes a spherulitic aggregation mechanism. For the photocatalytic solutions, the addition of methanol at pH 6 results in a turn-on in activity which can be attributed to the presence of self-assembled aggregates. When comparing self-assembly between a solvent switch and a pH-switch, the pH-switch provides stable and more photocatalytically-active structures, possibly due to the stability of fibrillar aggregates over spherulitic aggregates. In addition, the stability of the photocatalytic solutions was studied by collecting neutron scattering data during in-situ UV irradiation by using a custom sample environment. Measurements showed reversible in-situ changes in the most active photocatalytic solutions and that low molecular weight gels of PBIs are stable to irradiation. It is not understood why some PBI derivatives are more active than others but the extent of aggregation seems to be key to the activity. The UV-Vis study reaffirms that pH and aggregation are key to device performance. High concentrations of PBI can result in more instances of electron recombination which reduces the amount of free charge carriers available in solution, reducing the concentration to lower concentrations also reduces the solution viscosity which aids mixing and improves the light penetration through the sample. To further this work, a structural and rheological analysis and comparison should be carried out on PBI-V and PBI-F solutions with and without methanol at medium and low pH. At these pH a subtle turn-on and turn-off relationship was observed for photocatalysis which may be attributed to the presence of no aggregation (turn off), spherulitic aggregation in the presence of methanol (slight turn-on in activity) and long-range fibrous aggregation (significant turn-on in activity).

The second application studied within this thesis is the use of low molecular weight gels for 3D printing. Napthol- and Fmoc-based gelators have been used as proof-of-principle gelators and their gels prepared via both pH- and solvent-switch methods. The microstructure is strongly affected by the method of gel formation, where pH-switch gels form a homogeneous fibrous network and solvent-switch gels form heterogeneous spherical domains, as measured by neutron scattering and confocal microscopy. Solvent-switch gels showed good recovery after flow as these gels were able to be 3D printed using an extrusion printer and we able to recover their physical properties.

Ultra-small angle and small angle neutron scattering helped to understand how the networks were being altered after flow. The primary fibres (up to ~100 nm) remained unchanged after flow whereas the long-range network (~1-10 μm) remained unchanged for the solvent-switch gels but indicated a loss in homogeneity in the pH-switch gels. The preparation conditions and microstructure of gels should be carefully selected when considering low molecular weight gels for extrusion-based applications. It is anticipated that gels can be prepared with a spherulitic microstructure which can be printed with a range of properties. This should allow direct printing and patterning of substrates with photocatalytically-active materials, for example as photoelectrodes. To further this work, photocatalytically active gels inspired from solutions such as those studied in Chapters 2 and 3 should be 3D printed and studied in photocatalytic experiments. The proof-of-principle that certain gel networks can be designed for 3D printing should be studied with direct applications to show the success of designing printable gels. The stability and interactions of molecules such as co-catalysts or drug molecules within the gel network should also be studied before and after extrusion to understand the viability for use of these designed networks in delivery systems. In addition, this work would benefit from further structural understanding of the in-situ changes of pH 4.5 PBI solutions during irradiation, as these solutions were the most photocatalytically active and were also the only solutions which exhibited in-situ changes during the on-line irradiation USANS experiments.

Overall, this thesis has shown and re-affirmed the importance of molecular packing and network types in self-assembled materials. It is clear that it is insufficient when describing these materials to simply state that a specific molecule has been self-assembled. Instead, the exact

nature of the aggregates across many length scales needs to be described to fully capture the complexity of the system and effectively apply them in next generation technologies.